

MODELING PHOTOSYNTHETICALLY
AVAILABLE RADIATION FROM SATELLITE AND
FIELD DATA AND ITS IMPACT ON OCEAN
PRIMARY PRODUCTION

A Thesis Submitted to
Nirma University
In Partial Fulfilment of the Requirements for
The Degree of

Doctor of Philosophy

In

SCIENCE

BY

Madhumita Tripathy

(Reg. No. 09EXTPHDS19)



Institute Of Science
Nirma University
Ahmedabad- 382481
Gujarat, India
October, 2015

CERTIFICATE

This is to certify that the thesis entitled "Modeling photosynthetically available radiation from satellite and field data and its impact on ocean primary production" has been prepared by my Madhumita Tripathy under my supervision and guidance. The thesis is her own original work completed after careful research and investigation. The work of the thesis is of the standard expected of a candidate for Ph.D Programme in Science and I recommended that it be sent for evaluation.

Date: 7/10/2015



Signature of the Guide

Forwarded by:

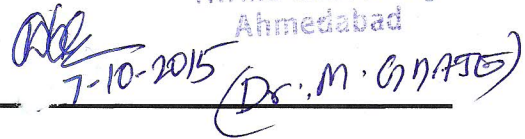


Name and signature of the Head of the Department
Dr. Prakash Chauhan
Group Head,
जैविक एवं ग्रहीय विज्ञान तथा अनुप्रयोग गृह (बीपीएमजी)
Sciences and Applications Group (BPSG)
भू, समुद्र, वायुमंडल, ग्रहीय विज्ञान और उपयोग क्षेत्र (ईपीएसए)
Earth, Ocean, Atmosphere, Planetary Sciences & Applications Area (EPSA)
अंतरिक्ष उपयोग केंद्र (इसरो) Space Applications Centre, (ISRO)
अंतरिक्ष विभाग, भारत सरकार Dept. of Space, Govt. of India
अहमदाबाद Ahmedabad 380 015



Name and signature of the Dean

Faculty of Science
Director
Institute of Science
Nirma University
Ahmedabad



7-10-2015 (Dr. M. G. NATE)

Name and signature of the Dean

Faculty of Doctoral Studies and Research

Executive Registrar

ABSTRACT

Ocean colour remote sensing is a useful tool and it provides quantitative information of seawater constituents. OCEANSAT-1 OCM and OCEANSAT-2 OCM are two Indian Ocean observation satellites which have been extensively used for various societal and scientific applications like Potential Fishing Zone identification, ocean primary productivity estimation, algal bloom detection and studying the coastal processes etc. Photosynthetically available radiation (PAR) with spatially invariant and uniform aerosol optical depth under clear sky condition has been used in current primary production models using OCM data. Thus, modeling PAR from OCM under variable aerosol loading and cloud coverage is a desirable input parameter to estimate ocean primary production from OCM more accurately.

PAR has been estimated from OCM using two different methods for spatially variable aerosols and cloudy condition. In method I, the atmosphere is treated as a single layer in clear sky condition or as double layer in cloudy conditions i.e., a layer above the cloud top and a layer from the cloud top downwards. The two main input parameters to estimate PAR i.e., aerosol optical depth (AOD) and cloud optical depth (COD) have been estimated from OCM data. Surface reflectance has been neglected in the first method. In method II, the effects of clouds and clear atmosphere can be decoupled with cloud system and surface albedo. In the second method, surface and cloud albedo have been estimated from OCM.

PAR estimated from OCM has been compared with PAR measured from surface downwelling flux measurement instrument during different seasons in the Arabian Sea. Other than *in-situ* data obtained from ship cruise, OCEANSAT-2 OCM estimated PAR have been validated with *in-situ* measured PAR obtained from surface irradiance data of a buoy located at the CAL-VAL site situated between Kavaratti and Agatti island in the Arabian Sea. The root mean square (r.m.s) difference between OCEANSAT-1 OCM PAR estimated using both the methods compared to *in-situ* measured PAR were within the accepted range ($\pm 10\%$) for PAR estimation from remote sensing. However, root mean square difference between PAR estimated from OCEANSAT-1 OCM and *in-situ* measured PAR was lower for method I compared to method II.

OCEANSAT-1 & 2 OCM estimated PAR also has been compared with PAR estimated from other ocean colour sensors such as SeaWiFS (Sea-viewing Wide Field-of-view Sensor) and MODIS (Moderate Resolution Imaging Spectroradiometer). OCEANSAT-1 OCM PAR estimated from method I had good correlation with correlation coefficient (r^2) 0.95 with SeaWiFS PAR under clear sky condition. The correlation coefficient (r^2) between OCEANSAT-1 OCM PAR estimated using method II with SeaWiFS PAR was 0.80. OCEANSAT-2 OCM estimated PAR using method I shows poor correlation (correlation coefficient 0.63) compared to OCEANSAT-1 OCM with *in-situ* measured PAR at CAL-VAL site situated between Kavaratti and Agatti island. The probable reason behind to get poor correlation between OCEANSAT-2 OCM PAR and *in-situ* measured PAR has been explained to the dynamic variability of clouds over Kavaratti region. However, OCEANSAT-2 OCM estimated PAR have good correlation (correlation coefficient r^2 0.84) with MODIS Aqua estimated PAR at Kavaratti region.

In order to understand the variability of PAR under different aerosol types and different aerosol loading, a simulation study has been carried out using COART (Coupled Ocean Atmosphere Radiative Transfer) model. Euphotic primary production has been estimated using an analytical non-spectral model for various PAR values under different aerosol loading and cloud coverage conditions. Sensitivity analysis showed that for maritime, maritime polluted, and desert aerosols, PAR has attenuated to about 11–25%, whereas it has attenuated to 44% for urban aerosol type compared to clear sky. PAR has been reduced by ~57% for high aerosol loading and for overcast sky. The decrease in euphotic primary production under various aerosol loading and cloud coverage was observed to depend on the photoadaptation parameters. Euphotic primary production was reduced by 38% for maximum maritime aerosol loading and for overcast sky compared to clear sky.

Thus, PAR estimated under various aerosols loading and cloud coverage has shown improvement in the quantification of ocean euphotic primary production from OCM. Validation results between OCM PAR and *in-situ* measured PAR and comparative study between OCM PAR and SeaWiFS, MODIS estimated PAR shows that PAR from OCEANSAT-1 & 2 OCM could be produced reasonably accurately over the tropical Indian

Ocean region. This approach can be extended to future OCEANSAT-3 OCM data for operational estimation of PAR for regional marine ecosystem applications.

DECLARATION

I, Madhumita Tripathy, registered as Research Scholar, bearing Registration No. 09EXTPHDS19 for Doctoral Programme under the Faculty of Science of Nirma University do hereby declare that I have completed the course work, pre-synopsis seminar and my research work as prescribed under R.Ph.D.3.5.

I do hereby declare that the thesis submitted is original and is the outcome of the independent investigations/research carried out by me and contains no plagiarism. The research is leading to the discovery of new facts/ techniques/ correlation of scientific facts already known. This work has not been submitted to any other University or Body in quest of a degree, diploma or any other kind of academic award.

I do hereby further declare that the text, diagrams or any other material taken from other sources (including but not limited to books, journals and web) have been acknowledged, referred and cited to the best of my knowledge and understanding.

Date: 07/10/2015

Madhumita Tripathy

Signature of the Student

ACKNOWLEDGEMENTS

I express my sincere gratitude to my Research guide and supervisor, **Dr. Prakash Chauhan**, Group Head, Biological and Planetary Sciences and Applications Group (BPSG), Earth, Ocean, Atmosphere, Planetary Sciences and Applications Area (EPSA), Space Applications Centre (SAC), Indian Space Research Organization (ISRO), for his inspiring guidance without which this work would not have been possible. It was his suggestions and comments, which gave this thesis its final shape.

I convey my heartfelt thanks to Director, Space Applications Centre (SAC), Indian Space Research Organization (ISRO), Ahmedabad, for granting me permission to pursue my Ph. D. study and for providing me all the necessary facilities during my research work. I also thankfully acknowledge the support of Deputy Director, Earth, Atmosphere, Planetary Sciences and Applications Area (EPSA), Space Applications Centre (SAC), Indian Space Research Organization (ISRO).

I feel privileged in expressing my gratitude to **Dr. Mini Raman**, Head, Marine Ecosystem Division, Biological and Planetary Sciences and Applications Group (BPSG), Earth, Ocean, Atmosphere, Planetary Sciences and Applications Area (EPSA), Space Applications Centre (SAC), Indian Space Research Organization (ISRO) for her guidance about instrument operation, *in situ* data collections and processing during different ship campaigns. Her perpetual encouragements, valuable suggestions about my research work are source of inspiration and motivation for me. I am also grateful to **Dr. A.S. Rajawat and Dr. Rashmi Sharma** for their valuable suggestions during my R.P.C (Research Progress Committee) meetings.

I am also thankful to **Dr. Anup Singh**, Director General, **Dr. A.S. Patel**, Deputy Registrar, Ph.D. Section, **Dr. Manjunath Ghate**, Dean Faculty of Doctoral Studies & Research, **Dr. C. Gopalkrishnan**, former Dean, Faculty of Doctoral Studies & Research, **Prof. Sarat Dalai**, Dean Faculty of Science, **Dr. G. Naresh Kumar**, former Dean, Faculty of Science, Nirma University, Ahmedabad, for allowing me to register as a Ph. D. student and for all the support

to carry out Ph.D. study. I want to thank to **Prashya Madam** and **Sachin Sir** of Ph.D. Section, Nirma University, Ahmedabad for providing guidance related to administrative support from time to time.

I sincerely acknowledge the cooperation and support given by the Scientists of EPSA/SAC, especially, **Dr. Manoj Kumar Mishra, Mr. Ratheesh Ramakrishnan, Dr. Arvind Sahay, Mr. Shard Chander, Mr. Debojyoti, Ganguly, Dr. K.N. Babu, Anurag Gupta**. Sincere thanks are due to my colleagues **Ami Desai, Rajeswari Chauhan, Meghal Saha, Shruti Patel, Nivedita Sanwlani, Mamata Chauhan, Rahul Rajan, Gunjan Motwani, Neha Nandkeolyar, Manik Mahapatra** for very fruitful discussions on various aspects of ocean colour remote sensing and for sharing with me their experience and knowledge on certain relevant topics.

The computer support provided by **Nikhil** and **Vimal** during the preparation of this thesis is gratefully acknowledged. I thank the satellite data library personnel, **Mr. Rathore** for his help in providing the data required for this research work. I am also thankful to library staff members of Space Applications Centre (SAC), Ahmedabad, for extending facilities of SAC library during my research work.

It is difficult for me to express my gratitude to my family in a few words. My parents have been a guiding force behind the entire endeavour. This work would have not been completed without the moral support of my husband **Sanjay**. I also thank to my little son **Ayush** for bringing many happy and cherishing moments during the course of writing this thesis. I also want to thank to my baby sitter **Kamala Masi** who always takes care of my son during my absence from home for research work.

(MADHUMITA TRIPATHY)

CONTENTS

	Page No.
Chapter 1: Introduction	1-17
1.0 Background	2
1.1 Atmospheric composition and interaction	3
1.1.1 Gas molecules	4
1.1.2 Ozone	4
1.1.3 Aerosol	5
1.1.4 Clouds	6
1.1.5 Green house gases	7
1.2 Carbon cycle	8
1.3 Ocean carbon process	9
1.3.1 Physical, chemical and biological process	9
1.4 Ocean primary production	11
1.4.1 Modeling ocean primary production	12
1.5 Photosynthetically available radiation	13
1.6 Objectives	15
1.7 Thesis structure	16
Chapter 2: Theoretical background & literature review	18-48
2.1 Fundamentals of atmospheric radiation	19
2.1.1 The Sun as an atmospheric radiation source	19
2.1.2 Position of the Earth around the Sun	20
2.1.3 Basic radiometric quantities	22
2.2 Solar spectrum at the top of the atmosphere and solar constant	22
2.3 Interaction of solar radiation with Earth's atmosphere	24
2.3.1 Scattering	26
2.3.2 Absorption	27
2.3.3 Extinction	28
2.3.4 Reflection and albedo	29
2.4 Radiation in the ocean	30
2.4.1 Optical properties of ocean water	30
2.4.2 Classification of ocean water	31

2.5	Ocean colour from space	31
2.5.1	Ocean colour remote sensors from space	33
2.5.2	Geophysical parameters retrieved from ocean colour remote sensors	35
2.6	Photosynthetically available radiation estimation from <i>in-situ</i> data	36
2.7	Photosynthetically available radiation estimation from ocean colour remote sensors	38
2.8	Photosynthetically available radiation estimation from other than ocean colour remote sensors	42
2.9	Modeling ocean primary production	44

Chapter 3: Modeling Photosynthetically Available Radiation and sensitivity study using *in-situ* data over Indian Ocean 49-71

3.1	Introduction	50
3.2	PAR estimation using radiative transfer (RT) model from <i>in-situ</i> data	52
3.2.1	Description of RT model	52
3.2.2	Inputs for RT model	53
3.2.3	Output from RT model	58
3.3	PAR measurement from <i>in-situ</i> observation above the ocean surface	58
3.4	Variation of types of aerosol during ship cruise period	61
3.5	Comparison between model PAR and <i>in-situ</i> PAR for different types of aerosol	63
3.6	Sensitivity analysis	64
3.6.1	Sensitivity analysis: AOD on PAR for different types of aerosol	65
3.6.2	Sensitivity analysis: Cloud coverage and PAR variability	68
3.7	Summary and conclusions	70

Chapter 4: Modeling Photosynthetically Available Radiation (PAR) from satellite data over Indian Ocean. 72-117

4.1	Introduction	73
4.2	OCEANSAT-1 & 2 OCM sensor characteristics	73
4.3	Sun glitter estimation in OCEANSAT-1 & 2 OCM	76
4.4	Distinction between clear and cloudy sky in OCEANSAT-1 & 2 OCM	78
4.5	PAR estimation from OCEANSAT-1 & 2 OCM using method I	81
4.5.1	Modeling PAR under clear sky condition	81
4.5.2	Inputs of PAR model under clear sky condition	85
4.5.3	Modeling PAR under cloudy sky condition	93
4.5.4	Input of PAR model under cloudy sky condition	96

4.5.5	Output of PAR model under clear and cloudy sky condition	105
4.5.6	Sensitivity study of PAR model (Method I)	107
4.6	PAR estimation from OCEANSAT-1 & 2 OCM using method II	111
4.7	Summary and conclusions	116
Chapter 5: OCEANSAT OCM derived PAR spatial distribution & validation		118-137
5.1	Introduction	119
5.2	<i>In-situ</i> data collection and data processing	119
5.3	OCEANSAT-1 & 2 OCM data processing	121
5.4	Steps for validation of satellite estimated PAR with <i>in-situ</i> measured PAR	122
5.5	Validation of OCEANSAT-1 OCM estimated PAR with <i>in-situ</i> measured PAR	123
5.6	Validation of OCEANSAT-2 OCM estimated PAR with <i>in-situ</i> measured PAR	128
5.7	Comparison of OCEANSAT-1 & 2 OCM PAR with other ocean colour remote sensors	129
5.7.1	Comparison between OCEANSAT-1 OCM PAR and SeaWiFS PAR	129
5.7.2	Comparison between OCEANSAT-2 OCM PAR and MODIS PAR	134
1.2	Summary and conclusions	136
Chapter 6: Role of PAR in primary production estimation in Sea water		138-162
6.1	Introduction	139
6.2	Different methods for estimation of column primary production	140
6.3	Modeling column primary production	141
6.4	Description of inputs for ocean primary production estimation	144
6.4.1	Chlorophyll-a	145
6.4.2	PAR at sea surface	146
6.4.3	Variation of PAR with depth within the water column	147
6.4.4	Euphotic depth	148
6.4.5	Vertical diffusion attenuation coefficient	149
6.4.6	Physiological parameters	149
6.5	Ocean primary production during ship cruise periods	154
6.6	Role of PAR in primary production estimation in sea water	154
6.6.1	Sensitivity study: AOD and euphotic primary production for different types of aerosol	156

6.6.2	Sensitivity study: Photoadaptation parameter and euphotic primary production	158
6.6.3	Sensitivity study: Cloud coverage and euphotic primary production	159
6.7	Summary and conclusions	161
 Chapter 7: Summary and Conclusions		163-170
7.1	Salient features of the research findings	164
7.2	Future scope	170
 References		 171
Publications of the author related to thesis work		200

LIST OF TABLES

	Page No.
Table 3.1	Different aerosol types used in COART model during ship cruise periods in the Arabian Sea. 62
Table 3.2	Decrease of PAR (%) for maximum and moderate aerosol loadings compared to no aerosol loading for different aerosol types. 67
Table 4.1	Major specifications and features of OCEANSAT-1 & 2 OCM 74
Table 4.2	Spectral bands and different cloud detection test for clouds over water from space observation 79
Table 4.3	Extraterrestrial solar irradiance, absorption coefficient of ozone (k_{oz}), absorption coefficient for mixed gas (au) at each wavelength band used in the PAR model 88
Table 4.4	Values of constants used to estimate phase function of clouds 100
Table 4.5	Input default parameters for sensitivity study 107
Table 4.6	Extraterrestrial solar irradiance and ozone absorption coefficient of six spectral bands of OCM used in method II 112
Table 5.1	Location of data points for validation of PAR model 120
Table 5.2	OCEANSAT-1 OCM PAR versus <i>in-situ</i> measured PAR 124
Table 5.3	OCEANSAT-2 OCM PAR versus <i>in-situ</i> measured PAR 129
Table 5.4	OCEANSAT-1 OCM daily averaged PAR estimated from method I and method II versus SeaWiFS PAR 131
Table 5.5	OCEANSAT-2 OCM daily averaged PAR versus MODIS Aqua PAR 135
Table 6.1	Decrease of euphotic primary production (%) for maximum and moderate aerosol loading compared to no aerosol loading for different aerosol types compared to clear sky. 157

LIST OF FIGURES

	Page No.
Figure 2.1 Major divisions of the electromagnetic spectrum	19
Figure 2.2 The celestial sphere	21
Figure 2.3 Pathway of light reaching the remote sensor	32
Figure 3.1 Location of data points of ship cruises in the Arabian Sea	54
Figure 3.2 Variability of AOD (500 nm) during different ship cruises	57
Figure 3.3 Variation of downwelling irradiance E_s at different wavelength with time and variation of PAR with time.	59
Figure 3.4 Variability of PAR during ship cruises.	60
Figure 3.5 Comparison of <i>in-situ</i> PAR with COART model derived PAR for different aerosol types.	62
Figure 3.6 Variation of PAR with AOD (500 nm) during ship cruise periods in the Arabian Sea.	64
Figure 3.7 The variation of PAR with AOD (500 nm) for different aerosol types	66
Figure 3.8 The variation of total PAR under different cloud coverage	69
Figure 4.1 Sunlint region showed in false colour composite (FCC) image of OCEANSAT-1 OCM data over the Arabian Sea	78
Figure 4.2 False colour composite, reflectance at 865 nm and reflectance ratio between 865 nm and 670 nm band for OCEANSAT OCM-1	80
Figure 4.3 Extraterrestrial solar radiation at the top of the atmosphere	86
Figure 4.4 Aerosol optical depth estimated at 865 nm band and angstrom coefficient of OCEANSAT-1 OCM	91
Figure 4.5 Comparison between OCEANSAT-1 OCM estimated AOD and <i>in-situ</i> measured AOD during November 2001 and January 2003	92
Figure 4.6 Variation of transmittance through a liquid water cloud	94

Figure 4.7	Reflectance estimated at 443 nm spectral band of OCEANSAT-1 OCM for cloudy pixels	99
Figure 4.8	Variation of TOA radiance at 443 nm of OCM with cloud optical depth obtained from COART model	103
Figure 4.9	Cloud optical depth estimated at 443 nm band of OCEANSAT-1 OCM for thick and thin clouds	103
Figure 4.10	Flow chart to estimate PAR from OCEANSAT-1 & 2 OCM	104
Figure 4.11	Variation of PAR at noon, daily total PAR and daily averaged PAR estimated from OCM over the Arabian Sea	106
Figure 4.12	Sensitivity to a) monthly variation b) ozone concentration c) aerosol optical depth d) angstrom coefficient for PAR estimation under clear sky	108
Figure 4.13	Different cloud types in terms of cloud top pressure and cloud optical thickness	109
Figure 4.14	Sensitivity to a) cloud optical depth and b) cloud top pressure for PAR estimation under cloudy sky condition	110
Figure 4.15	OCM derived average ocean surface albedo and cloud albedo in PAR wavelength range	115
Figure 5.1	3 ×3 pixel subset of OCM PAR image	122
Figure 5.2	Scatter plot of <i>in-situ</i> measured PAR at noon versus PAR at noon estimated from OCEANSAT-1 OCM in daily time scale for the two methods	123
Figure 5.3	Spatial variation of PAR at noon over the Arabian Sea for different dates in different seasons	127
Figure 5.4	Scatter plot of <i>in-situ</i> measured PAR at noon versus PAR at noon estimated from OCEANSAT-2 OCM in daily time scale	128
Figure 5.5	Comparison between SeaWiFS daily averaged PAR and OCEASAT-1 OCM daily averaged PAR in daily time scale	130
Figure 5.6	Comparision between daily averaged PAR estimated from OCEANSAT-1 OCM from method I and method II and SeaWiFS under a) clear sky, b) Thin cloud and c) Thick cloud	133
Figure 5.7	Comparison between SeaWiFS daily averaged PAR and OCEASAT-	135

2 OCM daily averaged PAR in daily time scale

Figure 6.1	Variation of chlorophyll-‘a’ during 3–17 November 2001, 4–19 January 2003 and 7–19 March 2011	145
Figure 6.2	Variability of PAR with depth	147
Figure 6.3	Variability of euphotic depth during 3–17 November 2001, 4–19 January 2003 and 7–19 March 2011 over the Arabian Sea	148
Figure 6.4	Variability of vertical diffusion attenuation coefficient during 3–17 November 2001, 4–19 January 2003 and 7–19 March 2011 over the Arabian Sea.	149
Figure 6.5	Idealized curve of photosynthetic rate as a function of irradiance	150
Figure 6.6	Components of photosynthetron instrument to measure photosynthesis	153
Figure 6.7	Variability of euphotic primary production during 3–17 November 2001, 4–19 January 2003 and 7–19 March 2011 over the Arabian Sea.	154
Figure 6.8	a) Variation of euphotic primary production with AOD, b) variation of euphotic primary production with PAR, c) variation of normalized primary production with PAR during ship cruise periods over the Arabian Sea.	155
Figure 6.9	Variation of euphotic primary production with AOD for different aerosol types	156
Figure 6.10	Decrease (%) in euphotic primary production with AOD for different photoadaptation parameters	159
Figure 6.11	Variation of euphotic primary production under different cloud coverage.	160

ABBREVIATIONS AND ACRONYMS

MOSDAC	Meteorological and Oceanographic Satellite Data Archival Centre
NRSC	National Remote Sensing Centre
NASA	National Aeronautics and Space Administration
GSFC	Goddard Space Flight Centre
OCM	Ocean Colour monitor
CZCS	Coastal Zone Color Scanner
SeaWiFS	Sea-viewing Wide Field-of-view Sensor
MODIS	Moderate Resolution Imaging Spectroradiometers
MERIS	Medium Resolution Imaging Spectrometer
AVHRR	Advanced very high resolution radiometer
IOCCG	International Ocean-Colour Coordinate Group
ISCCP	International Satellite Cloud Climatology Project
OPAC	Optical Properties of Aerosols and Clouds
SeaBass	SeaWiFS Bio-optical Archive and Storage System
SolRad-Net	Solar Radiation Network
AERONET	Aerosol Robotic Network
COART	Coupled Ocean Atmosphere Radiative Transfer
MODTRAN	MODerate resolution atmospheric TRANsmission
VGPM	Vertically Generalized Production Model
WRM	Wavelength resolved models
WIM	Wavelength- integrated models
TIM	Time integrated models
DIMS	Depth-integrated models
NIR	Near-infrared
HDF	Hierarchical Data Format
TOA	Top of the atmosphere
FCC	False Colour Composite
RSR	Relative Spectral Response
AOD	Aerosol optical depth
COD	Cloud optical depth
PAR	Photosynthetically Available radiation
EuPP	Euphotic primary production
Zeu	Euphotic depth

NOMENCLATURE

PAR at noon under clear sky, Watt m ⁻²	$I_{\text{par_clear}}$
PAR at noon under cloudy sky, Watt m ⁻²	$I_{\text{par_cloudy}}$
Daily averaged PAR, Einstein m ⁻² day ⁻¹	I_D
Extraterrestrial solar radiation at the top of the atmosphere, Watt m ⁻² μm ⁻¹	I_0
Extra-terrestrial solar irradiance derived using RSR function of OCM bands	F_0
Direct PAR, Watt m ⁻²	$I_{\text{dir}\lambda}$
Diffuse PAR, Watt m ⁻²	$I_{\text{diff}\lambda}$
Direct transmittance	T_{dir}
Diffuse transmittance	T_d
Transmittance of Rayleigh scattering	T_R
Transmittance of ozone	T_{OZ}
Transmittance of aerosol scattering	T_A
Transmittance of uniformly mixed gas	T_u
Relative optical mass at mean sea level	m_0
Relative optical mass at local pressure	m_p
Radiance detected by a satellite sensor	L_{λ}
Aerosol path radiance	$L_{a\lambda}$
Rayleigh path radiance	$L_{r\lambda}$
Solar zenith angle	$\theta_s, \mu_0 = \cos\theta_s $
Satellite view angle	$\theta_v, \mu = \cos\theta_v $
solar azimuth	φ_s
satellite azimuth	φ_v
Relative azimuth angle	φ
Aerosol optical depth	τ_a
Rayleigh optical depth	τ_r
Cloud optical depth	τ_c
Effective radius of cloud droplets	r_e
Asymmetry parameter of cloud	$g(r_e)$
Forward scatterance of aerosol	F_a
Scattering angle of aerosol	γ_a
Aerosol single scattering albedo	ω_{0a}
Rayleigh single scattering albedo	ω_{0r}
Rayleigh scattering phase function	p_r
Aerosol scattering phase function	p_a
Angstrom exponent of aerosol	α
Cloud top reflectance	R_{θ_s}
Backscattered fraction of incident radiation	β_{θ_s}
Transmittance through cloud	T_{θ_s}
Scattering angle of cloud	ζ
Phase function of cloud	$P(\zeta)$

Reflectance of an idealized semi-infinite non-absorbing water cloud	$R_{\infty}(\mu, \mu_0, \phi)$
Reflectance at 443 nm band of OCEANSAT-1 OCM.	$R_{443}(\tau_c; \mu, \mu_0, \phi)$
Escape function	$K_0(\mu), K_0(\mu_0)$
Daylength	D
Albedo of cloud	A
Albedo of ocean surface	A_s
Probability parameter	P_{σ}
Wind speed	W
Surface reflection angle	ω
Absorption coefficient for mixed gas	a_u
Ozone absorption coefficient	k_{oz}
Ozone thickness	l
Primary production	P
Depth	z
Time	t
Biomass	B (z,t)
Normalized primary production	P^B
Irradiance at sea surface	I_0
Irradiance at depth z	I(z)
Diffusion attenuation coefficient	k
Plank's constant	h
Velocity of light in vacuum	c
Euphotic depth	Z_{eu}

Chapter 1

Introduction

This chapter gives a brief illustration about the background, key issues and objectives of the present study with an outline of the organisation of this thesis.

1.0 Background

The ocean is the defining feature of our blue planet Earth. It covers 70 % of the Earth's surface to an average depth of upto 3800 m (Seger, 2008). Atmosphere is the gaseous envelope that surrounds our planet. There is no exact upper limit for the extent of the atmosphere (Saha, 2008). Earth's atmosphere gradually merges with the space. Solar radiation is the ultimate source of energy for motions in the atmosphere and ocean (IPCC, 2001). The Sun provides its energy primarily to the Earth's tropics and subtropics and then it redistributes to the middle and high latitudes by different atmospheric and oceanic transport processes.

The incoming solar radiation incident at the Earth's surface covers the entire electromagnetic spectrum. However, 80% of the incoming solar radiation lies from 400 nm to 1600 nm wavelength range (IPCC, 2001). Photosynthetically available radiation (PAR) is the part of total solar radiation incident at the Earth's surface and is used during photosynthesis process by plants. The spectral range of PAR is from 350 nm to 700 nm (Tyler, 1966). Ultraviolet region (350 nm to 400 nm) contributes only 5% to 7% of the total energy of PAR spectrum (Sakshaug et al., 1997). Generally, PAR is defined as the quantum energy flux in the spectral range from 400 nm to 700 nm (Asrar et al., 1989) for the lack of measurements in the ultraviolet region from the space. PAR is expressed in two types of units. In one unit, PAR is defined as the radiometric flux per unit area and is expressed as Watt per meter square ($W m^{-2}$). If $I(\lambda)$ is the downward spectral irradiance at wavelength λ , then PAR in $W m^{-2}$ is expressed by the equation 1.1) (Frouin and Pinker, 1995).

$$PAR (W m^{-2}) = \int_{400\text{ nm}}^{700\text{ nm}} I(\lambda)d\lambda \dots\dots\dots 1.1)$$

Introduction

In another unit, PAR is defined as the number of photon collected per unit area during unit time and is expressed as Micro Einstein per meter square per second ($\mu\text{E m}^{-2} \text{sec}^{-1}$). PAR in $\mu\text{E m}^{-2} \text{sec}^{-1}$ is expressed by equation 1.2) (Frouin and Pinker, 1995).

$$PAR (\mu\text{E m}^{-2} \text{sec}^{-1}) = \frac{1}{hc} \int_{400 \text{ nm}}^{700 \text{ nm}} \lambda I(\lambda) d\lambda \dots \dots \dots 1.2)$$

Where h is Plank's constant and c is the velocity of light in vacuum.

While PAR is propagating from the top of the atmosphere to the Earth's surface, it is modified by the composition of the Earth's atmosphere. Thus, atmospheric composition and changes of atmospheric composition with time plays an important role in controlling the amount of PAR incident at the Earth's surface.

1.1 Atmospheric composition and interaction

Earth's atmosphere is composed of mainly four layers. These layers starting from the sea level are troposphere, stratosphere, mesosphere and ionosphere (Saha, 2008). Earth's atmosphere within the first 25 km is mainly composed of nitrogen (78.1% by volume) and oxygen (20.9% by volume) (Saha, 2008). The remaining 1% atmospheric gases are present in small concentration and they are known as trace gases. Trace gases consist of noble gases such as argon, neon, helium, krypton and xenon and other gases such as hydrogen and green house gases. Another constituent of the atmosphere is water vapour and it stays in variable proportion in the atmosphere. Atmosphere also contains aerosols and clouds, which interact with the incoming and outgoing radiation in a very complex manner. Atmospheric composition interacts with solar radiation by three physical processes such as scattering, reflection and absorption. Concentrations of atmospheric compositions are studied locally by many observational studies and globally by

Chapter 1

satellite data and models. Interaction of light with various atmospheric constituents and changes of atmospheric composition is summarised in the following sections.

1.1.1 Gas molecules

The size of gas molecules is $\sim 10^{-8}$ cm and they are much smaller compared to the wavelength of the incoming solar radiation. Solar energy lying between the blue to red portion of the visible spectrum, is mostly Rayleigh scattered by the gaseous molecules. Rayleigh scattering indicates that the intensity scattered by the gas molecules in a specific direction is inversely proportional to the fourth power of the wavelength.

1.1.2 Ozone

In the stratosphere, maximum concentration of ozone lies between 25 km to 30 km height (Saha, 2008). Ozone has strong absorption band between 210 nm to 320 nm wavelength which is known as Hartley band. Huggins band (320 nm - 360 nm) and Chappius band (450 nm - 650 nm) absorb ozone weakly. In the stratosphere, ozone is formed by photodissociation process of oxygen molecules into atoms by the ultraviolet radiation. Oxygen atoms combine with the oxygen molecules to form ozone (Saha, 2008). In the troposphere, ozone is released through the chemical reaction of gases such as carbon monoxide, hydrocarbons and nitrogen oxide (IPCC, 2007). The role of ozone in radiation is unique. In the stratosphere, it absorbs solar ultra-violet radiation. However, in the troposphere, ozone acts as a greenhouse gas.

In the stratosphere, ozone is destroyed by the collision with light waves and atomic oxygen (Saha, 2008). Other gases such as nitrogen oxide, nitrogen dioxide, atoms of hydrogen, hydroxyl and chlorine acts as catalyst and destroys the ozone in the stratosphere. In recent years, reduction of ozone layer below 0.22 cm is observed over the Antarctica region (Saha, 2008). The causes of reduction of ozone layer are extra halocarbon released by humans (IPCC, 2007). The

Introduction

thinning of ozone layer is termed as ozone hole. Halocarbon gas concentrations have increased primarily due to extensively use of refrigeration agents and in other industrial processes (IPCC, 2007). Internationally, the Montreal protocol in 1987 had banned on the use of chlorofluorocarbons, which release chloride atoms in the atmosphere (Saha, 2008).

As ozone has important role in absorbing ultraviolet radiation, it is important to study the changes of halocarbon group and ozone concentration with time over different regions of the globe. The decrease of ozone layer has been more prominent (Douglass et al., 2011) in the southern hemisphere and this decrease is ~6% below from the mean value of the year 1964-1980 (Douglass et al., 2011). The concentrations of major chlorofluorocarbons are decreasing since 2005, whereas hydrofluorocarbons are continuing to increase (Hartmann et al., 2013). Surface ozone has decreased in North America and Western Europe (Hartmann et al., 2013). However, surface ozone is strongly increased in East Asia since 1990 (Hartmann et al., 2013).

1.1.3 Aerosols

Aerosols are solid or liquid particles suspended in the atmosphere with size ranging from a few nanometres to tens of micrometer (IPCC, 2007). Aerosols may be of either natural or anthropogenic origin. The main constituents of the atmospheric aerosol are inorganic species (such as sulphate, nitrate, ammonium, seasalts), organic species, black carbon, mineral species (mostly desert dust) and primary biological aerosol particles (Boucher et. al., 2013). In the troposphere, the residence time of aerosol is usually few days and in the stratosphere the residence time is one year (Textor et al., 2006). They vary greatly in size, chemical composition and shape. Concentrations and distribution of different types of aerosol over different region is controlled by the transport and deposition of wind (Textor et al., 2006).

Aerosol particles interact with solar radiation through absorption and scattering (Boucher et. al., 2013). Aerosol scattering generally makes the planet more reflective and cool the climate.

Chapter 1

However, aerosol absorption tends to warm the climate system. Black carbon is an absorbing type of aerosol (Bond and Bergstrom, 2006) and warms the Earth's atmosphere (Gadhavi and Jayaraman, 2010). The major sources of black carbon are diesel engines, forest fires and biomass burning (Gadhavi and Jayaraman, 2010). As it is difficult to measure black carbon compared to scattering aerosols, there is a great uncertainty from the overall radiative effect from anthropogenic aerosols (Boucher et al., 2013). Aerosols also serve as cloud condensation nuclei and ice nuclei upon which cloud droplets and ice crystals form. Except thin cloud layer or presence of absorbing aerosols located above or between clouds, the role of aerosol in radiation is weaker in cloudy conditions (Chand et al., 2009).

Aerosol optical depth at 550 nm over ocean adjacent to the southern and eastern Asia and Indian region was observed to increase from the year 2000 to 2009 (Zhang and Reid, 2010). During this past ten year period, average increased in aerosol optical depth is 0.07 in the Arabian Sea (Zhang and Reid, 2010). Trends of increasing aerosol optical depth are also observed over most of the tropical oceans (Hartmann et al., 2013). Sunphotometer measurements over coastal regions of Europe and near the east coast of USA showed that there is decrease of aerosol optical depth during 2000 to 2009 (Hartmann et al., 2013). Therefore, the changes of the concentration of aerosol are different in different regions of the globe.

1.1.4 Clouds

Clouds are formed when air containing water vapour rises, expands under lower pressure and thereby cools until some of the vapour condenses into tiny water droplets (Mason, 1975). Clouds may be composed of liquid water (possibly super cooled), ice or both (mixed phase). The radius of the cloud droplets are in range from 10 microns to about 60 microns (1 micron= 10^{-4} cm) with a mean value of about 20 micron (Saha, 2008). Generally, clouds are classified into four families depending upon the height and the layer of their formation. These are high clouds (Cirrus, Cirrocumulus, Cirrostratus), medium clouds (Altostratus, Altocumulus), low clouds (Stratus,

Introduction

Cumulus, Stratocumulus) and clouds with great vertical development (Cumulonimbus) (Saha, 2008).

Clouds absorb and emit outgoing longwave infrared radiation and warm the Earth's atmosphere. Again, cloud reflects incoming shortwave solar radiation and cools the Earth's atmosphere. However, whether cloud will cool or warm the Earth's surface depends upon variable height, type and optical properties of clouds (IPCC, 2001). The effect of cloud on radiation is estimated by comparing the difference between outgoing and incoming radiation at the top of the atmosphere in cloudy and non-cloudy condition. Clouds exert approximately mean global and annual -50 Wm^{-2} shortwave radiation and $+30 \text{ Wm}^{-2}$ longwave radiation (Loeb et al., 2009). The net global effect of cloud on radiation is to cool the Earth's atmosphere.

1.1.5 Green house gases

Main green house gases are carbon dioxide, methane, nitrous oxide, tropospheric ozone and the halocarbons (a group of gases containing fluorine, chlorine and bromine) (IPCC, 2001). The concentrations of green house gases are less in the atmosphere. However, the changes of concentrations of green house gases with time over different region of the globe are important as green house gases have important role in modulation of radiation. These gases do not absorb incoming solar radiation. However, they absorb and emit outgoing infrared radiation (IPCC, 2001) and warm the Earth's atmosphere.

The natural sources of carbon dioxide are respiration process by all living organism and decay of plant matter. Human induced carbon dioxide sources are fossil fuel use in transportation, manufacture of cement and other goods and deforestation (IPCC, 2007). Methane is released by human activities related with agriculture, natural gas distribution and landfills (IPCC, 2007). Natural processes in wetlands, in ocean and soil release also methane in the atmosphere. Nitrous oxide is released by human activities such as fertilizer use and fossil fuel burning (IPCC, 2007).

Chapter 1

International Panel on Climate Change (IPCC) reports the changes of atmospheric composition and greenhouse concentration every five yearly. Recently IPCC fifth assessment report in 2013 have reported that atmospheric nitrous oxide has increased 20% in 2011 compared to the year 1750 (Hartmann et al., 2013). Atmospheric methane was remained constant from the year 1999 to 2006 and the concentration is increasing from 2007 onwards (Hartmann et al., 2013). The concentration of carbon dioxide is increasing in the atmosphere and this increase is 40% greater in the year 2011 compared to the year 1750 (Hartmann et al., 2013). Atmospheric carbon dioxide is the main atmospheric phase of the global carbon cycle (Ciais et al., 2013).

1.2 Carbon cycle

In the Earth system, carbon dioxide flux is exchanged through a series of reservoirs and the cycle is called carbon cycle. The time of exchange of carbon dioxide flux from one reservoir to another is expressed as reservoir turnover times. Reservoir turnover time is defined as reservoir mass of carbon divided by the exchange flux (Ciais et al., 2013). In the carbon cycle some reservoir acts as source and adds carbon to the atmosphere. Again some reservoir acts as sink and removes carbon from the atmosphere. The carbon budget is the balance of carbon among the three reservoirs – atmosphere, land and ocean (Post et al., 1990).

There are two main domains in global carbon cycle. In the first domain, large amount of carbon dioxide flux is exchanged through different reservoirs at a fast rate. The turnover time of fast domain ranges from a few years to decades to millennia. The examples of fast domain carbon cycles are carbon exchange in the atmosphere, the ocean, surface ocean sediments, vegetation in land, soils and freshwater (Ciais et al., 2013). The second domain is the slow domain. Turnover time of slow domain is 10,000 years or more (Ciais et al., 2013). In this slow domain, carbon dioxide is stored in the rocks and sediments in the deep ocean floor. Natural processes of exchange of carbon from slow domain to fast domain are volcanic emission of carbon dioxide, chemical weathering, erosion etc (Sundquist, 1986). Natural exchange of carbon between fast and

Introduction

slow domain is relatively small before industrial era (Raymond and Cole, 2003). Since the beginning of the industrial era, removal of fossil fuels from the reservoirs and their burning is transferring carbon from slow domain to fast domain at a fast rate. This exchange causes human-induced disturbance in the carbon cycle (Ciais et al., 2013). The ocean stores total amount of carbon is about fifty times greater than the amount in the atmosphere (IPCC, 2001). As ocean is one of the largest reservoirs of carbon, it is essential to understand different ocean carbon processes that may affect the future carbon dioxide cycle.

1.3 Ocean carbon processes

The ocean absorbs carbon dioxide by three processes. Carbon dioxide gas passes through air- sea interface either by physical or biological process. It reacts chemically with dissolved inorganic carbon in the ocean's surface waters. Carbon is transported into the deeper waters through ocean circulation processes.

1.3.1 Physical, chemical and biological process

Physical processes by which carbon dioxide is exchanged from the atmosphere to the ocean is controlled by several factors such as chemical equilibrium between carbon dioxide and carbonic acid present in the sea water, difference between the partial pressure of carbon dioxide in the atmosphere and the ocean and the rate of exchange between air and sea (IPCC, 2005). Carbon dioxide is a weak acidic gas. It dissolves with sea water to form carbonic acid. Carbonic acid dissociates further into bicarbonate ion, carbonate ion and hydrogen ion.

Oceanic circulation is important in the carbon cycle because it affects carbon storage in the ocean. The circulation of the ocean is usually divided into two parts. A wind driven circulation that dominates in the upper few hundred meters. Another circulation is thermohaline

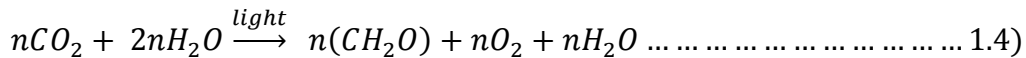
Chapter 1

circulation. It is generated mainly by density difference. The thermohaline circulation is often referred to as the ocean's "conveyor belt" because the water follows a continuous looping path and takes thousands of years to make a full circuit. Water follows this loop mainly because the ocean surface is cooler at high latitudes than at low latitudes. This difference in temperature (thermal forcing) pushes the tropical surface waters towards pole. Carbon dioxide is more soluble in cold water than in warmer water, so surface water from the tropics continues to absorb additional carbon dioxide as it moves toward higher latitudes and colder temperatures. The movement of carbon from shallow to deeper waters in the conveyor-belt circulation stores large amounts of carbon in the deep oceans (IPCC, 2005).

Biological processes have also important role to remove carbon dioxide from the atmosphere. These processes in the oceans are driven by phytoplankton. Phytoplankton is microscopic free floating organism living in the illuminated surface layer of the ocean. During the process of photosynthesis, phytoplankton converts dissolved inorganic carbon to organic carbon using energy from the Sun. This transformation is important in carbon cycle for two reasons. Firstly, carbon dioxide is removed from the atmosphere through the photosynthesis process. Secondly, organic carbon produced in the photosynthesis process, does not participate in the equilibrium of the carbonate system and thus, ocean's ability is increased to dissolve more carbon dioxide from the atmosphere through physical process. Marine phytoplankton and animals use carbon to manufacture shells and such as cell tissue. As the organisms die and sink, the organic carbon falls into the deeper ocean. This transport of carbon to the deep ocean is called the biological pump (Longhurst and Harrison., 1989). Photosynthesis is the first step in the biological pump. Through photosynthesis the rate of carbon fixed or the organic carbon produced per unit time in a unit volume of water is termed as ocean primary production (Parsons et al., 1984). The next section describes factors, which affect ocean primary production and modeling ocean primary from *in-situ* and space based observation.

1.4 Ocean primary production

The photosynthesis process is not a single reaction. It has three different steps. Initially it captures light energy transferring it chemical form, then the chemical forms changes into ATP (Adenosine triphosphate), NADPH (Nicotinamide adenine dinucleotide) and finally, fixing carbon dioxide using ATP and NADPH. In the ocean, mainly three types of phytoplankton i.e, algae, diatom and dinoflagellates are responsible for photosynthesis (Parsons et al., 1984). The basic equation of photosynthesis process can be expressed by the equation 1.4) (Parsons et al., 1984).



Photosynthetic pigments present in the algae absorb light and provide energy to the photosynthetic processes. The pigments can be grouped into chlorophylls (chlorophyll-‘a’, chlorophyll-‘b’, chlorophyll-‘c’), carotenoids (carotenes and xanthophylls) and phycobilins (biliproteins) (Dawes, 1998). Chlorophyll-‘a’ is the primary photosynthetic pigment in the phytoplankton (Dawes 1998).

The light energy required for photosynthesis is restricted to the PAR wavelength range. The fraction of radiant energy that is actually absorbed by algae is photosynthetically usable radiation (Parsons et al., 1984). Only a fraction of photosynthetically usable radiation is converted and stored as chemical energy in the form of organic carbon and it is defined as photosynthetically stored radiation (Parsons et al., 1984). The photosynthetic response of phytoplankton to available light is not linear. It is light dependent at the lower light intensities and becomes independent (saturated) at higher light intensities and produces a curve which is described by its slope α and the maximum photosynthesis P_{\max} (Platt and Saththyendranath, 1993). α and P_{\max} are known as photoadaptation parameter or P-I parameter.

Chapter 1

PAR incident at the sea surface is again reduced by absorption and scattering by the seawater and dissolved, suspended matter present in the water. The reduction of light in the water column can be expressed in terms of attenuation coefficient. Attenuation coefficient is highly dependent on wavelength. However, average attenuation coefficient in the wavelength of PAR is used rather than the value at particular wavelength for estimation of ocean primary production (Parsons et al., 1984).

As ocean primary production has important role in marine ecosystem and global carbon cycle, several methods are developed to estimate ocean primary production from *in-situ* data. Among them ^{14}C method is widely used to estimate ocean primary production. A known amount of ^{14}C is added to bottles containing the water samples. After incubation time, the organic carbon is separated from the remaining inorganic carbon by filtration (Peterson, 1980). *In-situ* estimation of ocean primary production provides information at discrete points over the global ocean. There are several constrains such as availability of ships, work force, funding etc. to collect water sample for *in-situ* estimation of ocean primary production in the season of interest over different regions of ocean. To get seasonal and temporal distribution of ocean primary production over the globe, space based observations have proved to be most robust (Frouin and Pinker, 1995).

1.4.1 Modeling ocean primary production

Ocean primary production can be estimated from the space observation using suitable algorithm or model. Chlorophyll-‘a’ concentration plays main role in modeling ocean primary production from space observation (IOCCG, 1999). Different bio-optical algorithms have been developed to estimate chlorophyll-‘a’ using satellite data (O’Reilly et al., 1998; Chauhan et al., 2002; Nagamani et. al., 2008). The basic principle to estimate chlorophyll-‘a’ using satellite data is that it absorbs relatively more blue and red light than green light. Chlorophyll-‘a’ absorbs light weakly in the 550 nm to 565 nm region. In general, 443 nm, 490 nm, 510 nm and 555 nm bands are used to formulate algorithms to estimate chlorophyll-‘a’ concentration.

Introduction

Primary production varies with the availability of light and takes place within the euphotic zone. Euphotic zone extends from the surface to a depth where there is 1% of the light intensity from the surface irradiance. Bio-optical algorithms provide concentration of chlorophyll-‘a’ for surface or upto first attenuation depth. First attenuation depth is defined as the depth at which 90% of the backscattered radiation originates (Joseph, 2005). Vertical profile of chlorophyll-‘a’ from the surface to euphotic depth is obtained by extrapolation of surface chlorophyll-‘a’ from the surface to euphotic depth. Extrapolation is based on the vertical profile of chlorophyll-‘a’ obtained from historical *in-situ* data or sea surface temperature data estimated using satellite observation (IOCCG, 2000).

Standard models use product of plant biomass, a scaling parameter that accounts variation in plant physiology and photosynthetically available radiation (PAR) at sea surface to estimate water column primary production (Platt et al., 1988a, 1988b, 1993, 2008; Longhurst et al. 1995; Antoine and Morel 1996; Behrenfeld and Falkowski 1997a).

1.5 Photosynthetically available radiation

Photosynthetically available radiation incident on the ocean surface is an important parameter needed by most of the ocean primary productivity models. A series of simple models (Leckner, 1978; Justus and Parsi, 1985; Bird and Riordan, 1986; Gregg and Carder, 1990; Frouin and Chertock, 1992) have been developed to estimate insolation. Insolation is defined as the solar radiation incident in the spectral range from 400 nm to 4000 nm at the Earth surface (Frouin and Pinker, 1995). In the absence of direct PAR measurements, PAR values were estimated from an empirical relationship with insolation (Blackburn and Proctor, 1983; Baker and Frouin 1987).

However, the relationship between insolation and PAR is highly dependent on different solar zenith angles and different atmospheric conditions (Baker and Frouin, 1987; Pinker and Laszlo, 1992a; Frouin and Pinker, 1995). Under cloudy skies, the ratio of PAR and insolation can

Chapter 1

be varied by more than 50% at low sun zenith angles (Frouin and Pinker, 1995). Pinker and Laszlo (1992a) showed that the spatial variability of the ratio of PAR and insolation was not negligible at global scale. One of the possible reasons for this variability is that there are water vapour and trace gas absorption features in the downwelling irradiance spectrum. Whereas, methane and carbon dioxide features are absent in PAR spectrum (Bouvet, 2006). The another reason could be due to presence of clouds, as clouds do not absorb significantly at PAR wavelengths but absorbs in the near-infrared (Frouin and Pinker, 1995) of the insolation. Practically, estimation of PAR at global scale using remote sensing data is the only approach to meet such type of large-scale requirements such as PAR measurements for primary production estimation. Knowledge of geographical distribution and temporal variability of PAR is also useful to understand the interactions between the atmosphere and biosphere and for different climate change study (Frouin and Pinker, 1995).

Photosynthetically available radiation had been estimated from ocean colour polar orbiting sensors such as SeaWiFS, MODIS-Terra and MODIS-Aqua, MERIS data (Frouin et al., 2003; Carder et al., 2003; Van Laake and Azofeifa, 2004; Liang et al., 2006; Bouvet 2006). Apart from ocean colour satellite, PAR had also been estimated from meteorological satellites like METEOSAT (Rubio et al., 2005), NOAA AVHRR (Runnstrom et al., 2006), GOES (Zheng et al., 2008). PAR had also been estimated from GOCI satellite (Frouin and McPherson 2012) and MTSAT (Janjai and Wattan, 2011; Li et al., 2012).

Ocean colour sensors also provide chlorophyll-‘a’ concentration, which is another key parameter to estimate ocean primary production. The main advantage to estimate PAR from ocean colour sensors is that both chlorophyll-‘a’ concentration and PAR would be estimated from the same platform. However, a single polar orbiting satellite cannot account diurnal variability of cloud property. The equatorial crossing time and viewing geometry of different ocean colour sensors are different. That is why, multiple ocean colour missions are needed to enhance our understanding about ocean (IOCCG, 1999; IOCCG, 2004; IOCCG, 2007).

Introduction

The Indian Space Research Organisation (ISRO) launched ocean colour satellite carrying Ocean Colour Monitor (OCM) on OCEANSAT-1 in May 1999 and a follow on satellite OCEANSAT-2 having modified Ocean Colour Monitor (OCM) in September 2009. OCM has high spatial resolution of 360 m and its data is used for various societal and scientific applications. The primary input variable of ocean primary production is chlorophyll-‘a’ and it was estimated from OCEANSAT-1 & 2 OCM (Chauhan et al., 2002; Nagamani et al., 2008). A non-spectral analytical model has been used to estimate mixed layer primary production and euphotic primary production from OCEANSAT- 1 & 2 OCM (Raman et al., 2011). PAR with spatially invariant and uniform aerosol optical depth has been used in current primary production model. Singh et al. (2007) used Bird’s clear sky model to estimate instantaneous PAR from OCEANSAT-1 OCM, which does not account cloud properties. PAR models based on climatological input and limited aerosol input do not characterize the regional and temporal variability of the PAR cycle (Arnone et al., 1998) over the Arabian Sea. Thus, modeling PAR from OCEANSAT-1 & 2 OCM under variable aerosol loading and cloud coverage is a desirable input parameter to estimate accurately ocean primary production from OCM.

1.6 Objectives

The major objective of this research work is to estimate PAR under natural conditions accounting for aerosol variation and to study effects of cloud cover. For this purpose, mainly OCEANSAT-1 & 2 OCM sensor data has been used. Further, sensitivity study of PAR on aerosol and cloud conditions have been studied. The sensitivity of PAR to estimate primary production also has been studied. Following are the detailed objectives.

- a) Modeling PAR under clear and cloudy sky.
- b) Estimation of PAR from OCEANSAT-1 & 2 OCM satellite data.
- c) Validation of PAR estimated from OCEANSAT-1 & 2 OCM with *in-situ* measured PAR.
- d) Sensitivity analysis of PAR under different atmospheric conditions.

Chapter 1

- e) Sensitivity analysis of ocean primary production for various PAR values under different atmospheric conditions.

1.7 Thesis Structure

The thesis is structured as follows

Chapter 1 “**Introduction**” illustrates the background, the importance of the study. It also describes objectives of the present study with an outline of the thesis structure.

Chapter 2 “**Theoretical Background & literature review**” gives a brief about the theoretical background of research problem. This chapter also illustrates basic concept of ocean colour remote sensing, brief history of different ocean colour remote sensors. Literature review of estimation of ocean primary production and PAR from different ocean colour remote sensors and other satellite remote sensors are also illustrated in the chapter 2.

Chapter 3 “**Modeling Photosynthetically Available Radiation (PAR) and sensitivity study using *in-situ* data over Indian Ocean**” briefs about PAR estimation using a *Coupled Ocean Atmosphere Radiative Transfer (COART)* model at a fixed geographical location during ship cruise periods in the Indian Ocean. In this radiative transfer model, input parameters have been obtained from *in-situ* measurements. PAR measurements using surface reference sensor of radiometer during different ship cruise period have been discussed. COART model estimated PAR has been compared with *in-situ* measured PAR and a sensitivity study has been done to understand the variation of PAR for various aerosol optical depths of different aerosol models and for various cloud coverage conditions.

Chapter 4 “**Modeling Photosynthetically Available Radiation (PAR) from satellite data over Indian Ocean**” briefs the modeling of different components of PAR for e.g. computation of extraterrestrial solar irradiance at the top of the atmosphere, Rayleigh scattering, aerosol

Introduction

scattering, ozone absorption, absorption by uniformly mixed gases and effect of clouds from OCM using two different methods. In the first method, the atmosphere is treated as a single layer in the clear sky conditions, or as a double layer in cloudy conditions. Surface reflectance has been neglected in the first approach. Aerosol optical depth and cloud optical depth has been estimated at 865 nm and 443 nm spectral band of OCM. PAR has been estimated from OCM using second method which assumes that the effects of clouds and clear atmosphere can be decoupled with cloud system and ocean surface albedo. Ocean surface and cloud albedo have been estimated from OCM.

Chapter 5 **“OCEANSAT OCM derived PAR spatial distribution & validation”** PAR estimated from OCM is validated with PAR estimated from surface reference sensor of radiometer during different ship campaigns and statistics are generated. PAR estimated from OCM have been compared with PAR estimated from other ocean colour sensors such as SeaWiFS (Sea-viewing Wide Field-of-view Sensor) and MODIS (Moderate Resolution Imaging Spectroradiometer). Spatial and temporal variability of PAR estimated from OCM in the Arabian Sea has been discussed.

Chapter 6 **“Role of PAR in primary production estimation in Sea Water”** briefs about the ocean primary production modeling. A non-spectral analytical model has been used to estimate euphotic primary production with inputs of chlorophyll-‘a’, diffused attenuation coefficient, euphotic depth, photoadaptation parameter and PAR at sea surface. Measurements of different inputs from *in-situ* observation have been discussed. A sensitivity study has been done to understand the variation of ocean primary production for various PAR values under different atmospheric conditions such as variable aerosol optical depth and cloud coverage for different photoadaptation parameters.

Chapter 7 **“Summary and Conclusions”** brings together all the research findings from the previous chapters. General conclusions have been provided and future work has been recommended.

Chapter 2

Theoretical background & literature review

This chapter gives a brief about theoretical background of the research problem. This chapter also illustrates basic concept of ocean colour remote sensing, brief history of different ocean colour remote sensors. Literature review of estimation of ocean primary production and PAR from in-situ measured data, different ocean colour remote sensors and use of other satellite remote sensors are also illustrated in this chapter.

2.1 Fundamentals of atmospheric radiation

Earth's atmosphere is a critical system for life on our planet. Together with the oceans, Earth's atmosphere shapes Earth's climate and weather patterns. The source of the energy to Earth's atmosphere and ocean is the radiation and the Sun is the ultimate natural source of this radiation.

2.1.1 The Sun as an Atmospheric Radiation source

The Sun is the natural source of electromagnetic radiation received at the atmosphere. In the Sun, nuclear reactions produce a full spectrum of electromagnetic radiations. Electromagnetic radiation is a form of energy. It has electric and magnetic field that simultaneously oscillate in planes mutually perpendicular to each other and to the direction of propagation through the space. It exhibits both wave properties and particle properties. Major components of the electromagnetic spectrum are shown in Figure 2.1.

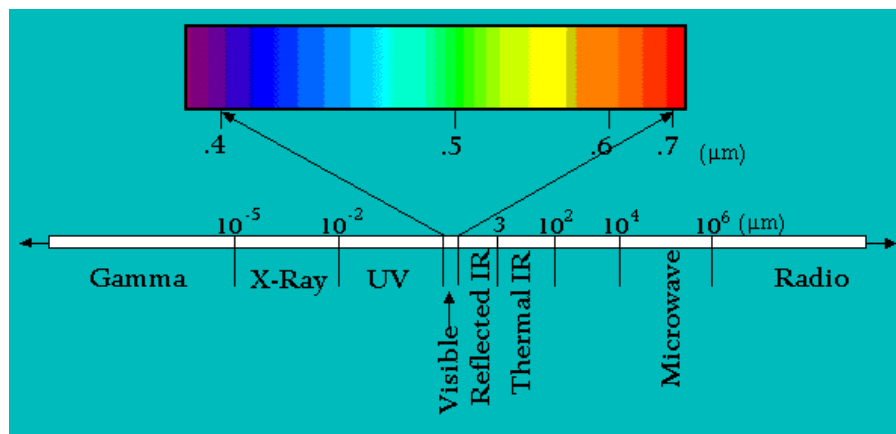


Figure 2.1: Major divisions of the electromagnetic spectrum

Most of the electromagnetic energy reaching the Earth, originates from the photosphere layer of the Sun. Photosphere layer is referred as the surface of the Sun. The temperature in this

Chapter 2

layer varies from 8000° K in lower layer to 4000° K in the upper layer with average temperature 6000° K (Liou, 1980). The region above the photosphere is called the solar atmosphere. The solar atmosphere is divided into two regions called the chromospheres and corona (Liou, 1980). Sunspots are one of the observable features of the Sun. They are relatively dark regions on the photosphere. The number of sunspots changes with periodically and the periodic change are referred to as the sunspot cycle. The average length of time cycle between sunspot maxima is about 11 years (Liou, 1980).

2.1.2 Position of the Earth around the Sun

The Earth moves around the Sun in an elliptical orbit with the Sun at one focus. Earth's obliquity to the Sun makes the position of the Sun oscillates between 23.5° N and 23.5° S (Saha, 2008). Sun is overhead at the equator at the equinoxes in March and September when days and nights are about equal. Earth is farthest from the Sun in June and July when the Sun is overhead at 23.5° N and the days are longer than nights. Again, Earth is closest to December and January when the Sun is overhead at 23.5° S and nights are longer than days. In order to calculate solar radiation at different times it is necessary to specify the position of the Sun in the sky. This is done by defining coordinate systems on the celestial sphere which is an imaginary transparent sphere surrounding the Earth and concentric with it (Paltridge and Platt, 1976).

Figure 2.2 shows the coordinate systems of celestial sphere where the Sun apparently moves round the Earth on a path which makes an angle of approximately 23.5° to the plane of the Earth's equator. The imaginary path is called ecliptic. Usually, it is convenient to use altitude, zenith angle, azimuth and hour angle to define position of the Sun in the sky (Paltridge and Platt, 1976). Some of the terminologies used to describe Sun's motion around the Earth are following.

- ❖ **Altitude:** Altitude of a body is its angular height above the observer's celestial horizon and is thus an angle between 0° and 90° .

Theoretical background and literature review

- ❖ **Zenith angle:** Zenith angle is the angular depression of the body from the observer's zenith and is thus the complement to the altitude.
- ❖ **Azimuth:** Azimuth of a celestial body is the angle between the plane of the observer's meridian and the plane of the great circle passing through the zenith and the body measured clockwise from the observer's meridian. The azimuth assumes value between 0° and 360° .
- ❖ **Hour angle:** Local hour angle of a body is the angle at the celestial pole between the observer's meridian and the meridian of the body measured westwards from the observer's meridian. Thus the Sun's hour angle counts from the midday position and changes 360° per day or 15° per hour.

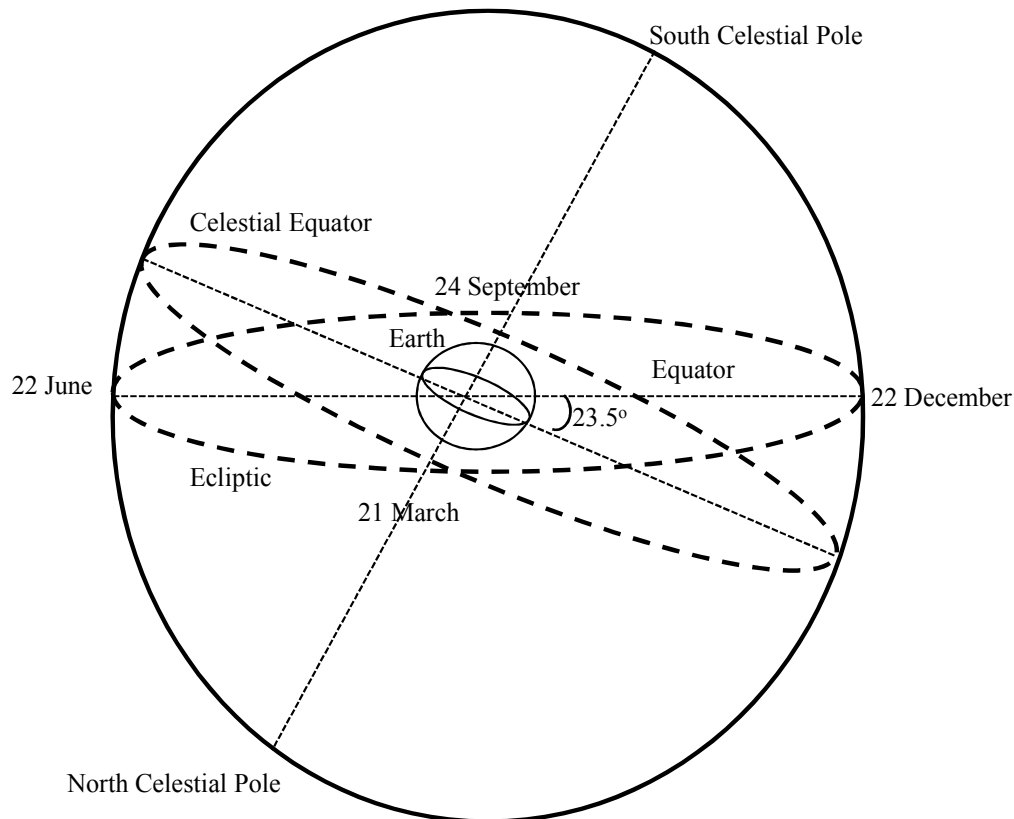


Figure 2.2: The celestial sphere (Paltridge and Platt, 1976)

2.1.3 Basic radiometric quantities

Two basic radiometric parameters that are commonly used to describe the distribution of light field are radiance and irradiance. Following Kirk (1984) and Mobley (1994) the definitions of these radiometric quantities have been described as:

- ❖ **Radiance:** The radiant power in a beam per unit solid angle per unit area perpendicular to the beam per unit wavelength interval. The solid angle is defined as the ratio of the area of a spherical surface intercepted by the core to the square of the radius.
- ❖ **Irradiance:** The radiant power per unit area per unit wavelength interval.
- ❖ **Upward irradiance:** The upward directed radiant power per unit area and downward facing horizontal surface.
- ❖ **Downward irradiance:** The downward directed radiant power per unit area and upward facing horizontal surface.

2.2 Solar Spectrum at the top of the atmosphere and solar constant

At the top of the atmosphere, the distribution of electromagnetic radiation emitted by the Sun is called solar spectrum. Energy of photon emitted from the Sun is inversely proportional to the wavelength. Of the electromagnetic energy emitted from the Sun, approximately 50% lies in the wavelengths longer than the visible region, about 40% in the visible region (400-700 nm) and about 10% in wavelengths shorter than the visible region (Liou, 1980). Sharp dips observed in the solar spectrum are called Fraunhofer lines. Fraunhofer lines are originated due to selective absorption of solar radiation by the elements in the Sun's outer atmosphere itself (Mobley, 1994).

Theoretical background and literature review

The irradiance of solar energy as received on a surface exposed normal to the Sun's rays at the mean Sun-Earth distance (1.495×10^{11} m) and in the absence of the atmosphere is known as solar constant. The value of solar constant is 139.5 mW cm^{-2} (Johnson, 1954). The solar constant is a quantity denoting the amount of total solar energy reaching at the top of the atmosphere. The accurate spectral distribution of solar irradiance is needed in variety of remote sensing applications and radiation budget models. The history of the solar irradiance measurements from ultraviolet to infrared region is summarised as under.

The measurements of solar spectrum in the UV region before 1985 were obtained mainly from balloons and rockets (Mentall et al., 1981; Mount and Rottman, 1983a, b; Mentall and Williams, 1984; Mentall, et al., 1985). Solar irradiance measurements in the spectral range 160 nm to 400 nm were obtained by the Solar Backscatter Ultraviolet (SBUV) instrument on board Nimbus-7, NOAA-9 and NOAA-11 (SBUV-2) satellites (Heath and Schlesinger, 1986; Cebula et al., 1991; DeLand and Cebula, 1993).

The visible and near infrared part of the solar spectrum can be estimated from ground based observations. However, the atmospheric absorption features are needed to be taken into account to derive absolute solar irradiance at the top of the atmosphere. Labs and Neckel (1968), Peytureaux (1968), Neckel and Labs (1984) measured solar irradiance from the ground by telescopes. For the estimation of solar spectrum from ground measurements, measurements are carried out from the high altitude to minimize the artifacts due to the atmospheric absorption. Labs and Neckel's solar spectrum was measured at 3600 m altitude at the centre of the solar disk. The solar spectrum was also corrected for centre to limb variations and atmospheric transmission. Arvesen et al. (1969) and Thekaekara (1974) measured solar irradiance from airplanes at an altitude of about 12 km. But still solar spectrum estimated from the high altitude ground or from the airplane need to be corrected as significant discrepancies (up to 10%) were observed in the ultraviolet region where gaseous absorptions are most important in the stratosphere (Pierce and Allen, 1977). Burlov-Vasiljev et al. (1995) measured solar spectrum in the visible and the near IR

Chapter 2

domains up to 1062 nm from the ground. Colina et al. (1996) compiled solar spectrum data from 120 to 2500 nm based on the previous study.

Solar spectral irradiance from 180 nm to 3000 nm at 1 nm resolution was measured by SOLSPEC instrument (Thuillier et al., 1997; Thuillier et al., 1998; Thuillier et al., 2003) from the space. SOLSPEC instrument consists of three spectrometers named UV, VIS and IR. It flew for the first time in December 1983 with the SpaceLab 1 mission (SL1) and later with the ATLAS (ATmospheric Laboratory for Applications and Science) missions after significant improvement of the instrument optics and calibration procedures. The mean absolute uncertainty of the solar spectral irradiance from 350 nm to 850 nm regions measured during ATLAS 1 mission is about 2-3 % (Thuillier et al., 1998). The sources of error are the pyronometer calibration, the weakness of the signal during calibration measurements at both the ends (Thuillier et al., 1998).

2.3 Interaction of solar radiation with Earth's atmosphere

The interaction of the Earth's atmosphere with solar radiation depends on the atmosphere's composition and structure. The atmosphere is composed of predominantly by gases such as nitrogen, oxygen and argon and trace gases such as carbon dioxide, neon, helium, krypton, xenon, hydrogen, methane, nitrous oxide, carbon monoxide etc (Liou, 1980). In addition, the atmosphere also contains various solid and liquid particles, such as aerosols, water vapour and ice crystals that are highly variable in space and time. The concentration of carbon dioxide and water vapour varies greatly both in space and time.

Based on the vertical temperature profiles standard atmosphere is divided into troposphere, stratosphere, mesosphere and thermosphere (Liou, 1980). The tops of these layers are called the tropopause, stratopause, mesopause and thermopause, respectively. The interaction of solar radiation with different atmospheric layers is different, as physical and chemical properties of these layers are varying.

Theoretical background and literature review

Upper atmospheric layers contain excited and ionized atoms and molecules (Saha, 2008). These ionized atoms are generated because of either solar wind or high frequency part of the radiation lying in the extreme ultraviolet and X-ray wavelengths (<200 nm). The gases affected by the ionisation process are mainly oxygen and nitrogen. The extensive ionized layer in the upper atmosphere around the Earth is known as ionosphere (Saha, 2008).

Mesosphere lies below ionosphere. The height of mesosphere lies from 50 km to 80 km from sea level. The temperature in this layer decreases with altitude (Saha, 2008). But the rate of decrease is slower than in the troposphere. Thin, noctilucent clouds are observed in this layer (Saha, 2008).

Stratosphere lies below the mesosphere. Sometimes this layer is called ozonosphere also as there is maximum ozone concentration between about 25 and 30 km altitude (Saha, 2008). Ozone absorbs all the ultraviolet radiation between 200 nm and 300 nm that enters this layer. Ozone has strong absorption band, known as Hartley band, between 210 nm and 320 nm. Ozone also absorbs in several other bands such as Huggins bands (320- 360 nm), Chappuis band (450- 650 nm) (Saha, 2008). In addition, thin layers of aerosol are observed to persist for a long period of time (Liou, 1980). In the stratosphere, the energy balance shows that the dissociative heating due to absorption of ultraviolet radiation more than balances the energy lost during destruction and radiation. Hence there is a net warming of the atmosphere in the upper layers of the stratosphere.

The troposphere is characterized by a decrease of temperature with respect to height with typical lapse rate of 6.5°C per km (Liou, 1980). All the water vapour, clouds and precipitation are confined to this layer. Clouds and aerosols play main role in attenuating solar radiation. They attenuate solar radiation either by scattering, absorption or reflection.

2.3.1 Scattering

Scattering is a physical process by which a particle in the path of an electromagnetic wave reradiated energy in the different directions (Liou, 1980). During scattering, a straight parallel beam of radiation changes direction either sideways or backwards. When a particle removes the incident light by scattering once, the scattering is known as single scattering. In the atmosphere, there are chances that the scattered radiation from one particle may get scattered again by other particles. This is called multiple scattering. However, the degree of scattering depends upon the size of the molecules or particles compared to the wavelength of the incident beam. There are three types of scattering is observed based on the size of the particles and incident wavelength. Different types of scattering are classified as nonselective, Rayleigh and Mie scattering (Lillesand, 1987).

In nonselective scattering, the diameters of the particles are much larger than the incident wavelength being sensed. Cloud shows non-selective scattering and appears as white as they scatter all wavelength equally.

Rayleigh scattering is common when radiation interacts with atmospheric molecules and other tiny particles that are much smaller in diameter than the wavelength of the interacting radiation (Liou, 1980). The effect of Rayleigh scatter is inversely proportional to the fourth power of wavelength. Hence, there is a much stronger tendency for short wavelengths to be scattered by this scattering mechanism than long wavelengths.

Another type of scatter is called Mie scattering, which exists when atmospheric particle diameters essentially equal to the incident wavelengths being sensed. This type of scattering tends to influence longer wavelengths compared to Rayleigh scattering. Water vapor and dust are major causes of Mie scattering (Lillesand, 1987) in the atmosphere.

2.3.2 Absorption

Scattering is often accompanied by absorption. During scattering process, radiation flux is not lost from the incident beam but it is redistributed over the total solid angle centred around the scatterer. During scattering processes, the internal energy state of the molecules is not changed. However, during absorption processes the internal energy state of the molecules is changed (Liou, 1980). Absorption process is spectrally selective. Incoming solar radiation is mainly absorbed in the atmosphere by different gas molecules such as O₂, O₃, N₂, CO₂, H₂O, O and N at different selective wavelength. Although NO, N₂O, CO and CH₄ occur in the atmosphere in very small quantity, exhibit absorption spectra. Most of the UV radiation is absorbed in the upper atmosphere. Mainly visible and infrared region of solar radiation is absorbed by various gases present in the troposphere (Liou, 1980).

Molecular oxygen absorbs UV radiation in the upper atmosphere. In addition, two weak oxygen absorption bands of oxygen are observed in the infrared region of the solar spectrum. The A band of O₂ at 700 nm is well known because of large solar flux contained in this region (Liou, 1980).

Carbon dioxide exhibits a number of weak absorption bands in the solar spectrum. The 2000, 1600 and 1400 nm CO₂ bands are so weak that for all practical purpose they can be ignored in solar absorption calculations (Liou, 1980). The 2700 nm band of CO₂, which overlaps with the 2700 nm band of water vapour, is somewhat stronger and should be included in absorption calculations. The 4300 nm band of CO₂ is more important in the thermal infrared region than the solar region because this band contains very little solar energy (Liou, 1980).

The most important absorber in the near infrared region is water vapour. The most important band of water vapour absorption is 2700 nm (Liou, 1980). Other bands of water vapour absorption bands are 940, 1100, 1380, and 1870 nm (Liou, 1980). The strong water vapour band centred at 6300 nm is important in the thermal infrared region (Liou, 1980).

Theoretical background and literature review

$$b_b(\lambda) = 2\pi \int_{\pi/2}^{\pi} \beta(\theta_s, \lambda) \sin(\theta_s) d\theta_s \dots \dots \dots (2.2)$$

$$b_f(\lambda) = 2\pi \int_0^{\pi/2} \beta(\theta_s, \lambda) \sin(\theta_s) d\theta_s \dots \dots \dots (2.3)$$

- ❖ **Spectral phase function** is defined as the ratio of the spectral volume scattering function to the spectral scattering coefficient.
- ❖ **Spectral single scattering albedo $\omega_0(\lambda)$** defined as the ratio of the spectral scattering coefficient to the spectral beam attenuation coefficient

$$\omega_0(\lambda) = \frac{b(\lambda)}{c(\lambda)} \dots \dots \dots (2.4)$$

2.3.4 Reflection and albedo

After travelling through the atmosphere, a part of solar radiation is absorbed by the Earth's surface and some portion is reflected back to the atmosphere again. Reflectance is defined as the ratio of the reflected to the incident radiance for a single incidence angle.

Albedo is the total reflectance of the surface integrated over all the angles of the upward hemisphere (Ranson et al., 1991) over all sun-view geometries. Oceans, lakes and forests reflect relatively small fractions of the incident sunlight and have low albedo whereas cloud, snow, sea ice and deserts reflect relatively large fractions of the incident sunlight and have large albedo (Saha, 2008).

2.4 Radiation in the ocean

The intensity of the solar radiation that ultimately reaches on the Earth's surface depends upon the value of solar constant, the transparency of the atmosphere, the latitude of the place and the seasonal, diurnal variation. After attenuation of radiation through the atmosphere, radiation reached at the ocean surface is modified by the optical properties of the ocean as it penetrate into the ocean column (Mobly, 1994).

2.4.1 Optical properties of ocean water

Optical properties of ocean water are connected with the biological, chemical and geological constituents present in the sea water. There are mainly three components in addition to pure water which influenced optical properties of water body. These are known as phytoplankton, suspended material and yellow substances (IOCCG 2000).

Phytoplanktons are single celled, free-floating organisms found in the illuminated layers of the ocean surface. The concentration of the main phytoplankton pigment, chlorophyll-‘a’ is often takes an index of phytoplankton biomass (IOCCG 2000). Suspended material represents a whole family of inorganic particulate materials with their own individual characteristics (IOCCG 2000). In shallow coastal and inland water bodies, wave and current bring bottom sediments and modify significantly optical properties of the ocean. The influence of suspended material is confined typically to the coastal and inland water bodies. Yellow substances are coloured, dissolve, organic substances. The absorption properties of yellow substances are variable. Light reflected from the bottom of a shallow water body can influence also in addition to phytoplankton, suspended material and yellow substances present in the water column. Optical properties of water are divided into two classes such as inherent optical properties (IOP) and apparent optical properties (AOP) (Joseph, 2005).

Theoretical background and literature review

Inherent optical properties are those properties that depend only upon the medium and therefore are independent on light field within the medium. The fundamental IOPs are the absorption coefficient and the volume scattering function. Other IOPs, such as the scattering coefficient, the beam attenuation coefficient and the single scattering albedo can be derived from these two fundamental IOPs. Apparent Optical Properties are those properties that depend both on the medium and on the geometric structure of the ambient light field. Irradiance, reflectance, the average cosines, various diffuse attenuation coefficients are example of AOPs.

2.4.2 Classification of ocean water

Depending on the presence of constitutes in the water, oceanic waters are divided into case I and case II waters (Jerlov, 1976; Joseph, 2005). Case I waters are those in which phytoplankton and their derivative products play a dominant role to determine the optical properties of the ocean. Case II waters are those in which inorganic/organic sediments make the dominant contribution.

2.5 Ocean colour from space

The colour of ocean is regulated by the ocean water molecules and the concentrations of different types of particles suspended in the upper water layer. Ocean water absorbs long wavelength of solar radiation and scatters the light of short wavelength. That is why ocean surface looks blue. Phytoplankton cells contain chlorophyll that reflect green colour and ocean surface looks in green. Ocean surface exhibits different colours depending upon the constituents present in the sea water. In highly productive region the coastal water often looks greenish yellow. Thus, ocean colour is a useful tool to study ocean water properties.

In satellite ocean colour remote sensing, a sensor is mounted on a satellite and is aimed at a point on the surface of the Earth. The sensor is having narrow field of view and is used to

monitor the radiometric flux at several selected wavelengths in the visible and near-infrared regions of the electromagnetic spectrum. Scanning device on the sensor and the movement of the platform acquires data from different points on the Earth. The sensor operates during the daylight hours and the ultimate source of the light reaching the sensor, is the Sun. However, the photons from the Sun can follow different pathway before detected at the remote sensor. Figure 2.3 shows the different pathways of light reaching the remote sensor.

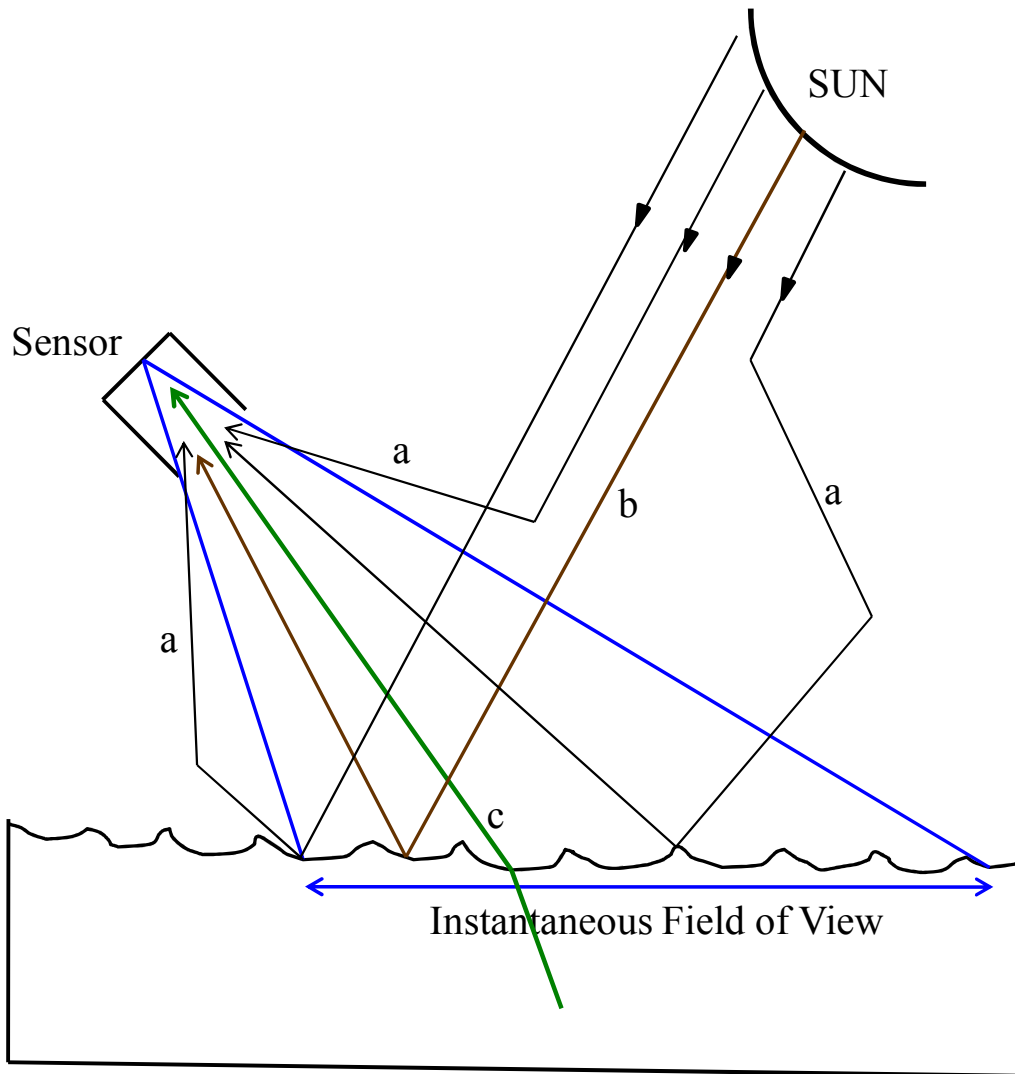


Figure 2.3: Pathway of light reaching the remote sensor (IOCCG, 2000)

Theoretical background and literature review

Figure 2.3 shows different contribution for an imaging ocean colour sensor, (a) shows the contributors to the remotely-sensed signal are scattered light from the atmosphere, (b) shows specular reflection of direct sunlight at the sea surface and (c) shows upwelling light leaving from the water surface and travelling in the direction of the sensor. Only the VIS-NIR (~ 400 to 700 nm) part of solar radiation penetrates into water. This radiation, after entering into the water, undergoes multiple scattering and absorption by water molecules and the ocean water constituents and small portion of this radiation part is scattered out of water, which is detected by the remote sensing sensors in the space.

Thus upwelling light from the sea surface carries useful information of the water body. Different types of particles present in the sea water including water molecules also play important role in the upwelling radiance. Several ocean colour sensors are designed to get water leaving radiance both for case I and case II ocean water through the space since 1978. The atmospheric contribution and specular reflection need to be corrected to get water leaving radiance. Specular reflection can be avoided with a desired tilt of a sensor. However, atmosphere contributes more than 80% of the light reaching at the detector of satellite (Morel, 1980). Different Ocean colour sensors are designed in such way that it has few bands in the visible region to understand the water properties and some bands in infra red region for atmospheric correction.

2.5.1 Ocean colour remote sensors from space

Ocean color sensors are designed to retrieve the spectral distribution of upwelling radiance just above the sea surface. The Coastal Zone Color Scanner (CZCS) was launched onboard by the National Aeronautics and Space Administration (NASA) Nimbus-7 spacecraft and provided the first ocean colour data set derived from a space borne sensor (Hovis et al., 1980) from 1978 to 1986. CZCS had six spectral bands, four of which were used primarily for ocean colour. These were of a 20 nm bandwidth centered at 443 nm, 520 nm, 550 nm and 670 nm. Band 5 had a 100 nm bandwidth centered at 750 nm. Band 6 operated in the 10500 to 12500 nm region and sensed

Chapter 2

emitted thermal radiance for derivation of equivalent black body temperature. The success of CZCS prompted launch of other ocean colour sensors MOS, OCTS, POLDER in 1996. Details about the past, current and future ocean colour sensors are regularly updated in IOCCG (International Ocean-Colour Coordinate Group) website (http://www.ioccg.org/sensors_ioccg.html).

NASA launched Sea-viewing Wide Field-of-view Sensor (SeaWiFS) in 1997 and two Moderate Resolution Imaging Spectroradiometers (MODIS) in 1999. The orbit of SeaWiFS was sun-synchronous and equatorial crossing time was 12 noon. It had eight spectral bands covering the visible and near-infrared (NIR) range from 400-900 nm. SeaWiFS mission operated during August 1997 to February 2011 (Frouin et al., 2005).

The MODIS instrument is currently flying on both Aqua and Terra platforms. The Terra platform was launched in December of 1999 into a sun-synchronous orbit. Equatorial crossing time of Terra platform is 10.30 a.m. MODIS instrument on Terra (MODIS-Terra) has been in continuous operation since February of 2000. The Aqua platform was launched in May 2002 into a sun-synchronous 1:30 p.m. orbit and MODIS-Aqua has been in continuous operation since June of 2002. The MODIS sensors measure radiance in 36 spectral channels covering the range from 400 nm to 14400 nm to support land, ocean and atmospheric measurements. The bands of primary interest to ocean colour applications are the first 9 channels covering the spectral range from 400-900 nm (Carder et al., 2003).

Another polar orbiting satellite ENVISAT was successfully launched on a polar orbit in March 2002 with on its board the Medium Resolution Imaging Spectrometer (MERIS). MERIS was operated up to May 2012. The equatorial crossing time was 10:00 am. The number of spectral bands was fifteen in the spectral range of 412-900 nm. MERIS is a multidisciplinary instrument designed to perform accurate ocean colour measurements and with secondary mission objectives such as atmospheric and land studies. Other than the polar orbiting satellites, GOCI is

Theoretical background and literature review

the first geostationary ocean colour satellite which was launched by KARI/KIOST of Korea dated on June 2010. It had 8 spectral bands from 400 nm to 865 nm (Bouvet 2006).

Ocean colour remote sensing from India started with the launch of OCEANSAT-1 OCM on May 1999. OCEANSAT-1 OCM provided ocean colour data around Indian subcontinent upto August 2010. It had eight bands. There were six visible and two near infrared (NIR) band centered at 412 nm, 443 nm, 490 nm, 510 nm, 555 nm, 670 nm, 765 nm and 865 nm in OCEANSAT-1 OCM satellite. The first six bands were used for analysing the ocean-colour components in the water column. The remaining two bands were used for measuring path radiance (aerosol and Rayleigh radiances), to apply atmospheric correction for ocean-colour analysis. The spectral resolution of the visible and NIR bands are 20 nm and 40 nm, respectively (Chauhan et al., 2002; Chauhan et al., 2003; Singh et al., 2007; Tripathy et al., 2015).

OCEANSAT-2 OCM is a follow-on instrument of OCEANSAT-1 OCM, which was launched in September 2009. OCEANSAT-2 OCM is almost identical to OCEANSAT-1 OCM with minor changes in the spectral bands 6 and 7, when compared to OCEANSAT-1 OCM spectral configuration. The spectral band 6 of OCEANSAT-1 OCM had a central wavelength at 670 nm and for OCEANSAT-2 OCM it has been shifted to a central wavelength of 620 nm. This change will lead to a better quantification of suspended sediment concentration. The spectral band 7 located at 765 nm for OCEANSAT-1 OCM has now been shifted to 740 nm for OCEANSAT-2 OCM to avoid oxygen absorption (Nagamani et al., 2008).

With the increasing importance of the study of ocean, launch of several ocean colour sensors are scheduled during 2016 to 2022 to continue the study of ocean through space. SGLI, HSI, VIIRS, OLCI, COCTS CZI, Multi spectral optical camera, OCI, OES, VSWIR and TIR instruments etc. are different polar orbiting satellite, which will be launched between 2016 to 2022 (http://www.ioccg.org/sensors_ioccg.html).

2.5.2 Geophysical parameter accessible from ocean colour remote sensing

Ocean color sensors are designed to retrieve the spectral distribution of upwelling radiance just above the sea surface, which is referred to as the water-leaving radiance. If the effect of the atmosphere can be removed from the radiance detected at the sensor, the spectral quality and quantity of the water leaving radiance has been used to determine different geophysical parameters from ocean. Normalized water leaving radiance, normalized reflectance and remote sensing reflectance are the basic three quantities used in different bio-optical algorithm to estimate different geophysical parameter such as chlorophyll-‘a’, diffuse attenuation coefficient, suspended sediments, photosynthetically available radiation, primary production etc. (IOCCG, 2012). Satellite derived chlorophyll-‘a’, along with the diffuse attenuation coefficient and photosynthetically available radiation (PAR) can further be used to compute primary production from the space (Platt et al., 1988a, 1988b, 1993, 2008; Longhurst et al. 1995; Antoine and Morel 1996; Behrenfeld and Falkowski 1997a). PAR products are either instantaneous or 24 hour averaged. The natural variability of instantaneous PAR is around 0 to 2200 $\mu\text{mol m}^{-2} \text{s}^{-1}$ and the natural variability of 24 hour averaged PAR is from 0 to 60 $\text{mol m}^{-2} \text{s}^{-1}$ (IOCCG, 2012). PAR estimation from *in-situ* data and satellite data has been described in the next section.

2.6 Photosynthetically available radiation estimation from *in-situ* data

Generally, PAR was measured from an empirical relationship with insolation measured by Pyronometer (Blackburn and Proctor, 1983) in absence of direct measurement from *in-situ* data. To understand the important role of PAR in the climate system, measurement of PAR from *in-situ* data has been increased. *In-situ* PAR has been measured at particular geographic location from the surface downwelling flux measurement instrument fixed at the top of buoys. PAR has been measured from buoy such as buoy from Halibut Bank (49.34° N, 123.73° W) off the west of

Theoretical background and literature review

Canada (0.00°N, 155.00 °W) in the central equatorial Pacific, Cove (36.9° N, 79.71° W) etc. from 1998 onwards and *in-situ* data are stored in SeaWiFS Bio-optical Archive and Storage System (SeaBass) maintained by the NASA Ocean Biology Processing Group (<http://seabass.gsfc.nasa.gov/>). PAR has been also measured from SolRad-Net (Solar Radiation Network). SolRad-Net is a network of ground based sensor and operated with companion to AERONET (Aerosol Robotic Network). AERONET is a system of globally distributed sunphotometer to investigate primarily aerosol optical depth (Zibordi et al., 2009). PAR has been measured from 2009 onwards at CAL-VAL (10°36'45''N, 72° 17'15''E) site developed under the Meteorology and Oceanography Programme of ISRO to validate different geophysical products obtained from OCM on regular basis (SAC Report, 2007).

In-situ PAR data also has been measured by surface reference sensor of radiometer carried in ship and PAR data has been measured at different geographic location during the ship cruise periods. During February – March, 1995 PAR values were measured in the eastern and central Arabian Sea (21°31' N, 64°E to 74°E) by National Institute of Oceanography under the JGOFS (India) programme (Suresh et al., 1996) with quantum PAR sensor. PAR has been measured with other biological, atmospheric and optical parameters by Space Applications Centre from 1999 onwards in the Arabian Sea and Bay of Bengal during different ship cruise periods for validation of OCEANSAT-1 OCM and OCEANSAT-2 OCM estimated geophysical parameters and for different scientific research purposes (Chauhan et al., 2002; Singh et al 2007; Raman et al., 2011; Tripathy et al., 2015). Thus, measurements of *in-situ* data are at discrete geographic locations over global oceans. Different methods to estimate PAR from space based observation has been discussed in the next section

2.7 Photosynthetically available radiation estimation from ocean colour remote sensor

In this section, different algorithms to estimate PAR from different ocean colour sensors are discussed. Two type of PAR products such as daily averaged PAR (i.e., 24 hour averaged) and instantaneous PAR (PAR is estimated at the satellite crossing time) are used in different primary production models (Platt and Sathyendranath 1993; Behrenfeld and Falkowski 1997a). Daily averaged PAR has been estimated from ocean colour remote sensors such as SeaWiFS, MODIS and MERIS (<http://oceancolour.gsfc.nasa.gov>). PAR was estimated from SeaWiFS, MODIS and MERIS by using algorithms developed by Frouin et al. (2003). Instantaneous PAR is estimated only from Terra and Aqua MODIS from February 2000 to till date. PAR data products are available in HDF (Hierarchical Data Format) files to a period of one day, eight days, a calendar month and a calendar year. The spatial resolution of SeaWiFS PAR products are 9 km (Frouin et al., 2003). However, spatial resolution of PAR products of MODIS Terra and Aqua and MERIS are 4 km (Carder et al., 2003; Bouvet 2006).

Daily averaged PAR has been estimated based on the approach by Dedieu et al. (1987) and Frouin and Chertock (1992). The PAR model uses plane parallel theory and assumes that the effects of clouds and clear atmosphere can be de-coupled by cloud albedo property. The planetary atmosphere is therefore modeled as a clear sky atmosphere positioned above a cloud layer. The algorithm works pixel by pixel. For each pixel SeaWiFS radiance expressed in $\text{mW cm}^{-2} \mu\text{m}^{-1} \text{sr}^{-1}$ was transformed into reflectance. Reflectance was corrected for gasses absorption, essentially due to ozone. The optical thickness of aerosol was calculated based on single scattering albedo approximation. The optical thickness of aerosols at each band was obtained from the optical thickness at spectral band 865 nm. Angström coefficient was estimated with ratio between bands 510 nm and 865 nm. Monthly climatology based on three years of SeaWiFS data (1997-2000) was used for aerosol optical depth (Frouin et al., 2003). To estimate single scattering albedo and phase function of aerosol, two closest aerosol models were selected. Daily PAR was obtained by

Theoretical background and literature review

integrating instantaneous PAR over the day. The sun glint areas were not selected because they would be interpreted as cloud in the PAR algorithm (Frouin et al., 2003). However, the cloud/surface system was assumed to be stable during the day and to correspond to the SeaWiFS observation time. In regions where clouds exhibit strong diurnal variability, PAR accuracy was found to be degraded. Still, useful daily PAR estimates would be obtained by averaging in space and time. Finally, the individual daily PAR obtained in units of $\text{mW cm}^{-2} \mu\text{m}^{-1}$, are converted into units of $\text{Einstein m}^{-2} \text{day}^{-1}$ and averaged into 9 km resolution.

The second product is instantaneous photosynthetically available radiation. This product is only available from MODIS. Instantaneous photosynthetically available radiation is the total downwelling photon just above the ocean surface integrated over the wavelength range 400 to 700 nm and PAR is measured in the instant when sensor views a given pixel. PAR model computed the downwelling irradiance just above the sea surface at 1 nm interval wavelength. The spectrum was then binned and weighted appropriately to give the irradiance in each of the visible MODIS channel. PAR under cloudy sky was not estimated in MODIS instantaneous PAR. MODIS instantaneous PAR was estimated based on Gregg and Carder (1990) spectral solar irradiance model for cloudless maritime atmosphere (Carder et al., 2003).

Gregg and Carder (1990) model estimated aerosol optical thickness using the Navy aerosol model (Gathman, 1983). The inputs in the aerosol model are air-mass type, 24 hour averaged wind speed, instantaneous wind speed and relative humidity. The model is an extension of Bird (1984) model which was developed for continental aerosol. Bird (1984) used simple mathematical expressions and tabulated look up tables to generate direct normal and diffuse horizontal irradiance under the clear sky condition. This model accounted Rayleigh scattering, aerosol scattering and absorption, water vapour absorption, ozone and uniformly mixed gas absorption. Rayleigh scattering transmittance has been estimated by LOWTRAN 5 (Kneizys et al., 1980) expression. Aerosol scattering and absorption are determined by Mie scattering theory for rural aerosol model. Water vapour transmittance is estimated from Leckner (1978) expression. Water vapor absorption coefficients are estimated from the 1978 Air Force

Chapter 2

Geophysics Laboratories line parameter data. Bird and Riordan (1986) modified Bird (1984) algorithm to estimate total insolation on a tilted surface. Furthermore, Gregg and Carder (1990) made some simplification compared to Bird and Riordan (1986) model based on the characteristics of the maritime environment and the spectral range under consideration. In this model, irradiance is attenuated in passing through the atmosphere by Rayleigh scattering, ozone, oxygen and water vapour absorption, and marine aerosol scattering and absorption and is finally modified by the reflectance at the air-sea interface. In instantaneous MODIS PAR, aerosol optical depth has been estimated at spectral band 869 nm, 667 nm and 412 nm. For marine non absorbing aerosol angstrom exponent was calculated using angstrom formula and ratio between 869 nm, 667 nm and 412 nm based on Gordon approach. Instantaneous PAR estimated from MODIS does not account cloud property (Carder et al., 2003).

Van Laake and Azofeifa (2004) developed a method to estimated instantaneous PAR using data from MODIS atmosphere products and this model is known as PARcalc model. In PAR calc model, direct MODIS products such as angstrom turbidity coefficient for aerosol scattering, single scattering albedo for different types of aerosol and cloud optical depth were used. In this method, the atmosphere is treated as a single layer in clear sky conditions or as a double layer i.e., a layer above the cloud top and a layer from the cloud top downwards. This method is based on the clear sky irradiance equation given in Iqbal (1983) and broadband cloud reflection algorithm given in Stephens et al. (1984). Surface reflectance is not included in the PARcalc method.

Liang et al. (2006) developed a new method based on the look-up table approach for estimating instantaneous incident PAR from the MODIS data. In this method, both the attenuation due to atmosphere and surface reflectance were included. This procedure had two steps. First step was to determine the surface reflectance from the clearest observations during a temporal window. Second step was to calculate incident PAR from the determined surface reflectance and top of the atmosphere reflectance using the table look-up approach. Aerosol

Theoretical background and literature review

optical depth, cloud optical depth and surface reflectance estimated from MODIS were used in this method.

Nasahara (2009) used a simple radiative transfer scheme which requires only one spectral channel (red) of MODIS data to estimate PAR. The algorithm is based on the principle of conservation of energy between incoming PAR flux at the top of the atmosphere, absorbed PAR flux in the atmosphere (including aerosol and cloud), reflected PAR flux at the top of the atmosphere and at the ground. Satellite data without atmospheric correction give reflectance of PAR at the top of the atmosphere. Reflectance from the ground should be estimated from the atmosphere corrected satellite data. Reflectance of PAR at the top of the atmosphere and from the ground was estimated from the red channel of MODIS.

Instantaneous PAR was estimated from the radiative transfer model developed by Gregg and Carder (1990) using MERIS data (Aiken and Moore, 1997; Bouvet, 2006). The inputs of the model are aerosol optical depth at 775 nm and 865 nm, ozone concentration, column water vapour, solar zenith angle and Earth Sun distance.

Frouin and Murakami (2007) estimated PAR at the ocean surface from Global Imager (GLI) data. Frouin and McPherson (2012) estimated PAR at the ocean surface using Geostationary Ocean Color Imager (GOCI) data at hourly intervals. The algorithms were based on Frouin et al. (2003) which has been used to estimate daily averaged PAR from SeaWiFS.

Singh et al. (2007) developed an approach to estimate PAR from OCEANSAT-1 OCM using Bird's clear sky model (Bird, 1984). In this approach, aerosol optical depth was estimated at spectral band 865 nm and 670 nm assuming the radiation detected at the sensor greater than 700 nm wavelength is totally contribution from the atmosphere. The aerosol transmittance was computed on a pixel by pixel basis. The transmittance due to Rayleigh scattering, ozone, uniformly mixed gas was also used at each pixel to obtain PAR during the satellite pass. The exponential relation was used to approximate the aerosol optical depth at all visible channels

from channels 670 nm and 865 nm. PAR has been also estimated from other than ocean colour satellites.

2.8 Photosynthetically available radiation estimation from other than ocean colour remote sensors

The International Satellite Cloud Climatology Project (ISCCP) is the first project of the World Climate Research Program (WCRP) to estimate solar irradiance field using cloud optical properties. There were five radiation products such as surface and top of the atmosphere incident and upwelling shortwave fluxes and downwelling PAR. 3-hourly monthly mean PAR during 1987 to 1988 and monthly mean PAR during 1983 to 1994 was estimated. The primary data sources in ISCCP are the four geostationary and two polar orbiting weather satellites (Schiffer and Rossow, 1985; Rossow and Schiffer, 1991). The four geostationary satellites are GMS, METEOSAT, Goes-west, Goes-east and polar orbiting satellites are NOAA afternoon and NOAA morning. PAR data sets are in global scale and have the resolution of 2.5 degree \times 2.5 degree. Pinker and Laszlo (1992b) generated five global radiation products from ISCCP archive using modified solar radiation model of Pinker and Ewing (1985). The method is based on the relating the broadband (200-4000 nm) transmissivity (ratio of irradiance at the surface to that at top of the atmosphere), to the broadband top of the atmosphere reflectivity (ratio of the reflected flux at top of the atmosphere to the top of the atmosphere irradiance) (Pinker and Laszlo, 1992b). This atmospheric radiative transfer model accounted of i) absorption by ozone and water vapour ii) multiple scattering by molecules iii) multiple scattering and absorption by aerosols and cloud droplets iv) multiple reflection between the atmosphere and the surface. This model had five or six layers depending on the aerosol profile and present of cloud. The vertical distribution of aerosols was assumed that the number of particles decreased exponentially with height. Four atmospheric aerosol profile of the standard radiation atmosphere (WCP-55 1983) was considered. At each aerosol model, values of aerosol asymmetry factor, albedo of single scattering and

Theoretical background and literature review

extinction coefficient was obtained from Mie theory. Cloud parameterization of Stephens et al. (1984) was obtained.

Eck and Dye (1991) estimated PAR incident at the Earth's surface under the cloudy condition using ultraviolet reflectance at 370 nm, based on the assumption that there is evidently constant reflectivity of clouds across ultraviolet and PAR wavebands. Ultra violet spectral reflectance data from the Total Ozone Mapping Spectrometer (TOMS) were used. First, PAR for clear sky condition is computed from a spectral model proposed by Goldberg and Klein (1980) and this model is theoretically independent on satellite measurement. Second, actual PAR was computed by adjusting the potential value by the proportion of PAR which is not received at the Earth's surface as result of reflectance by clouds or other scattering elements in the atmosphere (Eck and Dye, 1991). Dye and Shibasaki (1995) compared PAR estimated from ISCCP, MODIS and TOMS with *in-situ* data at a mid latitude site for non winter months. Comparison results showed that TOMS PAR provides most reliable estimation compared to ISCCP and MODIS estimated PAR.

Rubio et al (2005) developed a method to estimate hourly PAR using measurements from METEOSAT satellite. The clear sky model was based on parametric model proposed by Iqbal (1983). Then the effect of clouds was introduced using the measurements of the METEOSAT satellite. The ozone and water vapour transmittances were calculated with their respective absorptance following Lacis and Hansen (1974). Rayleigh and aerosol transmittance were estimated following Iqbal (1983). Schiller (2006) estimated PAR from METEOSAT data using two different models such as physical model and neural net.

Janjai and Watten (2011) presented a model for the estimation of monthly PAR sampled at hourly basis for tropical environment using Multifunctional Transport Satellite -1R (MTSAT-1R) visible data together with the ozone data from the Ozone Monitoring Instrument (OMI) onboard AURA satellite and ancillary ground-based data. The reason behind to estimate monthly PAR instead of daily PAR sampled at hourly basis in the tropical regions is that clouds are

Chapter 2

strongly random and inhomogeneous and a single scan per hour is not sufficient to represent the properties of clouds (Nunez et al., 2005).

To improve PAR product time resolution, Li et al. (2012) estimated hourly PAR based on the combination of geostationary satellite MTSAT and polar orbiting satellite MODIS. PAR value in clear day depends on aerosol optical thickness at 550 nm, water-vapor, ozone, altitude, surface albedo etc. In cloudy day, PAR value mainly depends on the characteristics of the cloud. This model proposed an approach to construct look-up table between PAR and different weather conditions for clear day. PAR under cloudy condition was estimated using cloud optical thickness property.

Some models were also developed to estimate PAR where *in-situ* parameters were obtained from *in-situ* measurements. Anjorin et al. (2014) estimated hourly PAR from an empirical model developed by Alados et al. (1996). This is a site based method in which routinely measured hourly global solar radiation are used as inputs to estimate PAR values for the period of three years (2003, 2004 and 2005). Kathilankal et al. (2014) developed a semi-parametric PAR model using commonly measured climatic variables from seventeen sites of United States. The climatic variables were relative humidity, clearness index, surface albedo and solar elevation angle. Estimated PAR from model or satellite data would be used in different radiation budget models. PAR data is also used as an important input parameter to model terrestrial or ocean primary production.

2.9 Modeling ocean primary production

One of the principle applications of ocean colour remote sensing is to estimate primary production. By definition, primary production is the amount of photosynthetically fixed carbon available to the first heterotrophic level. Models to compute daily water column production is a function of available light and biomass (Ryther, 1956; Talling, 1957).

Theoretical background and literature review

Total radiation in the wavelength range from 400 to 700 nm i.e PAR is important in the photosynthetic processes. Considering the actual utilization of radiant energy through the photosynthesis, two additional definitions for radiation are also important (Parsons et al., 1984). These are photosynthetically usable radiation (PUR) and photosynthetically stored radiation (PSR). PUR is the fraction of radiant energy which is actually absorbed by algae. PUR depends entirely on the pigment composition of the algal population and also spectral composition of the submarine radiant energy (Parsons et al., 1984). Only a fraction of PUR is stored as chemical energy in the form of organic matter during photosynthetic process is termed as PSR.

The curve which shows the variation of net photosynthesis rate as a function of PAR is known as P-I curve. Photosynthesis increases with increasing light intensity up to some asymptotic value P_{max} . After that, the system becomes light saturated. The two most important properties of the curve are the slope α and maximum photosynthesis rate P_{max} . P_{max} is termed as assimilation number. Initial slope of the P-I curve has been defined as the quantum yield.

Different models are developed to estimate primary production. Primary production models are categorized into empirical, semi-analytical and analytical type (Platt and Sathyendranath, 1993). However, Behrenfeld and Falkowski (1997b) proposed a more rational categorization scheme based upon inherent levels of integration. These models are i) Wavelength resolved models ii) Wavelength integrated models iii) Time integrated models and iv) Depth integrated models.

Wavelength resolved models (WRM) convert Photosynthetically usable radiation (Morel 1978) into net photosynthesis. Wavelength resolved models are based on the photosynthesis - irradiance variable such as chlorophyll-specific maximum photosynthetic rate P^B_{max} , initial light-limited slope for chlorophyll-‘a’ specific carbon fixation α^B (Sathyendranath and Platt 1989; Morel 1991). Daily water column primary production is thus calculated by integrating photosynthetic rates over wavelength, depth and time. Wavelength dependency in wavelength resolved model has been removed in wavelength- integrated models (WIM). In this model, net

Chapter 2

photosynthesis is described as a function of PAR rather than PUR. Primary production is estimated by integrating PAR-dependent photosynthesis- irradiance functions over depth and time.

Time-dependent resolution in solar irradiance is removed in time integrated models (TIM). This time integrated models maintain vertical resolution. The parameterization of these type of models are based from measurements taken over extended periods (typically 6-24 hour) under conditions of variable solar irradiance and thus have intrinsically integrated a range of photosynthetic rates into a single productivity value. Development of time integrated models follows the early observation of depth profiles of primary production typically exhibits predictable shapes similar to photosynthesis-irradiance functions (Ryther, 1956). That is why, instead of using terminology P_{\max}^B in TIM model P_{opt}^B has been used for discussions on the differences between TIM and photo-synthesis-irradiance variables (Behrenfeld and Falkowski, 1997b).

Depth-integrated models (DIMS) forms the final category of daily productivity models. It uses vertically integrated functions to relate environmental variables measured at sea surface to the water column integrated daily primary production. The input variables of depth- integrated models are euphotic depth, product of depth integrated chlorophyll, daylength, irradiance dependent function and photo-adaptive parameters (Wright 1959; Platt and Sathyendranath 1993; Behrenfeld and Falkowski 1997a).

Net ocean primary production is estimated from MODIS data (<http://www.science.oregonstate.edu/ocean.productivity/standard.product.php>) use Vertically Generalized Production Model (VGPM) developed by Behrenfeld and Falkowski (1997a). VGPM is a light and chlorophyll based depth integrated model and is similar in form to the early models of Ryther and Yentch (1957) and Talling (1957). In this model input parameters are surface chlorophyll concentration, sea surface temperature, cloud corrected daily averaged photosynthetically available radiation, euphotic depth and daylength. Surface chlorophyll

Theoretical background and literature review

concentration, sea surface temperature and daily averaged PAR have been estimated from MODIS data. Euphotic depth has been estimated from surface chlorophyll concentration using Morel and Benthon (1989) expression. The accuracy of the productivity algorithms in estimating euphotic primary production depends primarily upon optimal assimilation efficiency of the productivity profile (P^B_{opt}). A temperature dependent P^B_{opt} model has been used to estimate P^B_{opt} (Behrenfeld and Falkowski, 1997a).

A non-spectral analytical model developed by Platt and Sathyendranath (1993) has been used to estimate mixed layer primary production and euphotic primary production from OCEANSAT- 1 & 2 OCM (Raman et al., 2011). The input parameters are surface chlorophyll- 'a', vertical diffuse attenuation coefficient (K_d), vertical diffuse attenuation coefficient for PAR region (K_{PAR}), daylength, mixed layer depth, euphotic depth, PAR at noon and P-I parameter. In this model, P-I parameters (α^B , P^B_{max}) has been obtained from photosynthesis-irradiance curve from *in-situ* observations during different ship cruises in the north Indian Ocean. Chlorophyll- 'a' has been estimated using semi-analytical maximum band ratio algorithm Ocean Chlorophyll 4 developed by Nagamani et al. (2008) using OCM data. Vertical diffuse attenuation coefficient (K_d) of oceanic water defines the penetration of natural light into ocean depth. K_d has been computed as a function of ratio of water leaving radiance in 490 nm and 555 nm for case-I waters. PAR at noon at sea surface under cloud free conditions has been estimated using a clear sky spectral irradiance model of Bird (1984) for spatially uniform aerosol optical depth. Monthly climatological mixed layer thickness has been used for mixed layer depth. Euphotic depth has been estimated from vertical structure of phytoplankton biomass characterized by a shifted Gaussian model.

From the above discussion on the primary production modeling it is clear that accurate estimation of PAR is one of the key requirements for primary production modeling. However, there are many gap areas in the estimation of PAR from space based data sets, such as impacts of aerosols on PAR estimation, presence of cloudy sky and effects of diffuse radiation etc. In the

Chapter 2

present thesis, some of these issues has been attempted to estimate PAR under spatially variable and cloudy condition from OCM data.

Chapter 3

Modeling Photosynthetically Available Radiation (PAR) & sensitivity study using *in-situ* data over Indian Ocean

This chapter describes estimation of Photosynthetically available radiation (PAR) at a single geographic location during ship cruise period in the Arabian Sea using a Coupled Ocean Atmosphere Radiative Transfer (COART) model. During ship cruise period, surface PAR has been measured from a surface downwelling flux measurement instrument. COART model derived PAR has been compared with in situ measured PAR. A sensitivity study has been done to estimate various PAR values with varying aerosol optical depth from 0 to 1 to understand the variation of PAR for various aerosol optical depths and for different aerosol types. To understand the variability of PAR under different cloud coverage, direct and diffuse component of PAR has been computed using a non-linear relationship for variable cloud coverage.

3.1 Introduction

Indian Ocean is situated between 25°N and 40°S latitudes and 4°E and 115°E longitudes (Quasim, 1998). Broadly, Indian Ocean is divided into two regions - North Indian Ocean and South Indian Ocean. North Indian Ocean includes the Arabian Sea and the Bay of Bengal. Geographic location of the Bay of Bengal is between latitudes 0°N and 23°N and longitudes 80°E and 100°E. Arabian Sea is situated between latitudes 0°N and 25°N and longitudes 50°E and 80°E (Quasim, 1998). Northern, eastern and western sides of the Arabian Sea are bordered by the landmass of Asia and Africa. Arabian Sea is connected with the Persian Gulf through the Gulf of Oman. Gulf of Eden connects the Arabian Sea with the Red Sea.

Geographical location, wind pattern, ocean circulation, distribution of different physical and biological properties such as sea surface temperature (SST), salinity, chlorophyll, primary productivity etc. are unique in the Indian Ocean compared to the other oceans such as Atlantic and Pacific Ocean (Quasim, 1998). Indian Ocean is locked by land to the north side and does not extend into the cold climate regions of the northern hemisphere. Such a geographical structure causes asymmetry in wind and oceanic circulation over the Indian Ocean. Both the Bay of Bengal and the Arabian Sea are influenced by seasonally reversing southwest monsoon during June to September and northeast monsoon during October to December (Kripalani and Kumar, 2004).

Arabian Sea and Bay of Bengal are two most productive regions and contributes one third of the total photosynthetic productivity of the Indian Ocean. The range of the primary production within a 100 m column of water is around 0.001 to 6.5 g C m⁻² day⁻¹ (Quasim 1998). Primary production primarily depends on nutrients and photosynthetically available radiation, or PAR, (~400–700 nm wavelengths) at sea surface. From the top of the atmosphere while propagating through the atmosphere, PAR is absorbed or scattered by different atmospheric constituents like aerosols, clouds, ozone, water vapour and various gases. Total PAR is the summation of direct PAR and diffuse PAR. Direct PAR proceeds directly to the surface of the Earth after losses by absorption or scattering (Carder et al., 2003) in the atmosphere. Diffuse irradiance is scattered out

Modeling PAR and sensitivity study using *in-situ* data

of the direct beam but toward the surface (Carder et al., 2003). Reflection of the solar radiation from the ocean surface also affects PAR variation. In that case, PAR which reaches at the Earth's surface through the atmosphere, is reflected back into the atmosphere and interacts with Earth's atmosphere and reaches back to the Earth's surface again (Zheng, 2007). Because of the re-entry into the atmosphere of the reflected solar radiation, the magnitude of reflected PAR depends not only on Earth surface conditions but also on atmospheric optical properties (Zheng, 2007). On a daily level, cloudiness and aerosols have a significant influence on the amount of the radiation that reaches the Earth's surface (Hess et al., 1998; Runnström et al., 2006; Sarkar et al., 2006).

Aerosol loadings over the Arabian Sea and tropical Indian oceanic regions are influenced from Indo-Gangetic plain, Arabian peninsula, central India and south India (Verma et al., 2008). This region is dominated by high aerosol loading and it has been found that aerosol loading is on rise in the northern part of India compared to southern regions (Sarkar et al., 2006). The major constituents of continental aerosols those are influenced by the air mass from the Indian subcontinent, are sulphate and organic matter (Verma et al., 2007). Mineral dust coming from the Africa is also dominant over the Indian Ocean (Verma et al., 2007; Verma et al 2008). Aerosol size, types also show temporal and spatial variability over the Arabian Sea (Husar et al., 1997; Sarkar et al., 2006; Nair et al., 2005; Chauhan et al., 2009; Menon et al., 2011). The aerosol optical depth (AOD) value decreased from the coast to the open ocean (Moorthy et al., 2001; Chauhan et al., 2009; Menon et al., 2011). Relatively higher concentration of smaller size particles are dominated over the coastal regions as compared to that over the open ocean water (Chauhan et al., 2009) in the Arabian Sea.

Clouds scatter significantly in the visible region compared to absorption. In cloudy condition, direct component of PAR is reduced and diffused component is increased (Frouin et al., 1995). Arabian Sea is situated around Inter Tropical Convergence Zone belt and more likely remain cloudy compared to the other temperate oceans (Saunders, 1985).

In the view of above, PAR has been estimated at a single geographic location during the ship cruise period in the Arabian Sea using a *Coupled Ocean Atmosphere Radiative Transfer* (COART) model. COART model derived PAR has been compared with *in-situ* PAR measured using a surface reference sensor of a visible-NIR radiometer during 3–17 November 2001, 4–19 January 2003 and 7–19 March 2011 in the Arabian Sea. In the context of the increased aerosol concentration over the northern part of India, a sensitivity study through COART model has been carried out to understand the effect of increased aerosol optical depth on PAR. To understand the variability of PAR under different cloud coverage, direct and diffuse component of PAR has been computed using a non-linear relationship for variable cloud coverage.

3.2 PAR estimation using radiative transfer model from *in-situ* data

PAR has been estimated at a single geographic location using a *Coupled Ocean Atmosphere Radiative Transfer (COART)* model (<http://www-cave.larc.nasa.gov/cave/>). In this model, different input components have been estimated from *in-situ* observations. In COART model, the atmosphere and ocean is considered as one system. However, ocean and atmosphere has different refractive index. Atmosphere is again divided into four layers. Concentration of vertical structure of water vapour, ozone and of uniformly mixed gases and aerosols obtained from *in-situ* observation, are used in COART model. Description of radiative transfer model, input and output of the model are discussed in the next section.

3.2.1 Description of radiative transfer (RT) model

The basic equation of the coupled ocean and atmosphere system is described in the equation (3.1) (Jin et al., 1994; Jin et al., 2006)

$$\mu \frac{dI(\tau, \mu, \varphi)}{d\tau} = I(\tau, \mu, \varphi) - S(\tau, \mu, \varphi) \dots \dots \dots (3.1)$$

Modeling PAR and sensitivity study using *in-situ* data

$I(\tau, \mu, \varphi)$ is the radiance at vertical depth τ . τ is measured downward from the upper boundary in direction (μ, φ) . μ is the cosine of the solar angle, which is positive with respect to the upward normal, φ is the azimuth angle. S is source function. Source function is estimated using equation (3.2)

$$S(\tau, \mu, \varphi) = \frac{\omega(\tau)}{4\pi} \int_0^{2\pi} d\varphi' \int_{-1}^1 p(\tau, \mu, \varphi, \mu', \varphi') I(\tau, \mu', \varphi') d\mu' + Q(\tau, \mu, \varphi) \dots \dots \dots (3.2)$$

Where $\omega(\tau)$ is the single-scattering albedo and $p(\tau, \mu, \varphi, \mu', \varphi')$ is the phase function. $Q(\tau, \mu, \varphi)$ represents the actual internal source. The solar beam source in the atmosphere can be expressed by equation (3.3).

$$Q(\tau, \mu, \varphi) = \frac{\omega(\tau)}{4\pi} p(\tau, \mu, \varphi, -\mu_0, \varphi_0) \exp(-\tau/\mu_0) + \frac{\omega(\tau)}{4\pi} F_0 R(-\mu_0, n) p(\tau, \mu, \varphi, \mu_0, \varphi_0) \\ \times \exp\left[-\frac{2\tau_a - \tau}{\mu_0}\right] \dots \dots \dots (3.3)$$

Expanding the radiance $I(\tau, \mu, \varphi)$ into a Fourier cosine series of $2N$ and the phase function $p(\tau, \mu, \varphi, \mu', \varphi')$ into series of $2N$ Legendre polynomials, the discrete-ordinate method converts equation (3.1) into a system of azimuthally independent, coupled differential equations for each of the Fourier component.

3.2.2 Inputs for RT model

3.2.2.1 Geographical location and time

Several ship cruises were organised by Space Applications Centre, Indian Space Research Organisation (ISRO), India in the north-eastern Arabian Sea (NEAS) during 3–17 November 2001, 4–19 January 2003 and 7–19 March 2011 to measure optical parameters of sea water

Chapter 3

(radiance/irradiance profile, PAR) and atmospheric parameters (aerosol optical depth). The locations of the data collection during ship campaigns are shown in Figure 3.1. A total of 37 hydrographic stations were sampled during the entire study period and the area covered during the cruises was within 10–20°N and 66–75°E.

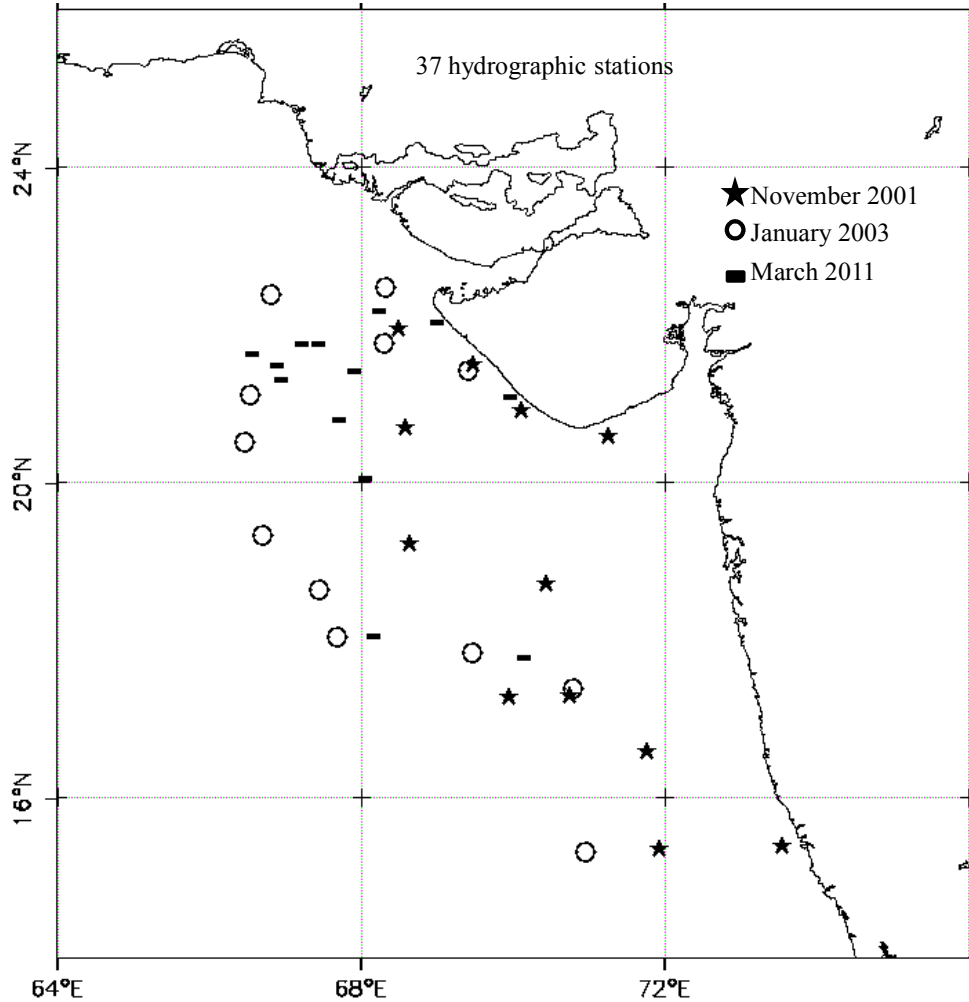


Figure 3.1: Location of data points of ship cruises in the Arabian Sea (date: 3–17 November 2001 (SK171), 4–19 January 2003 (SK186) and 7–19 March 2011 (FORV 286).

Modeling PAR and sensitivity study using *in-situ* data

Latitude and longitude positions of each hydrographic station at 6:30 GMT (Greenwich Mean Time) have been used as input to estimate PAR using COART model during ship cruise periods in the Arabian Sea.

3.2.2.2 Extraterrestrial solar irradiance at the top of the atmosphere

Extraterrestrial solar irradiance at the top of the atmosphere have been obtained from MODTRAN (MODerate resolution atmospheric TRANsmission) of version v3.5 in COART model (<http://snowdog.larc.nasa.gov/jin/rtnote.html>).

3.2.2.3 Atmosphere

3.2.2.3.1 Atmospheric absorption model

Vertical structure of temperature, pressure and absorbing gas concentration are different in tropical, mid latitude and Arctic atmosphere. Arabian Sea is situated in the tropical belt and all the ship cruise measurements are shown in Figure 3.1 were taken under cloud free condition. Tropical model has been used as atmospheric model and no cloud has been selected. Concentration of water vapour, ozone and concentration of uniformly mixed gases in tropical atmosphere upto 100 km height were listed in McClatchey et al. (1972). Atmospheric absorption is based on LOWTRAN7 band model (<http://snowdog.larc.nasa.gov/jin/rtnote.html>).

3.2.2.3.2 Vertical distribution of aerosol particle

The distribution of aerosol particle varies exponentially (Hess et al., 1998) with height in COART model. Based on the vertical distribution of aerosol, atmosphere is composed of four discrete layers. First layer is considered from the sea level and it consists with the combination of

Chapter 3

particles from different origin. On the top of this first layer, a desert dust layer is placed. The default value for the thickness of the second layer is zero. An additional layer thickness of 1.5 km, a particle number density of $11 \text{ particles cm}^{-3}$ and optical thickness of 0.1 is placed with the second layer. The third and fourth layers represent the free troposphere and the stratosphere. Free troposphere layer situates above the first layer in absence of mineral dust layer. The aerosol in the free troposphere is composed of the continental components at a relative humidity of 50% with a dominant part of the water-soluble component, a certain part of soot and some insoluble particles. The upper boundary of the free troposphere is always situated at 12 km (Hess et al., 1998). Therefore, the thickness of the third layer depends upon the thickness of the first layer and the presence of the mineral transported layer. Stratospheric aerosol layer is assumed to be situated between 12 km and 35 km (Hess et al., 1998).

PAR has been estimated with the input of aerosol optical depth (AOD) in the first layer at 500 nm measured using Sunphotometer during different ship campaigns in the Arabian Sea. Stratospheric aerosol has been assumed to be zero as there were no reports by volcanic activity or other events that would result in extra aerosol loading to the stratosphere during the ship cruise period. Estimation and variation of AOD at 500 nm during November 2001, January 2003 and March 2011 are illustrated in the next section.

3.2.2.3.3 Aerosol optical depth estimated from *in-situ* observation

EKO sunphotometer was used to measure AOD during November 2001 and January 2003. It had five filters at 368 nm, 500 nm, 675 nm, 778 nm and 865 nm. The function of these filters was to allow only the light corresponding to those wavelengths to pass through them. During March 2011, Microtop II hand held sunphotometer of Solar Light Company USA was used to measure AOD at five different wavelengths (380 nm, 440 nm, 500 nm, 675 nm, and 879 nm). The basic principle is similar to that of EKO Sunphotometer.

Modeling PAR and sensitivity study using *in-situ* data

If I_0 is the un-attenuated radiation and I is the radiation that reaches the sunphotometer after interaction with the air molecules and aerosols, then a straight line is obtained by plotting the logarithm of the voltage values against $1/(\cos$ of solar zenith angle), which is called the Langley plot. The negative slope of Langley plot gives the total optical depth comprising of Rayleigh optical depth and aerosol optical depth. Rayleigh optical depth has been calculated with the inverse relationship between Rayleigh optical depth and fourth power of wavelength (Moon et al., 2009) at mean sea level. Rayleigh optical depth has been subtracted from the total optical depth to get the value of aerosol optical depth during ship cruise periods. Sun photometer readings were taken at every half an hour throughout the day on all days. Figure 3.2 shows the variation of aerosol optical depth during ship cruise periods.

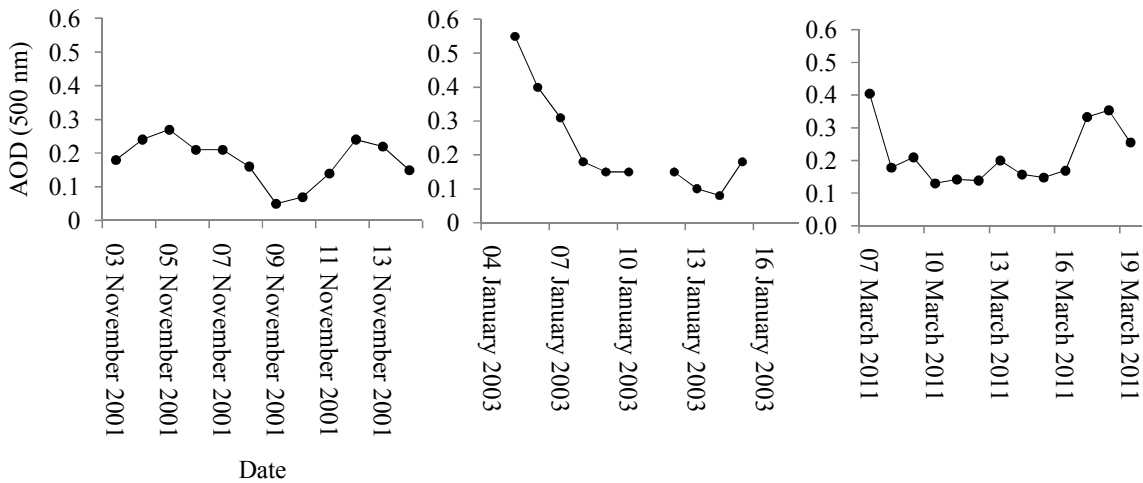


Figure 3.2: Variability of AOD (500 nm) during different ship cruises.

The variation of AOD (500 nm) was from 0.05 to 0.2 during November 2001, from 0.08 to 0.55 during January 2003 and from 0.13 to 0.41 during March 2011.

3.2.2.4 Surface reflectance

In COART model, the influence of surface reflectance is modelled with wind speed, albedo from the ocean surface, chlorophyll-‘a’ in water and ocean depth (<http://snowdog.larc.nasa.gov/jin/rtnote.html>). However, the influence of sea surface reflectance on PAR is negligible (Mallet et al., 2009). Ocean depth has been set as zero to neglect upwelling radiance from the ocean surface.

3.2.3 Output from RT model

The outputs of the model were integrated flux from 400 nm to 700 nm (PAR) at 10 nm spectral resolution at sea surface at *in-situ* aerosol optical depth at 12 p. m under clear sky condition. COART model derived PAR has been validated with *in-situ* measured PAR during different ship cruise periods.

3.3 PAR measurement from *in-situ* observation above the ocean surface

PAR was measured during the ship cruise period from a surface reference sensor of underwater radiometer (Satlantic Inc.). An underwater (Satlantic Inc.) radiometer having seven bands centered on 412 nm, 443 nm, 490 nm, 510 nm, 555 nm, 670 nm and 780 nm was used during 2001 and 2003. Surface PAR was obtained from SMSR (SeaWiFS Multi channel Surface Reference) sensor. Another underwater (Satlantic Inc.) radiometer having 1.2 nm spectral resolution was used in cruise conducted in 2011. Surface reference E_s sensor provided surface PAR. *In-situ* data has been processed using the software (Prosoft) provided with the Satlantic instrument.

Modeling PAR and sensitivity study using *in-situ* data

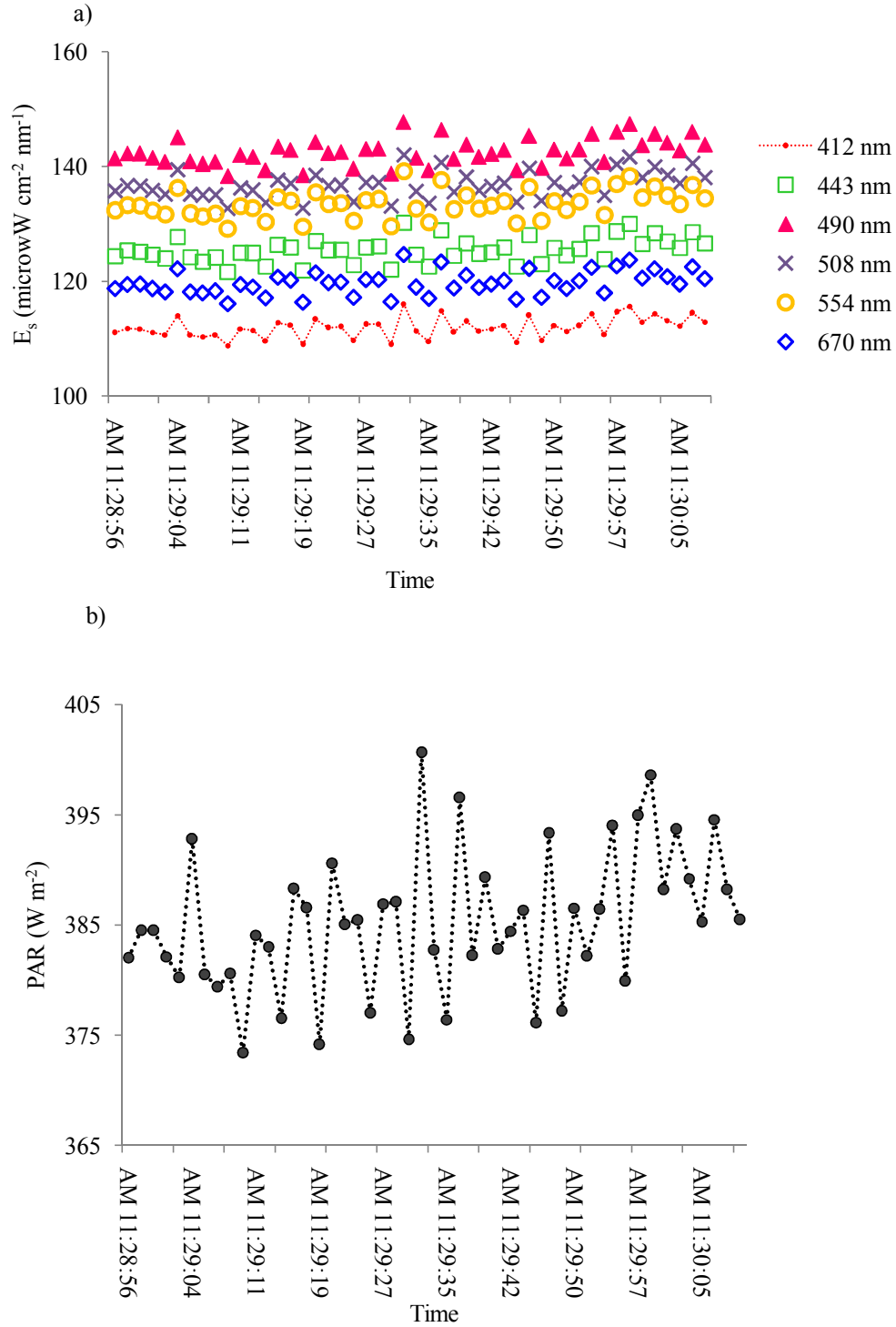


Figure 3.3: (a) Variation of downwelling irradiance E_s at different wavelength with time and (b) variation of PAR with time.

Chapter 3

In-situ data has been processed using the software (Prosoft) provided with the Satlantic instrument. Both the radiometers are calibrated every year according to the calibration protocols provided by the Satlantic Inc. company using NIST certified integrating spheres as calibration source. Reference sensor was kept on the deck of the ship away from the shadow of the ships superstructures and the shadow of the radar dome. Measurement of surface irradiance was carried out between 11:30 am and 12:30 pm. PAR has been estimated using the following equation (3.4).

$$PAR = \int_{400 \text{ nm}}^{700 \text{ nm}} \frac{\lambda}{hc} E_s(\lambda) d\lambda \quad \dots \dots \dots (3.4)$$

Figure 3.3 (a) shows the variation of downwelling irradiance E_s at different wavelengths at different time. Figure 3.2 (b) shows the variation of PAR in the range 400 nm to 700 nm at different times. PAR has been averaged within the time interval. Solar zenith angle has been calculated at each station at observation time (Woelf, 1968). PAR at local noon has been calculated by dividing PAR at observation time by cosine of solar zenith angle. The unit of PAR in micromole $\text{cm}^{-2} \text{sec}^{-1}$ has been converted to W m^{-2} unit (Dye, 2004). Figure 3.4 shows the variation of PAR during 3–17 November 2001, 4–19 January 2003 and 7–19 March 2011.

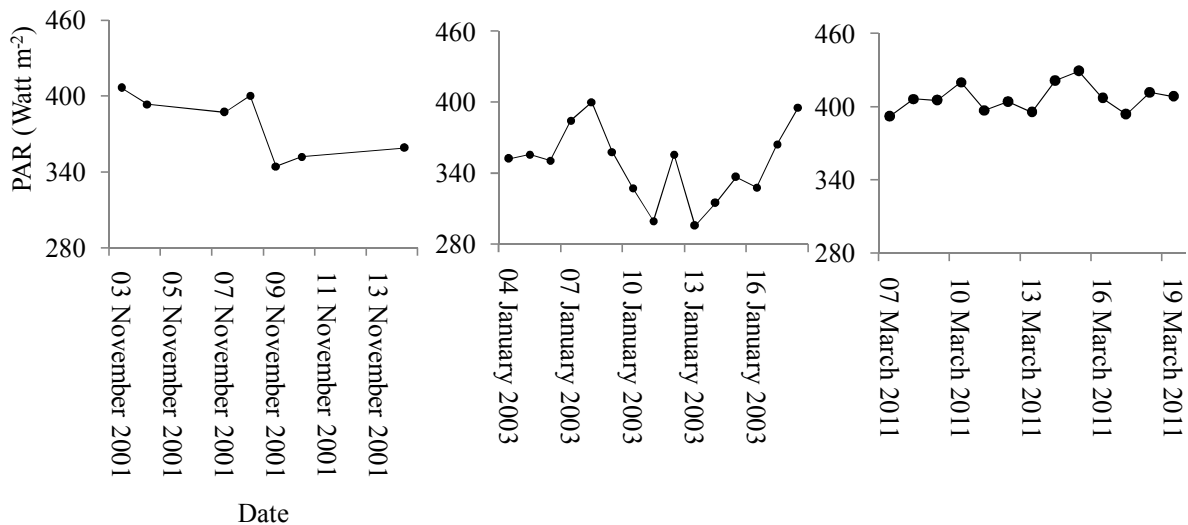


Figure 3.4: Variability of PAR during different ship cruises.

PAR varied from 344 to 403 $W m^{-2}$ during November 2001, from 290 to 400 $W m^{-2}$ during January 2003 and from 390 to 430 $W m^{-2}$ during March 2011. The variation of PAR was from 290 $W m^{-2}$ to 430 $W m^{-2}$ during different seasons in the Arabian Sea.

In-situ estimated PAR has been compared with COART model derived PAR at each hydrographic station during ship cruise periods in the Arabian Sea. During ship cruise periods only information about aerosol optical depth was measured. The information about the aerosol types were not obtained during ship cruise. In order to understand what type of aerosols was present during the ship cruise period, *in-situ* PAR was compared for different aerosol models used in the COART modeling approach.

3.4 Variation of aerosol types during ship cruise period

In COART model six aerosol types model such as MODTRAN maritime and Urban, OPAC (Optical Properties of Aerosols and Clouds) maritime clean, OPAC maritime polluted, OPAC maritime tropical and Desert (Hess et al., 1998) have been selected. Maritime aerosol contains sea salt particle. Maritime clean aerosol has no soot. Maritime polluted aerosol has highly variable amounts of soot and anthropogenic water-soluble particle. Maritime tropical aerosol has a low density of water-soluble substance and lower number density of sea salt (Hess et al., 1998). Desert aerosol consists of mineral aerosol. Urban aerosol represents strong polluted aerosol that is observed in the urban areas. The mass density of soot was very high and both water-soluble and insoluble substances are about twice the continental polluted aerosol found in centre area of large cities. Among all the different aerosol types, desert aerosol has only mineral composition. The rest of the aerosol types do not have role in adding micronutrient to sea water. In COART model along with the measured AOD, aerosol models at each station have been selected in such a way that the discrepancies between the model estimated PAR and *in-situ* measured PAR are the lowest. Table 3.1 shows the different aerosol model used in COART model along with the measured AOD during ship cruise dates in the Arabian Sea.

Chapter 3

Table 3.1: Different aerosol types used in COART model along with measured AOD data during ship cruise periods in the Arabian Sea.

Cruise ID (SK171)	Cruise ID (SK171)	Cruise ID (SK186)	Cruise ID (SK186)	Cruise ID (FORV 286)	Cruise ID (FORV 286)
Date	Type of aerosol	Date	Type of aerosol	Date	Type of aerosol
03 November 2001	T	05 January 2003	T	07 March 2011	T
04 November 2001	C	06 January 2003	T	08 March 2011	T
05 November 2001	D	09 January 2003	T	09 March 2011	T
06 November 2001	U	10 January 2003	T	10 March 2011	T
07 November 2001	T	11 January 2003	P	11 March 2011	T
08 November 2001	C	13 January 2003	U	12 March 2011	T
09 November 2001	U	14 January 2003	T	13 March 2011	P
10 November 2001	P	15 January 2003	T	14 March 2011	T
11 November 2001	U	16 January 2003	T	15 March 2011	T
12 November 2001	U			16 March 2011	T
13 November 2001	T			17 March 2011	C
14 November 2001	U			18 March 2011	M
				19 March 2011	P

M= Maritime aerosol

T= Maritime tropical aerosol

P = Maritime polluted aerosol

C=Maritime clean aerosol

U= Urban aerosol

D=Desert aerosol

From Table 3.1, it is evident that during cruise period, aerosol distribution was generally maritime tropical type of aerosol. The variety of aerosol types and variation in aerosol optical depth during different seasons were due to difference in wind direction during different seasons (Nair et al., 2005) in the Arabian Sea.

3.5 Comparison between model estimated PAR with *in-situ* measured PAR

The comparison of *in-situ* measured PAR with COART model estimated PAR for different aerosol types has been shown in the Figure 3.5.

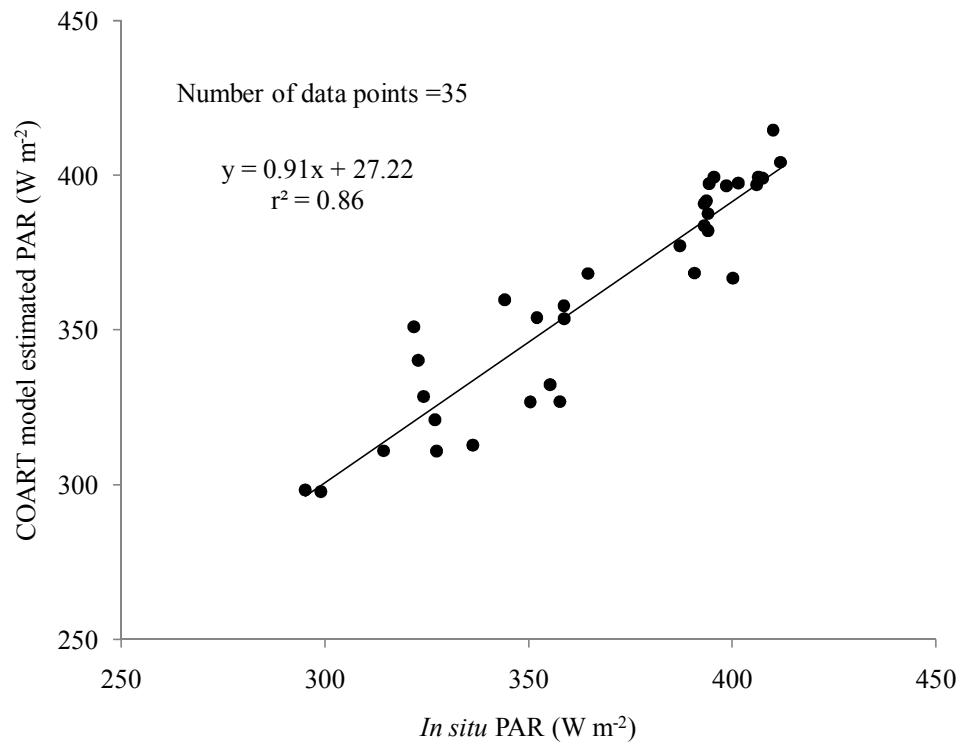


Figure 3.5: Comparison of *in-situ* measured PAR with COART model estimated PAR for different aerosol types.

Modeling PAR and sensitivity study using *in-situ* data

From the Figure 3.6, it is evident that there is a negative relationship between *in-situ* measured AOD (500 nm) and PAR. However, the correlation of determination was weak between *in-situ* measured PAR and AOD (500 nm). Normally, PAR and AOD values will have a good correlation if they are measured at same locations at different times (Moon et al., 2009). PAR varies with solar zenith angle and latitude in addition to AOD. In the Figure 3.6, *in-situ* measured PAR had been measured at different latitudes (Figure 3.6). That is why; to get good correlation of determination in the simulation study, model estimated PAR at different atmospheric conditions has been normalized to model estimated PAR under clear sky ($PAR_{\text{clear sky}}$) condition at a particular geographic location. PAR under clear sky has been defined as PAR had been estimated using COART model for no aerosol loadings and under no clouds. All the *in-situ* data were obtained under cloud free condition. There was a gap of information also about the variability of PAR under different cloud coverage conditions. To get the answers of these issues, a simulation study has been carried out to estimate PAR for different aerosol models at measured *in-situ* AOD using COART model. Secondly, a range of PAR values have been obtained when AOD was varied from 0 to 1. Similarly, for different cloud coverage, simulated PAR has been obtained using a nonlinear relationship with cloud coverage (Lestrade et al., 1990).

3.6.1 Sensitivity analysis: AOD on PAR for different aerosol types

Using COART model, variation of the ratio of PAR to PAR at clear sky ($PAR/PAR_{\text{clear sky}}$) under various aerosol loadings for different aerosol types have been studied through a sensitivity analysis. The results are shown in Figure 3.7.

Direct and diffuse component of PAR are varying exponentially with aerosol optical depth (Moon et al., 2009) according to the Beer-Bouguer-Lamberts law. Direct PAR decreases exponentially as AOD increases (Moon et al., 2009). Diffuse PAR increases as AOD increases at maximum value due to increased scattering effect of aerosol (Moon et al., 2009) for a given solar zenith angle. After a critical value of AOD, diffuse PAR decreases because of the excessive

extinction by aerosol (Cho et al., 2003). The critical AOD shows a maximum diffuse PAR and it increases as the solar zenith angle decreases (Moon et al., 2009). Mallet et al. (2009) fitted a second-order polynomial to the variation of PAR to $PAR_{clear\ sky}$ with dust optical depth for different single scattering albedo. Second-order polynomial has been fitted between $PAR/PAR_{clear\ sky}$ and AOD for various aerosol types based in the discussion of the above paragraph. The equation of the relationship between $PAR/PAR_{clear\ sky}$ and AOD is shown in Figure 3.7.

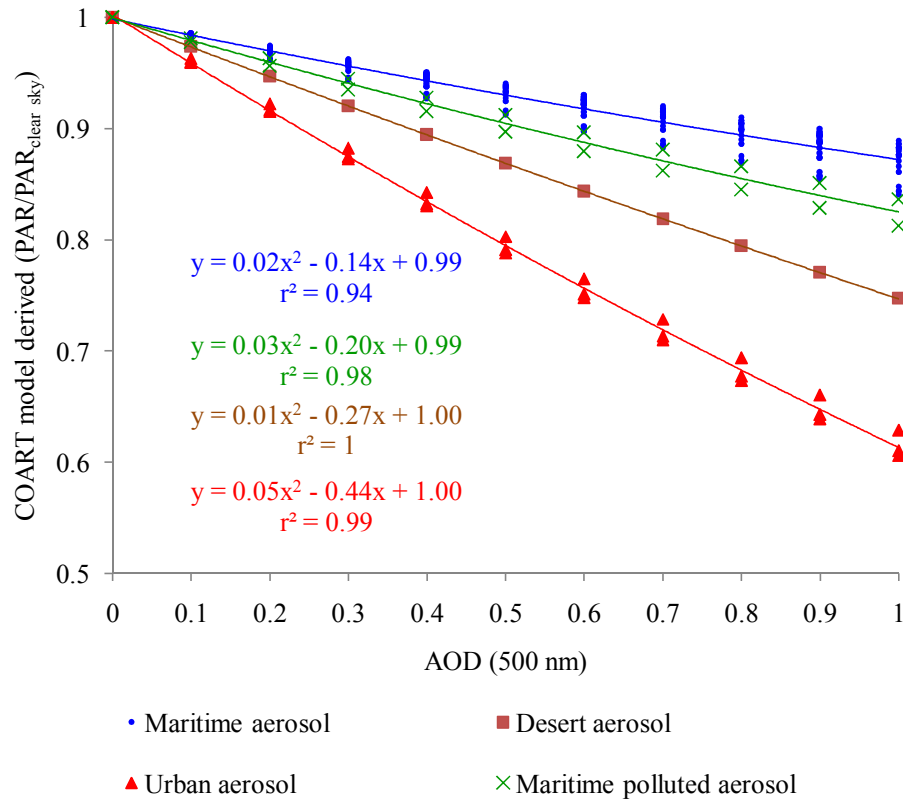


Figure 3.7: The variation of PAR with AOD (500 nm) for different aerosol types.

Figure 3.7 shows that urban type of aerosol attenuates PAR more compared to the other type of aerosols. During January 2003, decrease of $PAR/PAR_{clear\ sky}$ was more compared with other months. The decrease of PAR in percentage for maximum aerosol loading and moderate aerosol loading compared to no aerosol loading was tabulated in Table 3.2.

Table 3.2: Decrease of PAR (%) for maximum and moderate aerosol loadings compared to no aerosol loading for different aerosol types.

Type of aerosol	Decrease of (PAR/PAR _{clear sky}) in percentage for maximum aerosol loading(AOD=1) compared to no aerosol loading			Decrease of (PAR/PAR _{clear sky}) in percentage for moderate aerosol loading(AOD=0.3) compared to no aerosol loading		
	November 2001	January 2003	March 2011	November 2001	January 2003	March 2011
Maritime aerosol	11.42 to 13.42	13.88 to 16.37	11.04 to 12.46	3.84 to 4.79	4.79 to 5.84	3.78 to 4.35
Maritime polluted aerosol	~16.36	~18.76	13.05 to 13.88	~5.50	~6.49	3.90
Urban aerosol	37.15 to 39.40	~43.83		11.75 to 12.71	14.78	
Desert aerosol	~25.2			7.94		

For maritime type of aerosol, the decrease of PAR/PAR_{clear sky} for maximum aerosol loading was from 11-16% during November 2001, 13–19% during January 2003, and 11–14% during March 2011. The decrease of PAR/PAR_{clear sky} for moderate aerosol loading was 3–7% during ship cruise period for maritime aerosol. Similar results were observed at observatory for Atmospheric Radiation Research, Sukhothai, Thailand where PAR was reduced ~3% during May 2003 to April 2004 in the polluted conditions (Viriyathananont et al., 2009). For desert aerosol, PAR/PAR_{clear sky} was attenuated ~25% for maximum aerosol loading and ~8% for moderate aerosol loading during January 2003. Chami et al. (2012) showed that during spring and summer season, PAR was attenuated 14% and 17% over the Atlantic Ocean because of dust aerosol. The maximum decrease of PAR during summer was explained by the greater abundance of dust particle in the summer season compared to other seasons in the Atlantic Ocean (Chami et al., 2012).

In addition to the aerosol optical depth, single scattering albedo has also important role in modifying PAR (Cho et al., 2003; Mallet et al. 2009). The effect of single scattering albedo on PAR has been studied by researchers in terms of various type of aerosol. For maritime aerosol, maritime polluted, urban and desert aerosol single scattering albedo was taken as 0.99, 0.97, 0.817 and 0.888 (Hess et al., 1998) respectively.

3.6.2 Sensitivity analysis: Cloud coverage and PAR variability

To understand the variability of PAR under different cloud coverage, direct and diffuse component of PAR have been computed using a non-linear relationship for variable cloud coverage (Lestrade et al., 1990). The direct and diffuse components of PAR under different cloud coverage have been estimated using equations (3.5) and (3.6) as per Lestrade et al. (1990).

$$PAR_{dircloudy} = PAR_{dir} \times (1 - c) \dots \dots \dots (3.5)$$

$$PAR_{diffcloudy} = PAR_{diff} \times (1 + 3.8c + 2.58c^2) \dots \dots \dots (3.6)$$

Where *c* is cloud coverage. Cloud coverage 0 denotes cloud free atmosphere, whereas 1 denotes overcast sky. PAR_{dir} , PAR_{diff} , $PAR_{dircloudy}$, $PAR_{diffcloudy}$ are direct and diffuse component in cloudy free and cloudy condition. Total PAR in cloudy atmosphere has been obtained summing of $PAR_{dircloudy}$ and $PAR_{diffcloudy}$. Figure 3.8 shows the variation of total PAR under different cloud coverage for different aerosol loading.

The ratio $PAR/PAR_{clear\ sky}$ was observed to reduce in a quadratic way with increase in cloud coverage. For no aerosol ($AOD = 0$) loading $PAR/PAR_{clear\ sky}$ was reduced up to about 12% from the clear sky when cloud coverage was less than 50%. The ratio reduced 52% for overcast sky. For maximum aerosol loading ($AOD = 1$) and for overcast sky $PAR/PAR_{clear\ sky}$ was reduced 57% compared to clear sky. For moderate aerosol loading ($AOD = 0.3$) and for overcast sky

Modeling PAR and sensitivity study using *in-situ* data

PAR/PAR_{clear sky} was reduced 54% compared to clear sky. Second-order polynomial have been fitted with the variation of PAR/PAR_{clear sky} with cloud coverage for AOD values 0, 0.3 and 1 respectively and equations of the relationship between PAR/PAR_{clear sky} with cloud coverage for various aerosol loading is shown in Figure 3.8. Cloud coverage plays dominating role compared to aerosol in attenuating PAR.

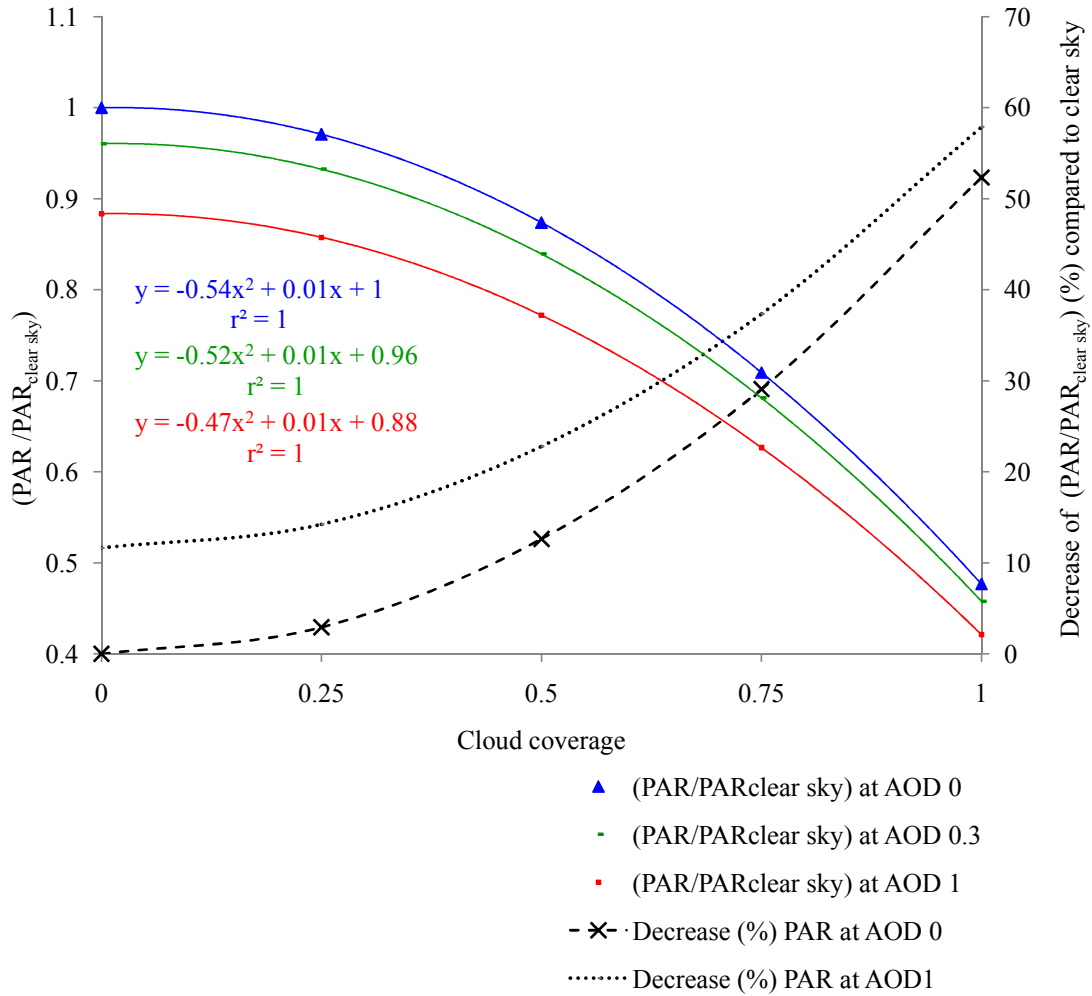


Figure 3.8: The variation of total PAR under different cloud coverage (Date: November 04, 2001).

Chapter 3

Cho et al. (2003) studied annual and seasonal variation of total, direct and diffuse PAR at Seoul (37.57°N, 126.97°E), South Korea with a rotating shadowband radiometer instrument. With the increase of cloud amount, direct PAR was continuously decreased. However, diffuse PAR was gradually increased and reached a maximum value (Cho et al., 2003). The direct and diffuse PAR was 71% and 29% of total PAR under cloud free conditions (Cho et al., 2003). For overcast sky, the direct PAR was decreased and it was 23% of total PAR (Cho et al., 2003). However, diffuse PAR was increased and it was 77% of the total PAR (Cho et al., 2003) for overcast sky. Hu et al. (2007) studied the spatial and temporal variation of PAR for 34 stations in China during January 2005 to June 2006. The study showed that cloudy days are 10% higher than that for clear days and the effect of cloudiness on flux of hourly PAR was significant (Hu et al., 2007). PAR was increasing gradually from spring, reaching a peak in summer, and then decreasing gradually to minimum in winter (Hu et al. 2007). Wang et al. (2014) studied PAR variability at Wuhan, central China during 2005 to 2012. PAR was more affected by cloudiness than the seasonal variation at Central China (Wang et al., 2014). PAR was decreased 22.3% during summer and 39.7% during winter season, when sky conditions changed from cloudless to overcast (Wang et al., 2014).

3.7 Summary and conclusions

PAR has been estimated at a single geographic location using a *Coupled Ocean Atmosphere Radiative Transfer (COART)* model during ship cruise periods 3–17 November 2001, 4–19 January 2003 and 7–19 March 2011 in the Arabian Sea. In this model, different input components have been from *in-situ* observation. Surface reflectance has been neglected. Output of PAR model has been compared with PAR measured using surface reference sensor during ship cruise periods for different six aerosol type models such as maritime and Urban, OPAC maritime clean, OPAC maritime polluted, OPAC maritime tropical and Desert. Aerosol types at each station have been selected in such a way that the discrepancies between the model and the measurements are the lowest. COART model derived PAR gives a good agreement with *in-situ* measured PAR.

Modeling PAR and sensitivity study using *in-situ* data

To understand the effect of aerosol optical depth and cloud coverage on PAR a sensitive analysis has been carried out for maritime, maritime polluted, urban and desert aerosol. It has been found that for maritime, maritime polluted and desert aerosol, PAR has attenuated to about 11–25%, whereas it has attenuated to 44% for urban aerosol type compared to clear sky. PAR is reduced ~57% for high aerosol loading and for overcast sky compared to clear sky. Reduction of PAR has been found more during January compared to the other seasons. Cloud coverage plays dominating role compared to aerosol in attenuating PAR. This sensitivity study demonstrates the effect of varying AOD, aerosol models and cloud coverage on estimation of PAR. It is also observed that aerosol types play significant role in PAR estimation under clear sky condition. To get spatial and temporal variation of PAR for variable aerosol loadings and cloud coverage over Indian Ocean, it is needed to model PAR from space based observations. PAR estimation using satellite data has been discussed in the next chapter.

Chapter 4

Modeling Photosynthetically Available Radiation (PAR) from satellite data over Indian Ocean

This chapter describes estimation of PAR from OCEANSAT-1 & 2 Ocean Colour Monitor (OCM) using two different methods under both clear and cloudy sky conditions. In the first method, the atmosphere is treated as a single layer in clear sky conditions, and as a double layer in cloudy conditions. Surface reflectance has been neglected in the first approach. Aerosol optical depth and cloud optical depth has been estimated at 865 nm and 443 nm spectral bands of OCM. PAR has been estimated from OCM using second method which assumes that the effects of clouds and clear atmosphere can be decoupled with cloud system and ocean surface albedo. Ocean surface albedo and cloud albedo have been estimated from TOA (top of the atmosphere) radiance data of OCM on a pixel by pixel basis.

4.1 Introduction

PAR estimation based on satellite observation has become increasingly important as PAR estimated from satellite provide information at desired temporal and spatial resolution required by different ecosystem models and radiation budget models. Ocean colour remote sensing is a useful tool and it provides quantitative information of seawater constituents. OCEANSAT-1 OCM and OCEANSAT-2 OCM are two Indian Ocean observation satellites which are extensively used for various societal and scientific applications like Potential Fishing Zone (PFZ) identification, estimation of primary productivity, algal bloom detection and studying the coastal processes. Ocean primary production models use PAR at noon (Platt and Sathyendranath 1993) and daily averaged PAR (Behrenfeld and Falkowski 1997a) as a one of the main input. Two PAR products such as PAR at noon and daily averaged PAR have been estimated from OCM using two different methods.

4.2 OCEANSAT-1 & 2 OCM characteristics

Indian Space Research Organisation launched Ocean Colour Monitor (OCM) sensor on-board OCEANSAT-1 satellite in May 1999 to realize the importance of ocean colour measurements from the space. OCEANSAT-1 OCM was the first Indian ocean colour satellite and provides ocean colour measurements around the sea adjoining the Indian subcontinent. OCEANSAT-1 OCM had eight bands. The first six bands centered at 412 nm, 443 nm, 490 nm, 510 nm, 555 nm and 670 nm are used for analyzing ocean colour components in the water column. The last two bands of central wavelength at 765 nm and 865 nm are used for atmospheric correction. The spectral resolution of the first six bands and last two bands are 20 nm and 40 nm, respectively.

Chapter 4

Table 4.1: Major specifications and features of OCEANSAT-1 & 2 OCM

Parameters	Specifications	
	OCEANSAT-1 OCM	OCEANSAT-2 OCM
Spectral Range(nm)	404-882	402- 885
No. of Channels	8	8
Wavelength (nm)	Band 1: 404-423 Band 2 :431-451 Band 3: 475-495 Band 4: 501-520 Band 5: 547-565 Band 6: 660-677 Band 7: 745-785 Band 8: 845-885	Band 1 : 404-424 Band 2: 431-451 Band 3: 476-496 Band 4: 500-520 Band 5: 546-566 Band 6: 610-630 Band 7: 725-755 Band 8: 845-885
Satellite altitude(km)	720	720
Spatial Resolution(m)	360× 236	360 ×250
Swath (km)	1420	1420
Repetitive(days)	2	2
Quantisation	12 bits	12bits
Equatorial crossing time	12 noon	12 noon
Along Track steering (to avoid sunglint)	± 20°	± 20°
Data acquisition modes	Local Area Coverage (LAC)	Local Area Coverage (LAC) & Global Area Coverage (GAC)

OCEANSAT-2 spacecraft of Indian Space Research Organization (ISRO) is the second satellite in ocean series, which was successfully launched on September 23, 2009. OCEANSAT-2 OCM is the continuity satellite of OCEANSAT-1 OCM. OCEANSAT-2 OCM satellite carried three main instruments namely i) Ku band pencil beam scatterometer, ii) modified Ocean Colour

Modeling PAR from satellite data

Monitor (OCM) and iii) Radio Occultation Sounder of Atmosphere (ROSA) instrument of Italian Space Agency (ASI). Spectral bands of OCEANSAT-2 OCM are almost identical to OCEANSAT-1 OCM. However, central wavelengths of two spectral bands i.e band 6 and 7 have been shifted. The spectral band of central wavelength 670 nm in OCEANSAT-1 OCM has been shifted to 620 nm in OCEANSAT-2 OCM to improve suspended sediments quantification. Another spectral band 7 centered at 765 nm in OCEANSAT-1 OCM has been shifted to 740 nm to avoid oxygen absorption in OCEANSAT-2 OCM. Table 4.1 provides the technical details of the OCEANSAT-1 & 2 OCM instrument.

Over the Indian Ocean region covering Bay of Bengal and Arabian Sea OCM (LAC) data was acquired by NRSC ground station. The OCEANSAT-1 OCM (1999-2010) and OCEANSAT-2 OCM (2009 to present) data are archived at NRSC (National Remote Sensing Centre, Hyderabad) for use in various ocean colour applications. Data products are available as standard RAD (radiometrically corrected) and GEO (radiometrically and geometrically corrected) products.

The raw data of OCEANSAT-1 OCM are provided in two-byte generic binary integer format. The header file of the OCEANSAT-1 OCM data contains information about the geographic grid and solar and sensor viewing geometry and calibration coefficients. The geographic control point (GCP) information for projecting the OCEANSAT-1 OCM image data onto a geographic map projection as well as the information on the solar and sensor viewing geometry such as sun zenith angle (θ_s), sun azimuth angle (ϕ_s), sensor zenith angle (θ_v), and sensor azimuth angle (ϕ_v) from OCEANSAT-1 OCM data CD are obtained by using an in-house developed program.

OCEANSAT-2 OCM data products are available in the HDF 4.0 format providing all the required ancillary information such as sun zenith angle (θ_s), sun azimuth angle (ϕ_s), sensor zenith angle (θ_v), and sensor azimuth angle (ϕ_v). The data products from OCEANSAT-2 OCM are available at 360 meter spatial resolution for regional studies, which are also called local area

coverage (LAC) products. The global area coverage (GAC) products are available at 1 km spatial resolution for global studies. The Level 1B top of the atmosphere (TOA) radiance data from all the eight bands of OCM sensor is used along with the ancillary information to generate various bio-geophysical data products.

Standard products of OCM are provided as Path/Row products based on a referencing scheme, which is a method for convenient geographic location of areas on Earth. This scheme is designated by Path and Rows based on the nominal orbital characteristics. The ground trace of a satellite's orbit in space is called a 'PATH'. Along a path, the continuous stream of data is segmented into a number of scenes. The lines joining the corresponding scene centers of different paths are parallel to the equator and are called 'ROWS'. The region of Arabian Sea (55°E-78°E and 6°N - 28°N) is covered by OCM orbital paths 8 and 9 and rows 13 and 14. In the present study, OCM data of eastern Arabian Sea (path 9; rows 13 & 14; 6°N-25°N and 68°E-78°E) were obtained in band-separated band-sequential (BSQ) binary format on CD-ROM media.

4.3 Sun glitter estimation in OCEANSAT-1 & 2 OCM images

In any satellite images, sunglint regions are observed when there is direct reflectance or specular reflectance of the incoming solar radiation from the ocean surface to the sensor. Specular reflection is the mirror like reflection of light from a surface, in which light from a single incoming direction is reflected into a single outgoing direction. The sunglint occurs at one point when zenith angle of Sun and satellite are same and their azimuth angles are opposite in absolutely flat ocean surface. However, ocean surface is never flat. Surface roughness generated because of wind enlarges the sunglint area (Mohan and Chauhan, 2001). The shape of the sunglint area is changing with the change of orientation of the sensor. For a given tilt angle of the sensor, sunglint area moves from the north to south or south to north with the change of solar declination angle. If sunglint region has been not masked, it will be treated as cloudy region and misleading PAR will be estimated under sunglint condition.

Modeling PAR from satellite data

The OCEANSAT-1 & 2 OCM was designed to tilt the sensor operationally $\pm 20^\circ$ (Mohan and Chauhan, 2001) away from the nadir to minimize sun glint affect. However, it has been observed that even with the scheme proposed by Mohan and Chauhan (2001) some OCEANSAT-1 & 2 OCM data shows sun-glint in the months of April and August. Sun glint area has been masked by a method proposed by McClain and Yeh (1994). The probability of a pixel affected by sunglint is function of sea surface wind speed W , solar azimuth (φ_s), solar zenith angle (θ_s), satellite azimuth (φ_v) and satellite zenith angle (θ_v). A probability parameter P_σ (McClain and Yeh, 1994) is defined by

$$P_\sigma = \frac{1}{\pi\sigma^2} \exp\left[\frac{-\tan^2\theta_n}{\sigma^2}\right] \dots \dots \dots (4.1)$$

σ^2 is the mean square surface slope distribution. σ^2 increases linearly with wind speed.

$$\sigma^2 = 0.003 + 0.00512W \dots \dots \dots (4.2)$$

θ_n is the vector normal to the surface vector for which sunglint will be observed. θ_n can be derived from the surface reflection angle, ω .

$$\theta_n = \cos^{-1}\left[\frac{\cos\theta_s + \cos\theta_v}{2\cos\omega}\right] \dots \dots \dots (4.3)$$

$$\cos 2\omega = \cos\theta_s \cos\theta_v + \sin\theta_s \sin\theta_v \sin(\varphi_v - \varphi_s) \dots \dots \dots (4.4)$$

Probability parameter greater than 1.5 (McClain and Yeh, 1994) has been chosen as sunglint affected region and it has been masked. Figure 4.1 shows false colour composite (FCC) image of OCEANSAT-1 OCM in the Arabian Sea dated on 18th April, 2006. Sunglint region has been estimated using equation (4.1). Masked elongated region oriented towards north-south direction in the Figure 4.1 shows sunglint affected area in the OCEANSAT-1 OCM and it has been masked.

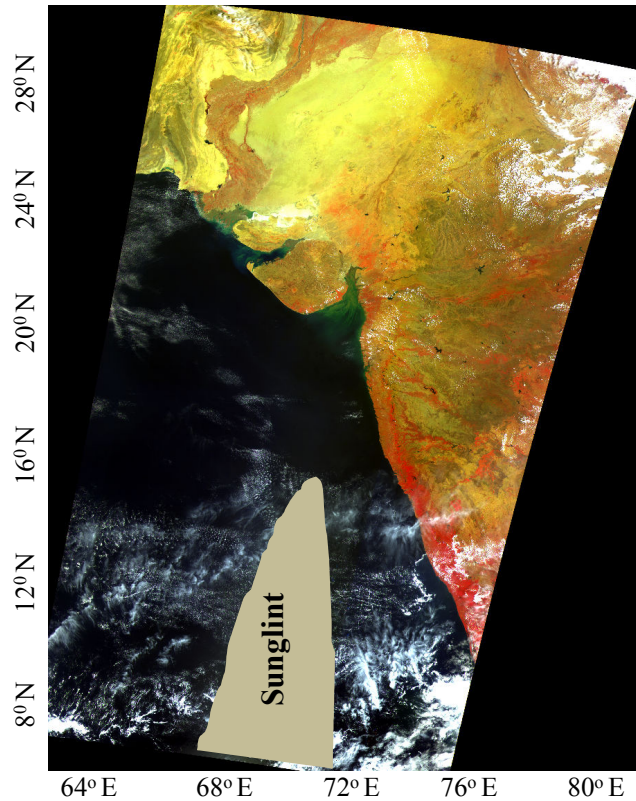


Figure 4.1: Sunglint region showed in false colour composite (FCC) image of OCEANSAT-1 OCM data over the Arabian Sea (18th April, 2006).

4.4 Distinction between clear and cloudy sky in OCEANSAT-1 & 2 OCM

Almost seventy percent of the Earth's surface is covered by clouds (Rossow and Schiffer, 1999). Clouds are generally characterized by higher reflectance and lower temperature (Ackerman, et al., 1998) compared to the underlying surface. Based on the properties, cloudy sky is distinguished from the clear sky from space using threshold value of reflectance estimated at visible band and brightness temperature estimated at infrared band. However, the type of the underlying surface of the clouds modifies the strength of the signal detected at the sensor.

Modeling PAR from satellite data

Different types of the clouds have different radiative properties and show various contrast with the underlying surface. Specially, thin cirrus clouds, low stratus at night and small cumulus are difficult to detect from space observation as they show insufficient contrast with the surface radiance (Ackerman, et al., 1998). Further field of view of sensor will not always be completely cloudy or clear at the cloud edge and it creates difficulty to detect cloudy sky at the edge of the clouds. There had been several algorithms developed to mask different types of cloud in MODIS, NOAA AVHRR (advanced very high resolution radiometer) and International Satellite Cloud Climatology Project (ISCCP) (Saunders and Kriebel, 1988; Gesell, 1989; Rossow, 1989; Seze and Rossow, 1991; Rossow and Schiffer, 1991; Rossow and Garder, 1993a; Rossow and Garder, 1993b; Ackerman, et al., 1998; Ackerman, et al., 2006) for different underlying surface such as water, snow, land vegetation and bare soil. Based on the previous work on masking of cloudy pixels from clear pixel, Table 4.2 lists spectral bands and algorithms used to separate cloudy sky from clear sky over water surface.

Table 4.2: Spectral bands and different cloud detection test for clouds over water from space observation (Ackerman, et al., 1998; Ackerman, et al., 2006)

Type of cloud	Bands	Cloud detection test
Low cloud over water	i. 870 nm ii. 670 nm iii. 11000 nm iv. 3700nm	i. R_{870} ii. $R_{870/670}$ iii. $BT_{11000-3700}$
High Thick cloud over water	i. 1380nm ii. 870nm iii. 670nm	i. R_{1380} ii. R_{870} iii. $R_{870/670}$
High Thin cloud over water	i. 1380nm	i. R_{1380}

BT= Brightness temperature
R = Reflectance

Chapter 4

OCEANSAT-1 & 2 OCM does not have infrared spectral bands such as 1380 nm, 3700 nm and 11000 nm. Reflection at 865 nm and 670 nm for OCEANSAT-1 OCM and 620 nm for OCEANSAT-2 OCM has been estimated. Figure 4.2 shows false colour composite, reflectance at 865 nm and reflectance ratio between 865 nm and 670 nm spectral bands for OCEANSAT-1 OCM.

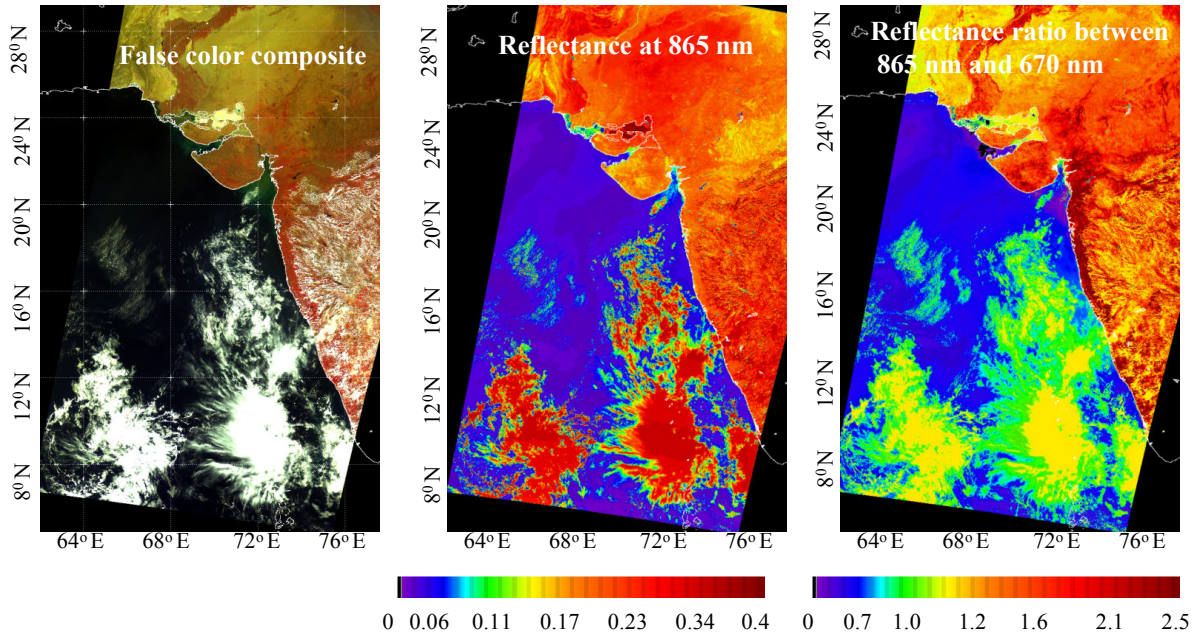


Figure 4.2: False colour composite, reflectance at 865 nm and reflectance ratio between 865 nm and 670 nm band for OCEANSAT OCM-1 dated on 16th November 2001.

Figure 4.2 shows that reflectance at 865 nm band is below 0.06 under clear sky. A threshold value of 0.055 reflectance at 865 nm has been taken to screen out cloud mask for MODIS image (Ackerman et al., 2006). Chauhan et al. (2002) have used 1.1% albedo at 865 nm band to screen out clouds, land and sunglint area in OCEANSAT-1 OCM. For thick clouds reflectance at 865 nm is very high and it is greater than 0.2 (Figure 4.2). However, the reflectance at 865 nm for thin clouds is highly variable and the ranges are between 0.06 to 0.2 (Figure 4.2).

The reflectance ratio between 865 nm and 670 nm is observed below 0.6 for clear sky (Figure 4.2) condition. For thick clouds, the ratio is very high and it is greater than 1.05 (Figure

Modeling PAR from satellite data

4.2). For thin clouds, the ratio is greater than 0.78 (Figure 4.2). In this study, a threshold value of reflectance 0.06 at 870 nm and ratio of reflectance at 870 nm and 670 nm greater than 0.9 has been used to distinguish between cloudy sky from clear sky of OCEANSAT-1 OCM images. In MODIS cloud masking algorithm, ratio between the reflectance at 865 nm and 660 nm has been found to be 0.9 to 1.1 in cloudy region (Ackerman et al, 1998). In NOAA- AVHRR, if the reflectance ratio between spectral channel 2 (720-1100 nm) to 1 (580-680 nm) is found in between 0.7 and 1.1, and then the pixel was declared as cloudy pixels (Saunders and Kriebel 1988). For cloud-free ocean, the ratio is expected to be less than 0.75 (Saunders and Kriebel 1988). So the application of cloud masking algorithm is of importance.

4.5 PAR estimation from OCEANSAT-1 & 2 OCM using method I

PAR has been estimated from OCM using method I which is based on a combination of clear sky irradiance equations given in Iqbal (1983), Bird (1984) and the broadband cloud reflection algorithm given in Stephens et al. (1984). The pixels have been separated first for clear sky or cloudy sky in OCM data as mentioned in section 4.4. For clear pixels, PAR has been estimated by the equations developed for clear sky condition and for cloudy pixels PAR has been estimated by the equations developed for cloudy sky conditions (Van Laake and Azofeifa, 2004). In this radiative transfer model, the atmosphere is treated as a single layer in clear sky conditions, or as a double layer in cloudy conditions i.e., a layer above the cloud top and a layer from the cloud top downwards. Surface reflectance is not included in this first method.

4.5.1 Modeling PAR under clear sky condition

Total PAR is the summation of direct PAR ($I_{dir\lambda}$) and diffuse PAR ($I_{diff\lambda}$). Direct PAR is modeled with extraterrestrial solar irradiance and transmittance of the atmosphere. Direct PAR $I_{dir\lambda}$ is

Chapter 4

expressed with the equation (4.5) (Bird, 1984; Bird et al., 1986; Carder et al., 2003; Van Laake and Azofeifa, 2004)

$$I_{dir\lambda} = I_0 T \dots \dots \dots (4.5)$$

I_0 is the extraterrestrial solar irradiance ($W\ m^{-2}\ \mu m^{-1}$) at the top of the atmosphere; T is transmittance of the atmosphere. I_0 varies slightly throughout the year because of the eccentric path of the Earth around the Sun.

$$I_0 = E_0 \left(1 + 0.0344 \cos \left(\frac{360N}{365} \right) \right) \dots \dots \dots (4.6)$$

E_0 is the extraterrestrial solar irradiance ($W\ m^{-2}\ \mu m^{-1}$) without correction for the Earth Sun distance. N is the day number.

Transmittance of the atmosphere is a dimensionless quantity. It depends on the wavelength. The transmittance of the atmosphere T is decomposed into transmittance of different atmospheric constituents such as gas molecules, ozone, aerosol etc. The transmittance of the atmosphere is expressed by the equation (4.7) (Bird, 1984; Bird et al., 1986; Carder et al., 2003; Van Laake and Azofeifa, 2004)

$$T = T_R T_{OZ} T_A T_u \dots \dots \dots (4.7)$$

In the equation (4.7) T_R is transmittance of Rayleigh scattering (R), T_{OZ} is transmittance of ozone (oz) absorption, T_A is transmittance of aerosol scattering and T_u is transmittance of uniformly mixed gas (u) absorption. The absorption by water vapour in the PAR range is negligible (Eck and Dye, 1991). Transmittances depend on the concentration of the attenuating element in the atmosphere and pressure corrected air mass.

Modeling PAR from satellite data

When considering absorption and scattering within the atmosphere it is always necessary to know the total mass of the absorbing or scattering substance. Absolute optical air mass m_a is defined as (Paltridge and Platt, 1976)

$$m_a(h) = \int \rho ds \dots \dots \dots (4.8)$$

Where ρ is the density of absorbing or scattering substance and ds is the geometrical path element along the solar beam. The integration is taken at a perpendicular height h above the ground surface to the top of the atmosphere along the beam. Further, the mathematics of scattering and absorption involve the approximation of a plane-parallel atmosphere where the optical path between two levels along some zenith angle is related to the vertical optical path between the same levels by the multiplying factor \sec of solar zenith angle. Again when referring to the direct solar beam, relative optical air mass m_r is defined formally as

$$m_r(h) = \frac{\int_h^\infty \rho ds}{\int_h^\infty \rho dh} \dots \dots \dots (4.9)$$

If m_p is the relative optical mass corrected for local pressure and m_0 is the relative optical mass at mean sea level, then m_p relates with m_0 by the equation (4.10) (Bird, 1984; Gregg and Carder, 1990; Van Laake and Azofeifa, 2004).

$$m_p = \frac{m_0 P_z}{1013.25} \dots \dots \dots (4.10)$$

If the local pressure P_z in hPa equals to the pressure at mean sea level 1013.25 hPa then $m_p = m_0$. Relative optical mass m_0 varies with the solar zenith angle and has been estimated with the equation (4.11) and equation (4.12) (Gregg and Carder, 1990; Van Laake and Azofeifa, 2004).

$$m_o = \frac{1}{\cos \theta_s}, \quad \theta_s \leq 60^\circ \dots \dots \dots (4.11)$$

$$m_o = \frac{1}{\cos \theta_s + 0.15(93.885 - \theta_s)^{-1.253}}, \quad \theta_s > 60^\circ \dots \dots \dots (4.12)$$

θ_s is the solar zenith angle.

The fraction of the direct beam irradiance that is scattered by the atmosphere is available as diffuse irradiance. It is much more difficult to model diffuse irradiance with any confidence like direct irradiance (Bird 1984). Brine and Iqbal (1982) first estimated diffuse irradiance based on the broadband method of Davis and Hays (1980). Bird (1984), Bird et al. (1986) estimated diffuse irradiance using Brine and Iqbal (1982) equations. In clear sky condition, diffuse PAR mainly originates from Rayleigh scattering and aerosol scattering if surface reflectance is neglected. Diffuse PAR of Rayleigh scattering origin is modeled with the assumption that 50% of the total Rayleigh scattering is scattered towards the surface (Bird 1984; Van Laake and Azofeifa, 2004). The aerosol scattered diffuse PAR is modeled with single scattering albedo of aerosol and forward scatterance (Van Laake and Azofeifa, 2004). The forward scatterance depends on the solar zenith angle. Van Laake and Azofeifa (2004) developed equation for forward scatterance based on the data given in Iqbal (1983). Forward scatterance F can be expressed by the equation (4.13) (Van Laake and Azofeifa, 2004).

$$F = 0.9302 \cos \theta_s^{0.2556} \dots \dots \dots (4.13)$$

Under the assumption of single scattering albedo and neglecting surface-reflected radiation, diffuse PAR $I_{diff\lambda}$ ($W m^{-2} \mu m^{-1}$) has been estimated by the equation (4.14) (Van Laake and Azofeifa, 2004).

$$I_{diff\lambda} = I_0 \cos \theta_s T_{oz}([0.5T_A(1 - T_R)] + [F\omega_0T_R(1 - T_A)]) \dots \dots \dots (4.14)$$

Modeling PAR from satellite data

The first term of the equation (4.14) in square brackets, refers to the diffuse radiation originating from Rayleigh direct beam scattering and the second term to aerosol direct beam scattering. The total PAR at each wavelength $I_{s\lambda}$ is now the sum of the direct PAR ($I_{dir\lambda}$) and diffuse PAR ($I_{diff\lambda}$)

$$I_{s\lambda} = I_{dir\lambda} \cos \theta_s + I_{diff\lambda} \dots \dots \dots (4.15)$$

Extraterrestrial solar irradiance from 400 nm to 700 nm has been divided into small wavelength intervals. Under clear sky condition, instantaneous PAR ($I_{par_clearsky}$) has been estimated by summing $I_{s\lambda}$ at each wavelength interval.

$$I_{par_clearsky} = \sum_{400\text{ nm}}^{700\text{ nm}} I_{s\lambda} \Delta\lambda \dots \dots \dots (4.16)$$

4.5.2 Inputs for PAR model under clear sky condition

4.5.2.1 Extraterrestrial solar irradiance

Extraterrestrial solar irradiance data at the top of the atmosphere from 400 nm to 700 nm at 1 nm resolution is obtained from Thullier et al. (1998). Figure 4.3 shows the variation of extraterrestrial solar irradiance at the top of the atmosphere with wavelength. The mean absolute uncertainty of the measured solar irradiance data of Thullier et al. (1998) is from 2% to 3%. Subsequently, this data has been subdivided into 15 wavelength band at 20 nm spectral intervals with central wavelength starting from 410 nm to 690 nm. I_0 at each wavelength band has been obtained by using trapezoidal method of integration.

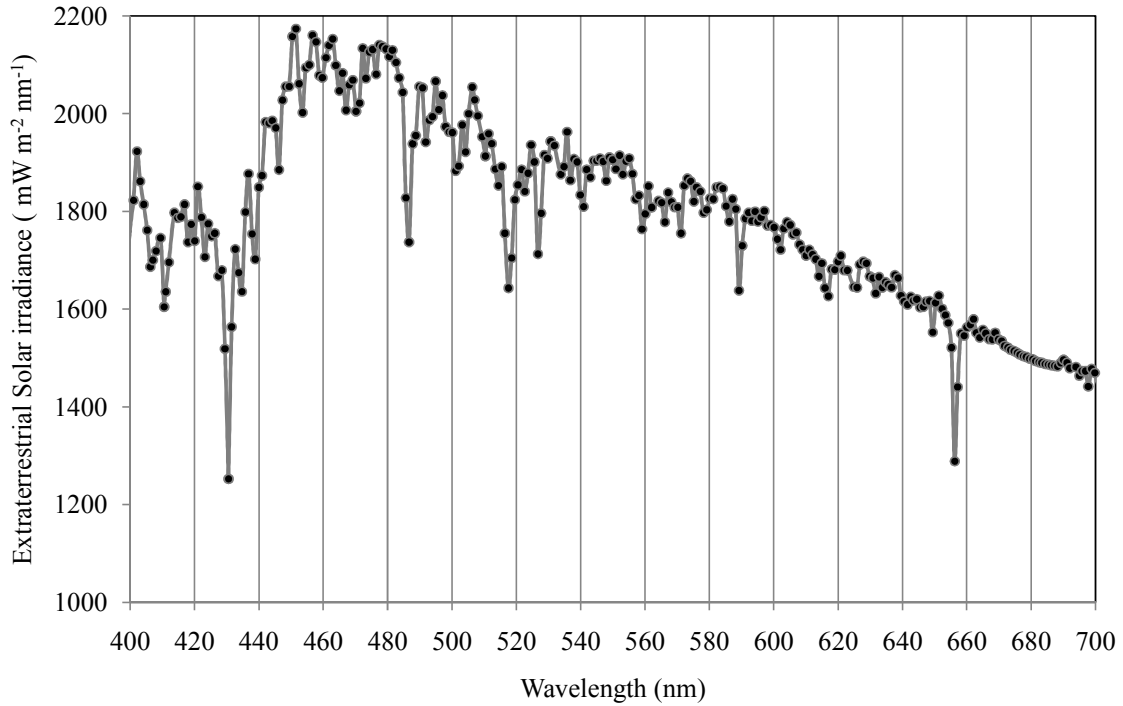


Figure 4.3: Extraterrestrial solar irradiance at the top of the atmosphere (Thullier et al., 1998).

4.5.2.2 Rayleigh scattering

Transmittance of Rayleigh scattering is computed by using equation (4.17) (Iqbal 1983, Van Laake and Azofeifa, 2004).

$$T_R = \exp[-0.008735\lambda^{-4.08}m_0] \dots \dots \dots (4.17)$$

4.5.2.3 Ozone absorption

Transmittance by ozone absorption is estimated using equation (4.18) (Iqbal 1983, Van Laake and Azofeifa, 2004).

Modeling PAR from satellite data

$$T_{oz} = \exp[-k_{oz}lm_0] \dots \dots \dots (4.18)$$

In the equation (4.18), ozone thickness is l and k_{oz} is ozone absorption coefficient. The value of ozone absorption coefficient is obtained from Nicolet (1981). Nicolet (1981) estimated ozone absorption coefficient at 1 nm wavelength resolution from 380 nm to 1110 nm. At each wavelength band, ozone absorption coefficient has been obtained by averaging ozone absorption coefficient at each wavelength band from 400 nm to 700 nm region.

Ozone thickness has been obtained from Ozone monthly data measurements made by the Earth Probe Total Ozone Mapping Spectrometer (EP/TOMS). The EP/TOMS experiment provides measurements of Earth's total column ozone by measuring the backscattered Earth radiance in the six 1-nm bands (308.60 nm, 313.50 nm, 317.50 nm, 322.30 nm, 331.20 nm, 360.40 nm) (McPeters et al., 1998). Retrieval of total ozone is done by using radiative transfer calculations to generate a table of backscattered radiance as a function of total ozone, viewing geometry, surface pressure, surface reflectivity and latitude. Level-3 ozone monthly data is available from the Goddard Space Flight Center (GSFC) in the form of Hierarchical Data Format (HDF) (<ftp://jwocky.gsfc.nasa.gov/pub/eptoms>). Level-3 product contains global total ozone on a fixed 1-degree latitude by 1.25-degree longitude grid.

4.5.2.4 Uniformly mixed gas absorption

The uniformly mixed gases has been computed by uniformly mixed gas absorption (Leckner 1978)

$$T_u = \exp \left[-1.41 \frac{a_u m_0}{(1 + 118.93 a_u m_0)^{0.45}} \right] \dots \dots \dots (4.19)$$

a_u is the absorption coefficient and obtained from Bird (1984). In this PAR model, wavelength interval, integrated extraterrestrial solar irradiance at the top of the atmosphere, ozone absorption coefficient and absorption coefficient for mixed gases are listed in the Table 4.3.

Chapter 4

Table 4.3: Extraterrestrial solar irradiance at the top of the atmosphere, absorption coefficient of ozone (k_{oz}), absorption coefficient for mixed gas (a_u) at each wavelength band used in the PAR model.

Wavelength interval (nm)	Central wavelength (nm)	Integrated extraterrestrial solar irradiance at the top of the atmosphere ($W\ m^{-2}$)	Ozone absorption coefficient k_{oz} (cm^{-1})	Absorption coefficient for mixed gas a_u
400-420	410	35.216	0.000769754	0
420-440	430	32.335	0.002042187	0
440-460	450	38.987	0.005253237	0
460-480	470	39.754	0.012178648	0
480-500	490	37.927	0.023915919	0
500-520	510	37.983	0.042220376	0
520-540	530	37.654	0.064968176	0
540-560	550	35.646	0.087357776	0
560-580	570	36.406	0.120187333	0
580-600	590	35.832	0.121824857	0
600-620	610	36.019	0.120865286	0
620-640	630	33.255	0.090607429	0
640-660	650	33.255	0.087357776	0
660-680	670	32.182	0.045572414	0
680-700	690	31.091	0.030667357	0.03

4.5.2.5 Aerosol transmission from OCM

Aerosol transmission is modeled with the spectrally varied aerosol optical depth (AOD) and relative optical mass at mean sea level. Aerosol transmission is computed by using equation (4.20) (Carder et al., 2003).

$$T_a = \exp(-m_0 \tau_a) \dots \dots \dots (4.20)$$

τ_a is aerosol optical depth. According to Angstrom (1964), the spectral variation of aerosol optical depth is expressed by the equation (4.21).

$$\tau_a \propto (\lambda)^{-\alpha} \dots \dots \dots (4.21)$$

α is known as angstrom coefficient. α depends on the size distribution of the aerosol.

AOD has been estimated from OCM at 865 nm wavelength. Same methodology developed by Chauhan et al. (2009) to estimate aerosol optical depth from OCEANSAT-1 OCM has been followed. AOD estimation from satellite observation is based on the principle that for case I water for the wavelength greater than 700 nm, open ocean water absorbs strongly and water leaving radiance detected at the satellite is the contribution of Rayleigh and aerosol scattering. Thus, at the top of the atmosphere in the wavelength greater than 700 nm, the radiance detected by a satellite sensor $L_{t\lambda}$ is summation of Rayleigh $L_{r\lambda}$ and aerosol path radiance $L_{a\lambda}$ (Doerffer, 1992).

$$L_{t\lambda}(\lambda) = L_{a\lambda}(\lambda) + L_{r\lambda}(\lambda) \dots \dots \dots (4.22)$$

Where

$$L_{a\lambda} = \frac{F_{0\lambda} \omega_{0a} \tau_{a\lambda} p_a}{4\pi \cos \theta_v} = \text{aerosol path radiance} \dots \dots \dots (4.23)$$

Chapter 4

$$L_{r\lambda} = \frac{F_{0\lambda}\omega_{0r}\tau_{r\lambda}p_r}{4\pi\cos\theta_v} = \text{Rayleigh path radiance} \dots\dots\dots (4.24)$$

$\omega_{0a/0r}$ = aerosol/Rayleigh single scattering albedo.

$\tau_{a\lambda/r\lambda}$ = aerosol/Rayleigh optical depth at spectral band λ .

$p_{a/r}$ = Function related to aerosol/Rayleigh scattering phase function.

$F_{0\lambda}$ is the extraterrestrial solar flux at the spectral band λ of OCEANSAT-1 & 2 OCM satellite. θ_v is the satellite view angle. Assuming $\omega_{0a}\cong 1$ and $\omega_{0r}\cong 1$ for marine aerosols (Chauhan et al., 2009), the aerosol optical depth is estimated using equation (4.25).

$$\tau_a = \left[\frac{(L_t - L_r)4\pi\cos\theta_v}{F_0\omega_{0a}p_{a\theta}} \right] \dots\dots\dots (4.25)$$

Rayleigh phase function is estimated using equation (4.26) (Doerffer, 1992).

$$p_r(\gamma^\pm) = \frac{3}{4}[1 + \cos^2(\gamma_a^\pm)] \dots\dots\dots (4.26)$$

The forward/backward scattering angle of aerosol is γ_{a^\pm} and it is computed using equation (4.27)

$$\cos\gamma_{a^\pm} = \pm(\cos\theta_v\cos\theta_s - \sin\theta_v\sin\theta_s\cos\phi) \dots\dots\dots (4.27)$$

ϕ is relative azimuth angle. Das et al. (2002) have shown that the aerosol phase function can be approximated by the two term Henyey-Greenstein phase function of the following form

$$p_a(\gamma^\pm) = Af(\gamma^\pm, g1) + (1 - A)f(\gamma^\pm, g2) \dots\dots\dots (4.28)$$

Modeling PAR from satellite data

$$f(\gamma^\pm, g) = \frac{1 - g^2}{\left[(1 + g^2 - 2g\cos\gamma^\pm)^{\frac{3}{2}} \right]} \dots \dots \dots (4.29)$$

With $A=0.985$, $g_1=0.8$, $g_2=0.5$ for marine aerosols (Doerffer, 1992). Figure 4.4 shows the spatial variation of aerosol optical depth at 865 nm band and angstrom exponent estimated from OCEANSAT-1 OCM in the Arabian Sea.

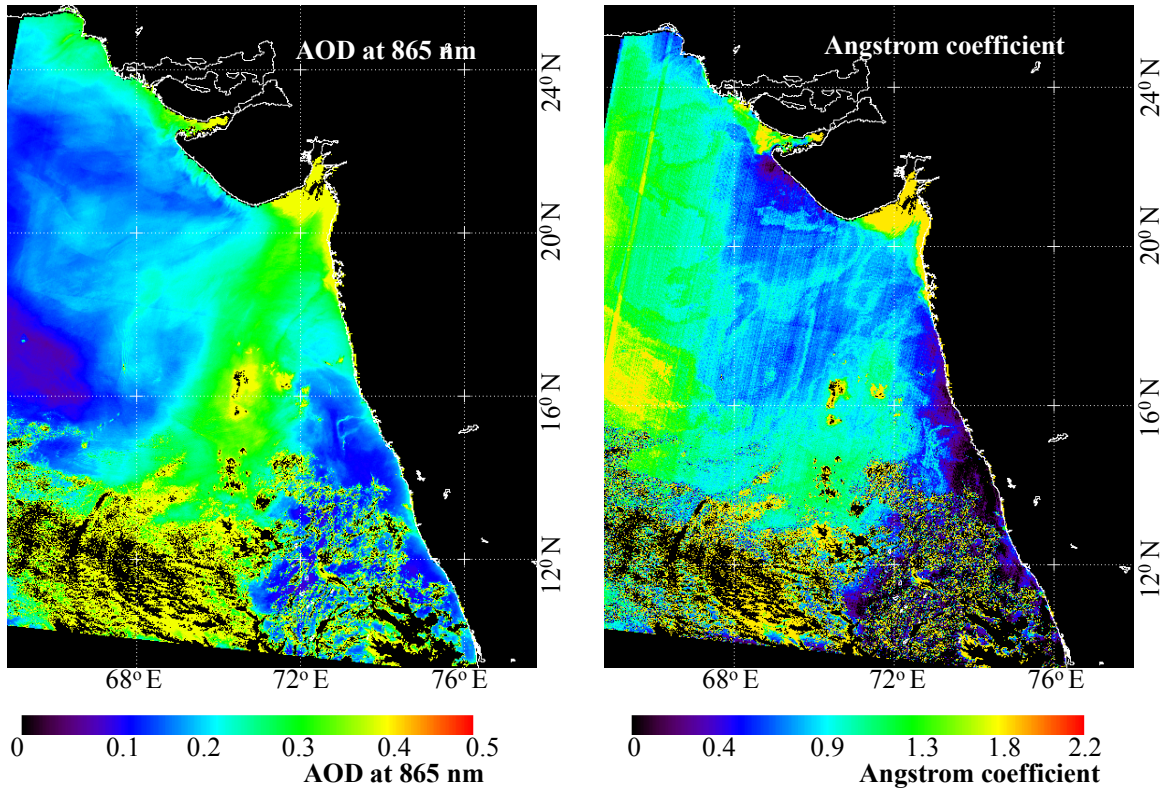


Figure 4.4: Aerosol optical depth estimated at 865 nm band and angstrom coefficient of OCEANSAT-1 OCM (Date: 8 November, 2001).

In the open ocean variation of AOD at 865 nm band was from 0.05 to 0.3. The retrieval range of AOD from ocean colour remote sensing in the open ocean is from 0.01 to 0.3 (IOCCG, 2012). The high aerosol loading around the cloud patches is because of high reflectance at the edge of the cloud. Correction at the edge of the cloud has not done at the present model. The

Chapter 4

variation of alpha is mainly 0.8 to 1.3 in the open ocean. OCEANSAT-1 OCM estimated AOD has been compared with limited *in-situ* measured AOD during November 2001 and January 2003. *In-situ* measurement of AOD by Sunphotometer has been discussed in Chapter 3 (Page No. 56). Figure 4.5 shows the comparison between OCEANSAT-1 OCM estimated AOD at 865 nm and *in-situ* measured AOD (865 nm). Figure 4.5 shows a good correlation between OCEANSAT-1 OCM estimated AOD (865 nm) and *in-situ* measured AOD (865 nm).

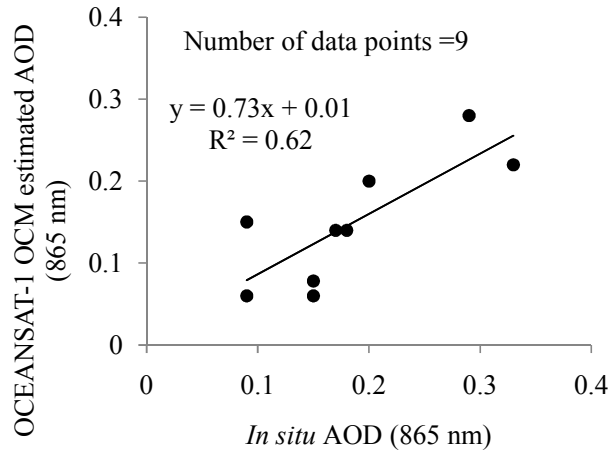


Figure 4.5: Comparison between OCEANSAT-1 OCM estimated AOD and *in-situ* measured AOD during November 2001 and January 2003 at oceanic locations.

Alpha has been estimated using a ratio at wavelength 865 nm and 765 nm. AOD at other wavelength has been estimated by angstrom relationship of AOD with wavelengths with the equation (4.30).

$$\tau_a = \tau_{865} \left(\frac{\lambda}{865} \right)^{-\alpha} \dots \dots \dots (4.30)$$

Aerosol transmission T_a at each of fifteen wavelength band has been computed using equation (4.20).

4.5.3 Modeling PAR under cloudy sky condition

Clouds regulates flow of radiant energy in the atmosphere through the process of scattering and absorption of shortwave and longwave radiation. They reflect incoming shortwave radiation to the space. Reflectance and transmittance of incoming solar radiation are both sensitive to optical thickness of the cloud (McBride et al., 2011). The optical thickness of a cloud involves the integration over cloud droplet size distribution $n(r)$ and cloud depth z varying from zero to Δz . Cloud optical depth is formally defined as (Stephens, 1978)

$$\tau_c = \int_0^{\Delta z} \int_0^{\infty} n(r) Q_{ext}(x) \pi r^2 dr dz \dots \dots \dots (4.31)$$

Where $x = 2\pi r/\lambda$, Q_{ext} is efficiency factor for extinction, r is the radius of the cloud droplets. Effective radius is an area weighted mean radius of the cloud droplets. Traditionally, effective radius is defined by the equation (4.32) (Stephens, 1978).

$$r_e = \frac{\int_0^{\infty} n(r) r^3 dr}{\int_0^{\infty} n(r) r^2 dr} \dots \dots \dots (4.32)$$

Figure 4.6 shows the variation of transmittance through the water cloud for different effective radius ranging from 5 μm to 25 μm . Larger droplet size is associated with stronger forward scattering and thus larger transmittance. However, because droplet absorption increases with wavelength, the opposite effect dominates at wavelengths greater than about 1400 nm and larger droplet size leads to decrease transmittance. From the Figure 4.6 it is evident that transmittance through the water cloud for a particular droplet size is constant in the wavelength region from 400 nm to 700 nm (McBride et al., 2011).

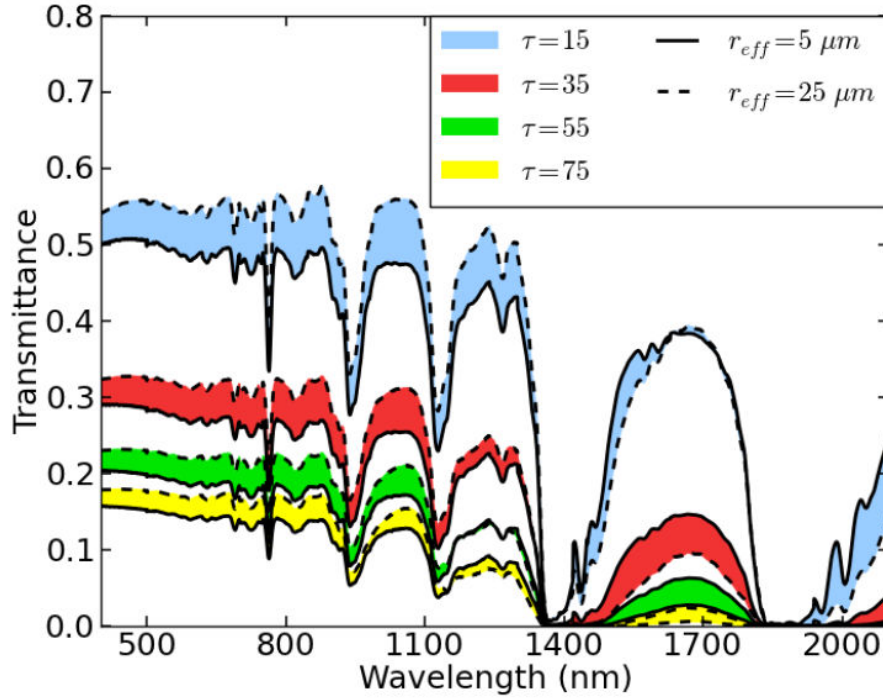


Figure 4.6: Variation of transmittance through a liquid water cloud (McBride et al., 2011)

In the wavelength region from 400 nm to 700 nm, Stephens et al. (1984) estimated cloud top reflectance R_{θ_s} for unit single scattering albedo based on the solution of parameterization model of radiation profile in the extended water clouds.

$$R_{\theta_s} = \frac{\beta_{\theta_s} \tau_c / \cos\theta_s}{(1 + \beta_{\theta_s} \tau_c / \cos\theta_s)} \dots \dots \dots (4.33)$$

τ_c is the optical thickness of the cloud, β_{θ_s} is the backscattered fraction of incident radiation as a function of the solar zenith angle. T_{θ_s} is the transmittance through the cloud and has been obtained from reflectance by using equation (4.34) (Stephens et al., 1984).

$$T_{\theta_s} = 1 - R_{\theta_s} \dots \dots \dots (4.34)$$

Modeling PAR from satellite data

In the presence of clouds, direct ($I_{dir_top_cloud}$) and diffuse ($I_{diff_top_cloud}$) PAR at the top of the cloud is estimated using equation (4.5) and (4.14). Cloud top pressure has been used to compute transmittance of aerosol absorption, uniformly mixed gas and Rayleigh scattering under cloudy conditions instead of mean sea level pressure since in cloudy condition. In cloudy condition, m_p is not equal to m_0 . To compute PAR under cloudy condition following assumptions have been made.

- i. All ozone absorption is assumed to occur above clouds.
- ii. Cloud cover is homogeneous, plane parallel and spatially stationary.
- iii. Satellite observations suggest that complex interactions occur between coexisting cloud and aerosol layers (Kaufman et al., 2005). Chauhan et al. (2009) showed that the variation of aerosol optical depth at 870 nm in the Arabian Sea was from 0.12 to 0.14 with average value 0.13. Fixed aerosol optical depth 0.13 at 865 nm wavelength was used to estimate PAR under cloudy condition.

The scattered radiation above the cloud top originates from Rayleigh and aerosol scattering have been estimated using equation (4.35).

$$I_{s\lambda_top_cloud} = I_{dir\lambda_top_cloud} \cos \theta_s + I_{diff\lambda_top_cloud} \dots \dots \dots (4.35)$$

The radiation transmitted through the clouds is then used to compute the attenuation in the lower part of the atmosphere. Total PAR under cloudy condition have been computed using equation (4.36).

$$I_{par_cloudy} = \sum_{400nm}^{700nm} I_{s\lambda_top_cloud} T_{\theta_s} \Delta\lambda \dots \dots \dots (4.36)$$

4.5.4 Inputs for PAR model under cloudy sky condition

4.5.4.1 Cloud top pressure

Cloud top pressure has a moderate influence on the estimation (Van Laake and Azofeifa, 2004) of PAR. ISCCP (International Satellite cloud climatology Project) global average cloud top pressure has been estimated 574 hPa (Kokhanovsky et al., 2011). A fixed cloud top pressure 574 hPa was used to compute PAR under cloudy condition.

4.5.4.2 Backscattered fraction of incident radiation (β_{0s})

The backscattering fraction is a function of solar zenith angle and cloud optical depth. Stephan et al. (1978) employed a detailed multiple scattering model to calculate a series of values of reflection, absorption and transmission for a number of model cloud types. These calculations were used to tune the value of β_{0s} . Values of β_{0s} have been obtained from Stephens et al. (1984) for wavelength less than 750 nm.

4.5.4.3 Cloud optical depth (COD)

Cloud optical depth is estimated using a suitable model which use transmitted radiance data measured by ground-based observation or reflected radiance data measured by space-based observation. However, ground based observation data are not available in systematic way globally. Transmission-based algorithm use spectral irradiance (Min and Harrison 1996) or broadband irradiances (Leontyeva and Stamnes 1994; Dong et al., 1997; Boers 1997; Barker et al., 1998).

Modeling PAR from satellite data

Cloud optical depth has been estimated from transmitted radiance data by ground-based observation at 415 nm, 440 nm, 675 nm, 870 nm wavelengths (Min and Harrison, 1996; Barnard and Long, 2004; Chiu et al., 2010). Barnard and Long (2004) use a simple empirical equation to calculate cloud optical thickness as a function of cosine of solar zenith angle, surface albedo, broadband diffuse irradiance and broadband clear sky total irradiance. The Aerosol Robotic Network (AERONET) is a ground-based network that is designed to measure microphysical and optical properties of aerosol at wavelengths of 440 nm, 675 nm, 870 nm and 1020 nm. In cloudy condition, radiance detected by AERONET radiometers has been used to estimate cloud optical depth (Chiu et al., 2010) at each wavelength.

To estimate cloud optical depth from space based observation, Nakajima and King (1990) showed that reflectance at 750 nm and 2160 nm can be used to estimate cloud optical thickness and mean effective radius. The measurements at 750 nm are preferred as it is free of considerable influence of atmospheric absorption due to gases or liquid water.

International Satellite Cloud Climatology Project provides cloud optical depth using radiance data from five geostationary such as GMS, METEOSAT, GOES-WEST, GOES-EAST, INSAT and two polar orbiting satellites such as NOAA-AVHRR-Afternoon, NOAA-AVHRR-morning (Rossow et al., 1996) for 280-km grid cell over the globe. Cloud optical thickness at 600 nm values retrieved using two different cloud microphysical models (Schiffer and Rossow, 1983; Schiffer and Rossow, 1985; Rossow and Schiffer, 1991; Rossow et al., 1996; Rossow and Schiffer, 1999). A liquid water droplet model with a water sphere size distribution described by a gamma distribution with effective mean radius 10 μm and effective variance 0.15 has been used. Second model is an ice crystal model with a random fractal crystal shape and power law size distribution from 20 μm to 50 μm , giving an effective radius of 30 μm and an effective variance of 0.10.

Cloud optical depth has been estimated from MODIS data based on asymptotic theory (King 1987; Nakajima and King, 1990; King et al., 1992; King et al., 1997). The wavelength are used to estimate cloud optical thickness are 645 nm over land surface, 858 nm over ocean surface

Chapter 4

and 1240 nm over snow surface. A combination of 645 nm, 1640 nm and 2130 nm bands was used for cloud thermodynamic phase function.

A polynomial approach is used to estimate cloud optical depth at 753 nm where cloud optical depth are related to a polynomial function of the MERIS radiance (Fischer et al., 2000). However, using ADEOS-POLDER radiance measurement, cloud optical depth has been estimated at 443 nm, 670 nm, 865 nm band (Parol et al., 2000).

Kokhanovsky et al. (2003) developed a simple semi-analytical model to estimate cloud optical depth. However, this algorithm is valid for optically thick clouds or clouds having cloud optical thickness greater than 5 m. The theory is based on the premise that reflectance estimated at visible (non-absorbing) wavelength is used to estimate cloud optical thickness and reflectance in near infrared and mid infrared is used to estimate effective radius of cloud droplet.

Using the equation (4.33), cloud optical depth (COD) from OCM for thick water clouds (COD > 4m) has been obtained from a semi-analytical model developed by Kokhanovsky et al. (2003) with input of OCM reflectance at 443 nm band. For thin clouds (COD < 4m), a quadratic relationship between COD and TOA radiance at 443 nm band of OCM was used as described in the section 4.5.4.3 (B).

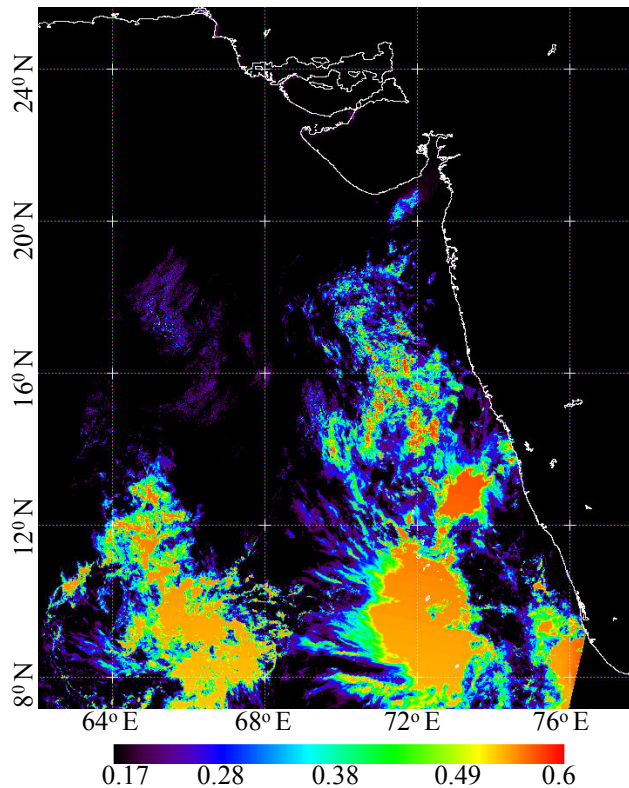
A) Cloud optical depth estimation for thick clouds

Cloud optical depth has been estimated at 443 nm spectral band of OCM using a semi-analytical model developed by Kokhanovsky et al. (2003). The reflectance $R_{443}(\tau_c; \mu, \mu_0, \phi)$ at 443 nm band of OCM has been calculated using equation (4.37).

$$R_{443}(\tau_c; \mu, \mu_0, \phi) = \frac{\pi L_{443}(\tau_c = 0; \mu, \phi)}{\mu_0 F_{443}} \dots \dots \dots (4.37)$$

Modeling PAR from satellite data

Here L_{443} denotes TOA radiance at 443 nm band of OCM, $\mu = |\cos\theta_v|$ and $\mu_0 = |\cos\theta_s|$. θ_v is the satellite view angle, θ_s is the solar zenith angle, ϕ is the relative azimuth angle between solar and satellite directions. F_{443} is the extra-terrestrial solar irradiance corresponding to the 443 nm spectral band of OCM sensor derived using band specific Relative Spectral Response (RSR) function of OCM band (Chauhan et al., 2002). Figure 4.7 shows the variation of reflectance estimated at 443 nm of OCM in the Arabian Sea under cloudy sky condition.



4.7: Reflectance estimated at 443 nm spectral band of OCEANSAT-1 OCM for cloudy pixels (16th November, 2001).

The variation of reflectance at 443 nm spectral band of OCEANSAT-1 OCM is 0.17 to 0.25 for very thin cloud. For thick cloud patches, reflectance value is less at the edge of the cloud and it is higher at the middle of the cloud patches.

Chapter 4

For ideally white reflector, the value of reflectance should be one. However, the value of reflectance of clouds estimated from OCM is not equal to one. Reflectance can be smaller and larger than one depending on the incidence angle (Karlgaard, 2008). This implies that, for a particular viewing geometry a cloud is even more reflective than ideally white reflector. This is mostly due to peculiarities of the scattering phase function of the cloud (Karlgaard, 2008). Phase function $P(\zeta)$ of a cloud describes the probability of a photon being scattered in the direction of scattering angle (ζ). For a given particle size and wavelength, the phase function $P(\zeta)$ can be derived using Mie solutions. Kokhanovsky et al. (2003) derived an approximate fifth order polynomial to estimate phase function using equation (4.38).

$$P(\zeta) = Qe^{-\sigma} + \sum_{i=1}^5 b_i e^{\beta_i(\zeta - \zeta_i)^2} \dots \dots \dots (4.38)$$

Scattering angle in radians is estimated using equation (4.39).

$$\zeta = \arccos(-\cos\theta_v \cos\theta_s + \sin\theta_v \sin\theta_s \cos\phi) \dots \dots \dots (4.39)$$

Constants such as $Q, \sigma, b_i, \beta_i, \zeta_i$ in the equation (4.39) have been obtained from Kokhanovsky et al. (2003)

Table 4.4: Values of constants used to estimate phase function of clouds.

i	b _i	β _i	ζ _i
1	1744.0	1200.0	0.0
2	0.17	75.0	2.5
3	0.30	4826.0	pi
4	0.20	50.0	pi
5	0.15	1.0	pi

Modeling PAR from satellite data

In the case of conservative scattering i.e, single scattering albedo of cloud =1, reflectance can be expressed by the equation (4.40) (King, 1987; Nakajima and King, 1990; Kokhanovsky et al., 2003; Kokhanovsky and Nauss, 2006)

$$R(\tau_c; \mu, \mu_0, \phi) = R_\infty^0(\mu, \mu_0, \phi) - \frac{t_c(r_e, w)(1 - A_s)K_0(\mu)K_0(\mu_0)}{1 - A_s(1 - t_c(r_e, w))} \dots \dots \dots (4.40)$$

$R_\infty(\mu, \mu_0, \phi)$ is the reflectance of an idealized semi-infinite non-absorbing water cloud. $R_\infty(\mu, \mu_0, \phi)$ can be represented by the simple approximate equation (4.41) (Kokhanovsky et al., 2003).

$$R_\infty^0(\mu, \mu_0, \phi) = \frac{b_1 + b_2 \cos\theta_s \cos\theta_v + P(\zeta)}{4(\cos\theta_s + \cos\theta_v)} \dots \dots \dots (4.41)$$

b_1 and b_2 are constants. $b_1=1.48$, $b_2=7.76$ (Kokhanovsky et al., 2003). In the equation (4.41), $K_0(\mu)$, $K_0(\mu_0)$ are escape functions. Escape functions describes the angular distribution of light escaping a semi-infinite cloud from sources located deep inside the medium. Because multiple scattering dominates in the cloud, typical features of single scattering becomes less pronounced and escape functions can be well represented for isotropic scattering by the functions represented in the equation (4.42) and (4.43) (Kokhanovsky et al., 2003).

$$K_0(\mu) = \frac{\sqrt{3}}{4}(1 + 2\mu) \dots \dots \dots (4.42)$$

$$K_0(\mu_0) = \frac{\sqrt{3}}{4}(1 + 2\mu_0) \dots \dots \dots (4.43)$$

In the equation (4.40), $t_c(r_e, w)$ is the diffused transmittance of a cloud. $t_c(r_e, w)$ is governed by the effective radius r_e and the liquid water path w . However, it can be expressed in terms of asymmetry parameter $g(r_e)$ and optical thickness τ_c (Kokhanovsky et al., 2003).

$$t_c = \frac{1}{\alpha_c + \frac{3}{4}\tau_c(1 - g(r_e))} \dots \dots \dots (4.44)$$

The value of α_c is 1.072 for water clouds (Kokhanovsky et al., 2003). The optical thickness is expressed by the equation (4.45).

$$\tau_c = \frac{4(t_c^{-1} - 1.072)}{3(1 - g(r_e))} \dots \dots \dots (4.45)$$

Where $t_c = \frac{1}{\left(\frac{K_0(\mu)K_0(\mu_0)}{R_{\infty}^0 - R(\tau_c; \mu, \mu_0, \phi)} - \frac{A_s}{1 - A_s}\right)}$ \dots \dots \dots (4.46)

In the above equation, ocean surface albedo $\frac{A_s}{(1 - A_s)}$ has been neglected. Asymmetry function $g(r_e)$ is taken as 0.85 for water clouds (King, 1987).

B) Cloud optical depth estimation for thin clouds

Semi-analytical model to estimate PAR is valid for optically thick clouds or clouds, which are having cloud optical depth greater than 4 m. For very thin ice clouds of 34.3 μm effective radius, a quadratic relationship between cloud optical depth and TOA radiance at 443 nm band at OCM viewing geometry has been obtained from COART (Coupled Ocean Atmosphere Radiative Transfer) model (<http://www-cave.larc.nasa.gov/cave/>). Figure 4.8 shows the relationship between TOA radiance at 443 nm band of OCM and cloud optical depth obtained from COART model. Figure 4.9 shows the variation of cloud optical depth both for thick and thin cloud. Based on the analysis, the minimum value of COD is fixed at 2 m. Clouds are having particle sizes much larger than the wavelength of light and show extremely weak wavelength dependence (Hu et al., 1993), in the wavelength region from 400 nm to 700 nm. Cloud optical depth estimated at any non-absorbing wavelength, has been used at other wavelengths in the PAR wavelength range.

Modeling PAR from satellite data

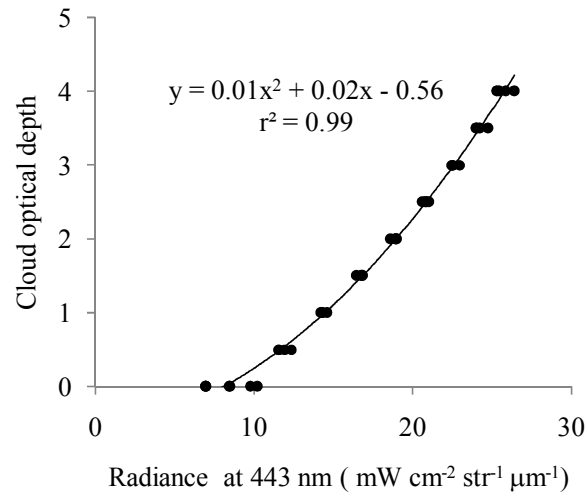


Figure 4.8: Variation of TOA radiance at 443 nm of OCM with cloud optical depth obtained from COART model.

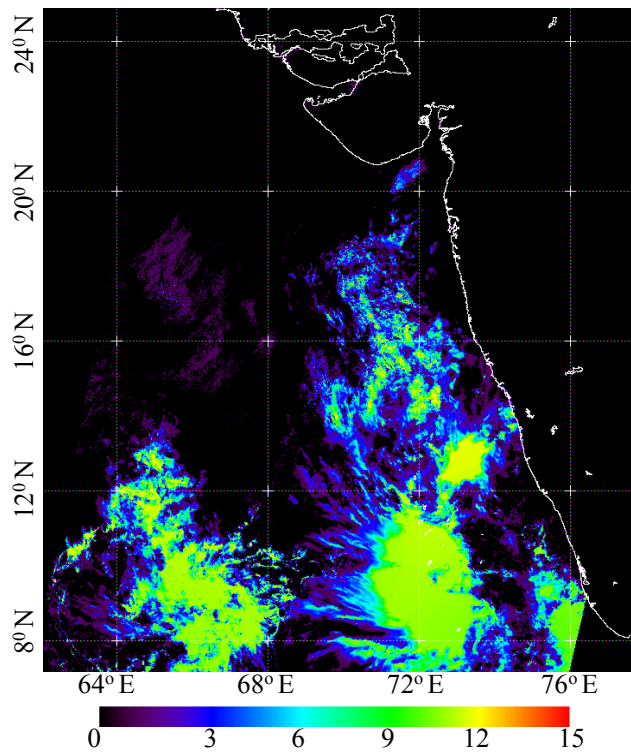


Figure 4.9: Cloud optical depth estimated at 443 nm band of OCEANSAT-1 OCM (16th November, 2001) for thick and thin clouds.

Chapter 4

Figure 4.10 shows Flow chart to estimate PAR from OCEANSAT-1 & 2 OCM using method I.

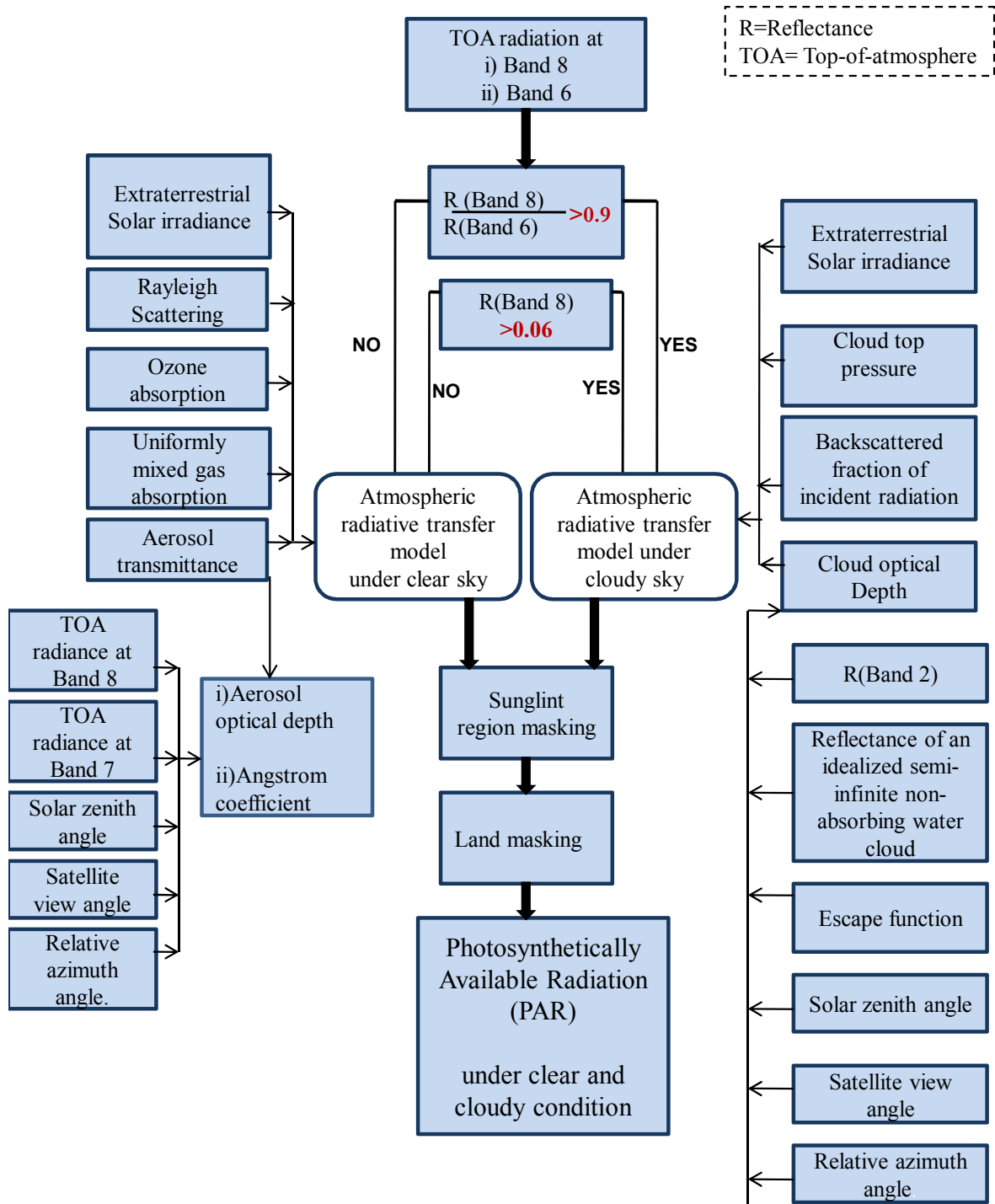


Figure 4.10: Flow chart to estimate PAR from OCEANSAT-1 & 2 OCM.

4.5.5 Output of PAR model under clear and cloudy sky condition

Instantaneous total PAR I_{par} in $W m^{-2}$ is calculated using equation (4.47) under both clear and cloudy condition.

$$\begin{aligned}
 I_{par} &= \sum_{400nm}^{700nm} I_{s\lambda} \Delta\lambda \text{ for clear sky} \\
 &= \sum_{400nm}^{700nm} I_{s\lambda_top_cloud} T_{\theta_s} \Delta\lambda \text{ for cloudy sky} \dots \dots \dots (4.47)
 \end{aligned}$$

Output of the PAR model is PAR estimated at noon in $Watt m^{-2}$ and daily (24 hour) averaged PAR in $Einstein m^{-2} day^{-1}$. As equatorial crossing time of OCM is 12 noon, PAR at noon I_{0m} is calculated based on the state of the atmosphere when satellite data was acquired. Daily total PAR has been calculated using equation (4.48) based on a sinusoidal approximation of light and assuming the state of the atmosphere is not going to change for full day. This is an assumption as observations at other times are not available.

$$\begin{aligned}
 I_T &= \int_0^D I_{0m} * \sin\left(t * \frac{\pi}{D}\right) dt \\
 I_T &= -\frac{I_{0m}D}{\pi} \left[\cos\left(t * \frac{\pi}{D}\right) \right]_0^D \\
 I_T &= -\frac{I_{0m}D}{\pi} [\cos\pi - \cos 0] = -\frac{I_{0m}D}{\pi} [-1 - 1] = \frac{2I_{0m}D}{\pi} \dots \dots \dots (4.48)
 \end{aligned}$$

I_T is daily total PAR, I_{0m} is PAR at noon and D is daylength. Daylength has been calculated using equations given by Teets (2003). To estimate daily (24 hour) averaged PAR (I_D), I_T is divided by 24 hours as done for SeaWiFS based calculations (Frouin et al., 2003). The unit of daily averaged PAR in $W m^{-2}$ was converted in $Einstein m^{-2} day^{-1}$ (Dye 2004) as shown in the equation (4.49).

$$I_D = \frac{I_T}{24} = \frac{2 \times I_{0m}D}{24 \times \pi} = 0.0104 \times I_{0m} \times D \dots \dots \dots (4.49)$$

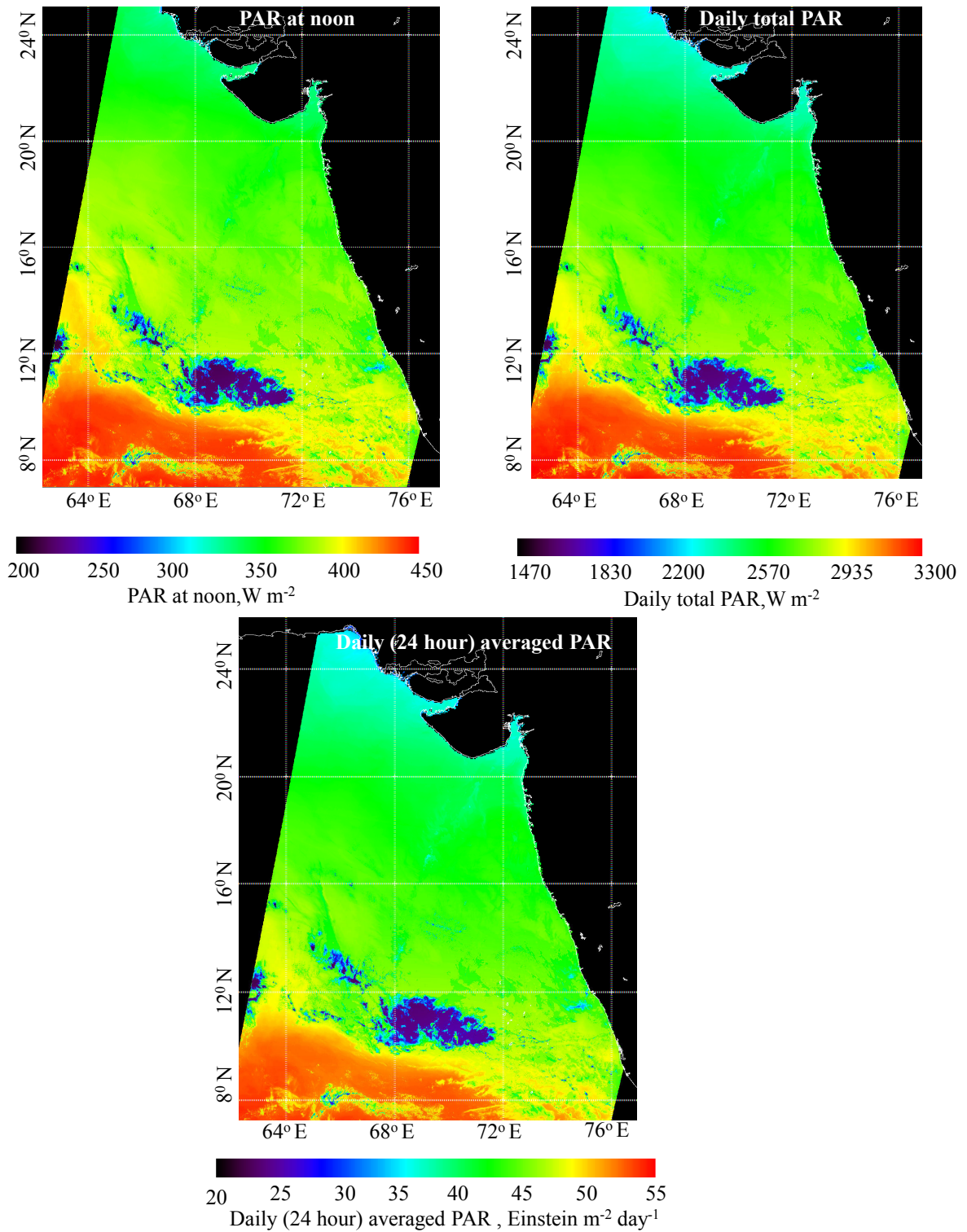


Figure 4.11: Variation of PAR at noon, daily total PAR and daily averaged PAR estimated from OCM over the Arabian Sea (Date 12 November, 2001).

Modeling PAR from satellite data

In the equation (4.49) I_{0m} is in $W\ m^{-2}$ and D is in hour, then daily averaged PAR I_D is in Einstein $m^{-2}\ day^{-1}$ unit. Figure 4.11 shows variation of PAR at noon ($W\ m^{-2}$), daily total PAR I_T ($W\ m^{-2}$) and daily averaged PAR I_D (Einstein $m^{-2}\ day^{-1}$) estimated from OCM.

4.5.6 Sensitivity study of the PAR model (Method I)

A sensitivity analysis has been studied to understand the importance of different input parameters to estimate PAR. The default parameter values used in the sensitivity study are listed in Table 4.5.

Table 4.5: Input default parameters for sensitivity study.

Input Default parameters		
Parameter	Clear Sky	Cloudy Sky
Ozone concentration	250 DU*	250 DU*
Aerosol optical depth at 865 nm	0.15	0.13
Angstrom exponent	1	1
Cloud top pressure		574mb
Cloud optical depth		9.5
Backscattered fraction of incident radiation		0.0692
Latitude, Longitude	19.18°N, 66.73°E	
Date, Time	10Jan2003, 12 p.m	

*DU= Dobson unit

Figure 4.12 shows sensitivity study of PAR at noon with changes of month (a), ozone concentrations (b), aerosol optical depth (c) and angstrom coefficient (d) under clear sky condition. PAR has been estimated at every month using default parameters mentioned in the Table 4.5. To understand monthly variation of PAR, PAR estimated at each month has been

normalized to the average value of PAR during 12 months. Minimum value of PAR has been observed in December. In May month, maximum PAR has been observed (Figure 4.12 a). During April to August the variation of PAR is minimum and it is situated at the plateau region of the graph (Figure 4.12 a).

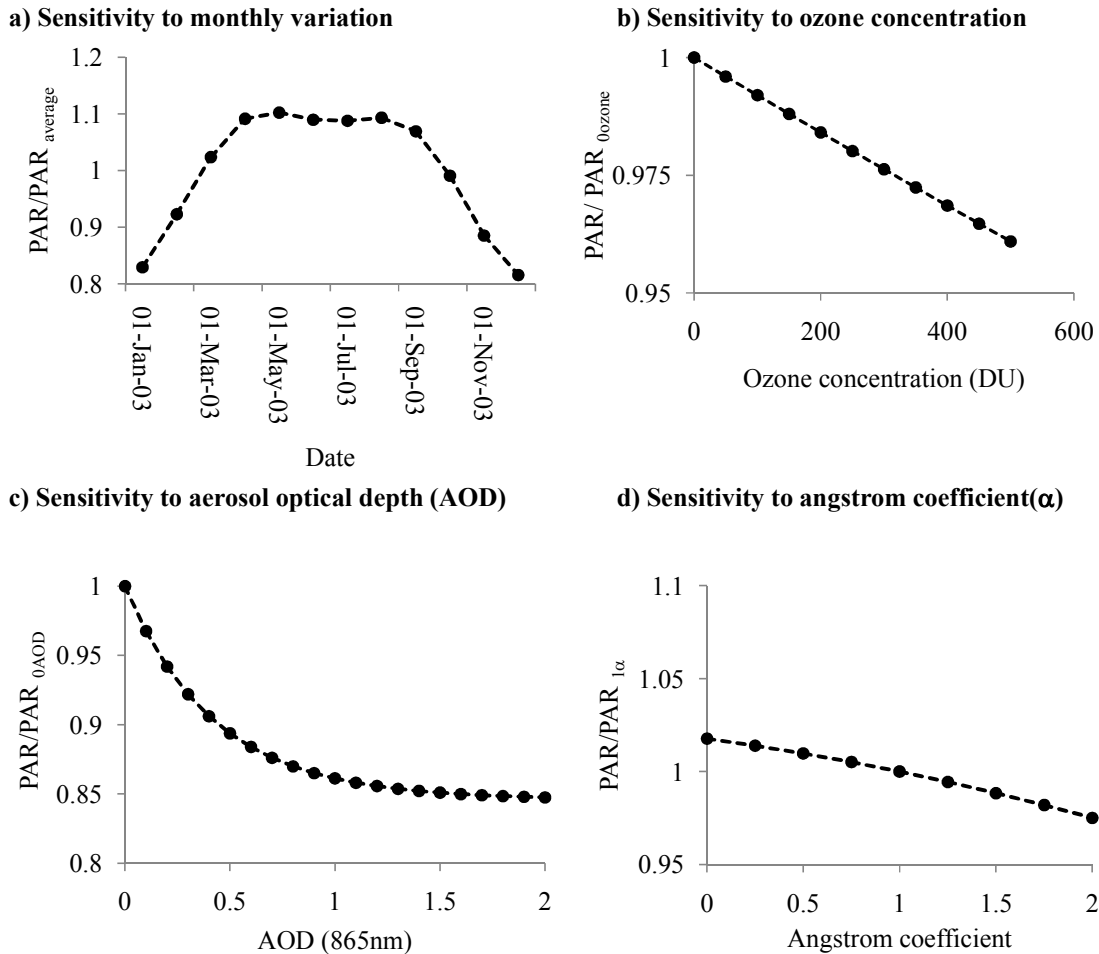


Figure 4.12: Sensitivity to a) monthly variation b) ozone concentration c) aerosol optical depth d) angstrom coefficient for PAR estimation under clear sky.

PAR has been decreased linearly with increase of ozone concentration (Figure 4.12 b). With the change of 500 D.U ozone concentrations PAR has decreased maximum 4% compared to 0 ozone concentration. This indicates that PAR estimation is not so much sensitive to ozone concentration.

Modeling PAR from satellite data

Up to aerosol optical depth 1, PAR has been decreased exponentially with increasing aerosol optical depth (Figure 4.12 c). However, greater than one aerosol optical depth value, decrease of PAR is almost constant with the change of aerosol optical depth (Figure 4.12 c). PAR has decreased 7.8 % and 13.8% for aerosol optical depths 0.3 and 1, respectively compared to no aerosol loading. The variation of PAR is observed only $\pm 2\%$ when angstrom coefficient varies from 0 to 1.8 compared to angstrom exponent 1 (Figure 4.12 d). Under clear sky condition, aerosol optical depth plays important role to attenuate PAR.

Figure 4.13 shows globally cloud classification in terms of cloud optical thickness and cloud top pressure obtained from International satellite Cloud Climatology Project (Rossow and Schiffer, 1999).

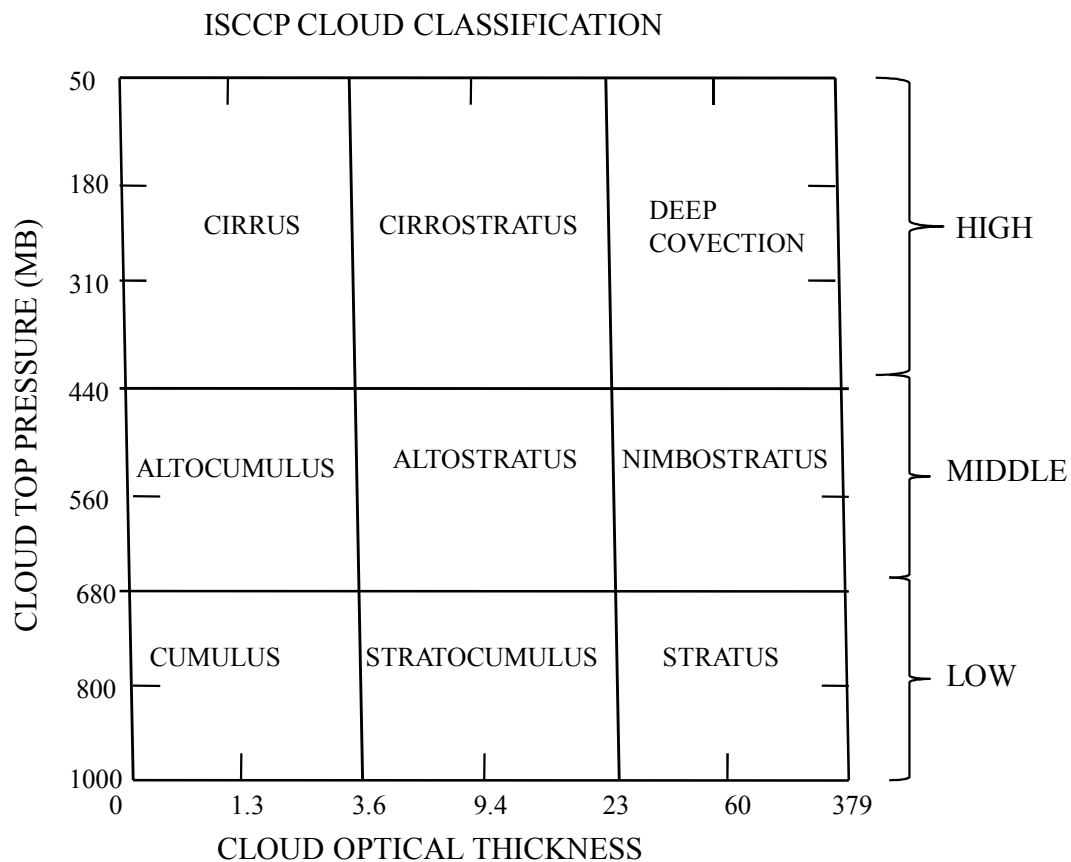
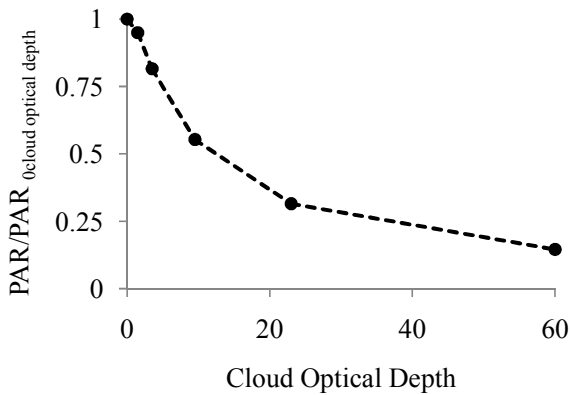


Figure 4.13: Different cloud types in terms of cloud top pressure and cloud optical thickness (Rossow and Schiffer, 1999).

Sensitivity study has also done to understand variation of PAR in terms of cloud optical thickness and cloud top pressure for different types of clouds mentioned in the Figure 4.13. Figure 4.14 shows sensitivity study about the effect of cloud optical depth (a) and cloud top (b) on PAR estimation. PAR estimation is highly sensitive to cloud optical depth, particularly at lower value of cloud optical depth above 10 (Figure 4.14 a). PAR has been decreased by 5%, 18%, 44%, 68% and 85%, respectively for cloud optical depth 1.5, 3.5, 9.5, 23 and 60 compared to clear sky (Figure 4.14 a).

a) Sensitivity to cloud optical depth



b) Sensitivity to cloud top pressure

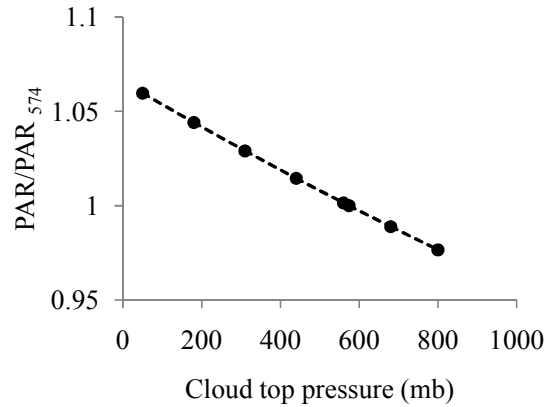


Figure 4.14: Sensitivity to a) cloud optical depth and b) cloud top pressure for PAR estimation under cloudy sky condition

A fixed cloud top pressure 574 mb has been taken to estimate PAR under cloudy condition. PAR value obtained at different cloud top pressure is normalized to PAR estimated at 574 mb and the variation of PAR/PAR_{574} is shown in the Figure 4.14 b). The sensitivity results of the effect of cloud top pressure on PAR estimation shows that if cloud top pressure is higher than 574 mb, maximum 2.3% lower PAR is estimated compared to PAR estimated at 574 mb. Higher value of PAR such as 0.15%, 1.45%, 2.90%, 4.40%, 5.96% has been observed for cloud top 560 mb, 440 mb, 310 mb, 180 mb and 50 mb, respectively compared to 574 mb.

4.6 PAR estimation from OCEANSAT-1 & 2 OCM using method II

PAR has been estimated using second method according to Frouin et al. (2003) which assumes that the effects of clouds and clear atmosphere can be decoupled with the cloud system and surface albedo. PAR under both the clear and cloudy sky I_{par} reaching at the ocean surface is then given by

$$I_{par} = \langle F_0 \rangle \cos(\theta_s) \langle T_d \rangle \langle T_g \rangle (1 - \langle A \rangle) (1 - \langle A_s \rangle)^{-1} (1 - \langle S_a \rangle \langle A \rangle)^{-1} \dots \dots \dots (4.50)$$

$\langle \rangle$ symbolizes average value over the PAR range. θ_s is the solar zenith angle, T_d is the clear sky diffuse transmittance, T_g is the gaseous transmittance, S_a is the spherical albedo for molecular and aerosol scattering. A_s is the ocean surface albedo and A is the cloud albedo. In the clear sky condition, ocean surface albedo A_s reduces to cloud albedo A . Absorption due to water vapour has been neglected in the method II, similar to method I.

F_0 is the extra-terrestrial solar irradiance corresponding to the six discrete spectral bands in the visible region of OCM sensor derived using band specific Relative Spectral Response (RSR) function of OCM bands. F_0 at each band of OCM is calculated with the equation

$$F_0 = \frac{\int_{\lambda_0}^{\lambda_n} I_0(\lambda) \cdot S(\lambda) d\lambda}{\int_{\lambda_0}^{\lambda_n} S(\lambda) d\lambda} \dots \dots \dots (4.51)$$

Where $S(\lambda)$ is the response function of OCM, λ is wavelength. It starts from λ_0 to λ_n for different spectral band of OCM from band 1 to band 6 as mentioned in the Table 4.1. F_0 varies slightly throughout the year because of the eccentric path of the Earth around the Sun. F_0 has been corrected for the Earth Sun distance (Gregg and Carder, 1990).

Chapter 4

Gaseous transmittance T_g essentially due to ozone has been estimated from Frouin et al (2003).

$$T_g = \exp \left[- \frac{k_{oz} \times l}{\cos \theta_s} \right] \dots \dots \dots (4.52)$$

k_{oz} is ozone absorption coefficient and l is ozone concentration. Table 4.6 shows values of F_0 and ozone absorption coefficient of each band starting from band 1 to band 6 of OCM used in the method II.

Table 4.6: Extraterrestrial solar irradiance and ozone absorption coefficient at six spectral bands of OCM used in method II.

Spectral Band	(OCEANSAT-1 OCM)		(OCEANSAT-2 OCM)	
	F_0 (mW cm ⁻² μm ⁻¹)	k_{oz} (cm ⁻¹)	F_0 (mW cm ⁻² μm ⁻¹)	k_{oz} (cm ⁻¹)
Band 1	170.7943	0.0006014	172.0	0.0006014
Band 2	189.4438	0.002996	185.977	0.002996
Band 3	193.6842	0.02297	195.895	0.02297
Band 4	188.3675	0.04291	186.206	0.04291
Band 5	185.3973	0.1011	182.415	0.1011
Band 6	153.3877	0.1090	165.667	0.1090

Average gaseous transmittance has been expressed by

$$\langle T_g \rangle = \frac{\sum_i T_{gi} \times F_{0i}}{\sum_i F_{0i}} \dots \dots \dots (4.53)$$

Modeling PAR from satellite data

i is the band numbers of OCM. i varies from 1 to 6.

Direct T_{dir} and Diffuse transmittance T_d has been computed using equation (4.54) and equation (4.55) (Tanre et al., 1979; Frouin et al., 2003).

$$T_{dir} = \exp[-(\tau_{r\lambda} + \tau_{a\lambda})/\cos\theta_s] \dots \dots \dots (4.54)$$

$$T_d = \exp[-(\tau_{r\lambda} + \tau_{a\lambda})/\cos\theta_s] \times \exp[-(0.52\tau_{r\lambda} + 0.83\tau_{a\lambda})/\cos\theta_s] \dots \dots \dots (4.55)$$

$\tau_{r\lambda}$, $\tau_{a\lambda}$ are Rayleigh optical depth and aerosol optical depth at six visible band of OCM. $\tau_{r\lambda}$ has been estimated from Bird (1984). $\tau_{a\lambda}$ has been estimated at each visible band from AOD at 865 nm band of OCM using angstrom relationship. AOD at 865 nm and angstrom coefficient estimated from OCM has been used in this method II as input.

Average direct and diffuse transmittance has been expressed by

$$\langle T_{dir} \rangle = \frac{\sum_i T_{diri} \times F_{oi}}{\sum_i F_{oi}} \dots \dots \dots (4.56)$$

$$\langle T_d \rangle = \frac{\sum_i T_{di} \times F_{oi}}{\sum_i F_{oi}} \dots \dots \dots (4.57)$$

Ocean surface albedo A_s and cloud albedo A has been estimated for clear and cloudy pixels for OCM. Albedo is the total reflectance of the surface integrated over all the angles of the upward hemisphere. Taylor et al. (1996) estimated ocean surface albedo based on aircraft measurement and proposed ocean surface albedo is a function of solar zenith angle. Frouin et al. (2003) incorporated the effect of atmospheric optical depth with solar zenith angle to estimate ocean surface albedo. Average ocean surface albedo has been calculated using equation (4.58) (Frouin et al., 2003).

Chapter 4

$$\langle A_s \rangle = \frac{\langle T_{dir} \rangle}{\langle T_d \rangle} \left[\frac{0.05}{1.1(\cos\theta_s)^{1.4} + 0.15} \right] + 0.08 \frac{(1 - \langle T_d \rangle)}{\langle T_d \rangle} \dots \dots \dots (4.58)$$

Spherical albedo represents the ratio of the total energy reflected by aerosol and molecules present in the entire atmosphere to the energy incident on it. Spherical albedo S_a has been computed using analytical formulas developed by Tanre et al. (1979).

$$S_a = (0.92\tau_{r\lambda} + 0.33\tau_{a\lambda}) \exp[-(\tau_{r\lambda} + \tau_{a\lambda})] \dots \dots \dots (4.59)$$

Average spherical albedo has been expressed by

$$\langle S_a \rangle = \frac{\sum_i S_{ai} \times F_{oi}}{\sum_i F_{oi}} \dots \dots \dots (4.60)$$

Average cloud albedo has been expressed by the reflectance measured by OCM in the PAR spectral range and angular factor F (Frouin et al., 2003)

$$\langle A \rangle = F \times \langle R(t^*) \rangle \dots \dots \dots (4.61)$$

Where t^* is the OCM observation time. Angular factor F has been calculated by analytical formulas proposed by Zege (1991).

For each pixel of OCM which is not contaminated by Sun glitter, OCM radiance L_i in band i ($i=1, 2, \dots, 6$) has been transformed into reflectance R_i .

$$R_i = \frac{\pi L_i}{\cos\theta_s F_{oi}} \dots \dots \dots (4.62)$$

Reflectance estimated at each band of OCM has been corrected for ozone and also for intrinsic atmospheric reflectance as given in Frouin et al. (2003). Intrinsic reflectance is defined

Modeling PAR from satellite data

as reflectance by photons that have not interacted with cloud or ocean surface layers. $\langle R(t^*) \rangle$ is average reflectance of six visible OCM bands. Average reflectance has been estimated by

$$\langle R(t^*) \rangle = \frac{\sum_i R_i(t^*) \times F_{0i}}{\sum_i F_{0i}} \dots \dots \dots (4.63)$$

Figure 4.15 shows the variation of ocean surface albedo and cloud albedo estimated from OCM on a pixel by pixel basis in the Arabian Sea. Ocean surface albedo estimated from OCM was varying from 5-6 % (Figure 4.15). For thin clouds, cloud albedo was varying 18-20%. Maximum 40-45 % cloud albedo was observed for thick clouds (Figure 4.15).

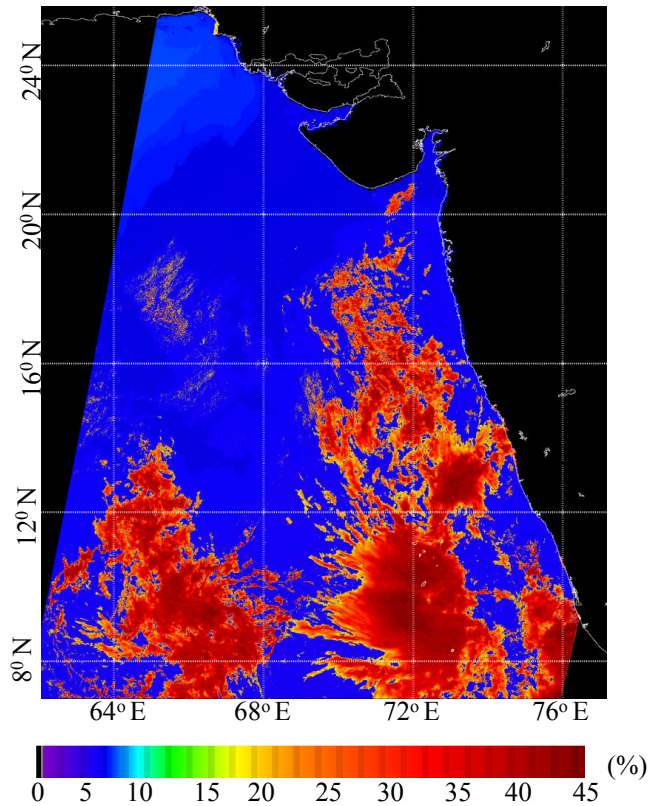


Figure 4.15: OCM derived average ocean surface albedo and cloud albedo in PAR wavelength range (Date: 16 November, 2001).

4.7 Summary and conclusions

Two PAR products such as PAR at noon and daily averaged PAR have been estimated from OCEANSAT-1 & 2 using two different methods for sunglint free region. Sunglint region in OCM has been estimated using wind climatology and it has been masked. Major specifications and features of OCEANSAT-1 & 2 OCM have been discussed. Pixels of OCEANSAT-1 & 2 OCM have been separated under clear and cloudy sky condition based on threshold value. Threshold value has been estimated from reflectance at band 8 and reflectance ratio between band 8 and band 6 of OCM data.

In the method I, the atmosphere is treated as a single layer for clear sky conditions, or as a double layer for cloudy conditions i.e., a layer above the cloud top and a layer from the cloud top downwards. Surface reflectance is not included in this method. Extra-terrestrial solar irradiance at the top of the atmosphere has been subdivided into continuous fifteen wavelength band at 20 nm spectral intervals. Extra-terrestrial solar irradiance at each wavelength band has been obtained by using trapezoidal method of integration. Extra-terrestrial solar irradiance at each band has been corrected for Rayleigh scattering, ozone absorption, uniformly mixed gas absorption, aerosol transmittance under cloud free condition. Aerosol transmittance is expressed in terms of aerosol optical depth and angstrom coefficient property. Methodology to estimate aerosol optical depth and angstrom coefficient from OCEANSAT-1 & 2 OCM have been discussed. Under cloudy sky input parameters are extra-terrestrial solar irradiance, cloud top pressure, backscatter fraction of incident radiation and cloud optical depth. A fixed cloud top pressure of 574 mb and fixed aerosol optical depth of 0.13 have been used to estimate PAR under cloudy sky. Cloud optical depth has been estimated at band 2 of OCM using a semi-analytical model for thick clouds. Reflectance at band 2 of OCM, reflectance of an idealized semi-infinite non absorbing cloud, escape function, solar zenith angle, satellite view angle and relative azimuth angle are used as input parameters to estimate cloud optical depth from OCM for thick clouds. For thin clouds i.e, clouds which are having cloud optical depth less than 4, a quadratic relationship between cloud optical depth and TOA radiance at band 2 of OCM has been used.

Modeling PAR from satellite data

In method I, sensitivity of input parameters such as monthly variation, ozone concentrations, aerosol optical depth, angstrom exponent, cloud optical depth and cloud top pressure has been studied. Sensitivity results show that PAR changes with month wise. PAR is maximum during April to August. Ozone is the least sensitive parameter. The variation of PAR is observed only $\pm 2\%$ when angstrom coefficient varies from 0 to 1.8. The variation of PAR is observed $\pm 3\%$ when cloud top pressure varies from 310 mb to 800 mb compared to fixed cloud top pressure 574 mb. The error to estimate PAR is under cloudy sky 4.5-6 % when cloud top pressure varies from 180 mb to 50 mb compared to fixed cloud top pressure 574 mb. PAR has decreased 7.8% and 13.8% for aerosol optical depths 0.3 and 1 respectively compared to no aerosol loading. PAR estimation is highly sensitive to cloud optical depth, particularly at lower value of cloud optical depth above 10. Under clear sky condition aerosol optical depth and under cloudy sky cloud optical depth plays important role for a particular season compared to the other variables in PAR estimation.

For method II, the effect of clouds and clear atmosphere is assumed to be decoupled with the cloud system and ocean surface albedo. In this method, mean of extra-terrestrial solar irradiance corresponding to six discrete bands in visible wavelength of OCM has been used. AOD at 865 nm, angstrom coefficient and ocean surface albedo estimated from OCM has been used in this method II as input. TOA radiance of OCM at each visible band has been used to estimate cloud albedo. Comparisons of OCM PAR estimated using two methods with *in-situ* measured PAR and also PAR estimated from other ocean colour sensors have been discussed in the next chapter.

Chapter 5

OCEANSAT OCM derived PAR spatial distribution & validation

Chapter 5 briefs about the validation of PAR estimated from OCEANSAT-1 & 2 OCM with in-situ measured PAR from surface downwelling flux measurements made during ship cruises in the Arabian Sea. Further PAR estimated from OCEANSAT-1 & 2 OCM has been compared with PAR estimated from other ocean colour sensors such as SeaWiFS (Sea-viewing Wide Field-of-view Sensor) and MODIS (Moderate Resolution Imaging Spectroradiometer). Statistical results have been generated between OCM estimated PAR, in-situ measured PAR and PAR estimated from other ocean colour satellite sensors. Temporal and spatial variability of PAR has also been discussed in this chapter.

5.1 Introduction

Two PAR products such as PAR at noon and daily averaged PAR have been estimated from OCM using two different methods discussed in the previous chapter 4. The unit of PAR at noon is Watt m^{-2} and the unit of daily averaged PAR is $\text{Einstein m}^{-2} \text{ day}^{-1}$. PAR estimated from OCM using two different methods have been compared with PAR measured from the surface reference (E_s) sensor during different ship campaigns in the Arabian Sea and also PAR estimated from other ocean colour satellites. Based on the results of these comparisons, a method suitable to estimate operational PAR product from OCM has been recommended.

5.2 *In-situ* data collection and data processing

Five ship cruises had been carried out by Space Applications Centre, Indian Space Research Organization to measure different atmospheric and bio-optical parameters during November 2001 to March 2011. Surface PAR was recorded from SMSR (SeaWiFS Multi channel Surface Reference) sensor of radiometer unit (Satlantic Inc.[®]) having seven spectral bands centered on 412 nm, 443 nm, 490 nm, 510 nm, 555 nm, 670 nm and 780 nm during sea –truth campaigns from 2001-2005. Another surface reference E_s sensor of radiometer (Satlantic Inc.[®]) having 1.2 nm resolutions was used in cruises for 2006 and 2011. Details about PAR at noon estimation from radiometer data has been discussed in the Section 3.3 of Chapter 3 (Page No. 58). Measurement of surface irradiance was carried out using a time window of \pm half an hour centered on the OCM pass, which had an equatorial crossing time at 12:00 noon \pm 10 minutes. The details of the cruise period and observation locations are listed in Table 5.1.

Table 5.1: Location of data points for validation of PAR model

Date during ship cruise period	Latitude (°N)	Longitude(°E)
04-Nov-01	15.60	71.79
06-Nov-01	17.49	70.39
08-Nov-01	19.19	68.93
10-Nov-01	21.58	68.37
12-Nov-01	20.47	70.18
14-Nov-01	18.48	70.05
16-Nov-01	18.06	70.16
04-Jan-03	15.11	72.43
06-Jan-03	17.23	70.55
08-Jan-03	17.89	67.69
10-Jan-03	19.18	66.73
12-Jan-03	20.91	66.87
14-Jan-03	22.52	68.24
16-Jan-03	21.20	69.29
18-Jan-03	18.89	69.73
01-Mar-03	20.89	67.08
03-Mar-03	20.65	66.96
05-Mar-03	18.95	69.45
16-Apr-06	10.72	74.78
18-Apr-06	14.84	73.12
20-Apr-06	16.37	72.06
22-Apr-06	19.06	68.65
24-Apr-06	21.41	65.84
26-Apr-06	21.69	69.19
08-March-11	21.35	66.80
10-March-11	21.98	67.01
14-March-11	21.30	67.75
18-March-11	17.94	68.03

Other than *in-situ* data obtained from ship cruise, a CAL-VAL site has been developed under the Meteorology and Oceanography Programme of ISRO to validate different geophysical products obtained from OCM on regular basis (SAC Report, 2007). The site is located at 30 km distance from Kavaratti island. The geographical coordinate of the site is (10°36'45''N, 72°17'15''E) (SAC Report, 2007). Sea depth of the site is 1900 m approximately (SAC Report, 2007). During November to May, 20-40% cloud cover is observed (SAC Report, 2007). The platforms for sensor installation are a pair of circular buoys. Two buoys each of 2.2 m diameter has been developed (SAC Report, 2007). Various optical and biological parameters are obtained

OCEANSAT OCM PAR spatial distribution and validation

from a pair of buoys on the site. One buoy named MET Buoy have main mooring systems attached to the bottom of sea surface at 1900 m depth and have all meteorological sensors. The other buoy named as optical buoy has 5 m long underwater structure for mounting radiometers and Flurometer below the sea surface. Optical buoy is connected to the main moored buoy through a semi rigid connector. The systems installed on the Kavaratti island provide aerosol optical depth for various wavelengths (SAC Report, 2007).

Daily surface irradiance data from 400 nm to 700 nm in $W\ m^{-2}\ nm^{-1}$ unit of 2.5 nm wavelength resolution on 11:30 a.m and 12:30 p.m have been obtained from Meteorological and Oceanographic Satellite Data Archieval Centre (MOSDAC) at CAL-VAL site (www.mosdac.gov.in) during February, 2011. Surface irradiance data are from morning 7:30 to evening 18:30 at 1 hour interval. PAR has been estimated by integrating surface irradiance from 400 nm to 700 nm using trapezoidal method. PAR at local noon has been calculated by dividing PAR at observation time by cosine of solar zenith angle. Then PAR at noon has been estimated by averaging PAR at noon at two observations time at 11:30 a.m and 12:30 p.m assuming the state of the atmosphere is not going to change during this 1 hour time period. These datasets are used for validation purposes.

5.3 OCEANSAT-1 & 2 OCM data processing

OCEANSAT-1 & 2 OCM satellite data was obtained corresponding to the *in-situ* data collected in the Arabian Sea from November 2001 to March 2011. Details about the spectral characteristics of OCEANSAT-1 & 2 OCM have been discussed in the Section 4.2 of Chapter 4 (Page No. 73). Since OCEANSAT-1 & 2 OCM has two day repetivity, every alternative data has been taken for the study. The study area covered the path 9 and rows numbers 13 and 14. ETOPO2v2 bathymetry data has been obtained from National Geophysical Data Centre (<http://www.ngdc.noaa.gov>) to mask land area. The methods described in the chapter 4 are used to estimate OCM derived PAR.

5.4 Steps used in validation of satellite estimated PAR with *in-situ* measured PAR

For validation of PAR estimated from OCEANSAT-1 & 2 OCM with *in-situ* measured PAR, each longitude, latitude position of each hydrographic station during ship cruise period have been considered as central location. A subset of 3×3 pixel has been prepared around the center location of OCM estimated PAR using software ERDAS IMAGINE 9.1. Statistics of 3×3 pixel has been estimated. Mean value of 3×3 pixel subset has been taken for validation with *in-situ* data. Figure 5.1 shows a subset image of OCEANSAT-1 OCM dated on 4th November 2001. Based on the analysis standard deviation of 3×3 pixel greater than 3 has been rejected for validation.

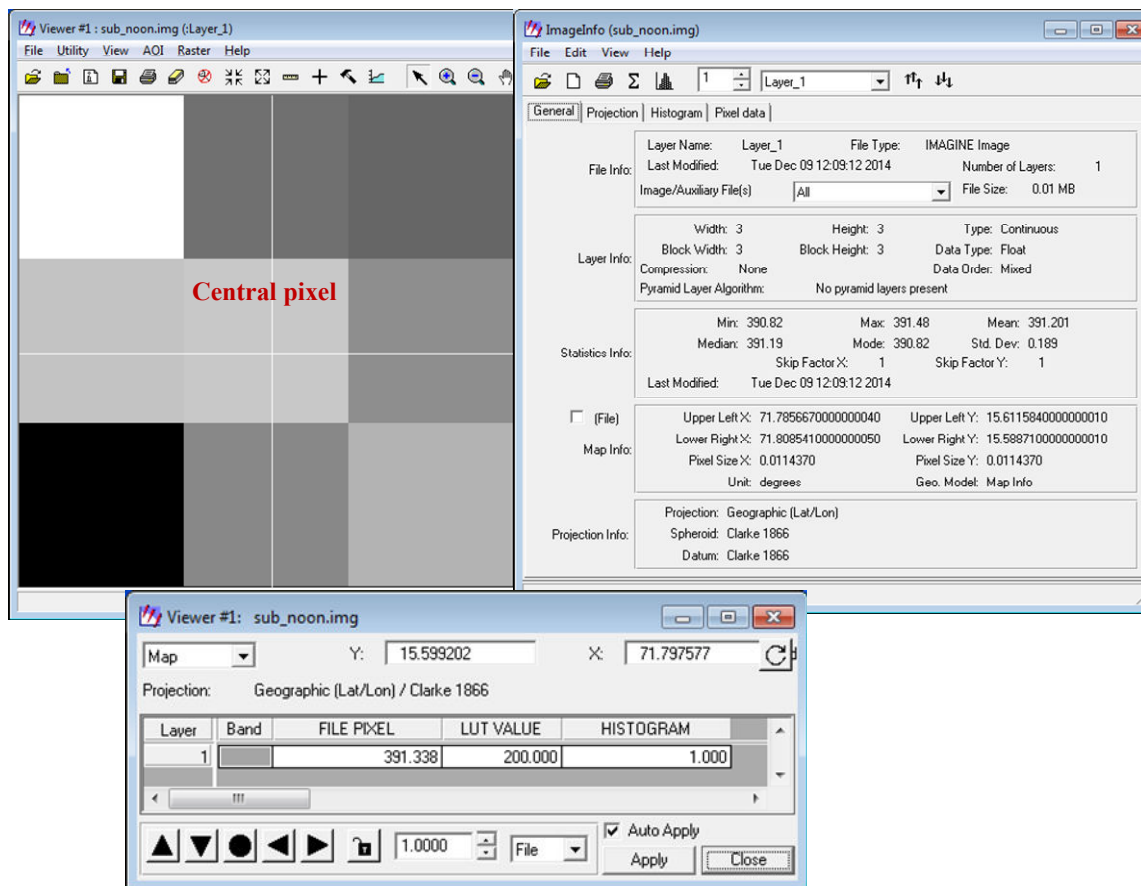


Figure 5.1: 3×3 pixel subset and statistics of OCM PAR image for validations.

5.5 Validation of OCEANSAT-1 OCM estimated PAR with *in-situ* measured PAR

PAR at noon has been estimated from OCEANSAT-1 OCM and compared with PAR estimated from *in-situ* data during ship cruise periods from November 2001 to April 2006 (Table 5.1). The simplest method to compare satellite estimated PAR with *in-situ* PAR to plot scatter diagram or dot diagram. Two perpendicular axes of co-ordinates have been taken. One coordinate is for *in-situ* measured PAR (X axis) and another is for satellite estimated PAR (Y axis). Each pair of values is plotted as a point on graph paper. The whole set of points constitutes a scatter diagram. Figure 5.2 shows the scatter diagram between PAR estimated from OCEANSAT-1 OCM using method I and method II and *in-situ* measured PAR in daily time scale.

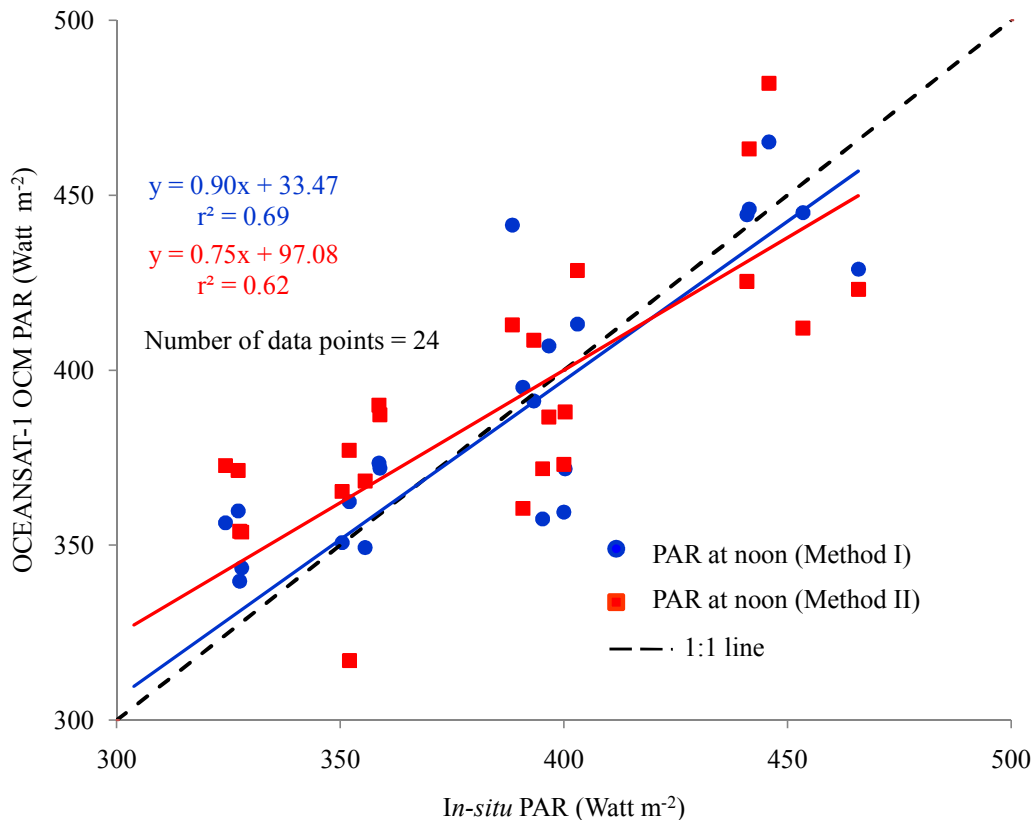


Figure 5.2: Scatter plot of *in-situ* measured PAR at noon versus PAR at noon estimated from OCEANSAT-1 OCM in daily time scale for the two methods.

Chapter 5

A total of 24 *in-situ* PAR measurements coincided with OCEANSAT-1 OCM overpass from the ship campaigns in the Arabian Sea. During the ship cruise periods, most of the observations were under clear sky condition. Only for three days (16 November 2001, 4 January 2003 and 26 April 2006) PAR was measured under cloudy sky condition. OCEANSAT-1 OCM estimated PAR at 1 km resolution was compared with the *in-situ* measured PAR at each hydrographic station during the ship cruise period in the Arabian Sea. Statistical analysis was done between OCEANSAT-1 OCM PAR at noon and *in-situ* measured PAR at noon in daily time scale. The results are listed in Table 5.2.

Table 5.2: OCEANSAT-1 OCM PAR versus *in-situ* measured PAR

	Method I		Method II	
Time scale	Daily		Daily	
Condition of sky	Clear and cloudy sky	Clear sky	Clear and cloudy sky	Clear sky
Correlation coefficient, r^2	0.69	0.72	0.62	0.60
Slope	0.90	0.82	0.75	0.64
Intersect, Watt m ⁻²	+33.47	+72.25	+97.08	+145.5
Bias, Watt m ⁻²	-1.25 (-0.32%)	+5.37 (+1.40)	+4.52 (1.18%)	+10.52 (2.75%)
Root mean square difference, Watt m ⁻²	27.70 (7.26%)	22.27 (5.82%)	29.13 (7.63%)	27.71 (7.24%)
Mean of <i>in situ</i> PAR, Watt m ⁻²	381.39	382.46	381.39	382.46
Number of data points	24	21	24	21

The strength of the linear relationship between *in-situ* and satellite estimated measurements have been studied to estimate correlation coefficient using equation (5.1).

$$r^2 = \frac{[\sum_{i=1}^n (y_i - \bar{y}) \sum_{i=1}^n (x_i - \bar{x})]^2}{\sum_{i=1}^n (y_i - \bar{y})^2 \sum_{i=1}^n (x_i - \bar{x})^2} \dots \dots \dots (5.1)$$

In the equation (5.1) number of data points n were 24 under both the clear and cloudy condition. \bar{x} and \bar{y} were the mean value of *in-situ* and satellite estimated PAR. Another statistical tool bias defines a systematic difference between satellite and *in-situ* estimated PAR. Bias has been calculated using equation (5.2).

$$Bias = \frac{1}{n} \sum_{i=1}^n (y_i - x_i) \dots \dots \dots (5.2)$$

Root mean square difference (R.M.S.D) measures the deviation of satellite estimated data from *in-situ* measured data. Root mean square Difference (R.M.S.D) has been calculated using equation (5.3).

$$R. M. S. D = \sqrt{\frac{\sum_{i=1}^n (y_i - x_i)^2}{n}} \dots \dots \dots (5.3)$$

Statistical Results of Table 5.2 show correlation coefficient between OCEANSAT-1 PAR estimated from method I and *in-situ* data was 0.69 and root mean square difference was 27.70 Watt m⁻² (7.26%) under both clear and cloudy condition. Under clear sky conditions, the correlation coefficient between OCEANSAT-1 PAR estimated from method I and *in-situ* data improved to 0.72 and also R.M.S difference decreased (5.82%). However, correlation coefficient between OCEANSAT-1 OCM PAR estimated from the method II and *in-situ* data was less (~0.6) and also R.M.S difference was high compared to method II. OCEANSAT-1 OCM PAR was slightly positively biased compared to *in-situ* measured PAR for both types of methods under clear sky condition. However, positive bias was more for OCEANSAT-1 OCM PAR estimated from method II compared to method I. Validation of SeaWiFS PAR versus *in-situ* data shows that root mean square difference was 15% in daily time scale (Frouin et al., 2003) under both

Chapter 5

clear and cloudy condition. Results of Table 5.2 shows that the R.M.S difference between OCEANSAT-I OCM estimated PAR from method I and method II and *in-situ* measured PAR were within 8% under both clear and cloudy conditions. However, PAR estimation using method I gave less error compared to method II for OCM sensor. The differences between the two method are in i) selection of continuous fifteen bands in method I and discrete six bands corresponding to OCM in method II, ii) use of integrated extra-terrestrial solar irradiance (Thullier et al., 1998) at each band in method I and use of mean extra-terrestrial solar irradiance corresponding to the six visible spectral band of OCM sensor derived band specific Relative Spectral Response (RSR) function in method II, iii) ocean surface reflectance has been neglected in the method I and ocean surface reflectance has been included in method II and iv) PAR under cloudy condition has been estimated with reflectance of one single spectral OCM band at 443 nm in method I and PAR under cloudy condition has been estimated using reflectance of six spectral OCM bands in the visible region. However, according to Mallet et al. (2009), the influence of sea surface reflectance on PAR is negligible. Thus, selection of band numbers and OCM specific parameters play important role in PAR estimation from remote sensing.

Figure 5.3 shows the daily spatial variation of PAR at noon during different months in the Arabian Sea. Spatial variation of PAR in the Arabian Sea varies with month, latitude and with different types of cloud and area of the cloud coverage. Moreover, patchy distributions of PAR have been observed because of different types of clouds. Arnone et al. (1998) also showed that PAR varies with latitude, season with patchy nature of spatial distribution in the Arabian Sea. PAR at noon was minimum during January and it was maximum during April (Figure 5.3). Average PAR at noon in the Arabian Sea basin (4.5-28°N, 61.5-78°E) was 375.73 W m⁻², 349.69 W m⁻², 415.55 W m⁻² and 446.86 W m⁻² during November 2001, January 2003, March 2003 and April 2006. Arnone et al (1998) showed that two elevated PAR periods were observed at each year in the Arabian Sea. The bimodal PAR distribution showed maximum peaks in May and October and minima in December and July (Arnone et al., 1998).

OCEANSAT OCM PAR spatial distribution and validation

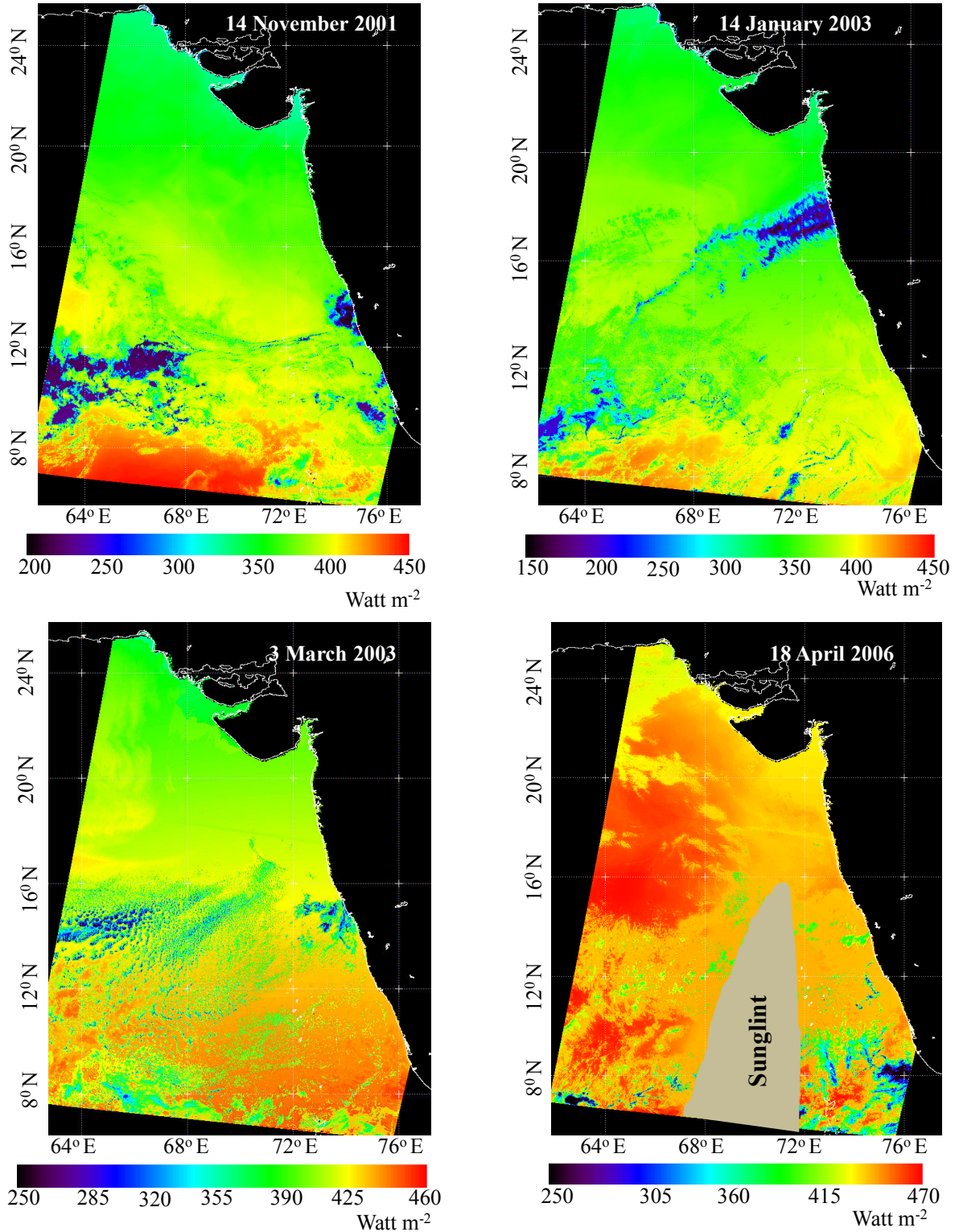


Figure 5.3: Spatial variation of PAR at noon over the Arabian Sea for different dates in different seasons.

However, clouds play an important role with season and latitude to estimate basin average PAR value. For example during 16 November 2001, average basin PAR mean had decreased by ~8% from monthly mean value due to thick cloud coverage. For thin clouds during 3 March 2003, average basin PAR mean had decreased by 1.3% from the monthly mean value of Arabian Sea.

5.6 Validation of OCEANSAT-2 OCM estimated PAR with *in-situ* data

PAR has been estimated from OCEANSAT-2 OCM during February 2011 and March 2011 using method I. OCEANSAT-2 OCM PAR has been compared with PAR measured from the surface reference sensor during March 2011 in the Northern Indian Ocean (Table 5.1) and also at Kavaratti region during February 2011. Figure 5.4 shows the comparisons between *in-situ* measured PAR and OCEANSAT-2 OCM estimated PAR using method I. Statistical results are tabulated in the Table 5.3.

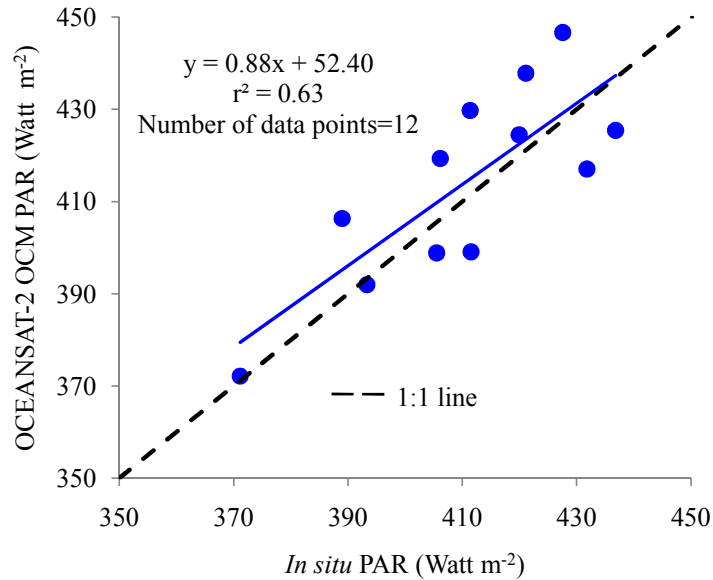


Figure 5.4: Scatter plot of *in-situ* measured PAR at noon versus PAR at noon estimated from OCEANSAT-2 OCM at daily time scale.

Table 5.3: OCEANSAT-2 OCM PAR versus *in-situ* measured PAR

Time scale	Daily
Correlation coefficient, r^2	0.63
Bias, Watt m^{-2}	+ 3.67 (0.88%)
Root mean square difference, Watt m^{-2}	13 (3.13%)
Mean, Watt m^{-2}	414.10
Number of data points	12

The numbers of data points are few for any statistical analysis. However, correlation coefficient between OCEANSAT-2 OCM estimated PAR and *in-situ* PAR is 0.63. In Kavaratti region, clouds are very dynamic. The variability of thin clouds is more in the Kavaratti region compared to the northern Arabian Sea. Moreover, *in-situ* data has been taken at every 1 hour interval time from morning 6:30 am to evening 5:30 p.m at Kavaratti region. The observation at 11:30 and 12:30 discussed in the previous Section 5.2 has taken for validation. However, the equatorial crossing time of OCEANSAT-2 OCM is 12:00 noon \pm 10 minutes. The time lag between satellite overpass time and *in-situ* observation time contribute more error in validation at Kavaratti region particularly where cloud variability is very dynamic.

5.7 Comparison between OCM estimated PAR with other ocean colour satellites

5.7.1 OCEANSAT-1 OCM PAR and SeaWiFS PAR

SeaWiFS (Sea-viewing Wide Field-of-view Sensor) Level-3 binned daily averaged PAR data at 9 km pixel resolution has been obtained from <http://oceancolour.gsfc.nasa.gov/> website. SeaWiFS

Chapter 5

launched on August 1997, has total eight bands similar to OCEANSAT-1 OCM. The methodology for estimating SeaWiFS daily averaged PAR was from Frouin et al. (2003). The unit of daily averaged PAR is Einstein $\text{m}^{-2} \text{day}^{-1}$. SeaWiFS daily PAR was obtained corresponding to the same dates of OCEANSAT-1 OCM during ship cruise periods shown in the Table 5.1. The overpass of OCEANSAT-1 OCM coincided with the overpass of SeaWiFS for the 14 stations during the ship cruise period.

The OCM data has been binned at the same pixel resolution as SeaWiFS spatial resolution (9 km) and at the same map projection for comparison. Daily averaged PAR has been estimated from OCEANSAT-1 OCM in Einstein $\text{m}^{-2} \text{day}^{-1}$ using equation (4.49) discussed in the Section 4.5.5 of Chapter 4 (Page No. 105). Figure 5.5 shows the scatter plot between SeaWiFS daily averaged PAR and OCEANSAT-1 OCM daily averaged PAR using both method I and method II.

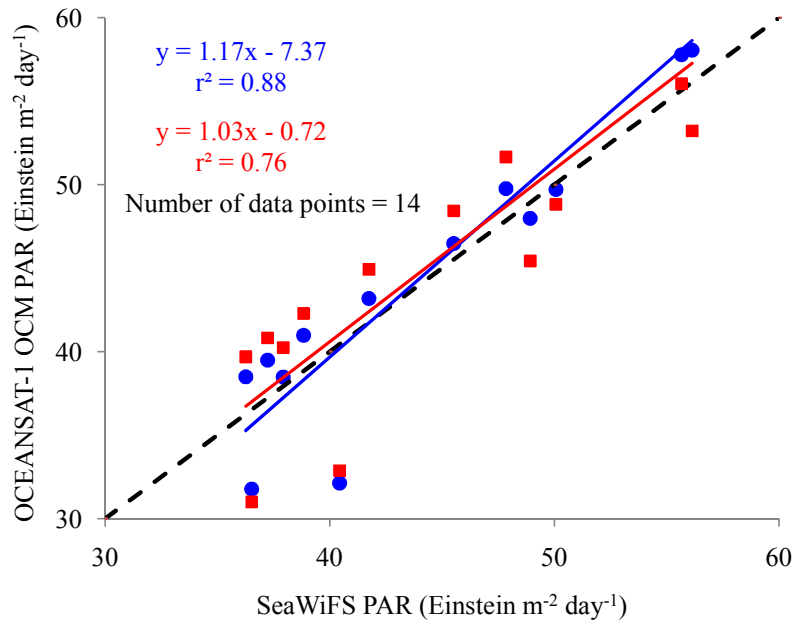


Figure 5.5: Comparison between SeaWiFS daily averaged PAR and OCEASAT-1 OCM daily averaged PAR at daily time scale.

OCEANSAT OCM PAR spatial distribution and validation

Table 5.4 shows the comparative statistics between OCEANSAT-1 OCM PAR estimated from method I and method II with SeaWiFS PAR.

Table 5.4: OCEANSAT-1 OCM daily averaged PAR estimated from method I and method II versus SeaWiFS PAR

	Method I		Method II	
Time scale	Daily		Daily	
Condition of sky	Clear and cloudy sky	Clear sky	Clear and cloudy sky	Clear sky
Correlation coefficient, r^2	0.88	0.95	0.76	0.80
Slope	1.17	1.04	1.03	0.86
Intersect, Einstein $m^{-2} day^{-1}$	-7.37	-0.38	-0.72	+8.07
Bias, Einstein $m^{-2} day^{-1}$	+ 0.51 (+1.15%)	+1.69 (+3.68%)	+0.76 (+1.69%)	+1.97 (+4.30%)
Root mean square difference, Einstein $m^{-2} day^{-1}$	3.37 (7.52%)	2.38 (5.18%)	4.25 (9.49%)	3.72 (8.10%)
Mean of SeaWiFS PAR, Einstein $m^{-2} day^{-1}$	44.86	45.92	44.86	45.92
Number of data points	14	12	14	12

Comparative statistics of Table 5.4 shows that the correlation coefficient between OCEANSAT-1 OCM PAR estimated using method II with SeaWiFS PAR was 0.76 and R.M.S difference was 4.25 Einstein $m^{-2} day^{-1}$ (9.49%) under both the clear and cloudy sky. Under clear sky, the correlation coefficient between OCEANSAT-1 OCM PAR from the method II improved to 0.80. The positive bias was larger (+4.30%) in OCEANSAT-1 OCM PAR estimated using method II compared to SeaWiFS PAR. Although the approach for estimating OCM-PAR (method-II) and SeaWiFS PAR was same, they differed in the estimation of AOD. Climatology of AOD with two different types of aerosol model were used as inputs to estimate SeaWiFS PAR (Frouin et al., 2003). Satellite estimated AOD was used in OCEANSAT-1 OCM PAR for both method I & II. The relatively poor correlation and higher bias may be related to the use of OCM

Chapter 5

band reflectance for estimating cloud albedo since moderate marine aerosol type with 0.3 AOD (500nm) has negligible influence on PAR estimation (Tripathy et al., 2014).

OCEANSAT-1 OCM PAR estimated from the method I had good correlation with SeaWiFS PAR. The correlation coefficient between SeaWiFS PAR and OCEANSAT-1 OCM PAR using method I was 0.88 under both clear and cloudy condition. Under clear sky condition the correlation coefficient was improved from 0.88 to 0.95. The root mean square difference was $2.38 \text{ Einstein m}^{-2} \text{ day}^{-1}$ (5.18%) between OCEANSAT-1 OCM PAR estimated using method I and SeaWiFS PAR. Under clear sky condition, OCEANSAT-1 OCM PAR estimated from method I was positively biased (3.68%) compared to SeaWiFS PAR. SeaWiFS PAR was again 1.3% negatively biased from ISCCP PAR (Frouin et al., 2003).

Figure 5.6 shows comparison between OCEANSAT-1 PAR estimated from both the methods and SeaWiFS PAR dated on 16th November, 2001. Spatial distribution of both SeaWiFS PAR and OCEANSAT-1 OCM PAR estimated using two methods showed an almost parallel distribution of PAR with patchy nature because of clouds (Figure 5.6). Singh et al. (2007) showed the effect of dynamic nature of AOD on OCEANSAT-1 OCM estimated PAR under clear sky condition. As clouds play more dominant role compared to aerosols in the attenuation of PAR, the effect of spatial variation of AOD on PAR was suppressed in the present OCM PAR methods.

Under clear sky condition, OCEANSAT-1 OCM PAR estimated from both the method matched well with SeaWiFS PAR (Figure 5.6a). However, OCEANSAT-1 OCM PAR estimated from method II is overestimated by ~3% compared to method I under clear sky condition (Figure 5.6a). OCEANSAT-1 OCM PAR estimated from both the methods, was comparable with SeaWiFS PAR values for thin clouds, small patches of clouds and at the edge of the thick clouds (Figure 5.6b). At the edge of the clouds, both SeaWiFS and OCEANSAT-1 OCM PAR decreased by 20-23% from the clear sky. For very thin clouds, SeaWiFS and OCEANSAT-1 OCM PAR decreased by 5-10 %.

OCEANSAT-1 OCM PAR spatial distribution and validation

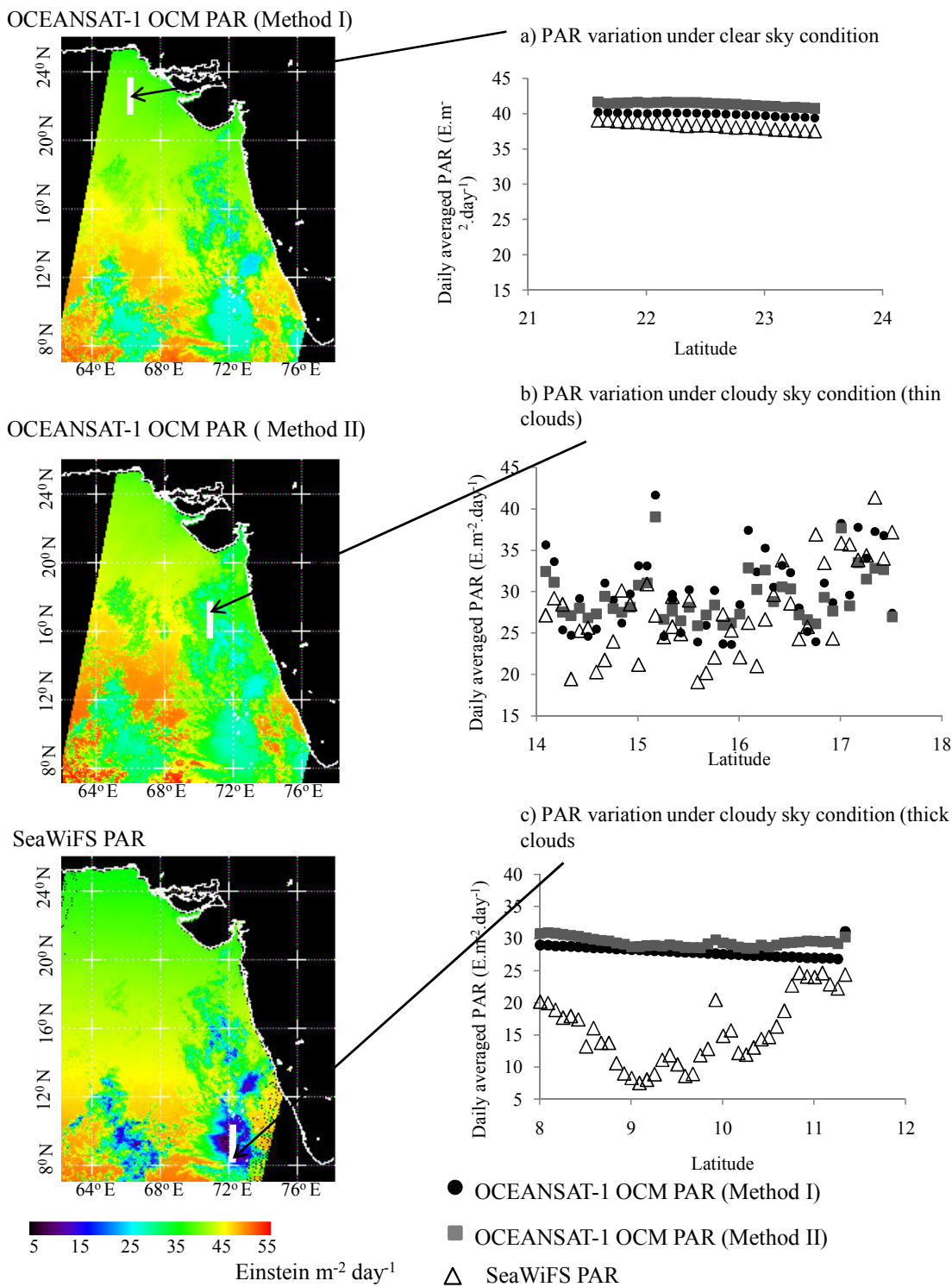


Figure 5.6 : Comparison between daily averaged PAR estimated from OCEANSAT-1 OCM from method I and method II and SeaWiFS under a) clear sky, b) Thin cloud and c) Thick cloud (Date: 16 November 2001).

Chapter 5

However, at the middle of some cloud patches, SeaWiFS PAR was quite lower than OCEANSAT-1 OCM PAR (Figure 5.6c). Under cloudy conditions, minimum value of SeaWiFS PAR was $5.09 \text{ Einstein m}^{-2} \text{ day}^{-1}$. Maximum of $\sim 89\%$ decrease in SeaWiFS PAR was observed at the middle of the cloud. Under cloudy conditions, minimum OCEANSAT-1 OCM PAR was $21.73 \text{ Einstein m}^{-2} \text{ day}^{-1}$ i.e. maximum $\sim 49\%$ decrease was observed in OCEANSAT-1 OCM PAR compare to clear sky.

Sensitivity analysis of the effect of cloud on PAR showed that PAR reduced maximum by $\sim 57\%$ for overcast sky (Tripathy et al. 2014). A study about the variability of PAR on central China during 2005 to 2012 showed that PAR was more affected by cloudiness rather than the seasonal variation and for overcast sky, PAR decreased maximum by 22.3% during summer and 39.7% during winter (Wang et al. 2014).

The differences between OCEANSAT-1 OCM and SeaWiFS PAR estimated under thick clouds could be attributed to the saturation radiance settings for OCM spectral bands. Saturation radiance of OCM was kept low to enhance the signal to noise ratio for water surface. Due to this effect, high reflectance over middle of the thick cloud was not detected in the OCM bands. However due of bilinear gain setting in SeaWiFS sensor, spectral variability of radiance over cloud was maintained in the SeaWiFS sensor.

5.7.2 OCEANSAT-2 OCM PAR and MODIS PAR

MODIS Aqua Level-3 binned daily averaged PAR data at 4 km pixel resolution has been obtained from <http://oceancolour.gsfc.nasa.gov/> website. The methodology for estimating MODIS daily averaged PAR is from Frouin et al. (2003). The MODIS daily PAR was obtained during January 2011 to May 2011. The OCM data has been binned at the same pixel resolution as MODIS Aqua spatial resolution (4 km) and at the same map projection for comparison. The overpass of OCEANSAT-2 OCM coincided with the overpass of MODIS for the 26 observation

OCEANSAT OCM PAR spatial distribution and validation

points at kavaratti location. Figure 5.7 shows the comparison between SeaWiFS daily averaged PAR and OCEANSAT-2 OCM PAR using method 1 and statistical results are tabulated in the Table 5.5.

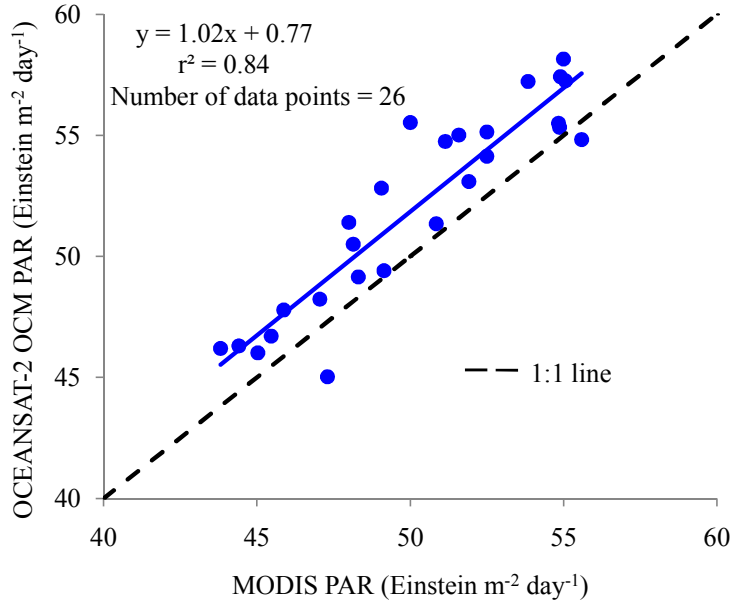


Figure 5.7: Comparison between MODIS daily averaged PAR and OCEASAT-2 OCM daily averaged PAR at daily time scale.

Table 5.5: OCEANSAT-2 OCM daily averaged PAR versus MODIS Aqua PAR

Time scale	Daily
Correlation coefficient, r^2	0.84
Bias, Einstein $m^{-2} day^{-1}$	+ 1.85 (3.55%)
Root mean square difference, Einstein $m^{-2} day^{-1}$	2.43 (4.68%)
Mean, Einstein $m^{-2} day^{-1}$	52.08
Number of data points	26

Chapter 5

Results of Table 5.5 show that there is good correlation between OCEANSAT-2 OCM PAR and MODIS Aqua PAR. The correlation coefficient between OCEANSAT-2 OCM estimated PAR and MODIS PAR is 0.84. OCEANSAT-2 OCM PAR is positively (+3.55%) biased compared to OCEANSAT-2 OCM. The equatorial crossing time of MODIS Aqua is noon 1:30 p. m and equatorial crossing time of OCM is 12:00 noon. Difference in equatorial crossing time in OCM and MODIS also could contribute error in comparison.

5.8 Summary and conclusions

Two PAR products such as PAR at noon and daily averaged PAR have been estimated from OCM using two different methods. PAR at noon has been compared with *in-situ* measured PAR during different ship cruise periods in the Arabian Sea and also with PAR measured at CAL-VAL site at Kavaratti region.

Comparison of PAR estimated from both the methods show good agreement with *in-situ* data and within the accepted range ($\pm 10\%$) for PAR estimation from remote sensing. However, the R.M.S difference in OCEANSAT-1 OCM PAR is less in the first method for both cloudy and clear sky conditions when compared with *in-situ* measured PAR. Comparison with SeaWiFS PAR estimates shows agreement with little bias (+1.15%) for the first method. The bias and R.M.S difference increases for second method when compared with SeaWiFS PAR. The performance of OCEANSAT-1 OCM PAR for thin clouds and at the cloud edges compared well with SeaWiFS PAR for both the methods. However, at the middle of some cloud patches SeaWiFS PAR decreased by $\sim 89\%$ compared to the clear sky, whereas the decrease in OCEANSAT-1 OCM PAR estimated from both the methods was observed to be less ($\sim 49\%$) compared to the clear sky. The probable reason could be attributed to difference in saturation radiance settings in OCEANSAT-1 OCM and SeaWiFS sensor.

OCEANSAT OCM PAR spatial distribution and validation

The correlation coefficient between OCEANSAT-2 OCM estimated PAR using first method and *in-situ* PAR is 0.63 at CAL-VAL site in Kavaratti region. The reason behind weak correlation between OCEANSAT-2 OCM PAR at CALVAL site has been explained by the dynamic variability of clouds in Kavaratti region. OCEANSAT-2 OCM estimated PAR shows good correlation (correlation coefficient 0.84) with MODIS estimated PAR using first method. However, OCEANSAT-2 OCM PAR is positively 3.55% biased compared to MODIS estimated PAR.

Methodology adopted to estimate PAR from OCEANSAT-1 and 2 using first method can produce reasonably accurate PAR estimates over the tropical Indian Ocean region. This approach can be extended to future OCEANSAT-3 OCM data for operational estimation of PAR for regional marine ecosystem applications such as ocean primary production estimation. The modulation of ocean primary production for various aerosol optical depths and cloud coverage has been discussed in the next chapter.

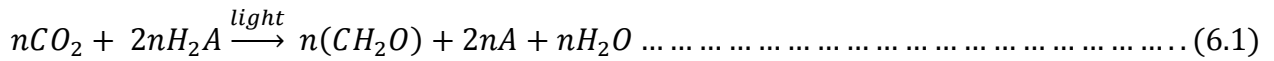
Chapter 6

Role of PAR in primary production estimation in sea water

This chapter gives a brief overview about the modeling of ocean primary production. Different inputs to estimate ocean primary production are chlorophyll-‘a’, diffused attenuation coefficient, euphotic depth, photoadaptation parameter and PAR at sea surface. Measurements of each input from in-situ observations for ocean primary production model have been discussed. A sensitivity study has done to understand the variation of ocean primary production for various PAR values under different atmospheric conditions for different photoadaptation parameters.

6.1 Introduction

Ocean primary production is commonly defined as the photosynthetic rate per unit volume of sea water by ocean phytoplankton. Phytoplanktons are microscopic, free floating plants. Photosynthesis is a process by which phytoplankton convert inorganic matter (carbon dioxide, water, nutrients, light) into organic matter (carbohydrate). Primary production is represented by the following general equation (6.1) (Parsons et al., 1984)



H₂A represents the H-donor to the photosynthetic process. H₂A can be H₂O, H₂, H₂S, H₂S₂O₃ etc. The entire photosynthetic process is not a single reaction. However, it is further broken into three different steps (Parsons et al., 1984) such as

- i) Capturing light energy and transferring the energy into chemical forms.
- ii) Changing the chemical forms into another suitable chemical form ATP (Adenosine Triphosphate) and NADPH (Nicotinamide adenine dinucleotide phosphate) for biochemical reactions.
- iii) Fixing CO₂ using ATP and NADPH generated by the earlier steps.

Photoautotrophs or phytoplankton which include algae and some photosynthetic bacteria require H₂O as the H donor and the above equation can be modified for algal photosynthesis as



Photosynthesis is primarily controlled by nutrients and temperature. To a lesser extent pH and salinity of ocean water also control photosynthesis. Phytoplankton require macro nutrients (C, H, N, Si, P, Mg, K and Ca) and micronutrients (Fe, Mn, Cu, Zn, B, Na, Mo, Cl, V, and Co)

Chapter 6

for their growth (Parsons et al., 1984). Nitrogen and phosphorous are two most important macro nutrients for phytoplankton growth. The uptake of carbon, nitrogen and phosphorous by marine phytoplankton is generally found to be in the ratio of 106:16:1 and this ratio is known as ‘Redfield number’ (Parsons et al., 1984).

Photosynthesis process requires energy of ~ 112 kcal per mole of carbohydrate formed (Parsons et al., 1984). The source of the energy is light in the PAR wavelength range, absorbed by photosynthetic pigments present in the algae (Geider and Osborne, 1991; Sakshaug et al., 1997). Each group of phytoplankton contains chlorophyll-‘a’ and several accessory pigments such as a) chlorophyll-‘b’ for green and euglenoid algae, b) chlorophyll-‘c’ and carotenoids for diatoms, dinoflagellates and brown algae, c) phycobilins for red and blue-green algae (Fujita, 1970). The light absorption patterns are different in each algal group depending on their pigment systems. Light of wavelengths shorter than 600 nm is absorbed mainly by chlorophyll-‘a’ and accessory pigments. Above 600 nm light for photosynthetic process is absorbed only by chlorophyll-‘a’ (Parsons et al., 1984).

Study about the spatial and temporal variability of ocean primary production is very important for several reasons. Ocean primary productivity is one of the important parameters in studying the ocean’s role in global biogeochemical cycle. The carbon fixed during photosynthesis process by marine ecosystem is $\sim 48\%$ (Field et al., 1998). Primary production is the base of food chain (Sigman et al., 2012). Therefore it is important parameter to describe ocean ecosystem and fishery resources assessment. Next section discusses different methods to estimate ocean primary production.

6.2 Different methods for estimating primary production

In-situ estimation of ocean primary production can be categorized broadly into two groups. The groups are *in vitro* methods and bulk property methods. ^{14}C (Steemann Nielsen, 1952; Eppley,

Role of PAR in primary production estimation in sea water

1980), ^{13}C assimilation (Slawyk et al., 1977), $^{18}\text{O}_2$ evolution (Williams and Robertson 1991), $^{15}\text{NO}_3$ assimilation (Dugdale and Goering, 1967), $^{15}\text{NH}_4$ assimilation (Dugdale and Goering, 1967) are *in vitro* methods used for primary production measurements. In these methods, measurements are made on samples enclosed in glass or other containers. Primary production is measured by uptake of isotopic tracers or occasionally by changes in the chemical composition of the medium. The size of the containers for sample ranges from a few milliliters to a few liters and the incubation time ranges from less than one to few hours.

Bulk property methods are NO_3 flux to photic zone, O_2 utilisation rate below photic zone (Quay et al., 1995), $^{238}\text{Uranium} / ^{234}\text{Thorium}$ method (Bhat et al., 1969), net O_2 accumulation in the photic zone etc. These methods are based on the changes in chemical composition of the free medium induced by the activity of the organism in a certain time. The concentration ratios of initial and final isotopes are used to establish the time scales over which the chemical changes have occurred. The characteristic time scale for these methods is from one day to several years.

Apart from *in-situ* measurements, ocean primary production can be estimated also from remote sensing observations using suitable bio-optical models. The key biological components of bio-optical models of primary production are biomass, sunlight and response of photosynthesis to solar irradiance (Platt and Sathyendranath, 1993; Antoine and Morel, 1996). Various bio-optical models are developed to estimate ocean primary production from remote sensing with the advancement of operational ocean-colour sensors (Platt and Sathyendranath, 1988b; Sathyendranath and Platt, 1989; Morel, 1991; Behrenfield and Falkowski, 1997b).

6.3 Modeling column primary production

Modeling primary production P at any particular location, depth z and time t involves product of biomass $B(z, t)$ and a function, which describes the photosynthetic response of phytoplankton to the available radiation. The primary cause of variation in rates of primary production is the

Chapter 6

variation of biomass. Therefore, for given information of irradiance I, it is important to account for the effects of variations in biomass (Banse and Yong, 1990). Thus normalised primary production (primary production normalized to biomass) P^B is more acceptable compare to absolute value for modeling primary production. Normalized primary production is stable against local variability of the biomass at any region and season (Platt and Sathyendranath, 1993). Thus, normalized primary production is expressed as

$$P^B = \frac{P}{B} \dots \dots \dots (6.3)$$

To estimate absolute primary production P equation (6.3) is inverted.

$$P = B \times P^B \dots \dots \dots (6.4)$$

The pigment biomass varies with depth and equation (6.4) can be written as

$$P(z) = B(z) \times P^B(z) \dots \dots \dots (6.5)$$

The normalized primary production is a function of available irradiance and irradiance is also function of depth (Jerlov, 1976; Kirk, 1983). Thus, normalized primary production is formally stated as

$$P^B(z) = p^B(I(z)) \dots \dots \dots (6.6)$$

Irradiance at surface I_0 varies with depth according to Lambert Beer's law. I (z) is a function of surface irradiance I_0 .

$$I(z) = I_0 e^{-kz} \dots \dots \dots (6.7)$$

Role of PAR in primary production estimation in sea water

k is diffusion attenuation coefficient. k defines the propagation of spectral downwelling irradiance from the surface to the interior of the ocean and controls the availability of light within the water column for photosynthesis and other biological processes (Platt et al., 1988a; Marra et al., 1995). Given the surface irradiance field, the flux at any depth in the ocean can be computed by knowing the diffuse attenuation coefficient (Sathyendranath and Platt, 1988). Diffusion attenuation coefficient is an apparent optical property and therefore varies with solar zenith angle, sky and surface conditions. From equation (6.5) and (6.6)

$$P(z) = B(z) \times p^B(I(z)) \dots \dots \dots (6.8)$$

I (z) in the above equation is a time dependent variable. Therefore, the above equation can be rewritten as

$$P(z, t) = B(z, t) \times p^B(I(z, t)) \dots \dots \dots (6.9)$$

Equation (6.9) computes primary production at different discrete depths. For estimation of water column primary production equation (6.9) is integrated over depth. Thus, water column production P_z can be computed as

$$P_z = \int P(z, t) dz = \int_0^\infty B(z, t) \times p^B(I(z, t)) dz \dots \dots \dots (6.10)$$

Irradiance decays with seawater depth exponentially. That is why; the upper limit of integration is set to infinity as contributions to the integral at this limit will be insignificantly small (Platt and Sathyendranath, 1993). To estimate water column production for the day, equation (6.10) is integrated over the day. Thus,

$$P_{z,T} = \int_0^\infty \int_0^D B(z, t) \times p^B(I(z, t)) dz dt \dots \dots \dots (6.11)$$

Chapter 6

D is the day length in hour. It is assumed that the changes in biomass are sufficiently slow and the variation of biomass with time is insignificant. Equation (6.11) is the basic equation to estimate water column primary production. Generally, water column production is estimated as euphotic primary production. Euphotic depth is defined as the depth at which irradiance is decayed 1% from the surface irradiance. Then the basic equation of daily rate of euphotic zone production $P_{Z_{eu}}$, is given as (Platt and Sathyendranath, 1993).

$$P_{Z_{eu},T} = \int_0^D \int_0^{Z_{eu}} B(z,t) p^B(I(z,t)) dz dt \dots \dots \dots (6.12)$$

Platt and Sathyendranath (1993) have shown that under certain assumptions, a fifth order polynomial provides an approximation to the analytical solution for daily rate of water column primary production as a function of surface irradiance at local noon. This is given as

$$P_{Z_{eu},T} = \left(\frac{B P_m^B D}{k_{par}} \right) \times \left[\sum_{x=1}^5 \Omega_x \left(\frac{I_* \exp^{-k_{par} z_{sur}} \alpha^B}{P_m^B} \right)^x - \Omega_x \left(\frac{I_* \exp^{-k_{par} z_{eu}} \alpha^B}{P_m^B} \right)^x \right] \dots \dots \dots (6.13)$$

Where B is chlorophyll-‘a’ concentration, k_{par} is vertical diffusion attenuation coefficient for euphotic depth (Z_{eu}), I_0^m is surface Irradiance at noon and α^B , P_m^B are photo physiological parameter. Dimensionless irradiance = I_*^m is given as I_0^m / I_k and I_k is calculated as ratio of P_m and α . I_k was termed as photoadaptation parameter, Ω is weights for fifth –order polynomial fit for $x=5$. Weights have been obtained from Platt and Sathyendranath (1993) for the range of $0.2 \leq I_*^m \leq 20$. D is day length (D) in hours and D has been calculated using Brock (1981) model.

6.4 Description of inputs for ocean primary production estimation

There were several ship campaigns for sea-truth data collections by Space Applications Centre as a part of validation programme of OCEANSAT-1 & 2 OCM. Different parameters such as optical parameters (radiance/irradiance profile, PAR), biological parameters and atmospheric parameters

Role of PAR in primary production estimation in sea water

(aerosol optical depth) were measured during the ship campaigns in different seasons in the Arabian Sea. Different input parameters measured during 3–17 November 2001, 4–19 January 2003 and 7–19 March 2011 have been used to estimate euphotic primary production using equation (6.13). Total 37 hydrographic stations were sampled during the entire study period. During winter monsoon season (December–March), phytoplankton blooms are observed in the entire northern Arabian Sea, covering coastal shelf regions and open ocean adjacent to Oman and Gujarat coast (Kumar and Prasad, 1996). However, typical oligotrophic conditions prevail during April and November in the northern Arabian Sea, characteristic of inter monsoon phase. That is why, these periods are important to understand the maximum and minimum variation of euphotic primary production. Location of data points have been discussed in the Section 3.2.2.1 of Chapter 3 (Page No. 53).

6.4.1 Chlorophyll-‘a’

Figure 6.1 shows the variation of chlorophyll-‘a’ during ship cruise periods.

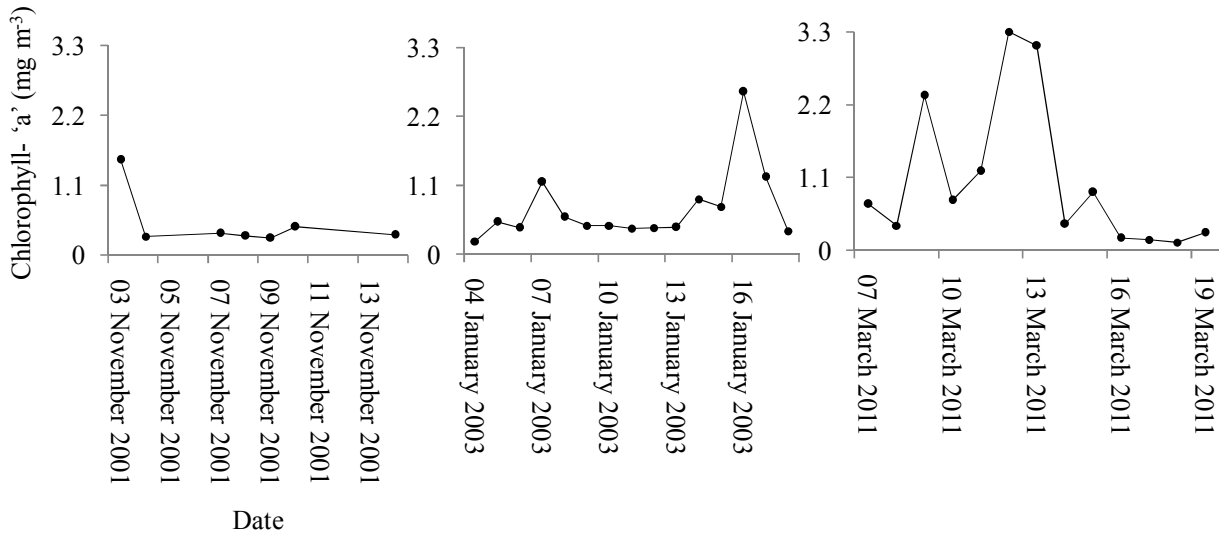


Figure 6.1: Variation of chlorophyll-‘a’ during 3–17 November 2001, 4–19 January 2003 and 7–19 March 2011.

Chapter 6

Water samples collected during ship cruises were analyzed following ocean optics protocols for field measurements of chlorophyll-‘a’ concentration by fluometer. The basic principle of the estimation of chlorophyll-‘a’ from the sample collected during ship cruise period is that water samples were filtered and filtered samples were excited by broadband blue light and resulting fluorescence in the red was detected by a photomultiplier. The variation of chlorophyll-‘a’ was from 0.22 to 1.5 mg m⁻³ during November 2001, 0.17–2.6 mg m⁻³ during January 2003, and 0.12–3.3 mg m⁻³ during March 2011 (Figure 6.1). The mean value chlorophyll-‘a’ was 0.54 mg m⁻³, 0.69 mg m⁻³, 1.06 mg m⁻³ during November 2001, January 2003 and March 2011 respectively. The mean value of chlorophyll-‘a’ was higher in March month compared to other months.

6.4.2 PAR at sea surface

PAR at sea surface and variations of PAR with depth in the water column have been measured using Satlantic radiometer. An underwater (Satlantic Inc.) radiometer having seven bands centered on 412 nm, 443 nm, 490 nm, 510 nm, 555 nm, 670 nm and 780 nm was used during ship cruises of 2001 and 2003. That radiometer had SMSR (SeaWiFS Multi channel Surface Reference) sensor and SPMR (SeaWiFS Profiling Multi channel Radiometer) sensor. Another underwater (Satlantic Inc.) radiometer having 1.2 nm resolution was used in 2011. It had also E_s and E_d sensor.

SMSR sensor and E_s sensor radiometer have been used to measure surface PAR. Estimation and variation of surface PAR has been discussed in the Section 3.3 of chapter 3 (Page No. 58). Another sensor SPSR and E_d was lowered in the ocean in free fall mode to measure downwelling irradiance at discrete depth of the ocean. Estimation and variation of PAR with depth has been discussed in the next section.

6.4.3 Variation of PAR with depth within the water column

Downwelling irradiance at each depth of the ocean during cruise period was obtained from E_d and SPMR sensor of Satlantic radiometer when it was operated in free fall mode. PAR variability at each depth of each station has been estimated using

$$PAR = \int_{400 \text{ nm}}^{700 \text{ nm}} \frac{\lambda}{hc} E_d(\lambda) d\lambda \quad \dots \dots \dots (6.14)$$

E_d is downwelling irradiance in micro $W \text{ cm}^{-2} \text{ nm}^{-1}$ at each depth in the ocean column. λ is wavelength, h is Plank's constant and c is the velocity of light in vacuum. Figure 6.2 shows depth wise variability of PAR.

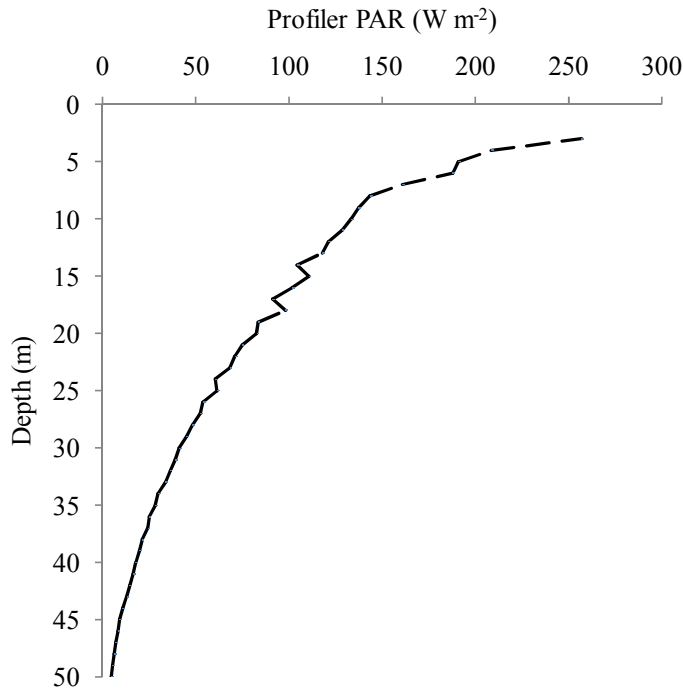


Figure 6.2: Variability of PAR with depth.

The data about the PAR variation with depth has been used to estimate euphotic depth and vertical diffusion coefficient, which are other input parameters to estimate euphotic primary production.

6.4.4 Euphotic depth

Euphotic depth was taken as the depth of 1% decrease from the sea surface PAR at each station during ship cruise period. Figure 6.3 shows the variability of euphotic depth during ship cruise period. The variation of euphotic depth was from 33-64 m during November 2001, 21– 66 m during January 2003, and 17–67 m during March 2011.

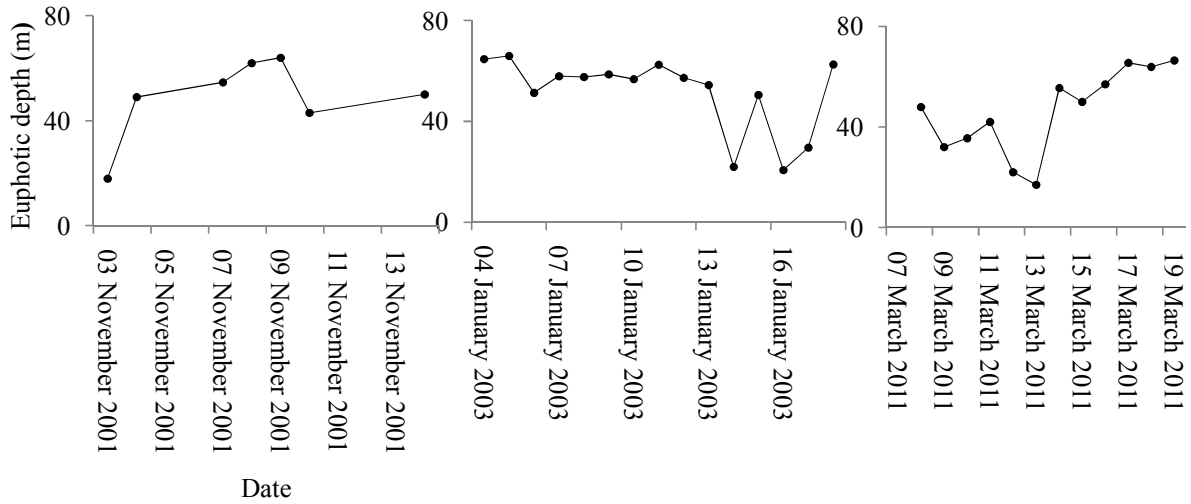


Figure 6.3: Variability of euphotic depth during 3–17 November 2001, 4–19 January 2003 and 7–19 March 2011 over the Arabian Sea.

6.4.5 Vertical diffusion attenuation coefficient

Water column attenuation upto euphotic depth k_{par} was calculated following Lambert Beer's relationship $I_{zeu}=I_{sur} \exp(-k_{par}\times Z_{eu})$. Estimation of euphotic depth (Z_{eu}) was discussed in the previous Section 6.4.4. I_{zeu} and I_{sur} was PAR at euphotic depth and at surface. The values of I_{zeu} and I_{sur} were obtained from E_d and SPMR sensor of Satlantic radiometer operated in free fall mode during cruise periods. The variation of k_{par} is shown in the Figure 6.4.

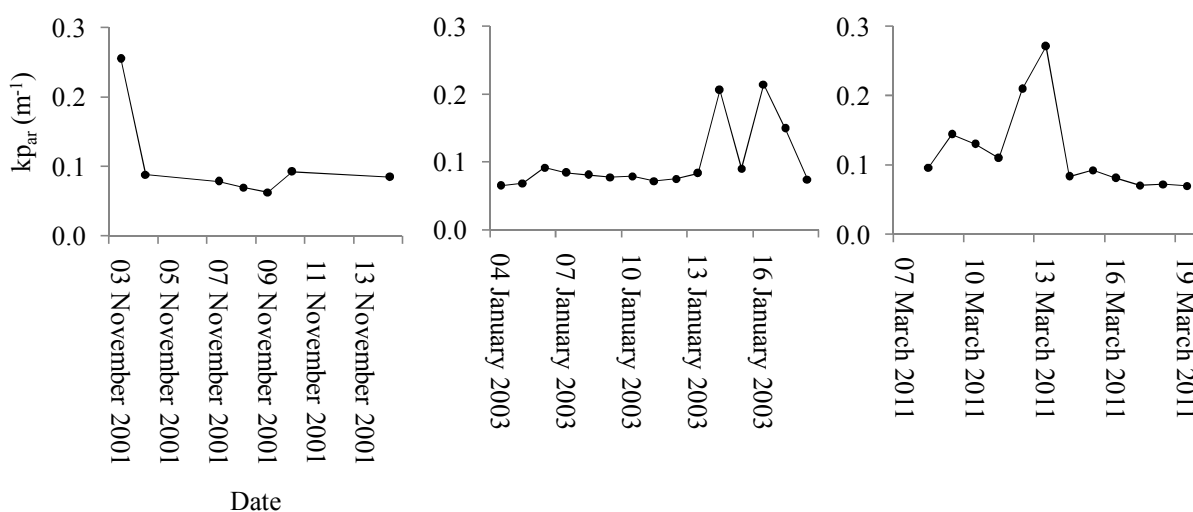


Figure 6.4: Variability of vertical diffusion attenuation (k_{par}) coefficient during 3–17 November 2001, 4–19 January 2003 and 7–19 March 2011 over the Arabian Sea.

k_{par} ranged from 0.06 to 0.25 m^{-1} during November 2001, 0.07–0.21 m^{-1} during January 2003, and 0.07–0.27 m^{-1} during March 2011.

6.4.6 Physiological parameter

Photosynthesis is a photochemical process and the response of phytoplankton to available light is studied with photosynthesis-light (PI) curve. The relationship between light and photosynthesis is

called the light saturation curve or PI curve (Kirk, 1994). PI curve indicates different environmental effects such as nutrients and temperature on photosynthesis (Cullen et al., 1992). PI curve also is used to detect community structure of algal species (Bouman et al., 2005). Figure 6.5 shows the ideal variation of photosynthetic rate as a function of irradiance.

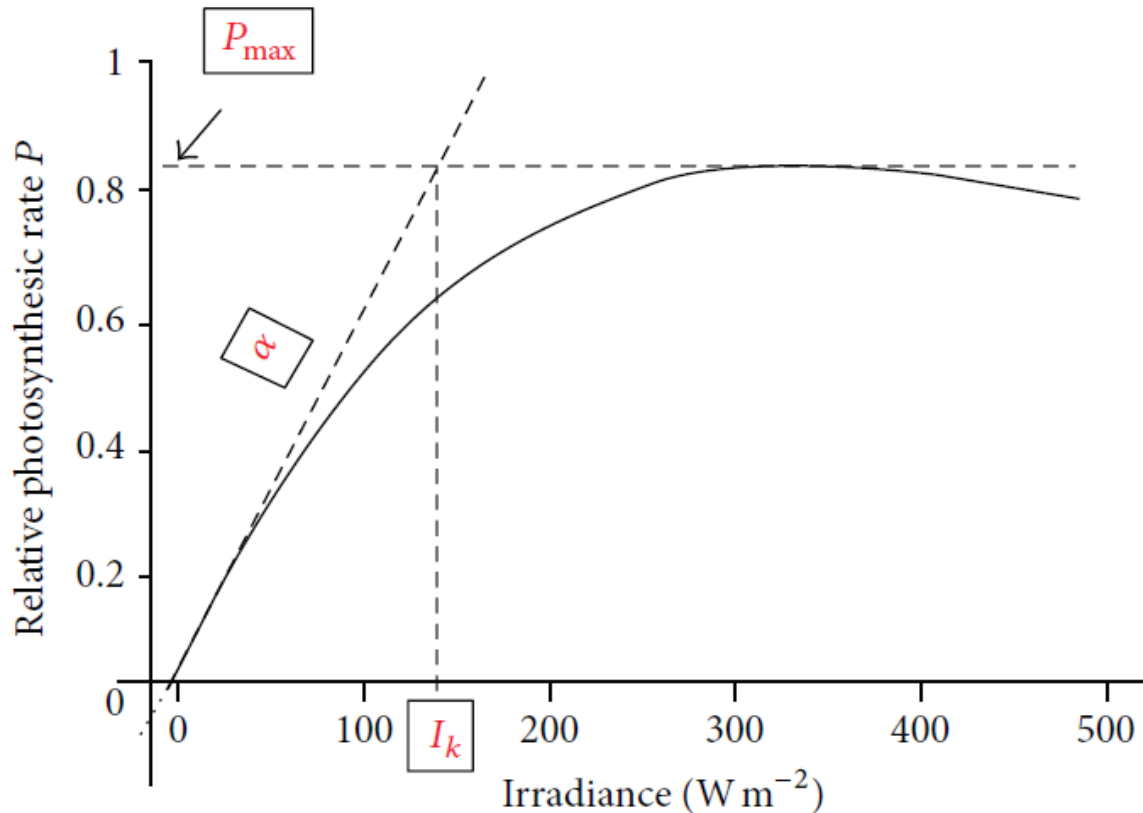


Figure 6.5: Idealized curve of photosynthetic rate as a function of irradiance (Raman et al., 2011, Tripathy et al., 2014).

It can be seen from the Figure 6.5 that rate of photosynthesis increases with increasing light intensity up to some asymptotic value where the photosynthetic process becomes light saturated. The parameters that describes PI curve are known as PI parameters. PI parameters are used as input parameters to estimate water column primary production over larger time and space scales (Platt and Sathyendranath 1988b; Longhurst et al., 1995).

6.4.6.1 Descriptions of PI parameters

- ❖ In the PI curve the point where the curve cuts the abscissa is the compensation point. It is defined as the irradiance for which the photosynthesis just balances the dark respiration.
- ❖ The PI curve is quasi-linear close to the abscissa with a slope ($\Delta P/\Delta I$) known as initial slope (α^B).
- ❖ At higher irradiances, the slope of the curve decreases progressively until the curve reaches a maximum value P_{max}^B or P_m^B . P_{max}^B is called the assimilation number or biomass specific primary production at saturating irradiance (Platt et. al., 1980).
- ❖ In nature, much of the variability of the PI curve can be characterized through changes in α^B and P_{max}^B . These two parameters are slowly-varying properties that can be obtained only from *in-situ* observation (Raman et al., 2011).
- ❖ The photo-adaptation parameter is the projection of the intersection of the initial slope with the plateau onto the abscissa or in other words the ratio of P_m^B to α^B . It is designated as I_k . It has the same dimensions of irradiance and it is therefore used as a scale to normalise the irradiance and it is dimensionless. i.e.

$$I_* = \frac{I}{I_K} \dots \dots \dots (6.15)$$

- ❖ The curves are divided into two regimes around the value of I_* equals 1, (corresponding to $I = I_k$). For I_* less than or equal to 1, photosynthesis depends strongly on irradiance. For I_* greater than 1, photosynthesis depends less strongly on irradiance, eventually becoming independent of it.

Chapter 6

- ❖ Sometimes, the curve after reaching the maximum amplitude may drop down at higher irradiances as in the case of tropical seas during peak summer season. This is due to photoinhibition, where photosynthesis decreases as irradiance increases. This may be characterised by another parameter β^B (Platt and Sathyendranath, 1993). However, in general and for most cases, the curve can be characterised by two parameters α and P_m assuming that the curve passes through the origin and can be written as

$$P(I) = p^B(I; \alpha^B, P_m^B) \dots \dots \dots (6.16)$$

- ❖ In other words photosynthesis light curve is a function of one variable, irradiance and two parameters. This function P^B defines a family of curves, the individual members are identified by the value or magnitude of parameters α^B and P_m^B . Since α^B and P_m^B vary for different areas and seasons, it is necessary to know the local magnitude of α^B and P_m^B to compute primary production.
- ❖ Slope of the P versus I curve is also spectral in nature, a consequence mainly of the spectral absorption of light by phytoplankton. Because the spectral composition of the submarine light field changes with depth, depth-dependent changes in α^B can be expected (Sathyendranath and Platt., 1989). As a result, photosynthesis models may be based on spectral or non-spectral formulations. In spectral models, the spectral effects of light transmission and spectral dependence of α are taken into consideration. In non-spectral models the spectral dependencies in α are ignored.

6.4.6.2 Measurements of PI parameters

A more convenient laboratory based procedure is to measure photosynthesis in combination with a photosynthetron. Different components of photosynthetron are shown in Figure 6.6.

Role of PAR in primary production estimation in sea water

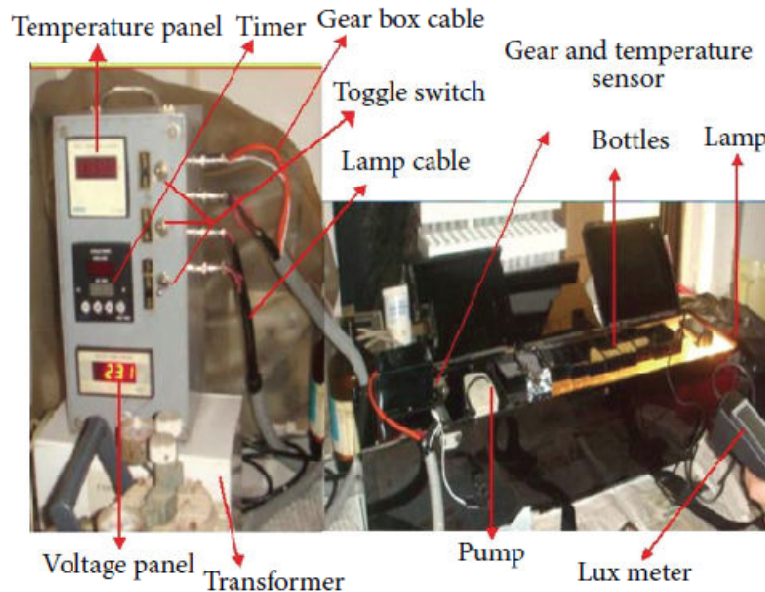


Figure 6.6: Components of photosynthetron instrument to measure photosynthesis.

This photosynthetron was designed and fabricated at Space Applications Centre, Ahmedabad. Phytoplankton samples were incubated with $[^{14}\text{C}]\text{-HCO}_3^-$ for a period of three hours at the same temperature of the water body and a series of irradiance value designed to correspond to different depths in the euphotic zone was provided from an artificial source (250W quartz halogen lamp). The water tight incubation chamber was made with flat acrylic material and was designed to contain a stack of thirteen 300 mL flat rectangular bottles. Bottles were attached to a gearbox unit with a motor to move the rack. A submersible pump was used at the other end of the chamber to circulate water inside the chamber and flow around the rack of bottles. This arrangement kept the algal cells inside the bottle well mixed and prevented their settlement at the bottom of the bottle. Production was computed according to equations in JGOFS protocols reference and normalized to chlorophyll concentration. The chlorophyll specific α^B and P^B_m were derived by fitting to the experimental data points and hyperbolic tangent function as given in Jassby and Platt (1976).

6.5 Ocean primary production during ship cruise periods

Euphotic depth primary production has been estimated using equation (6.13). Input parameters such as chlorophyll-‘a’, k_{par} , euphotic depth, α^{B} and P^{B}_{m} and PAR at sea surface have been estimated from *in-situ* based observation discussed in the above section. Figure 6.7 shows the variation of euphotic primary production during cruise period in the Arabian Sea.

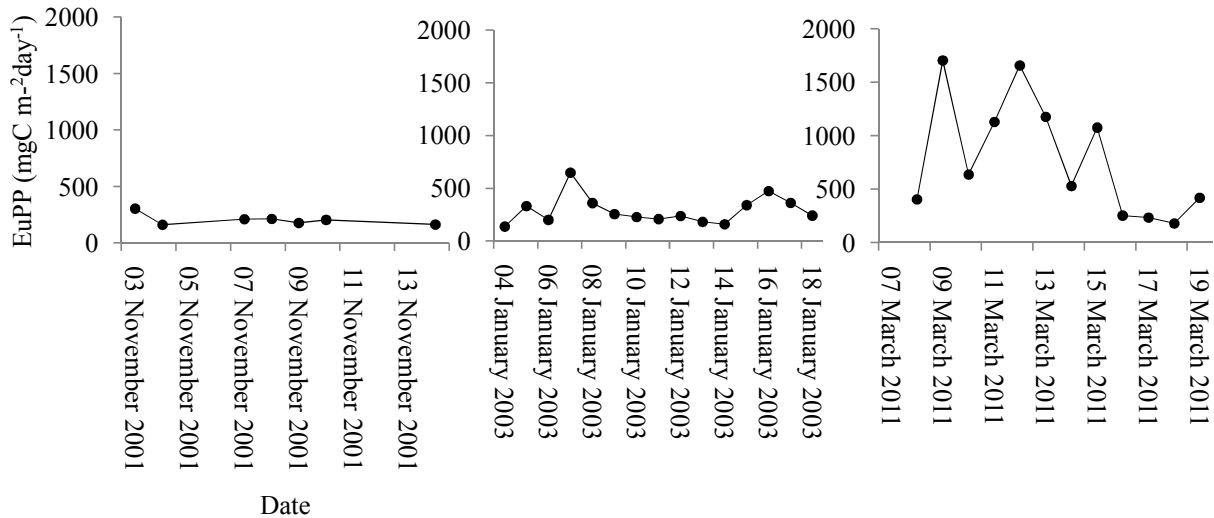


Figure 6.7: Variability of euphotic primary production during 3–17 November 2001, 4–19 January 2003 and 7–19 March 2011 over the Arabian Sea.

Euphotic primary production was varying from 160 to 305 mg m⁻² day⁻¹ during November 2001, 135–650 mg m⁻² day⁻¹ during January 2003, and 180–1705 mg m⁻² day⁻¹ during March 2011.

6.6 Role of PAR in primary production estimation in sea water

During the ship cruise period, the variation of estimated euphotic primary production with PAR and AOD is shown in the Figure 6.8 a) and Figure 6.8 b). Figure 6.8 c) shows the variation of normalized euphotic primary production $\int \text{PP}/(\text{BP}mD/k_{\text{par}})$ (primary production per unit biomass,

Role of PAR in primary production estimation in sea water

unit photosynthetic rate, unit hour, and unit vertical diffusion attenuation coefficient) with *in-situ* measured PAR in the Arabian Sea.

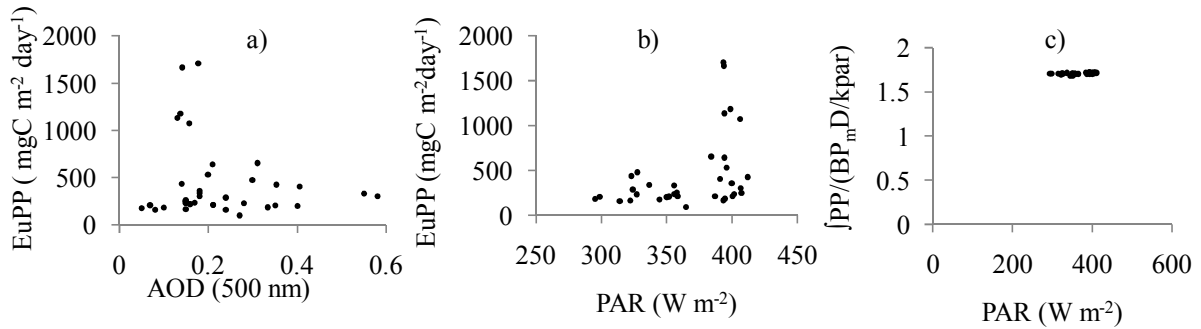


Figure 6.8: a) Variation of euphotic primary production with AOD, b) variation of euphotic primary production with PAR, c) variation of normalized primary production with PAR during ship cruise periods over the Arabian Sea.

From the Figure 6.8 c) it is evident that normalized euphotic primary production plotted against PAR had been found to occur in a region where photosynthesis was maximum and independent of irradiance according to Figure 6.5. *In-situ* data was measured under clear sky condition and also not under very high aerosol optical depth. To understand the effect of PAR under high aerosol optical depth and under cloudy sky in primary production estimation, a simulation study has been done. For that purpose firstly a range of PAR values have been obtained when AOD has been varied from 0 to 1 through COART model and for different cloud coverage, simulated PAR has been obtained using nonlinear relationship with cloud coverage discussed in the Section 3.6.2 of Chapter 3 (Page No. 68). Finally, a study has been carried out to estimate euphotic primary production using equation (6.13) with measured value of chlorophyll-‘a’, attenuation diffusion coefficient, euphotic depth, PI parameter and variable value of simulated PAR. The role of dust aerosol in primary production is in two different ways. The addition of micronutrient iron from mineral dust to sea water can influence ocean productivity (Bonnet and Guieu 2004; Cropp et al., 2005). On the other hand, aerosols that remain in the atmosphere and are not deposited in the sea water can reduce the solar energy at the sea surface and can influence ocean primary production

(Mallet et al., 2009; Chami et al., 2012). In the present study the second effect of reduction of PAR under various aerosol optical depth and cloud coverage have been studied. The following sections describe results for the modulation of PAR and ocean primary production under different aerosol and cloud coverage conditions for different PI parameter.

6.6.1 Sensitivity analysis: AOD on euphotic primary production (EuPP) for different types of aerosol

Figure 6.9 shows the variation of euphotic primary productin with AOD (500 nm). Clear sky is defined as when PAR is estimated at zero AOD and unde cloud free condition.

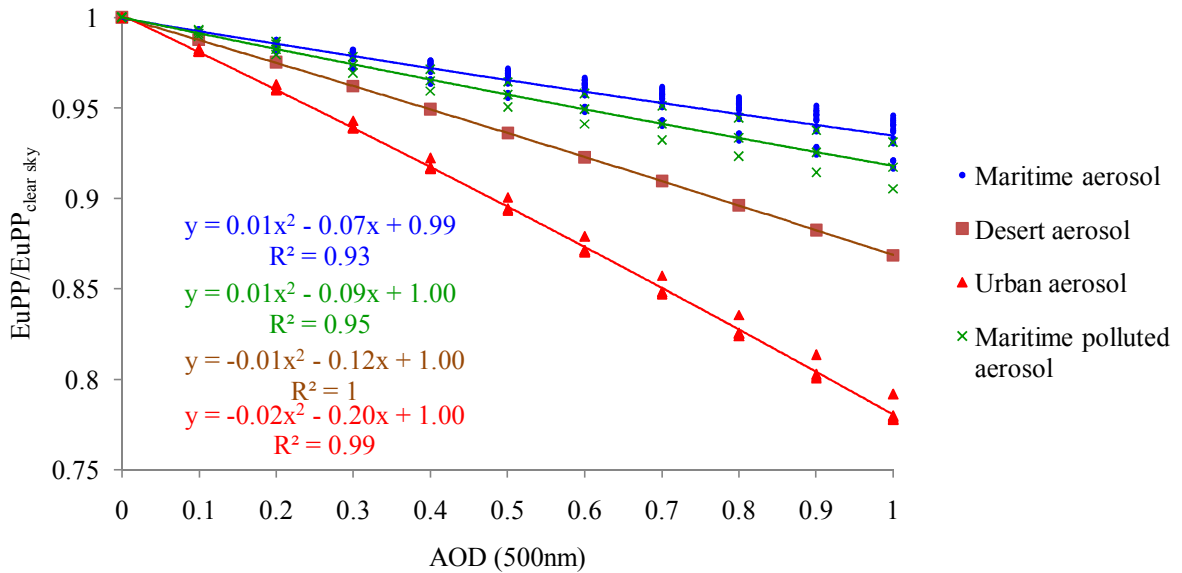


Figure 6.9: Variation of euphotic primary production with AOD for different aerosol types.

Using the analytical model as described in equation (6.13), it has been observed that euphotic primary production decreased (Figure 6.9) as aerosol loading increased during different months of the year. The photosynthetic response to available light is not linear (Platt and Sathyendranath, 1993). A second-order polynomial has been fitted with the variation of ratio

Role of PAR in primary production estimation in sea water

$\text{EuPP}/\text{EuPP}_{\text{clear sky}}$ and equations of the relationship between $\text{EuPP}/\text{EuPP}_{\text{clear sky}}$ and AOD for different types of aerosol are given in Figure 6.9. The decrease of $\text{EuPP}/\text{EuPP}_{\text{clear sky}}$ for different type of aerosol during ship cruise period for maximum aerosol loading and moderate aerosol is tabulated in Table 6.1.

Table 6.1: Decrease of euphotic primary production (%) for maximum and moderate aerosol loading compared to no aerosol loading for different aerosol types compared to clear sky.

Type of aerosol	Decrease of ($\text{EuPP}/\text{EuPP}_{\text{clear sky}}$) in percentage for maximum aerosol loading(AOD=1) compared to no aerosol loading			Decrease of ($\text{EuPP}/\text{EuPP}_{\text{clear sky}}$) in percentage for moderate aerosol loading(AOD=0.3) compared to no aerosol loading		
	November 2001	January 2003	March 2011	November 2001	January 2003	March 2011
Maritime aerosol	5.68 to 6.64	6.94 to 8.35	5.44 to 6.33	1.84 to 2.17	2.29 to 2.83	1.80 to 2.11
Maritime polluted aerosol	8.26	9.45	6.44 to 6.90	2.63	3.08	2.01 to 2.17
Urban aerosol	20.81 to 22.24	26.04		5.68 to 6.13	7.33	
Desert aerosol	13.12			3.77		

For maximum maritime types of aerosol loading, the decrease of $\text{EuPP}/\text{EuPP}_{\text{clear sky}}$ was from 5 to 10% during ship cruise periods (Tripathy et al., 2014). The decrease was from 13-26% for maximum urban and desert types of aerosol loading (Tripathy et al., 2014). Ocean primary production decreased by ~35% (Chami et al., 2012) in the case of intense dust aerosol (AOD > 0.6) in the Atlantic Ocean. The variation of $\text{EuPP}/\text{EuPP}_{\text{clear sky}}$ with AOD in the Arabian Sea is

different from the variation of primary production in the West African Coast (Mallet et al., 2009) for same aerosol optical depth. Nature of variations of euphotic primary production with AOD in the Arabian Sea can be different for same aerosol optical depth as the PI parameters are different in those Oceans. For moderate aerosol loading, $\text{EuPP} / \text{EuPP}_{\text{clear sky}}$ was decreased from 3–7% for urban and desert type of aerosol loading (Tripathy et al., 2014). The decrease was negligible (1–3%) for moderate maritime type of aerosol (Tripathy et al., 2014). Weak effects of dust on ocean primary production were also observed in the Atlantic Ocean when dust optical depth was lower than 0.2–0.3 (Mallet et al., 2009). The variation of ocean primary production for different value of photoadaptation is discussed in the next Section 6.6.2.

6.6.2 Sensitivity analysis: Photoadaptation parameter and euphotic primary production

A sensitivity study has been also carried out to understand how euphotic primary production varies with increase of aerosol optical depth for different photoadaptation parameters. Photoadaptation parameter I_k is defined as the ratio between maximum photosynthesis P_m^B to initial slope α^B of PI curve (Figure 6.5). During the ship cruise period, photoadaptation parameter was varied from 52-265 W m^{-2} . Euphotic primary production was estimated on November 03, 2001 with photoadaptation parameter 71.53 W m^{-2} . For maximum maritime aerosol loading, the decrease in euphotic primary production was 5.68% for the photoadaptation parameter 71.53 W m^{-2} . Figure 6.10 shows decrease (%) in euphotic primary production with increase aerosol optical depth for different photoadaptation parameters. Figure 6.10 shows that decrease of euphotic primary production with same aerosol optical depth was different for different photoadaptation parameters. With higher value of photoadaptation parameter the decrease of euphotic primary production was high. For maximum maritime aerosol loading, the decrease in euphotic primary production was increased from 5.34% to 9.25% when PI parameter increased from 52.7 W m^{-2} to 265.42 W m^{-2} (Tripathy et al., 2014).

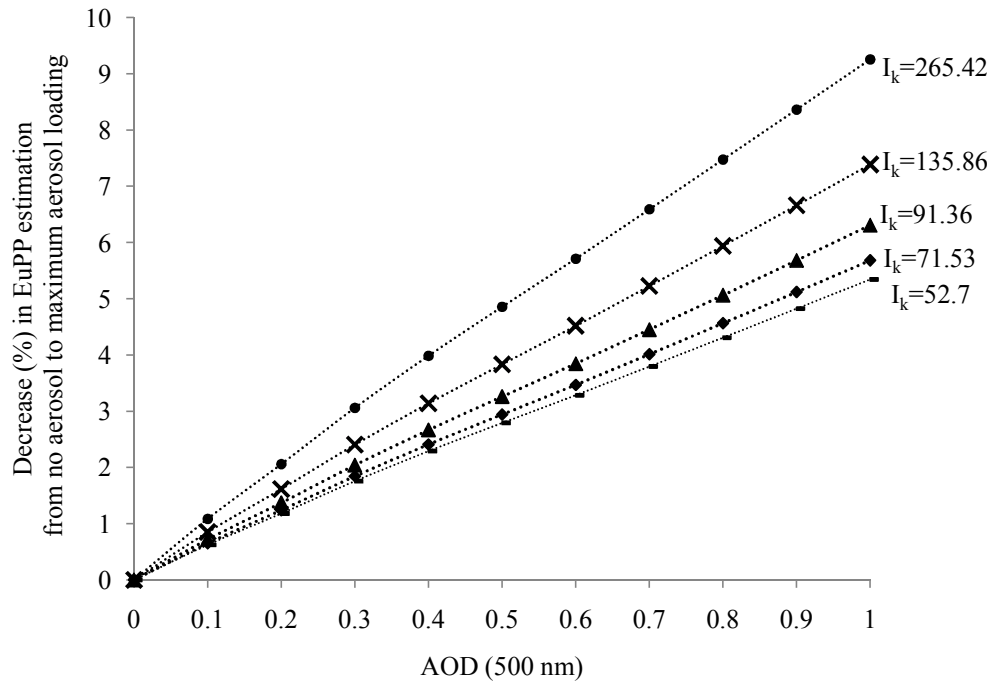


Figure 6.10: Decrease (%) in euphotic primary production with AOD for different photoadaptation parameters (I_k).

After discussion about the variation of PAR and euphotic primary production under different aerosol loadings for different value of photoadaptation, the variation of PAR and euphotic primary production under different cloud coverage is discussed in the next Section 6.6.3.

6.6.3 Sensitivity analysis: Cloud coverage and euphotic primary production

Simulation based study also has been carried out to understand attenuation of euphotic primary production at different aerosol and cloud coverage conditions. The variation of euphotic primary production with cloud coverage is shown in Figure 6.11. For overcast sky and for maritime clean

aerosol when AOD varied from no aerosol to maximum aerosol loading, decrease of $\text{EuPP}/\text{EuPP}_{\text{clear sky}}$ was observed from 33% to 38% (Tripathy et al., 2014). For 50% cloud coverage the decrease was from 6% to 11% compared to clear sky (Tripathy et al., 2014). Second-order polynomial was fitted with the variation of $\text{EuPP}/\text{EuPP}_{\text{clear sky}}$ with cloud coverage for AOD values 0, 0.3 and 1, respectively, and equations of the relationship between $\text{EuPP}/\text{EuPP}_{\text{clear sky}}$ with cloud coverage for various aerosol loading is shown in Figure 6.11.

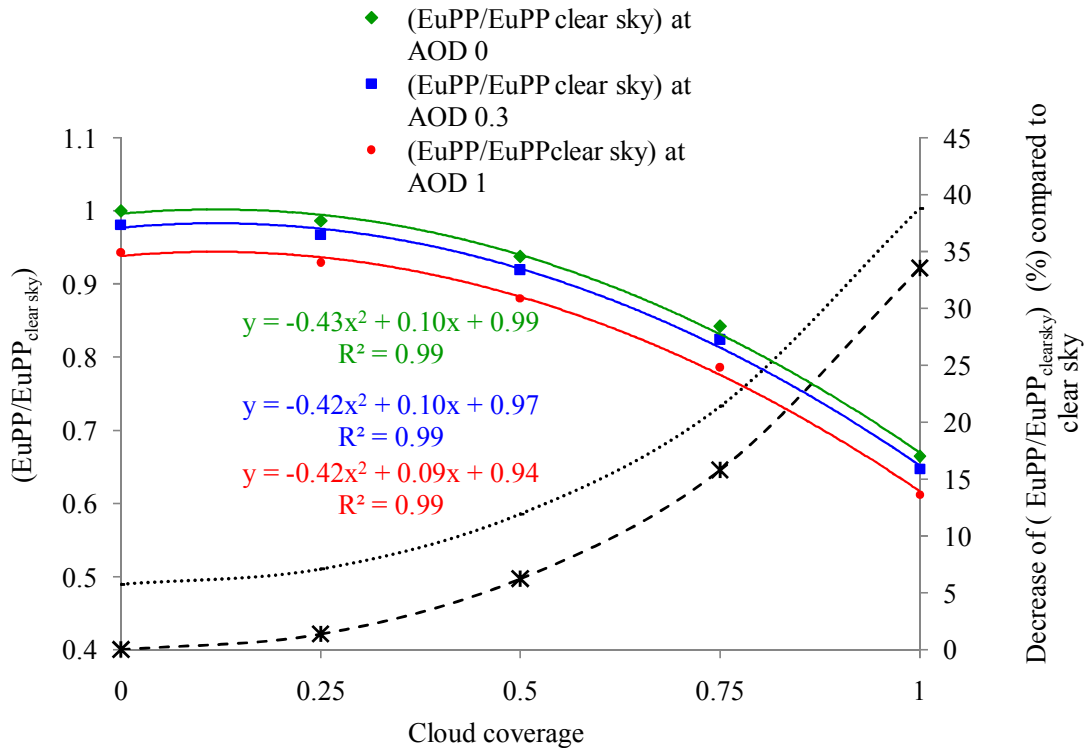


Figure 6.11: Variation of euphotic primary production under different cloud coverage (Date: November 04, 2001).

Cloud coverage plays dominating role compared to aerosol in attenuating PAR and finally on ocean primary production. Kumar et al. (2010) showed that cloud cover has a secondary effect in comparison to turbidity of ocean water to reduce PAR and primary productivity during summer and fall inter-monsoon in the northern Bay of Bengal.

6.7 Summary and conclusions

Modeling of ocean water column primary production has been discussed in this chapter. An analytical non-spectral irradiance model has been used to estimate euphotic primary production during ship cruise periods in the Arabian sea with inputs of chlorophyll-‘a’, diffuse attenuation coefficient in PAR wavelength range (k_{par}), euphotic depth, PAR at sea surface, PI parameter and daylength. Chlorophyll-‘a’, k_{par} , euphotic depth, PAR at sea surface and PI parameter have been measured from *in-situ* data. The variation of chlorophyll-‘a’ was from 0.22 to 1.5 mg m⁻³ during November 2001, 0.17–2.6 mg m⁻³ during January 2003, and 0.12–3.3 mg m⁻³ during March 2011. The variation of euphotic depth was from 33-64 m during November 2001, 21– 66 m during January 2003, and 17–67 m during March 2011. K_{par} ranged from 0.06 to 0.25 m⁻¹ during November 2001, 0.07–0.21 m⁻¹ during January 2003, and 0.07–0.27 m⁻¹ during March 2011. Estimated value of euphotic primary production varied from 135–1705 mg m⁻² day⁻¹ during the ship cruise periods (November 2001, January 2003 and March 2011) in the Arabian Sea. Dependence of PAR on AOD and its impact on ocean primary production has been investigated through sensitivity analysis and statistical equations have been generated between AOD, cloud coverage and euphotic primary production in the Arabian Sea.

The decrease in euphotic primary production under various aerosol loadings and cloud coverage has been observed to depend on photoadaptation parameter. The decrease in euphotic primary production has been observed to be about 10% for higher value of PI parameter when compared with lower value of PI parameter (~5%) for maximum maritime aerosol loading. Euphotic primary production has been reduced by about 26% for maximum urban type of aerosol compared to clear sky. Moderate maritime, maritime polluted, and desert aerosol have negligible influence (1.8% to 3.7%) on euphotic primary production estimation. Euphotic primary production has been reduced by 38% for maximum maritime aerosol loading and for overcast sky compared to clear sky. Reduction of euphotic primary production has been more during January compared to other seasons. Cloud coverage plays dominating role compared to aerosols in attenuating PAR and reducing the ocean primary production. This sensitivity study demonstrates

Chapter 6

the effect of varying AOD and aerosol models on PAR and subsequently on primary production estimation. The relationships developed between AOD and PAR and cloud coverage will improve the quantification of euphotic primary production.

Chapter 7

Summary and conclusions

This chapter carries a summary of the entire work presented in this thesis and the future scope.

7.1 Salient features of the research findings

Ocean colour remote sensing from space based observations is a well-known tool to provide quantitative information of ocean water constituents. Ocean colour remote sensing from Indian context had started with the launch of ocean colour satellite carrying ocean colour monitor OCEANSAT-1 Ocean Colour Monitor (OCM) data in May 1999 by Indian Space Research Organisation (ISRO). The study about ocean from space has been continued from second Indian satellite in ocean series OCEANSAT-2 spacecraft, which was successfully launched on September 23, 2009. Various geophysical variables such as chlorophyll-‘a’ concentration, vertical diffuse coefficient, Potential Fishing Zone (PFZ) identification, ocean primary production, algal bloom detection and studying the coastal processes etc. has been estimated from OCEANSAT-1 & 2 OCM data. For estimation of ocean primary production from space, standard model uses product of chlorophyll-‘a’, a scaling parameter that accounts for variation in plant physiology and photosynthetically available radiation (PAR) at sea surface. PAR with spatially invariant and uniform aerosol optical depth has been used in current primary production model from OCM. Thus, modeling PAR from OCEANSAT-1 & 2 OCM under variable aerosol loading and cloud coverage was found to be a desirable input parameter to estimate accurate ocean primary production.

This thesis aims to model PAR under natural conditions accounting for aerosol variation and effects of cloud cover. For this purpose, mainly OCEANSAT-1 & 2 OCM sensor data have been used. The pixels of OCM data have been separated first for clear sky or cloudy sky based on threshold test of reflectance at band 8 (865 nm) and reflectance ratio between band 8 (865 nm) and band 6 (665 nm) of OCM. The OCEANSAT-1 & 2 OCM was designed to tilt the sensor operationally $\pm 20^\circ$ away from the nadir to minimize sun glint contamination. However, it has been observed that some OCM data shows sun-glint during the months of April and August. Sun glint area has been masked using monthly wind climatology in OCM data. Accurately masking highly reflected sun glint region is very important for PAR modeling from space. If sunglint

Summary and conclusions

region has not masked properly, then it will be treated as cloudy region as clouds and sunglint region both shows high reflection in remote sensing data and vague PAR values will be generated over sun-glnt affected regions.

PAR from OCM has been estimated using two different methods under both clear and cloudy conditions. In the first method (method I), the atmosphere is treated as a single layer in clear sky conditions, or as a double layer in cloudy conditions i.e., a layer above the cloud top and a layer from the cloud top downwards. Global average cloud top pressure 574 hPa obtained from ISCCP (International Satellite cloud climatology Project) has been used to compute PAR under cloudy condition. Sea Surface reflectance has been neglected in the first approach. Extraterrestrial solar irradiance data at the top of the atmosphere from 400 nm to 700 nm has been subdivided into continuous fifteen wavelength band at 20 nm spectral interval. Extraterrestrial solar irradiance at each wavelength band has been obtained by using trapezoidal method of integration. The effects of Rayleigh scattering, ozone absorption, uniformly mixed gas absorption and aerosol scattering have been corrected at each band. Aerosol optical depth has been estimated at 865 nm spectral band of OCEANSAT-1 & 2 OCM assuming open ocean water absorbs strongly for the wavelength greater than 700 nm and water leaving radiance detected at the satellite altitude is the contribution of Rayleigh and aerosol scattering. Thus aerosol optical depth has been estimated after correction for Rayleigh scattering from the sensor detected water leaving radiance for the wavelength greater than 700 nm. Aerosol optical depths at other visible wavelengths have been estimated using angstrom exponent based spectral relationship.

PAR under cloudy sky conditions in method I has been estimated by an empirical relationship between cloud top reflectance with cloud optical thickness and backscattered fraction of incident radiation as a function of solar zenith angle. Cloud optical depth for very thick clouds (cloud optical depth greater than 4 m) has been estimated at 443 nm spectral band of OCEANSAT-1 & 2 OCM using a semi-analytical model. For very thin ice clouds having 34.3 μm effective radius, a quadratic relationship between cloud optical depth and TOA radiance at

Chapter 7

443 nm band for OCM viewing geometry has been obtained from COART (Coupled Ocean Atmosphere Radiative Transfer) model.

PAR has been estimated from OCM using second method (method II) which assumes that the effects of clouds and clear atmosphere can be decoupled with cloud system and ocean surface albedo. Extra-terrestrial solar irradiance has been estimated corresponding to the six discrete spectral bands in the visible region of OCM sensor derived using band specific Relative Spectral Response (RSR) function for OCM bands. Ocean surface albedo and cloud albedo have been estimated from TOA radiance of OCM data on a pixel by pixel basis. AOD at 865 nm and angstrom coefficient estimated from OCM have been used in this method as input.

Spatial distribution of OCM PAR showed latitudinal distribution of PAR with patchy nature because of clouds. OCM estimated PAR using two methods has been compared with PAR measured from the surface downwelling flux measurement instrument during different seasons in the Arabian Sea. Other than *in-situ* data obtained from ship cruise, OCEANSAT-2 OCM estimated PAR has also been validated with *in-situ* measured PAR obtained from the surface irradiance data of buoy at the CAL-VAL site situated between Kavaratti and Agatti island in the Arabian Sea.

The root mean square (r.m.s) difference between OCEANSAT-1 OCM PAR estimated using both the methods compared to *in-situ* measured PAR were within the accepted range ($\pm 10\%$) for PAR estimation from remote sensing. However, r.m.s difference between PAR estimated from OCEANSAT-1 OCM and limited *in-situ* measured PAR was lower for method I compared to method II. Correlation coefficient between OCEANSAT-1 PAR estimated from method I and *in-situ* data was 0.69 under both clear and cloudy condition. Under clear sky conditions, the correlation coefficient between OCEANSAT-1 PAR estimated from method I and *in-situ* data improved to 0.72. However, correlation coefficient between OCEANSAT-1 OCM PAR estimated from method II and *in-situ* data was less (~ 0.6) under clear sky compared to method I.

Summary and conclusions

OCEANSAT-1 & 2 OCM estimated PAR also has been compared with PAR estimated from other ocean colour sensors such as SeaWiFS (Sea-viewing Wide Field-of-view Sensor) and MODIS (Moderate Resolution Imaging Spectroradiometer). OCEANSAT-1 OCM PAR estimated from method I had good correlation having correlation coefficient (r^2) 0.95 with SeaWiFS PAR under clear sky condition. However, OCEANSAT-1 OCM PAR estimated from method I was positively biased (3.68%) compared to SeaWiFS PAR. The correlation coefficient (r^2) between OCEANSAT-1 OCM PAR estimated using method II with SeaWiFS PAR was 0.80 and r.ms difference was $3.72 \text{ Einstein m}^{-2} \text{ day}^{-1}$ (8.10%) under clear sky condition. The positive bias was larger (+4.30%) in OCEANSAT-1 OCM PAR estimated using method II, when compared to SeaWiFS PAR.

OCEANSAT-1 OCM PAR estimated from both the methods I & II, was comparable with SeaWiFS PAR values for thin clouds, small patches of clouds and at the edge of the thick clouds. At the edge of the clouds, both SeaWiFS and OCEANSAT-1 OCM PAR decreased by 20-23% from the clear sky. For very thin clouds, SeaWiFS and OCEANSAT-1 OCM PAR decreased by 5-10 %. However, at the middle of some cloud patches, SeaWiFS PAR was quite lower than OCEANSAT-1 OCM PAR. Maximum of ~89% decrease in SeaWiFS PAR was observed at the middle of the cloud. Under cloudy conditions, OCEANSAT-1 OCM PAR was decreased maximum ~49% observed in OCEANSAT-1 OCM PAR compare to clear sky. The differences between OCEANSAT-1 OCM and SeaWiFS PAR estimated under some thick clouds may be attributed to the saturation radiance settings for OCM spectral bands. Saturation radiance of OCM was kept low to enhance the signal to noise ratio for water surface. Due to this effect, high reflectance over middle of the some thick cloud was found to be saturated in the OCM bands. However due to bilinear gain setting in SeaWiFS sensor, spectral variability of radiance over cloud was maintained in the SeaWiFS sensor.

OCEANSAT-2 OCM estimated PAR using method I shows poor correlation (correlation coefficient 0.63) compared to OCEANSAT-1 OCM with *in-situ* measured PAR at CAL-VAL site situated between Kavaratti and Agatti island. The probable reason behind to get poor correlation

Chapter 7

between OCEANSAT-2 OCM PAR and *in-situ* measured PAR has been explained as the variability of clouds are very dynamic over Kavaratti region. However, OCEANSAT-2 OCM estimated PAR have good correlation (correlation coefficient 0.84) with MODIS Aqua estimated PAR at Kavaratti region. Methodology adopted to estimate PAR from OCEANSAT-1 & 2 OCM can produce reasonably accurate PAR estimates over the tropical Indian Ocean region. This approach can be extended to future OCEANSAT-3 OCM data for operational estimation of PAR for regional marine ecosystem applications.

Further, sensitivity study of PAR for various aerosol optical depths has been carried out for maritime, maritime polluted, urban and desert aerosol. For that purpose, PAR has been estimated at a single geographic location during ship cruise periods such as 3–17 November 2001, 4–19 January 2003 and 7–19 March 2011 in the Arabian Sea using a Coupled Ocean Atmosphere Radiative Transfer (COART) model. COART model derived PAR has been compared with *in-situ* PAR measured using a surface reference sensor of a visible-NIR radiometer. Output of COART model has been compared with *in-situ* measured PAR for different six aerosol models such as maritime, Urban, OPAC (Optical Properties of Aerosols and Clouds) maritime clean, OPAC maritime polluted, OPAC maritime tropical and desert. Aerosol model at each station has been selected in such a way that the discrepancies between the model and the measurements are the lowest. COART model derived PAR gives a good agreement with *in-situ* measured PAR.

A sensitivity study through COART model has been carried out to understand the effect of increased aerosol optical depth on PAR for different types of aerosol model. Clear sky has been defined as there are no aerosol loading and clouds. It is found that for maritime, maritime polluted and desert aerosol, PAR has attenuated to about 11–25%, whereas it has attenuated to 44% for urban aerosol type compared to clear sky. Reduction of PAR has been found more during January compared to other seasons. To understand the variability of PAR under different cloud coverage, direct and diffuse components of PAR have been computed using a non-linear

Summary and conclusions

relationship for variable cloud coverages. PAR is reduced by ~57% for high aerosol loading and for overcast sky. Cloud coverage plays dominating role compared to aerosols in attenuating PAR.

To estimate ocean primary production, an analytical non-spectral photosynthesis-irradiance model has been used. The inputs of the primary production model are chlorophyll-‘a’, diffuse attenuation coefficient in PAR wavelength range, euphotic depth, PI parameter, PAR at sea surface and daylength. Chlorophyll-‘a’, diffuse attenuation coefficient in PAR wavelength range, euphotic depth, PI parameter, PAR at sea surface were measured from *in-situ* observations during ship cruise periods in the Arabian Sea and daylength was calculated using astronomical equations. Dust aerosol has two way effects on ocean primary production. The addition of micronutrient iron from mineral dust to sea water can influence ocean productivity. On the other hand, aerosols that remain in the atmosphere and are not deposited in the sea water can reduce the solar energy at the sea surface and can influence ocean primary production. The second effect of reduced PAR under various aerosol optical depth and cloud coverage in primary production estimation has been done by a sensitivity study for various PI parameters.

The decrease in euphotic primary production has been observed to be about 10% for higher value of PI parameter when compared with lower value of PI parameter (~5%) for maximum maritime aerosol loading. Euphotic primary productions have been reduced by about 26% for maximum urban type of aerosol compared to no aerosol loading. Moderate maritime, maritime polluted and desert aerosol types have negligible influence (1.8% to 3.7%) on euphotic primary production estimation. Euphotic primary production has been reduced by 38% for maximum maritime aerosol loading and for overcast sky compared to clear sky. Thus PAR under variable aerosol loading and cloud coverage has significant role in ocean primary production estimation. However, modeling PAR from OCM has few limitations which are needed to be taken care in future studies. Future scope of modeling PAR from OCM data has been discussed in the next section.

7.2 Future Scope

The work presented in this thesis has attempted for modeling photosynthetically available radiation using OCEANSAT-1 & 2 OCM data for spatially variable aerosol optical depth and different cloudy conditions. Aerosol optical depth has been estimated at 865 nm of OCEANSAT-1 & 2 OCM assuming there is no radiance from water for wavelength greater than 700 nm due to strong infrared absorption by water. This approach is valid only for case-I open ocean water. A high density sampling over the coastal regions should be taken up in the future to better characterize the spectral properties of aerosols in coastal regions and their effect on PAR estimation from ocean color satellite data should be taken up for future studies.

Diffuse PAR has been computed under cloudy conditions using cloud optical depth estimated at 443 nm of OCEANSAT-1 & 2 OCM. However, algorithm for very thin high altitude cloud detection over water surface, estimation of effective radius of cloud droplets, cloud top pressure and correction of TOA radiance at the edge of clouds need to be improved in the future study. Further, different algorithms need to be used to detect thin clouds and thick dust aerosols separately. Saturation of spectral TOA radiance over cloud patches should be avoided in the future OCEANSAT missions similarly like SeaWiFS and MODIS.

Comparisons between PAR estimated from OCEANSAT-1 & 2 OCM with *in-situ* estimated PAR show a good validation under clear sky condition. However, *in-situ* data points are less for validation of PAR estimated from OCEANSAT-1 & 2 under cloudy condition. More observations of *in-situ* measurements under different types of cloudy condition are recommended in the future study. OCEANSAT-1 & 2 is polar orbiting satellite and does not account diurnal variability of the cloud property. Error is increased in estimation of daily averaged PAR in the southern part of the north Indian Ocean where variability of PAR under cloudy condition is more. It is recommended to explore use of geostationary data sets to measure daily PAR using high temporal resolution data.

REFERENCES

1. Angström, A., 1964. The parameters of atmospheric turbidity. *Tellus*, vol. 16, pp. 64–75.
2. Arvesen, J. C., Griffin, R. N., Jr., and Pearson, B. D., 1969, Determination of Extraterrestrial Solar Spectral Irradiance from a Research Aircraft, *Applied Optics*, vol. 8, no. 11, pp. 2215-2232.
3. Asrar, G., Myneni, R., Kanemasu, E.T, 1989, Estimation of plant canopy attributes from spectral reflectance measurements, *Theory and Application of Optical Remote Sensing* (G.Asrar,Ed.),Wiley, New York, pp. 252-295.
4. Antoine, D., Morel, A., 1996, Oceanic primary production 2. Adaptation of a spectral light-photosynthesis model in view of application to satellite chlorophyll observations. *Global Biogeochemical Cycles*, vol. 10, pp. 43–55.
5. Alados, I., Foyo-Moreno, I., Alados-Arboledas, L., 1996, Photosynthetically active radiation: measurements and modelling, *Agricultural and Forest Meteorology*, vol. 78, pp. 121-131.
6. Aiken J. and Moore, G., 1997, Photosynthetic Available Radiation, MERIS ATBD 2.18, version 5.
7. Ackerman, S., Strabala, K.I., Menzel, W.P., Frey, R.A., Moeller, C.C., Gumley, L.E, 1998, Discriminating clear sky from clouds with MODIS, *Journal of Geophysical Research*, vol. 103, no., D24, pp. 32141-32157.
8. Ackerman, S., Strabala, K., Menzel, P., Frey, R., Moeller, C., Gumley, L., Baum, B., Seemann, S.W., Zhang, H., 2006, Discriminating clear-sky from cloud with MODIS, Algorithm theoretical basis document (MOD 35), version 5., pp. 1-122.

9. Arnone, R.A., Ladner, S., Violette, P.E.L., Brock, J.C., Rochford P.A., 1998, Seasonal and interannual variability of surface photosynthetically available radiation in the Arabian sea, *Journal of Geophysical Research*, vol. 103, no. C4, pp. 7735-7748.
10. Anjorin, O.F., Utah, E.U., Likita, M.S., 2014, Estimation of hourly Photosynthetically-Active Radiation (PAR) from hourly global solar radiation in Jos, Nigeria, *Asian Review of Environmental and Earth Sciences*, vol. 1, no. 2, pp. 43-50.
11. Bhat, S.G., Krishnaswami, S., Lal, D., Rama and Moore, W.S, 1969, $^{234}\text{Th}/^{238}\text{U}$ ratios in the Ocean, *Earth and Planetary Science Letters*, vol. 5, pp. 483-491.
12. Brock, T.D., 1981, Calculating solar radiation for ecological studies, *Ecological Modelling*, vol. 14, no. 1-2, pp. 1-19.
13. Brine, D.T., Iqbal, M., 1982, Solar spectral diffuse irradiance under cloudless skies, *The Renewable Challenge: (Edited by B.H. Glenn and W.A. Kolar)* vol. 2, p.1271.
14. Blackburn, W.J., Proctor, J.T.A., 1983, Estimating photosynthetically active radiation from solar irradiance, *Solar Energy*, vol. 31, no.2, pp. 233-234.
15. Bird, R.E., 1984, A simple solar spectral model for direct-normal and diffuse horizontal irradiance, *Solar Energy*, vol. 32, no. 4, pp. 461-471.
16. Bird, R.E and C. Riordan, 1986, Simple solar spectral model for direct and diffuse irradiance on horizontal and tilted planes at the earth's surface for cloudless atmospheres, *Journal of Climate and Applied Meteorology*, vol. 25, pp. 87-97.
17. Baker, K., and Frouin, R., 1987, Relation between photosynthetically available radiation and total insolation at the ocean surface under clear skies, *Limnology and Oceanography*, vol. 32, no. 6, pp. 1370-1377.

18. Banse, K., Yong, M., 1990, Sources of variability in satellite-derived estimates of phytoplankton production in the Eastern Tropical Pacific, *Journal of Geophysical Research*, vol. 95, pp. 7201-7215.
19. Burlov-Vasiljev, K. A., Gurtovenko, E. A, and Matvejev, Y. B., 1995, New absolute measurements of the solar spectrum 310-685 nm, *Solar Physics*, vol. 157, pp. 51-73.
20. Behrenfeld, MJ, Falkowski, PG., 1997a, Photosynthetic rates derived from satellite-based chlorophyll concentration, *Limnology and Oceanography*, vol. 42, pp. 1-20.
21. Behrenfeld, M., Falkowski, PG., 1997b, A consumer's guide to phytoplankton primary productivity models. *Limnology and Oceanography*, vol. 42, no. 7, pp. 1479-1491.
22. Bores, R., 1997, Simultaneous retrieval of cloud optical depth and droplet concentration from solar irradiance and microwave liquid water path, *Journal of Geophysical Research*, vol. 102, pp. 29881-29891.
23. Barker, H.W., Curties, T.J., Leontieva, E., Stamnes, K., 1998, Optical depth of overcast cloud across Canada: Estimates based on surface pyranometer and satellite measurements, *Journal of Climate*, vol. 11, pp. 2980-2993.
24. Barnard, J.C., Long, C.N., 2004, A simple empirical equation to calculate cloud optical thickness using shortwave Broadband Measurements, *Journal of Applied Meteorology*, vol. 43, pp. 1057-1066.
25. Bonnet S., Guieu, C., 2004, Dissolution of atmospheric iron in seawater, *Geophysical Research Letters*, vol. 31, no. 3, pp. 1-4.
26. Bouman, H., Platt T., Sathyendranath, S, Stuart, V., 2005, Dependence of light-saturated photosynthesis on temperature and community structure. *Deep-Sea Research*, 52, 1284-1299.

27. Bond, T. C. and Bergstrom, R. W., 2006, Light Absorption by Carbonaceous Particles: An Investigative Review, *Aerosol Science and Technology*, vol. 40, pp. 27–67.
28. Bouvet, M., 2006, MERIS Photosynthetically Available Radiation: a product quality assessment. Proceedings of the Second Working Meeting on MERIS and AATSR Calibration and Geophysical Validation (MAVT-2006), ESRIN, Frascati, Italy. Available at http://envisat.esa.int/workshops/mavt_2006/papers/56_bouve.pdf
29. Boucher, O., D. Randall, P. Artaxo, C. Bretherton, G. Feingold, P. Forster, V.-M. Kerminen, Y. Kondo, H. Liao, U. Lohmann, P. Rasch, S.K. Satheesh, S. Sherwood, B. Stevens and X.Y. Zhang, 2013, Clouds and Aerosols. In: *Climate Change 2013: The Physical Science Basis. Contribution of Working Group I to the Fifth Assessment Report of the Intergovernmental Panel on Climate Change* [Stocker, T.F., D. Qin, G.-K. Plattner, M. Tignor, S.K. Allen, J. Boschung, A. Nauels, Y. Xia, V. Bex and P.M. Midgley (eds.)]. Cambridge University Press, Cambridge, United Kingdom and New York, NY, USA.
30. Cebula, R. P., DeLand, M. T., Hilsenrath, E., Schlesinger, B. M., Hudson, R. D., and Heath, D. F., 1991, Intercomparisons of the Solar Irradiance measurements from the Nimbus-7 SBUV, the NOAA-9 and NOAA-11 SBUV/2, and the STS-34 SSBUV Instruments: A preliminary assessment, *Journal of Atmospheric and Terrestrial Physics*, vol. 25, pp. 993-997.
31. Cullen, J.J., Neale, P.J., Lesser, M., 1992, Biological weighting function for the inhibition of phytoplankton photosynthesis by ultraviolet radiation. *Science*, vol. 258, pp. 646-650.
32. Colina, L., Bohlin, R. C., and Castelli, F., 1996, The 0.12-2.5 micron absolute flux distribution of sun for comparison with solar analog star, *The Astrophysical Journal*, vol. 112, pp. 307-315.

33. Chauhan, P; M. Mohan, P. Matondkar, Beena kumara and Shailak Nayak, 2002, Surface chlorophyll-a estimation using IRS-P4 OCM data in the Arabian Sea, *International Journal of Remote Sensing*, vol. 23, no. 8, pp. 1663-1676.
34. Chauhan, P., Mohan, M., Nayak., S., 2003, Comparative analysis of ocean color measurements of IRS-P4 OCM and SeaWiFS in the Arabian Sea, *IEEE Transactions on Geosciences and Remote Sensing*, vol. 41, no. 4, pp. 922-926.
35. Chauhan, P., Sanwlani, N., Navalgund R.R, 2009, Aerosol optical depth variability in the northeastern Arabian Sea during winter monsoon: a study using in-situ and satellite measurements, *Indian Journal of Marine Sciences*, vol. 38, no. 4, pp. 390-396.
36. Carder, K.L., Chen, F.R., Hawes, S.K., 2003, Instantaneous Photosynthetically Available Radiation and Absorbed Radiation by Phytoplankton, MODIS Ocean Science Team Algorithm Theoretical Basis Document ATBD 20, Version 7 , February 2003, pp. 1- 24.
37. Cho, H. K., Jeong, M. J., Kim J. and Kim, Y. J., 2003, Dependence of diffuse photosynthetically active solar irradiance on total optical depth, *Journal of Geophysical Research*, vol.108, no. D9, 4267, doi:10.1029/2002JD002175.
38. Cropp, R. A., Gabric, A. J., McTainsh, G.H., Braddock, R. D., Tindale, N., 2005, Coupling between ocean biota and atmospheric aerosols: dust, dimethylsulphide, or artifact? *Global Biogeochemical Cycles*, vol. 19, no. 4, pp. 1-13.
39. Chand, D., Wood, R., Anderson, T. L. Satheesh, S. K. and Charlson, R. J., 2009, Satellite-derived direct radiative effect of aerosols dependent on cloud cover. *Nature Geoscience*, vol. 2, pp. 181–184.
40. Chiu, J.C., Huang, C.H, Marshak, A., Slutsker, I., Giles, D.M., Holben, B.N, Knyazikhim, Y., Wiscombe, W.J., 2010, Cloud optical depth retrieval from the

Aerosol Robotic Network (AERONET) cloud mode observations, *Journal of Geophysical Research*, vol. 115, no. D142024, doi: 10.1029/2009JD013121.

41. Chami, M., Mallet, M. and Gentili, B., 2012, Quantitative analysis of the influence of dust sea surface forcing on the primary production of the subtropical Atlantic Ocean using a ten-year time series of satellite observations, *Journal of Geophysical Research*, vol. 117, no. C07008, pp. 1–14.
42. Ciais, P., Sabine, G., Bala, L., Bopp, V., Brovkin, J., Canadell, A., Chhabra, R., DeFries, J., Galloway, M., Heimann, C., Jones, C., Le Quéré, R.B., Myneni, S., Piao and P. Thornton, 2013, Carbon and Other Biogeochemical Cycles. In: *Climate Change 2013: The Physical Science Basis. Contribution of Working Group I to the Fifth Assessment Report of the Intergovernmental Panel on Climate Change* [Stocker, T.F., D. Qin, G.-K. Plattner, M. Tignor, S.K. Allen, J. Boschung, A. Nauels, Y. Xia, V. Bex and P.M. Midgley (eds.)]. Cambridge University Press, Cambridge, United Kingdom and New York, NY, USA.
43. Dugdale, R.C, Goering, J.J., 1967, Uptake of new and regenerated forms of nitrogen in primary productivity, *Limnology and Oceanography*, vol. 12, pp. 196-206.
44. Davis, J.A., Hay, J.E., 1980, Calculation of solar radiation incident on a horizontal surface, Proc. 1st Canadian Solar Radiation Data Workshop (Edited by J. Hay and T.K. Won), p.32.
45. Dedieu, G., Deschamps, P.Y., Kerr, Y.H., 1987, Satellite estimation of solar irradiance at the surface of the Earth and of surface albedo using a physical model, *Journal of Climate and Applied Meteorology*, vol. 26, pp. 79-87.
46. Doerffer R., 1992, Imaging spectroscopy for detection of chlorophyll and suspended matter, in *Imaging spectroscopy: Fundamentals and Prospective Applications*, edited by F. Toselli and Bodechtel, (Kluwer Academic Publishers, Dordrecht/Boston/London), pp. 215-255.

47. DeLand, M. T. and Cebula, R. P., 1993, Composite MgII solar activity index for solar cycles 21 and 22, *Journal of Geophysical Research.*, vol. 98, pp. 12809-12823.
48. Dye, D.G., and Shibaski, R., 1995, Intercomparison of global PAR data sets, *Geophysical Research Letters*, vol. 22, issue 15, pp. 2013-2016.
49. Dye, D.G., 2004, Spectral composition and quanta-to-energy ratio of diffuse photosynthetically active radiation under diverse cloud conditions, *Journal of Geophysical Research D*, vol. 109, no.D10.
50. Dong, X., Ackerman T.P., Clothiaux, E.E., Pilewskie, P., Han, Y., 1997, Microphysical and radiative properties of boundary layer stratiform clouds deduced from ground-based measurements, *Journal of Geophysical Research.*, vol. 102, pp. 23829-23843.
51. Dawes, Clinton J., 1998, *Marine Botany*, second edition, John Wiley & Sons, Inc., 605 Third Avenue, New York, NY-10158-0012, pp. 479, ISBN 978-0-471-19208-4.
52. Das, I., Mohan, M., Krisnamoorthy, K., 2002, Detection of marine aerosols with IRS-P4 Ocean colour Monitor, *Proceedings of the Indian Academy of Sciences-Earth and Planetary Sciences*, vol. 111, pp. 425-435.
53. Douglass, A., Fioletov, V. (Coordinating Lead Authors), Chapter 2 in *Scientific Assessment of Ozone Depletion: 2010*, Global Ozone Research and Monitoring Project–Report No. 52, 516 pp., World Meteorological Organization, Geneva, Switzerland, 2011.
54. Eppley, R.W., 1980, Estimating Phytoplankton growth rates in the central oligotrophic oceans. In Falkowski, P.G. (ed.), *Primary Productivity in the Sea*. Plenum Press, New York, pp 231-242.

55. Eck, T.F, and Dye, D.G.,1991, Satellite estimation of incident Photosynthetically Active Radiation using ultraviolet reflectance, *Remote Sensing of Environment*, vol. 38, pp. 135-146.
56. Fujita, Y., 1970, Photosynthesis and plant pigments, *Bull. Plank. Soc. Japan.*, vol. 17, pp. 20-31.
57. Frouin, R., Chertock, B., 1992, A technique for global monitoring of net solar irradiance at the ocean surface, Part I: Model, *Journal of Applied Meteorology*, vol. 31, pp. 1056-1066.
58. Frouin, R. and Pinker, R.T., 1995, Estimating Photosynthetically Active Radiation (PAR) at the Earth's surface from satellite observations. *Remote Sensing of Environment*, vol. 51, pp. 98-107.
59. Frouin, R., Franz, B.A., and Werdell, P.J., 2003, The SeaWiFS PAR product. In: Algorithm updates for the fourth SeaWiFS data reprocessing. Hooker, S.B. and Firestone, E.R. (eds.), NASA Technical Memorandum, NASA-GSFC, Greenbelt, Maryland, 22, 2000-206892.
60. Frouin, R., Franz, B., Wang. M., 2005, Algorithm to estimate PAR from SeaWiFS data. Version 1.2 – documentation. Available at http://oceancolor.gsfc.nasa.gov/DOCS/seawifs_par_wfigs.pdf.
61. Frouin, R. and Murakami, H., 2007, Estimating Photosynthetically Available Radiation at the Ocean Surface from ADEOS-II Global Imager Data, *Journal of Oceanography*, vol. 63, pp. 493-503.
62. Frouin, R. and McPherson, J., 2012, Estimating photosynthetically available radiation at the ocean surface from GOCI data, *Ocean Science Journal*, vol. 47, pp. 313-321.

63. Field, B.C., Behrenfeld, M.J., Randerson, J.T., Falkowski, P., 1998, Primary Production of the Biosphere: Integrating Terrestrial and Oceanic Components, *Science*, vol., 281, pp. 237-240.
64. Fischer, J., Schüller, L., Preusker, R., 2000, Cloud albedo and cloud optical thickness, Algorithm Theoretical Basis Document, ATBD 2.1 and 2.2, Issue 4, Rev. 1, pp. 30.
65. Goldberg, B., and Klein, W.H., 1980, A model for determining the spectral quality of daylight on a horizontal surface at any geographical location, *Solar Energy*, 24, pp. 351-357.
66. Gathman, S.G., 1983, Optical properties of the marine aerosol as predicted by the Navy aerosol model, *Optical Engineering*, vol. 22, pp. 57–62.
67. Gesell, G., 1989, An algorithm for snow and ice detection using AVHRR data: An extension to the APOLLO software package, *International Journal of Remote Sensing*, vol. 10, pp. 897-905.
68. Gregg, W.W., and K.L. Carder, 1990, A simple spectral solar irradiance model for cloudless maritime atmosphere, *Limnology Oceanography*, vol. 35, no. 8, pp. 1657-1675.
69. Geider, R.J, Osborne, B.A, 1991, Algal Photosynthesis: Measurement of Algal Gas Exchange. New York, Chapman & Hall, 256p.
70. Gadhavi, H. And Jayaraman, A., 2010, Absorbing aerosols: contribution of biomass burning and implications for radiative forcing, *Annales Geophysics*, vol. 28, pp. 103–111.
71. Hu, Y.X., Stamnes, K., 1993, An accurate parameterization of the radiative properties of water clouds suitable for use in climate model, *Journal of Climate*, vol. 6, pp. 728-742.

72. Husar, R. B., Prospero, J.M., Stowe, L.L, 1997, Characterization of tropospheric aerosols over the ocean with the NOAA advanced very high resolution radiometer optical thickness operational product, *Journal of Geophysical Research*, vol. 102, no. D14, pp. 16889-16909.

73. Hess, M., Koepke, P. and Schult, I., 1998, Optical properties of aerosols and clouds: the software package OPAC, *Bulletin of American Meteorological Society*, vol. 79, no. 5, pp. 831–844.

74. Hu, B., Wang, Y., Guangren Liu, G., 2007, Spatio temporal characteristics of photosynthetically active radiation in China, *Journal of Geophysical Research*, vol. 112, no. D14106, doi:10.1029/2006JD007965.

75. Hartmann, D.L., A.M.G. Klein Tank, M. Rusticucci, L.V. Alexander, S. Brönnimann, Y. Charabi, F.J. Dentener, E.J. Dlugokencky, D.R. Easterling, A. Kaplan, B.J. Soden, P.W. Thorne, M. Wild and P.M. Zhai, 2013, Observations: Atmosphere and Surface. In: *Climate Change 2013: The Physical Science Basis. Contribution of Working Group I to the Fifth Assessment Report of the Intergovernmental Panel on Climate Change* [Stocker, T.F., D. Qin, G.-K. Plattner, M. Tignor, S.K. Allen, J. Boschung, A. Nauels, Y. Xia, V. Bex and P.M. Midgley (eds.)]. Cambridge University Press, Cambridge, United Kingdom and New York, NY, USA.

76. Hovis, W.A., Clark, D.K., Anderson, F., Austin, R.W., Wilson, W.H., Baker, E.T., Ball, D., Gordon, H.R., Mueller, J.L., El Sayed, S.Y., Sturm, B., Wrigley, R.C., and Yentsch, C.S., 1980, Nimbus-7 Coastal Zone Color Scanner: System description and initial imagery. *Science*, vol. 210, pp. 60-63.

77. Heath, D. F. and Schlesinger, B. M., 1986, The Mg 280-nm doublet as a monitor of changes in solar ultraviolet irradiance, *Journal of Geophysical Research*, vol. 91, pp. 8672-8682.

78. Iqbal, M., 1983, An introduction to solar radiation (pp. 107-152). Toronto, ON: Academic Press Canada.
79. IPCC, 2001: Climate Change 2001: The Scientific Basis. Contribution of Working Group I to the Third Assessment Report of the Intergovernmental Panel on Climate Change [Houghton, J.T., Y. Ding, D.J. Griggs, M. Noguer, P.J. van der Linden, X. Dai, K. Maskell, and C.A. Johnson (eds.)]. Cambridge University Press, Cambridge, United Kingdom and New York, NY, USA, 881pp.
80. IPCC, 2005, "IPCC Special Report on Carbon Dioxide Capture and Storage", Bert Metz, Ogunlade Davidson, Heleen de Coninck, Manuela Loos, Leo Meyer (Eds), Cambridge University Press, UK, pp. 431.
81. IPCC, 2007: Climate Change 2007: The Physical Science Basis. Contribution of Working Group I to the Fourth Assessment Report of the Intergovernmental Panel on Climate Change. [Solomon, S., D. Qin, M. Manning, Z. Chen, M. Marquis, K.B. Averyt, M. Tignor and H.L. Miller (eds.)]. Cambridge University Press, Cambridge, United Kingdom and New York, NY, USA, 996 pp.
82. IOCCG, 1999, Status and Plans for Satellite Ocean-Colour Missions: Considerations for Complementary Missions. Yoder, J. A. (ed.), Reports of the International Ocean-Colour Coordinating Group, No. 2, IOCCG, Dartmouth, Canada. ISSN: 1098-6030.
83. IOCCG, 2000, Remote Sensing of Ocean Colour in Coastal, and Other Optically-Complex, Waters. Sathyendranath, S. (ed.), Reports of the International Ocean-Colour Coordinating Group, No. 3, IOCCG, Dartmouth, Canada.
84. IOCCG, 2004, Guide to the Creation and Use of Ocean-Colour, Level-3, Binned Data Products. Antoine, D. (ed.), Reports of the International Ocean-Colour Coordinating Group, No. 4, IOCCG, Dartmouth, Canada.

85. IOCCG, 2007, Ocean-Colour Data Merging. Gregg, W. (ed.), Reports of the International Ocean-Colour Coordinating Group, No. 6, IOCCG, Dartmouth, Canada.
86. IOCCG, 2012, Ocean-Colour Observations from a Geostationary Orbit. Antoine, D. (ed.), Reports of the International Ocean-Colour Coordinating Group, No. 12, IOCCG, Dartmouth, Canada.
87. Johnson, F.S., 1954, The solar constant, *Journal of Meteorology*, vol. 11, pp. 431-439.
88. Jerlov, N.G., 1976, Marine optics, 2nd edition, New York: Elsevier press.
89. Jassby, A. D., T. Platt, 1976, Mathematical formulation of the relationship between photosynthesis and light for phytoplankton,” *Limnology and Oceanography*, vol. 21, pp. 540–546.
90. Justus, C.G. and M.V. Paris, 1985, A model for solar spectral irradiance at the bottom and top of a cloudless atmosphere, *Journal of Climate Applied Meteorology*, vol. 24, pp. 193-205.
91. Jin, Z. and Stamnes, K., 1994, Radiative transfer in non uniformly refracting layered media: atmosphere-ocean system, *Applied Optics*, vol. 33, no. 3, pp. 431–442.
92. Jin, Z., Charlock, T. P., Rutledge, K., Stamnes, K. and Wang, Y., 2006, Analytical solution of radiative transfer in the coupled atmosphere-ocean system with a rough surface, *Applied Optics*, vol. 45, no. 28, pp. 7443–7455.
93. Joseph, G., 2005, Fundamentals of remote sensing, University Press, Hyderabad.
94. Janjai, S., Wattan, R., 2011, “Development of a model for the estimation of photosynthetically active radiation from geostationary satellite data in a tropical environment”, *Remote Sensing of Environment*, vol. 115, pp. 1680–1693.

95. Kneizys, F.X., Shettle, E.P., Gallery, W.O., Chetwynd, J.H., Abreu, Jr.L.W., Selby, J.E.A., Fenn, R.W. and McClatchey, R.A., 1980, Atmospheric Transmittance/Radiance: Computer code LOWTRAN 5, Tech Rep. AFGL-TR-80-0067, U.S. Air Force Geophysics Laboratory, Bedford, Massachusetts.
96. Kirk, J.T.O, 1983, *Light and photosynthesis in aquatic ecosystems*. Cambridge University Press, Cambridge.
97. Kirk, J. T.O., 1984, Dependence of relationship between inherent and apparent optical properties of water on solar altitude, *Limnology and Oceanography*, 29, 350-356.
98. Kirk, J.T.O, 1994, *Light and photosynthesis in aquatic ecosystems*. 2nd Edition. Cambridge University Press, Cambridge.
99. King, M.D, 1987, Determination of the scaled optical thickness of clouds from reflected solar radiation measurements, *Journal of the Atmospheric Sciences*, vol. 44, no.13, pp. 1734- 1751.
100. King, M.D, Kaufman, Y. J., Menzel W. P., Tanré, D., 1992, Remote sensing of cloud, aerosol and water vapor properties from the Moderate Resolution Imaging Spectrometer (MODIS). *IEEE Transactions on Geosciences and Remote Sensing*, vol. 30, pp. 2–27.
101. King, M.D, Tsay, S., Platnick, S.E., Wang, M., Liu, K., 1997, Cloud retrieval algorithms for MODIS: optical thickness, effective particle radius, and thermodynamic phase, MODIS Algorithm Theoretical Basis Document No. ATBD-MOD-05, pp. 79.
102. Kumar, S.P., Prasad, T.G., 1996, Winter cooling in the northern Arabian Sea, *Current Science*, vol. 71, no. 11, pp. 834-841.

103. Kumar, S. P., Narvekar, J., Nuncio M., Kumar, A., Ramaiah, N., Sardesai, S., Gauns, M., Fernandes, V., Paul, J., 2010, Is the biological productivity in the Bay of Bengal light limited? *Current Science*, vol. 98, no. 10, pp. 1331–1339.
104. Kokhanovsky, A.A., Rozanov, V.V., Zege, E.P., Bovensmann, H., Burrows, J.P., 2003, A semianalytical cloud retrieval algorithm using backscattered radiation in 0.4–2.4 μm spectral region, *Journal of Geophysical Research*, vol. 108, no. D1, 4008, doi:10.1029/2001JD001543.
105. Kokhanovsky, A.A., Nauss, T., 2006, Reflection and transmission of solar light by clouds: asymptotic theory, *Atmospheric Chemistry and Physics*, vol. 6, pp. 5537–5545.
106. Kokhanovsky, A., Vountas, M., Burrows, J.P., 2011, Global Distribution of Cloud Top Height as Retrieved from SCIAMACHY Onboard ENVISAT Space borne Observations, *Remote Sensing*, vol. 3, pp. 836–844; doi:10.3390/rs3050836.
107. Kripalani, R.H., Kumar, P., 2004, Northeast monsoon rainfall variability over south peninsular india vis-a` -vis the indian ocean dipole mode, international journal of climatology, *International Journal of Climatology*, vol. 24, pp. 1267–1282. Published online in Wiley InterScience (www.interscience.wiley.com). DOI: 10.1002/joc.1071.
108. Kaufman, Y., Remer, L.A., Tanre, D., Li, R.R., Kleidman, R., Matto, S., Levy, R.C., Eck, T.F., Holbel, B.N., Ichoku, C., Martins, J.V., Koren, I., 2005, A critical examination of the residual cloud contamination and diurnal sampling effects on MODIS estimates of aerosol over ocean, *IEEE Transactions on Geosciences and Remote Sensing*, vol. 43, pp. 2886–2897, doi:10.1109/TGRS.2005.858430.
109. Karlgard, J., 2008, Estimating cloud droplet effective radius from satellite reflectance data, Diploma work of 15 ESCTs, Department of Physics, Lund University, pp.29.

110. Kathilankal, J.C., O'Halloran, T. L., Schmidt, A., Hanson, C. V. , Law, B. E., 2014, Development of a semi-parametric PAR (Photosynthetically Active Radiation) partitioning model for the United States, version 1.0, *Geoscientific Model Development*, 7, pp. 2477–2484, doi:10.5194/gmd-7-2477-2014.
111. Labs, D. and Neckel, H., 1968, The radiation of the solar photospherch from 2000 Å to 100mm, *Z. Astrophysics*, vol. 69, pp. 1-73.
112. Lacis, A., Hansen, J.E., 1974, A parameterization for the absorption of solar radiation at the Earth's surface. *Journal of the Atmospheric Science*, vol. 31, pp. 118–133.
113. Leckner, B., 1978, The spectral distribution of solar radiation at the earth's surface – elements of a model, *Solar Energy*, vol. 20, pp. 143-150.
114. Liou, K.N, 1980, An introduction to atmospheric radiation, Academic Press, Inc., Orland, Florida, pp. 390.
115. Lillesand, T. M., 1987, Remote Sensing and Image interpretation, John Wiley, New York.
116. Longhurst, A. R. and Harrison, W. G., 1989, The biological pump: profiles of plankton production and consumption in the upper ocean, *Progress in Oceanography*, vol. 22, pp. 47-123.
117. Longhurst, A., Sathyendranath, S., Piatt, T., Caverhill, C., 1995. An estimate of global primary production in the ocean from satellite radiometer data, *Journal of Plankton Research*, vol. 17, pp. 1245–1271.
118. Lestrade, J. P., Acock, B. and T. Trent, 1990, The effect of cloud layer plane albedo on global and diffuse insolation, *Solar Energy*, vol. 44, no. 2, pp. 115–121.

119. Leontyeva, E., Stamnes, K., 1994, Estimation of cloud optical thickness from ground-based measurements of incoming solar radiation in the Arctic, *Journal of Climate*, vol. 7, pp. 566-578.

120. Liang, S., Zheng, T., Liu, R., Fang, H., Tsay, S., Running, S., 2006, Estimation of incident photosynthetically active radiation from Moderate Resolution Imaging Spectrometer data, *Journal of Geophysical Research*, vol. 111, no. D15208. doi:10.1029/2005JD006730.

121. Loeb, N. G., Wielicki, B.A., Doelling, D.R., Smith, G.L., Keyes, D.F., Kato, S., Manalo-Smith, N., Wong, T., 2009, Toward optimal closure of the Earth's top-of-atmosphere radiation budget, *Journal of Climate*, vol. 22, pp. 748–766.

122. Lavender, S., 2010, Photosynthetically Active Radiation. Algorithm Theoretical Basis Document, OLCI Level 2, S3-L2-SD-03-C12-ARG-ATBD, SD-03-C, version 1.2, pp. 1-15.

123. Li, L., Xin, X., Zhang, H., Liu, Q., 2012, Hourly photosynthetically active radiation estimation based on the combination of geostationary and polar orbital satellites *IEEE International Geoscience and Remote sensing Symposium*, pp. 5081-5084.

124. McClatchey R. A., Fenn, R.W., Selby, J. E. A., Volz, F. E. and Garing, J. S., 1972, Optical properties of the atmosphere, AFCRL report AFCRL-72-0497. Air Force Cambridge Laboratories, Bedford.

125. Mason, B.J., 1975, *Clouds, Rain and Rainmaking*, second edition, Cambridge University Press, Cambridge, London, New York, Melbourne, pp.183.

126. Morel, A., 1978, Available, usable, and stored radiant energy in relation to marine photosynthesis , *Deep Sea Research* , vol. 25, pp. 673-688 .

127. Morel, A., 1980, In-water and remote measurements of ocean color, *Boundary Layer Meteorology*, vol. 18, pp. 177-201.
128. Morel, A., J-F Berthon, 1989, Surface pigments, algal biomass profiles, and potential production of the euphotic layer: Relationships reinvestigated in view of remote-sensing applications, *Limnology and Oceanography*, vol. 34, pp. 1545-1562.
129. Morel, A., 1991, Light and marine photosynthesis: A spectral model with geochemical and climatological implications. *Progress in Oceanography*, vol. 26, pp. 263-306.
130. Mentall, J. E., Frederick, J. E., Herman, J. R., 1981, The solar irradiance from 200 to 330 nm, *Journal of Geophysical Research*, vol. 86, pp. 9881-9884.
131. Mount, G. H. and Rottman, G. J.: 1983a, The solar absolute spectral irradiance 1150-3173 Å: May 17, 1982, *Journal of Geophysical Research*, vol. 88, pp. 5403.
132. Mount, G. H. and Rottman, G. J.: 1983b, The solar absolute spectral irradiance at 1216 Å and 1800-3173 Å: January 12, 1983, *Journal of Geophysical Research*, vol. 88, pp. 6807.
133. Mentall, J. E., Guenter, B., and Williams, D. E., 1985, The solar spectral irradiance between 150-200nm, *Journal of Geophysical Research*, vol. 90, pp. 2265-2271.
134. Mentall, J. E. and Williams, D. E.: 1988, Solar ultraviolet irradiances on December 7, 1983 and December 10, 1984, *Journal of Geophysical Research*, vol. 93, pp. 735-746.
135. McClain, C.R., Yeh, E., 1994, Sun glint Flag Sensitivity study, NASA Technical Memorandum 104566, vol 13, McClain, C.R., Comiso, J.C., Fraser, R.S., Firestone, J.K., Schieber, B.D., Yeh, E., Arrigo, K.R., Sullivan, C.W., Eds., Goddard Space Flight Centre, Greenbelt, Maryland 20771, pp.52.
136. Mobley, C. D., 1994, *Light and Water: Radiative Transfer in Natural Waters*, Academic Press, San Diego.

137. Marra, J., Langdon, C., Knudson, C., 1995, Primary production, water column changes and the demise of a *Phaeocystis* bloom at the ML-ML site in the northeast Atlantic Ocean. *Journal of Geophysical Research*, vol. 100, pp. 6645-6653.
138. Min, Q., Harrison, L.C., 1996, Cloud properties derived from surface MFRSR measurements and comparison with GOES results at the ARM SGP Site, *Geophysical Research Letters*, vol. 23, pp. 1641-1644.
139. McPeters, R.D., Bhartia, P.K., Krueger, A.J., Herman, J.R., Wellemeyer, C.G., Seftor, G.J., Torres, O., Moy, L., Labow, G., Byerly, W., Taylor, S.L., 1998, Earth Probe Total Ozone Mapping Spectrometer (TOMS) Data Products User's guide, NASA Technical Publication, pp. 64.
140. Mohan, M., Chauhan, P., 2001, Simulations for optimal payload tilt to avoid sunglint in IRS-P4 Ocean Colour Monitor (OCM) data around the Indian subcontinent, *International Journal of Remote Sensing*, vol. 22, no.1, pp.185-190,. DOI: 10.1080/014311601750038929.
141. Moorthy, K.K, Saha, A., Niranjana, K., 2001, Spatial variation of aerosol spectral optical depth and columnar water vapour content over the Arabian Sea and Indian Ocean during the IFP of INDOEX", *Current Science (SUPPLEMENT)*, vol. 80, pp. 145-150.
142. Mallet, M., Chami, M., Gentili, B., Semp'ér'e, R. and Dubuisson, P., 2009, Impact of sea-surface dust radiative forcing on the oceanic primary production: a 1D modeling approach applied to the west african coastal waters, *Geophysical Research Letters*, vol. 36, no. 15, Article ID L15828, pp. 1-6.
143. Moon, K. J., Kim, J., Cho, H. K., Lee, J., Hong, S. Y. and Jeong, M. J., 2009, Effect of aerosol optical depth on diffuse photosynthetically active solar irradiance, *Asia-Pacific Journal of Atmospheric Sciences*, vol. 45, no. 3, pp. 307–317.

144. Menon, H. B., Sangekar, N., Lotliker, A., Krishnamoorthy, K. and Vethamony, P., 2011, Aerosol optical thickness and spatial variability along coastal and offshore waters of the eastern Arabian Sea, *ICES Journal of Marine Science*, vol. 68, no. 4, pp. 745-750.
145. McBride, P.J., Schmidt, K.S., Pilewskie, P., Kittelman, A.S, Wolfe, D.E, 2011, A spectral method for retrieving cloud optical thickness and effective radius from surface-based transmittance measurements, *Atmospheric Chemistry and Physics*, vol. 11, pp. 7235-7252.
146. Neckel, H., Labs, D., 1984, The solar radiation between 3300 and 12, 500 AA. *Solar Physics*, vol. 90, pp. 205–258.
147. Nunez, M., Fienberg, K., Kuchinke, C., 2005, Temporal structure of the solar radiation field in cloudy conditions: implications for satellite mapping of surface solar radiation. *Journal of Applied Meteorology*, vol. 44, pp. 167–185.
148. Nagamani, P. V., Chauhan, P., and Dwivedi R. M., 2008, Development of Chlorophyll-*a* Algorithm for Ocean Colour Monitor Onboard OCEANSAT-2 Satellite, *IEEE Geoscience and Remote Sensing Letters*, vol. 5, no. 3, pp. 527- 531.
149. Nicolet, M., 1981, The solar spectral irradiance and its action in the atmospheric photodissociation processes, *Planetary and Space Science*, vol. 29, pp. 951-974.
150. Nakajima, T., King, M.D., 1990, Determination of the optical thickness and effective particle radius of clouds from reflected solar radiation measurements. Part I: Theory, *Journal of the Atmospheric Science*, vol., 47, no.15, pp. 1878-1893.
151. Nair, S. K., Parameswaran, K. and Rajeev, K., 2005, Seven year satellite observations of the mean structures and variabilities in the regional aerosol distribution over the oceanic areas around the Indian subcontinent, *Annales Geophysicae*, 23, pp. 2011–2030.

152. Nasahara, K.N., 2009, Simple algorithm for estimation of Photosynthetically Active Radiation (PAR) using satellite data, *SOLA*, vol. 9, pp. 37-40, doi:10.2151/sola.2009-010.
153. O'Reilly, J.E, Maritonena, Mitchell, B.G., Seigal, D.A., Carder, K.L., Graver, S.A., Kahru, M and McClain, C.R., 1998, Ocean color chlorophyll algorithms for SeaWiFS, *Journal of Geophysics*, 103, pp. 24937-24963.
154. Peytureaux, R., 1968, La mesure absolue de l' energie emise par le centre du disque solaire de 4477 à 8638 Å, *Annual review of Astronomy and Astrophysics*, vol. 31, pp. 227.
155. Paltridge, G.W., Platt, C.M.R, 1976, Radiative processes in meteorology and climatology, Elsevier Scientific Publishing Company, Amsterdam, Oxford, New York, pp. 314.
156. Pierce, A. K. and Allen, R. G., 1977, in O. R. White (ed.), *The Solar Output and Its Variation*, Colorado Associated University Press, Boulder, p. 169.
157. Peterson, B.J. 1980, Aquatic primary productivity and the ¹⁴C-CO₂ method: A history of the productivity problem. *Annual Review of Ecology and Systematics*, vol.11, pp. 359-385.
158. Parsons, T. R., Takahashi, M., and Hargrave, B., 1984, Biological Oceanographic process, Third Edition, Pergamon Press, Oxford, pp. 330.
159. Pinker, R.T., and Ewing, J., 1985, Modeling surface solar radiation: Model formulation and validation, *Journal of Climate and Applied Meteorology*, 24, pp. 389-401.
160. Pinker, R. T. and I. Laszlo, 1992a. Modeling surface solar irradiance for satellite applications on global scale. *Journal of Applied Meteorology*, vol. 31, pp. 194-211.

161. Pinker, R.T., and Laszlo, I., 1992b, Global distribution of photosynthetically active radiation as observed from satellites, *Journal of Climate*, vol. 5, pp. 56-65.
162. Platt, T., Gallegos, C.L., Harrison, W.G., 1980, Photo inhibition of photosynthesis in natural assemblages of marine phytoplankton, *J. Mar. Res.*, vol. 38, pp. 687-701.
163. Platt, T., Sathyendranath, S., Caverhill, C. and Lewis, M.R., 1988a, Ocean primary production and available light: further algorithms for remote sensing. *Deep Sea Research*, vol. 35, pp. 855-879.
164. Platt, T. and Sathyendranath, S., 1988b, Oceanic primary production: estimation by remote sensing at local and regional scales. *Science*, vol. 241, pp. 1613-1620.
165. Platt, T. and Sathyendranath, S., 1993, Estimators of primary production for interpretation of remotely sensed data on ocean color, *Journal of Geophysical Research*, vol. 98, no. C8, pp. 14561-14576.
166. Platt, T., Sathyendranath, S., Forget, M.-H., White, G.N., Caverhill, C., Bouman, H., Devred, E. And SeungHyun, S., 2008, Operational estimation of primary production at large geographical scales. *Remote Sensing of Environment*, vol. 112, no. 8, pp. 3437-3448.
167. Post, W. M., T.H. Peng, W. R. Emanuel, A. W. King, V. H. Dale, and D. L. De Angelis. 1990., The Global Carbon Cycle. *American Scientist*, vol. 78, pp. 310–326.
168. Parol, F., Descloitres, J., Fouquart, Y., 2000, Cloud optical thickness and albedo retrievals from bidirectional reflectance measurements of POLDER instruments during ACE-2, *Tellus*, vol. 52B, pp. 888–908.
169. Quay, P.D., Wilbur, D.O., Richey, J.E., Devol, A.H., Benner, R., Forsberg, B.R., 1995, The $^{18}\text{O}/^{16}\text{O}$ of dissolved oxygen in rivers and lakes in the Amazon basin: a

- tracer of the ratio respiration to photosynthesis. *Limnology and Oceanography*, vol. 40, pp. 718-729.
170. Qasim, S. Z., 1998, Glimpes of the Indian Ocean, Universities Press (India) Limited, 3-5-819, Hyderguda, Hyderabad 50029, pp. 206.
171. Ryther, JH., 1956, Photosynthesis in the ocean as a function of light intensity, *Limnology and Oceanography*, vol. 1, pp. 61-70.
172. Ryther, JH, CS Yentsch, 1957, The estimation of phytoplankton production in the ocean from chlorophyll and light data , *Limnology and Oceanography*, vol. 2, pp. 281-286.
173. Rossow, W. B., Measuring cloud properties from space. A review, 1989, *Journal of Climate*, vol. 2 , pp. 201-213.
174. Rossow, W.B., and R.A. Schiffer, 1991, ISCCP cloud data products. *Bulletin of the American Meteorological Society*, vol. 72, pp. 2-20.
175. Rossow, W. B., and L. C. Garder, 1993a, Cloud detection using satellite measurements of infrared and visible radiances for ISCCP, *Journal of Climate*, vol. 6, pp. 2341-2369.
176. Rossow, W. B., and L. C. Garder, 1993b, Validation of ISCCP cloud detections, *Journal of Climate*, vol. 6, pp. 2370-2393.
177. Rossow, W.B., Walker, A.W., Beuschel, D.E., Roiter, M.D., 1996, International satellite cloud climatology project (ISCCP), Documentation of new cloud datasets, Science Systems and Application Inc. at NASA Goddard Institute for Space Studies, pp. 115.
178. Rossow, W.B., and R.A. Schiffer, 1999, Advances in understanding clouds from ISCCP, *Bulletin of the American Meteorological Society*, vol. 80, pp. 2261-2287.

179. Ranson, K.J., Irons, J.R., Daughtry, C.S.T, 1991, Surface albedo from bidirectional reflectance, *Remote Sensing of Environment*, vol. 35, pp. 201-211.
180. Raymond, P. A., and J. J. Cole, 2003, Increase in the export of alkalinity from North America's largest river. *Science*, vol. 301, pp. 88–91.
181. Rubio, M.A., Lo'pez, G., Tovar, J., Pozo, D., Batlles, F.J., 2005, The use of satellite measurements to estimate photosynthetically active radiation, *Physics and Chemistry of the Earth*, vol. 30, pp. 159–164.
182. Runnstr'om, M., Brogaard,S., and Olsson, L., 2006, Estimation of PAR over Northern China from daily NOAA AVHRR cloud cover classifications, *Geocarto International*, vol. 21, no. 1, pp. 51–60.
183. Raman, M., Dwivedi, R.M., 2011, Algorithm Theoretical Basis Document (ATBD) on ocean primary production algorithm for Oceansat II Ocean colour Monitor, Doc. No. SAC/EPSSA/MPSG/MBD/TR/3/2011, version 1.0, pp.21.
184. Steeman Nielsen, E., 1952, The use of radio-active carbon (^{14}C) for measuring organic production in the sea, *J.cons. perm. int. Explor. Mer.*, vol. 18, no. 2, pp. 117-140.
185. Slawyk, G., Collos, Y., Auclair, J.C, 1977, The use of the ^{13}C and ^{15}N isotopes for the simultaneous measurement of carbon and nitrogen turnover rates in marine phytoplankton. *Limnology and Oceanography*, vol. 22, pp. 925-932.
186. Stephens, G.L., 1978, Radiation profiles in extended water clouds. II Parameterization schemes, *Journal of the Atmospheric Science*, vol. 35, pp. 2123-2132.
187. Stephens, G. L., Ackerman, S., Smith, E.A., 1984, A shortwave parameterization revised to improve cloud absorption, *Journal of Atmospheric Sciences*, vol. 41, pp. 687-690.

188. Schiffer, R.A., and W.B. Rossow, 1983: The International Satellite Cloud Climatology Project (ISCCP): The first project of the World Climate Research Programme. *Bulletin of the American Meteorological Society*, vol. 64, pp. 779-784.
189. Schiffer, R.A., and W.B. Rossow, 1985: ISCCP global radiance data set: A new resource for climate research. *Bulletin of the American Meteorological Society*, vol. 66, pp. 1498-1505.
190. Saunders, R.W., 1985, Monthly mean cloudiness observed from Meteosat-2, *Journal of Climate and Applied meteorology*, vol. 24, pp. 114-127.
191. Saunders, R. W., and K. T. Kriebel, 1988, An improved method for detecting clear sky and cloudy radiances from AVHRR data, *International Journal of Remote Sensing*, vol. 9, pp. 123-150.
192. Sathyendranath, S., Platt, T., 1988, The spectral irradiance field at the surface and in the interior of the ocean: A model for applications in oceanography and remote sensing, *Journal of Geophysical Research*, vol. 93, no. C8, pp. 9270-9280.
193. Sathyendranath, S., Platt. T., 1989, Computation of aquatic primary production: Extended formalism to include effect of angular and spectral distribution of light. *Limnology and Oceanography*, vol. 34, pp. 188-198.
194. Sundquist, E. T., 1986, Geologic analogs: Their value and limitations in carbon dioxide research. In: *The Changing Carbon Cycle*, J. R. Trabalka and D. E. Reichle (eds.), Springer-Verlag, New York, pp. 371-402.
195. Seze, G., and W. B. Rossow, 1991, Time-cumulated visible and infrared radiance histograms used as descriptors of surface and cloud variations, *International Journal of Remote Sensing*, vol. 12, pp. 877-920.

196. Suresh, T., Desa, E., Desai, R.G.P., Jayraman, A., Mehra, P., 1996, Photosynthetically available radiation in the central and eastern Arabian Sea, *Current Science*, vol. 71, no. 11, pp. 883-887.
197. Sakshaug, E., A. Bricaud, Y. Dandoneau, P. G. Falkowski, D.A. Kiefer, L. Legendre, A. Morel, J. Parslow and M. Takahashi, 1997, Parameters of photosynthesis: Definitions, theory and interpretation of results, *Journal of Plankton Research*, vol. 19, pp.1637–1670.
198. Sarkar, S., Chokngamwong, R., Cervone, G., Singh, R. P. and Kafatos, M., 2006, Variability of aerosol optical depth and aerosol forcing over India, *Advances in Space Research*, vol. 37, no. 12, pp. 2153– 2159.
199. Schiller, K., 2006, Derivation of Photosynthetically Available Radiation from METEOSAT data in the German Bight with Neural Nets, *Ocean Dynamics*, vol. 56, pp. 79–85, DOI 10.1007/s10236-006-0058-1.
200. Singh, S. K., Raman, M., Dwivedi, R. M., Nayak, S. R., 2007 , An approach to compute Photosynthetically Active Radiation using IRS P4 OCM , *International Journal of Remote Sensing*, pp. 1 – 10. doi: 10.1080/01431160701264219.
201. SAC Report, 2007, Development of CAL-VAL Site at Kavaratti, SAC/RESA/MESG/MOP/CALVAL-1/07, pp. 203.
202. Saha, K., 2008, The Earth's Atmosphere its Physics and Dynamics, Springer, USA, pp.361.
203. Segar, D. A., 2008, Introduction to Ocean Sciences, International Thomson Publishing Europe, London, United State of America, pp.498.
204. Sigman, D. M., Hain, M. P., 2012, The Biological Productivity of the Ocean. Nature Education Knowledge, vol. 3, no. 10, pp. 21.

205. Talling, J.F., 1957, The phytoplankton population as a compound photosynthetic system, *New Phytologist*, vol 56, pp. 133-149
206. Tyler, J. E., 1966, Report on the second meeting of the joint group of experts on photosynthetic radiant energy, *UNESCO Technical Papers in Marine Science*, 2, pp.1-11.
207. Thekaekara, M. P., 1974, Extraterrestrial solar spectrum, 3000-6100 Å at 1-Å intervals, *Applied Optics*, vol. 13, pp. 518-522.
208. Tanre, D., Herman, M., Deschamps, P. Y., de Leffe, A., 1979, Atmospheric modeling for space measurements of ground reflectances, including bidirectional properties, *Applied Optics*, vol. 18, no. 21, pp. 3587-3594.
209. Taylor, J.P., Edwards, J.M., Glew, M.D, Hignett, P., Slingo, A., 1996, Studies with a flexible new radiation code. II: comparisons with aircraft short-wave observations, *Quarterly Journal of the Royal Meteorology Society*, vol. 122, pp. 839-861.
210. Thuillier, G., Herse, M., Simon, P.C., Labs, D., Mandel, H., Gillotay, D., 1997, Observation of the UVsolar irradiance between 200 and 350 nm during the ATLAS-1 mission by the SOLSPEC spectrometer; *Solar Physics*, vol. 171, pp. 283-302.
211. Thuillier, G., Herse, M., Simon, P. C., Labs, D., Mandel, H., Gillotay, D., Foujols, T., 1998, The visible solar spectral irradiance from 350 to 850 nm as measured by the SOLSPEC spectrometer during the ATLAS-1 mission; *Solar Physics*, vol. 177, pp. 41-61.
212. Thuillier, G., Hersé, M., Labs, D., Foujols, T., Peetermans, W., Gillotay, D., Simon, P.C., Mandel, H., 2003, The solar spectral irradiance from 200 to 2400 nm as measured by the SOLSPEC spectrometer from the ATLAS and EURECA missions. *Solar Physics* vol. 214, pp. 1-22.

213. Teets, D.A., 2003, Predicting Sunrise and Sunset Times, *The college mathematics journal*, vol. 34, no. 4, pp. 317-321.
214. Textor, C., et al., 2006, Analysis and quantification of the diversities of aerosol life cycles within AeroCom , *Atmospheric Chemistry and Physics*, vol. 6, pp. 1777–1813.
215. Tripathy, M., Raman, M., Chauhan, P., Ajai, 2014, Modulation in ocean primary production due to variability of photosynthetically available radiation under different atmospheric conditions, *International journal of Oceanography*, vol. 2014, no. 279412, pp. 1-12. (<http://dx.doi.org/10.1155/2014/279412>)
216. Tripathy, M., Raman, M., Chauhan, P., 2015, Estimation of photosynthetically available radiation (PAR) from OCEANSAT -I OCM using a simple atmospheric radiative transfer model, *Advances in Space Research*, vol. 56, pp. 1441-1452. doi: <http://dx.doi.org/10.1016/j.asr.2015.06.042>.
217. Van Laake, P.E., Azofeifa A.S., 2004, Simplified atmospheric radiative transfer modelling for estimating incident PAR using MODIS atmospheric products, *Remote Sensing of Environment*, vol. 91, pp. 98-113.
218. Verma, S., Venkataraman, C., Boucher, O. and Ramachandran, S., 2007, Source evaluation of aerosols measured during the Indian Ocean Experiment using combined chemical transport and back trajectory modeling, *Journal of Geophysical Research*, vol. 112, no. D11210, pp. 1-14, doi:10.1029/2006JD007698.
219. Verma, S., Venkataraman, C. and Boucher O., 2008, Origin of surface and columnar Indian Ocean Experiment (INDOEX) aerosols using source- and region-tagged emissions transport in a general circulation model, *Journal of Geophysical Research* , vol. 113, no. D24211, pp. 1-13, doi:10.1029/2007JD009538.
220. Viriyathanant, P., Thanaand, B. and A. Chabangborn, A., 2009, Effect of aerosol on photosynthetically active radiation, *BEST*, vol. 2, no. 1-2, pp. 71–72.

221. Wright, J. C., 1959, Limnology of Canyon Ferry Reservoir: Phytoplankton standing crop and primary production, *Limnology and Oceanography*, vol. 4, pp. 235-245.
222. Woolf, H.M., 1968, On the computation of solar elevation angles and the determination of sunrise and sunset times, Tech. Rep. NASA TM X-1646.
223. WCP-55, 1983, Report of WMO (CAS)/ Radiation Commission of IAMAP meeting of experts on aerosols and their climatic effects. Williamsburg, VA, A. Deepak and H.E. Gerber, Eds., pp. 107.
224. Williams, P.J., Robertson, J.E., 1991, Overall planktonic oxygen and carbon dioxide metabolisms: the problem of reconciling observations and calculation of photosynthetic quotients. *Journal of Plankton Research*, vol.13, pp. 153-169.
225. Wang, L., Wei Gong, W., Aiwon Lin, A., Bo Hu, B., 2014, Analysis of photosynthetically active radiation under various sky conditions in Wuhan, Central China, *International Journal of Biometeorology*, vol. 58, no. 8, pp. 1711-1720. DOI 10.1007/s00484-013-0775-3.
226. Zege, E. P., A. P. Ivanov, and I. L. Katsev, 1991, Image transfer through a scattering medium. Springer-Verlag, New York, 349 pp.
227. Zheng, T., 2007, Mapping photosynthetically active radiation (PAR) using multiple remote sensing data, Dissertation submitted to the Faculty of the Graduate School of the University of Maryland, College Park, in partial fulfilment of the requirements for the degree of Doctor of Philosophy, pp. 115.
228. Zheng, T., Liang, S., and Wang, K., 2008, "Estimation of Incident Photosynthetically Active Radiation from GOES", *Journal of Applied Meteorology and Climatology*, vol. 47, pp. 853-868.

229. Zibordi, G., Holben, B., Slutsker, I., Giles, D., D'Alimonte, D., Melin, F., Berthon, J., Vandemark, D., FENG, H., Schuster, G., Fabbri., B., Kaitala, S., Seppala, J., 2009, AERONET-OC: A Network for the Validation of Ocean Color Primary Products, *Journal of Atmospheric and Oceanic Technology*, vol. 26, pp. 1634-1651.
230. Zhang, J., and J. S. Reid, 2010, A decadal regional and global trend analysis of the aerosol optical depth using a data-assimilation grade over-water MODIS and Level 2 MISR aerosol products, *Atmospheric Chemistry and Physics*, vol. 10, pp. 10949–10963.

PUBLICATIONS

Publications from the thesis work in peer reviewed Journals

- 1) **Madhumita Tripathy, Mini Raman, R.M. Dwivedi, Ajai, 2012**, “Frequency of cyclonic disturbances and changing productivity patterns in the north Indian Ocean region: A study using Sea surface temperature and Ocean colour data”, *International Journal of Geosciences*, **3**, 490-506 doi:10.4236/ijg.2012.33052 Published Online July 2012 (<http://www.SciRP.org/journal/ijg>)
- 2) **Madhumita Tripathy, Mini Raman, Prakash Chauhan, Ajai, 2014**, “Modulation in ocean primary production due to variability of photosynthetically available radiation under different atmospheric conditions”, *International journal of Oceanography*, vol 2014, Article ID 279412, 12 pages. (<http://dx.doi.org/10.1155/2014/279412>)
- 3) **Madhumita Tripathy, Mini Raman, Prakash Chauhan, 2015**, “Estimation of photosynthetically available radiation (PAR) from Oceansat -I OCM using a simple atmospheric radiative transfer model”, *Advances in Space Research*, vol. 56, pp. 1441-1452. doi: <http://dx.doi.org/10.1016/j.asr.2015.06.042>

Publications in Conference/ Symposium

- 1) **Madhumita Tripathy, Mini Raman, R.M. Dwivedi, Ajai, 2009**, “ Frequency of cyclonic events and changing productivity patterns in the Indian Ocean region - Indications of climate change: A study using Sea Surface Temperature and Ocean Colour data”, presented in ISG conference during 4-6 February, 2009 in Deharadun.
- 2) **Madhumita Tripathy, Mini Raman, R.M. Dwivedi, Ajai, 2010**, “Primary Production in the north- eastern Arabian Sea off Gujarat coast using satellite data”. presented in ISG conference during 4-6 February, 2010 in Ahmedabad.
- 3) **Madhumita Tripathy, Mini Raman, Prakash Chauhan, R.M. Dwivedi, Ajai, 2012**, “Modeling of Photosynthetically Available Radiation (PAR) in various aerosols and

cloud cover condition and its effect on ocean primary productivity”, accepted in PORSEC-2012 held in Kochi, Kerala, India during November 05-09, 2012.

- 4) Mini Raman, Rahul Rajan, Neha Nandkeolyar, **Madhumita Tripathy**, R.M. Dwivwadi, Ajai, Prabhu Matondkar, **2012**, “ Estimation of Oceanic Primary Production in the Northeastern Arabian Sea using Oceansat 2 OCM-2”, Pan Ocean Remote Sensing Conference (PORSEC) 2012, 2012 held in Kochi, Kerala, India during November 05-09, 2012.